Single cell visual psychophysics

Dissertation

zur Erlangung des Doktorgrades
Doctor rerum naturalium
der Mathematisch-Naturwissenschaftlichen Fakultät
der Rheinischen Friedrich-Wilhelms-Universität Bonn

Vorgelegt von

Niklas Domdei

aus Düsseldorf, Germany

Bonn 2021

Angefertigt mit Genehmigung der Mathematisch-Naturwissenschaftlichen Fakultät der Rheinischen Friedrich-Wilhelms Universität Bonn.

1. Gutachter: Dr. Wolf M. Harmening
2. Gutachter: Prof. Dr. Gerhard von der Emde

Tag der Promotion: 03.09.2021

Erscheinungsjahr: 2021

Parts of this dissertation have already been published (* denotes equal contribution):

1. Domdei N, Reiniger JL, Holz FG, Harmening WM (2021) The Relationship Between Visual Sensitivity and Eccentricity, Cone Density and Outer Segment Length in the Human Foveola. *Investigative Ophthalmology and Visual Science*, 62(9): 31. DOI: 10.1167/iovs.62.9.31

2. Domdei N, Linden M, Reiniger J, Holz FG, Harmening WM (2019) Eye tracking based estimation and compensation of chromatic offsets for multi wavelength retinal microstimulation with foveal cone precision. *Biomedical Optics Express*, 10(8): 4126–4141. DOI: 10.1364/BOE.10.004126

3. Domdei N*,Domdei L*, Reiniger J, Linden M, Holz FG, Roorda A, Harmening WM (2018) Ultra-high contrast retinal display system for single photoreceptor psychophysics. *Biomedical Optics Express*, 9(1): 157-172. DOI: 10.1364/BOE.9.000157

Summary

On the one hand, the eye is the human being's window to the world. On the other hand the eye is a window to the human brain enabling noninvasive and *in vivo* assessment of nervous tissue. With adaptive optics scanning laser ophthalmoscopy (AOSLO) based microstimulation and psychophysical methods, it is possible to not only image but also stimulate the individual photoreceptor cells, and thereby test their impact on perception. Due to technical limitations, most of these psychophysical experiments addressing the fundamentals of human vision are currently conducted outside the foveola, the very center of the retina. This thesis focuses on determining and solving these limitations to enable human visual psychophysics in the foveola on an individual cellular level.

To convert the AOSLO into a display system for psychophysics, a fast modulation of the scanning laser beam is needed. The best solution in terms of switching time and contrast range is an acousto-optic modulator (AOM). However, these AOM leak a significant amount of residual light, producing a visible background and thereby limiting the experimental options. By cascading two AOMs, we not only eliminated the background, but also boosted the radiant power contrasts up to $1{:}10^{10}$, which is the highest visual contrast reported for any display system so far. A psychophysical validation experiment showed that this contrast ratio is sufficient to probe single foveal photoreceptor cells with small and easily perceivable stimuli that do not contain a detectable background. This background-free stimulation allows the photoreceptors to be probed (i) with lower light intensities and (ii) closer to the absolute threshold. Furthermore, a larger dynamic range in displayable light levels can drive photoreceptor responses in cones as well as in rods.

Commonly occurring small shifts in eye position during *in vivo* testing displace a stimulus by a significant amount when the transverse chromatic offset (TCO) is only statically compensated, thus ruling out reliable testing of an individual cell. Therefore a method was developed that requires only a single measurement of the TCO during controlled horizontal and vertical displacements of the eye to map retinal chromatic image shifts to the image space of a pupil camera. After such a calibration, the TCO was compensated for by continuously monitoring the eye position during experimentation and by interpolating correction vectors from a linear fit to the calibration data. This solution enabled real-time compensation of the TCO with high spatial precision an essential element for accurate foveolar cone-targeted psychophysical experimentation.

These refinements were successfully applied in order to conduct the first study assessing sensitivity in the foveola by single cell stimulation. Therein, it was tested how far the special cellular organization at the very center of human retina is reflected in the sensitivity to light. Eccentricity, cone size as well as outer segment length showed a significant influence on the sensitivity thresholds. Furthermore, variability between individual test sites was much higher than compared to intra test site variability (0.6 log10 versus 0.1 log10 photons) which was assumed to be the result of individual cone weighting.

These findings regarding foveolar sensitvity as well as the developed optimizations itself, will positively impact future fundamental research assessing the foveolar cone-cone interactions, ultimately leading to a better understanding of retinal pathologies and their treatment.

Zusammenfassung

Zum einen ist das Auge das Fenster des Menschen zur Welt, zum anderen ist das Auge ein Fenster zum menschlichen Gehirn, wodurch eine nicht-invasive und *in vivo* Untersuchung des Nervengewebes möglich wird. Mit Hilfe der auf der Adaptiven Optik Scanning Laser Ophthalmoskopie (AOSLO) basierenden Mikrostimulation und psychophysikalischen Methoden können nicht nur die einzelnen Photorezeptorzellen abgebildet, sondern auch stimuliert werden, um so deren Einfluss auf die Wahrnehmung zu testen. Aufgrund technischer Einschränkungen werden die meisten dieser psychophysikalischen Experimente zu den Grundlagen des menschlichen Sehens derzeit außerhalb der Foveola, dem Zentrum der Netzhaut, durchgeführt. In dieser Arbeit lag der Fokus darauf diese Einschränkungen zu ermitteln und zu lösen, um visuelle Psychophysik in der Foveola auf der Ebene einzelner Zellen zu ermöglichen.

Um das AOSLO in ein Displaysystem für die Psychophysik zu verwandeln, wird eine schnelle Modulation des abtastenden Laserstrahls benötigt. Die beste Lösung in Bezug auf Schaltzeit und Kontrastumfang ist ein akusto-optischer Modulator (AOM). Diese AOMs lassen jedoch eine beträchtliche Menge an Restlicht durch, was einen sichtbaren Hintergrund erzeugt und damit die experimentellen Möglichkeiten einschränkt. Durch die Kaskadierung zweier AOMs konnte nicht nur der Hintergrund eliminiert, sondern auch die Strahlungskontraste auf bis zu $1{:}10^{10}$ erhöht werden, was der höchste visuelle Kontrast ist, der bisher für ein Displaysystem berichtet wurde. Ein psychophysikalisches Validierungsexperiment zeigte, dass dieses Kontrastverhältnis ausreichend ist, um einzelne foveale Photorezeptorzellen mit kleinen und gut sichtbaren Stimuli zu reizen, frei von dem sonst deutlich sichtbaren Hintergrund. Eine solche hintergrundfreie Stimulation ermöglicht es (i) die Photorezeptoren mit geringeren Lichtintensitäten und (ii) näher an der absoluten Schwelle zu reizen. Darüber hinaus kann ein größerer dynamischer Bereich an verfügbaren Lichtintensitäten Photorezeptorantworten sowohl in Zapfen als auch in Stäbchen anregen.

Kleine Verschiebungen der Augenposition, die während der *in vivo* Experimente auftreten, verschieben einen Stimulus um einen signifikanten Betrag, wenn der transversale chromatische Versatz (TCO, englisch: "transverse chromatic offset") nur statisch kompensiert wird, was eine zuverlässige Testung der einzelnen Zelle ausschließt. Ich habe eine Methode entwickelt, die nur eine einzige Messung des TCO während kontrollierter Augenbewegungen erfordert, um die chromatischen Bildverschiebungen der Retina auf den Bildraum einer Pupillenkamera abzubilden. Nach einer solchen Kalibrierung wurde TCO durch kontinuierliche Überwachung der Augenposition während des Experiments und durch Interpolation von Korrekturvektoren aus einem linearen Fit an die Kalibrierungsdaten kompensiert. Unsere Lösung ermöglichte eine kontinuierliche Kompensation des TCO mit hoher räumlicher Präzision, die für foveale, zapfengezielte psychophysikalische Experimente notwendig ist.

Die Optimierung wurden erfolgreich angewandt, um die erste Studie zur Evaluierung der Empfindlichkeit in der Foveola durch Stimulation einzelner Zellen durchzuführen. Im Fokus lag hierbei, inwieweit sich die besondere zelluläre Organisation im Zentrum des menschlichen Sehens in der Lichtempfindlichkeit widerspiegelt. Sowohl die Exzentrizität, als auch die Zapfengröße und die äußere Segmentlänge zeigten alle einen signifikanten Einfluss auf die Empfindlichkeitsschwellen. Darüber hinaus war die Variabilität zwischen den einzelnen Teststellen viel höher als im Vergleich zur Variabilität innerhalb der Teststelle (0.6 log10 versus 0.1 log10 Photonen), die vermutlich auf die individuelle Zapfengewichtung zurückzuführen war.

Diese Erkenntnisse über die foveale Sensitivität sowie die entwickelten Optimierungen werden für die zukünftige Grundlagenforschung zur Beurteilung der fovealen Zapfen-Zapfen-Interaktionen von grossem Nutzen sein und somit zu einem besseren Verständnis von Netzhautpathologien und deren Behandlung beitragen.

Contents

1 Introduction 1

1.1 Human visual system . . . 2
  1.1.1 The retina . . . 3
  1.1.2 Photoreceptor cells . . . 3
  1.1.3 Light sensitivity . . . 5
  1.1.4 Fixational eye movements . . . 7
1.2 Optics of the eye . . . 7
  1.2.1 Monochromatic aberrations . . . 8
  1.2.2 Chromatic aberrations . . . 9
1.3 Retinal imaging . . . 9
  1.3.1 Fundus camera . . . 11
  1.3.2 Scanning laser ophthalmoscope . . . 11
  1.3.3 Adaptive Optics . . . 11
  1.3.4 Adaptive Optics Scanning Laser Ophthalmoscopy . . . 13
  1.3.5 Optical coherence tomography . . . 14
1.4 Psychophysics . . . 14
  1.4.1 The psychometric function . . . 14
  1.4.2 Psychophysical methods . . . 15
  1.4.3 QUEST . . . 16
  1.4.4 Single Cone Psychophysics . . . 17
1.5 AOSLO based Microstimulation . . . 17

2 Aims of the project 20

3 Characterization of an AOSLO as a display for psychophysics 22

3.1 Simulation of cone stimulation . . . 23

4 Ultra-high contrast retinal display system 27

4.1 Introduction . . . 27
4.2 Materials and methods . . . 29
  4.2.1 Acousto-optic light modulation and radiometry . . . 29
  4.2.2 Temporal alignment and AOSLO micro stimulation . . . 30
  4.2.3 Human psychophysics . . . 30
4.3 Results . . . 32
  4.3.1 Light modulation characteristics . . . 32
  4.3.2 Switching latency and temporal alignment . . . 32
  4.3.3 Psychophysics: background extinction and small spot sensitivity . . . 35
4.4 Discussion . . . 36

5 Eye tracking-based estimation and compensation of TCO 40

5.1 Introduction . . . 40
5.2 Material and methods . . . 41
  5.2.1 Adaptive optics scanning laser ophthalmoscope (AOSLO) . . . 41
  5.2.2 Eye tracking camera . . . 41
  5.2.3 Eye tracking software . . . 42
  5.2.4 TCO measurement . . . 43
  5.2.5 Calibration procedure . . . 43
  5.2.6 Experimental validation . . . 44
5.3 Results . . . 44
5.4 Discussion . . . 47

6 Human foveolar sensitivity **53**
6.1 Introduction . . . 53
6.2 Material and Methods . . . 54
6.2.1 Adaptive optics scanning laser ophthalmoscope microstimulator . . . 54
6.2.2 Cone density maps and cone density centroid . . . 54
6.2.3 Determination of cone outer segment length . . . 55
6.2.4 PRL determination . . . 55
6.2.5 Increment sensitivity thresholds . . . 55
6.2.6 Conversion of arbitrary power units to number of photons at the cornea . . . 58
6.2.7 Modelling of cone light capture and ISETBio . . . 58
6.3 Results . . . 59
6.3.1 Retinal topography and the PRL . . . 59
6.3.2 Small spot sensitivity . . . 59
6.3.3 Correlation between retinal structure and function . . . 60
6.3.4 Modelling the impact of cone density, OS length and distance from PRL on sensitivity . . . 63
6.3.5 Modelling the impact of stimulus position and cone class composition . . . 66
6.4 Discussion . . . 68
6.4.1 The factor “Distance from PRL” . . . 68
6.4.2 The factor “Cone density” . . . 69
6.4.3 The factor “Outer segment length” . . . 70
6.4.4 Variability of threshold estimates . . . 71
6.4.5 Estimation of the number of isomerizations at threshold . . . 72

7 Discussion **73**
7.1 AOSLO microstimulation . . . 73
7.2 Rod psychophysics . . . 74
7.3 Psychophysics: subjective function testing . . . 75
7.4 Objective function testing . . . 76
7.5 Clinical relevance . . . 77
7.6 Conclusions and Outlook . . . 79

References **viii**

List of Abbreviations and Units **xxviii**

List of Publications **xxx**

Acknowledgements **xxxii**

1 Introduction

One of the biggest mysteries of mankind nowadays is the human brain, and studying this very special organ is a challenge within itself. Most parts of the nervous system are embedded deeply within the tissue, which makes it difficult to investigate the intact neuronal circuits *in vivo*. There is, however, one exception to this rule: the eye. Firstly, the exposure of the retina to light enables *in vivo* imaging without the necessity to remove covering tissue by simply shining light into the eye and capturing the reflected photons. Secondly, controlled activation of the photoreceptor cells can be achieved by accurate stimulation with light. Taken together, these features enable researchers as well as physicians to examine this specific nervous system without damaging the surrounding or targeted tissue.

Additionally, due to its origin within the embryogenesis the retina is part of the central nervous system and inhabits a readily comprehensible circuitry for processing of visual inputs. Thus, the eye is an attractive study object for basic research of neuronal systems. Given the fact that one third of the cerebral cortex is predominantly devoted to visual processing [Van Essen and Drury 1997; Van Essen 2004], vision is the most important sense in humans. Consequently, clinicians are interested in retinal research as well. A recent technology called adaptive optics scanning laser ophthalmoscopy (AOSLO) enables investigation of human visual perception at a single cell level *in vivo* and therefore provides an optimal tool to study the intact human retina. Ultimately, this technology can be utilized to improve our understanding of the role of individual photoreceptor cells in human visual perception and thus unravel the mystery of neuronal network organization. Furthermore, the AOSLO may help clinicians to gain a better understanding of retinal diseases and their specific progression, as well as evaluate the success of new treatments and substances.

The following sections provide an overview of the fundamentals related to this dissertation. Initially, the human visual system and its optical implications are outlined. The following third section outlines retinal imaging techniques with a focus on adaptive optics scanning laser ophthalmoscopy (AOSLO), and the fourth introduces the field of psychophysics. The last section of the introduction shortly reviews previous AOSLO studies using stimulation at the single cell level.

1.1 Human visual system

The eye is a human's sensory organ for vision specialized to detect electromagnetic waves with a wavelength between 780 and 350 nm, the so-called visible light. Incident light is focused via cornea, lens and vitreous into the fovea (Figure 1A). The human eye is an inverse eye, meaning that the light has to pass the cells of the downstreaming circuitry first, until it reaches the photoreceptor cells outer segments, where the photo transduction takes place. The first processing station of the visual system is the retina itself (see below). Next, the information is transmitted via the optical nerve, which is formed by the ganglion cell's axons. On its way the two optical nerves of the left and right eye cross at the optic chiasm, where the fibers from the nasal hemiretina cross to the contralateral brain hemisphere. Therefore, now the fibers of the optic tract convey the information of the contralateral hemifield of vision (Figure 1B). Ninety percent of the optic tract fibers project to the lateral geniculate nucleus (LGN) and further to the primary visual cortex. Thus, the primary pathway is also called the geniculostriate pathway of visual processing. The remaining ten percent of fibers project to the superior colliculus (Figure 1C) and pretectal region [Gilbert 2013]. If the pathway via the LGN is lost, there is still an unconscious vision called blindsight, presumably mediated through the projections to the superior colliculus [Stoerig and Cowey 2007].

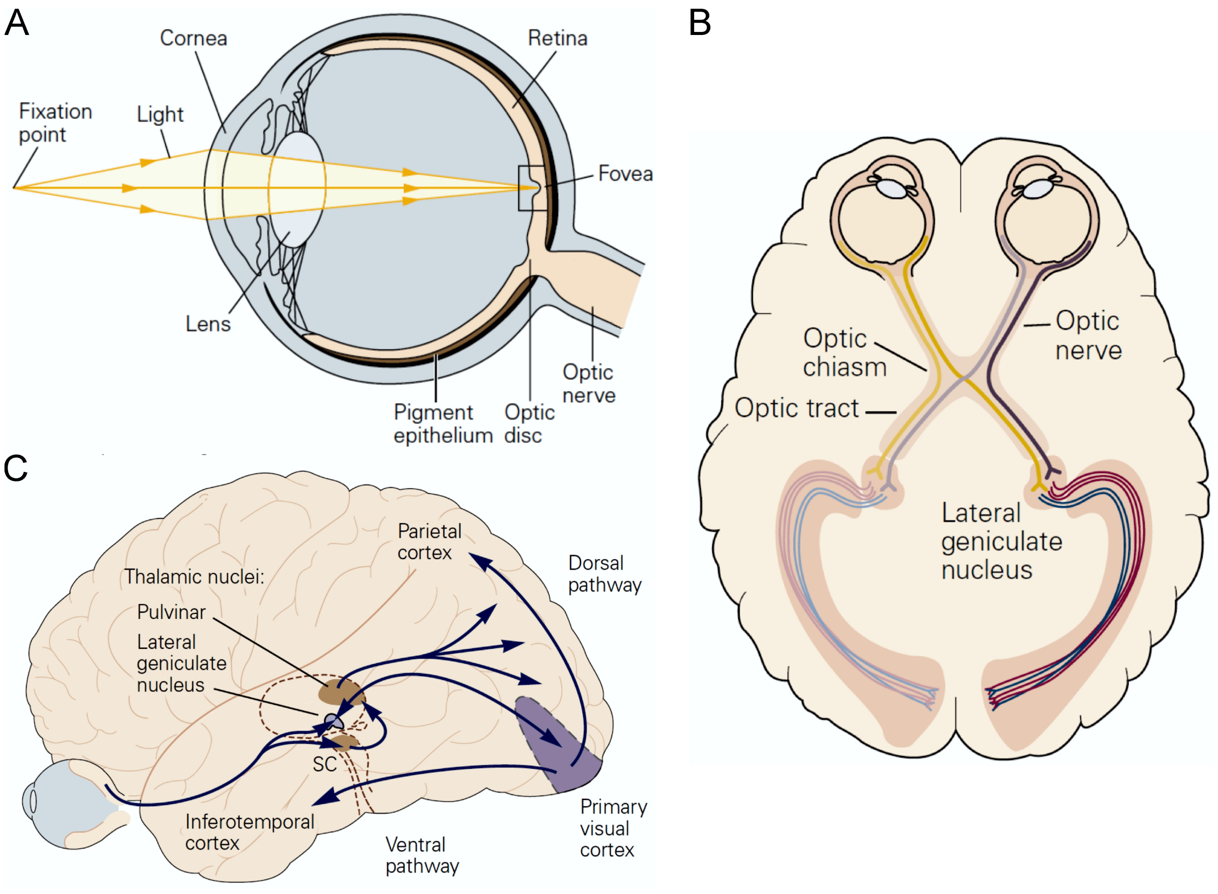

Figure 1: *The human visual system. A) Anatomy of the eye. B) The primary or "geniculostriate" pathway for visual processing. C) Complete pathway of visual processing, including the superior colliculus (SC). Source: A) Meister and Tessier-Lavigne 2013; B&C) Gilbert 2013.*

1.1.1 The retina

The retina is arranged in a very strictly layered organization pattern [Rodieck 1998] (Figure 2A,B). The outermost layer is the retinal pigment epithelium (RPE) supplying the photoreceptor cells (PR) with nutrients. Furthermore, the outer segment tips of the PRs are embedded in the RPE, which in turn metabolizes the shed disks with the depleted photopigment. While the inner and outer segments of the PR are arranged within their own layers, and the somata of the PRs are forming the outer nuclear layer, the PR and horizontal cell axons are connecting via the PR-horizontal cell synapses within the outer plexiform layer. The cell bodies of the horizontal, bipolar, and amacrine cells lie in the subsequent inner nuclear layer. The inner plexiform layer contains the axons of the bipolar and amacrine cells, as well as the synapses between the bipolar and ganglion cells. The ganglion cell layer contains the somata of the ganglion cells, together with the displaced amacrine cell's somata of the on-cholinergic pathway [Curcio and Allen 1990]. The innermost layer is the nerve fiber layer formed by the ganglion cell axons leaving the eye bundled at the blind spot (also known as the optic nerve head or optic disc, see Figure 1A).

The transduced signal propagates through the retina from the PR to the bipolar cell, and further to a ganglion cell. The retina also is the first processing station, since the receptor cells' signals converge and form retinal field units. These receptive fields of the bipolar cells and the ganglion cells are organized in a center-surround arrangement [Rodieck 1998]. While the centers of these cells are directly linked to individual photoreceptor cells, the surround is mediated for bipolar cells by horizontal cells and for ganglion cells by amacrine cells (Figure 2C). This so-called lateral inhibition of the retina becomes perceivable for example at an object's edge as contrast enhancement [Meister and Tessier-Lavigne 2013].

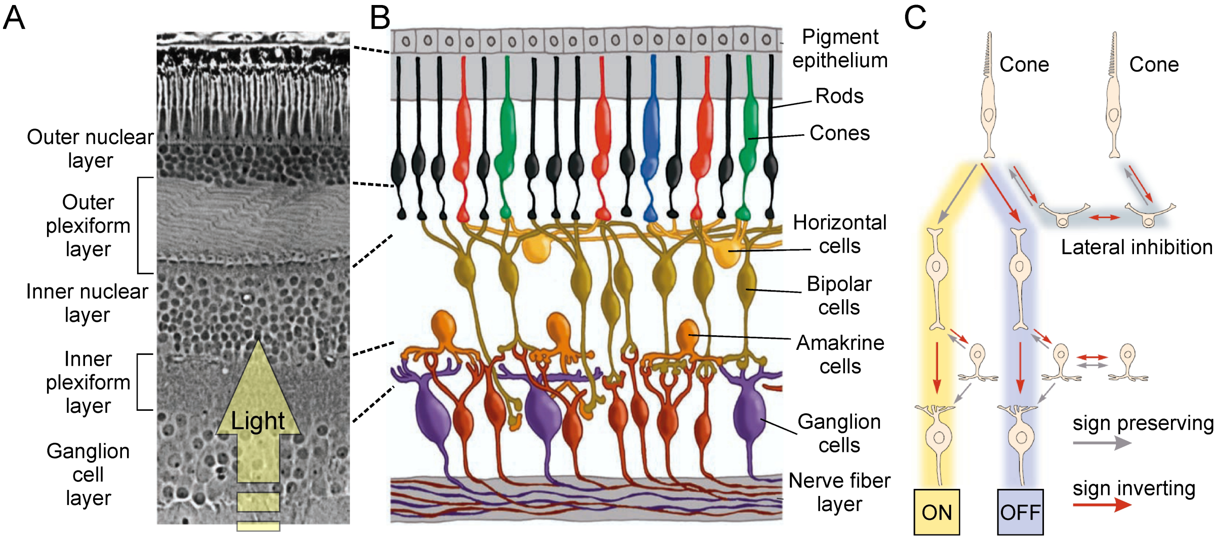

Figure 2: *Cells and circuitry of the retina. A) Light microscopic and B) schematic illustration cross section showing the retinal cells. The pigment epithelium cells and the photoreceptor cells are at the top. The plexiform layers contain Axon-to-dendrite neural connections, nuclear layers the cell bodies. C) The cone circuitry, showing the ON and OFF pathways as well as the lateral inhibition via horizontal cells in the outer layer. Source: A&C) Meister and Tessier-Lavigne 2013, B) Kolb and Marshak 2003.*

1.1.2 Photoreceptor cells

Vision starts in the retina, where a mosaic of specialized neurons, the photoreceptor cells, captures light and converts it into internal signals, forming the basis of human visual perception. The healthy human retina consists of two photoreceptor types, the rods and the cones (Figure 3A). The about 92 million rods [Curcio et al. 1990] are sensitive to low light levels and therefore only operational at scotopic and mesopic vision. Rod cells are - next to the foveal cones - the smallest photoreceptor cells with a diameter of about 2.4 μm [Curcio et al. 1990]. The about 4.6 million cones [Curcio et al. 1990] are functional at high light levels (mesopic and photopic vision) and make color vision possible. The cones vary in size with the smallest cones sitting in the foveal center with a diameter of about 2.1 μm. With increasing retinal eccentricity their respective diameter grows rapidly to about 7 μm at 5 degree eccentricity, beyond which the diameter is relatively stable [Curcio et al. 1990; Scoles et al. 2014]. There are three classes of cones differentiated by their wavelength sensitivity (Figure 4B). The L-cones show high absorbance to larger wavelengths with a maximum sensitivity at 564 nm, M-cones have a maximal sensitivity to light with 534 nm wavelength and S-cones are mostly responsive to short wavelengths with highest sensitivity at 420 nm [Bowmaker and Dartnall 1980]. Also S-cones make only ten percent of cones and are excluded, like rods, from the foveal center. All the photoreceptor cells have in common to be composed of an inner segment, divisible in ellipsoid and the tapered myoid, and an outer segment. The inner segment is supposed to have light guidance characteristics, thereby collecting and transmitting the light into the outer segment where the photo transduction takes place (Figure 3B) [Enoch 1963; Roorda and Williams 2002; Vohnsen et al. 2005; Liu et al. 2015].

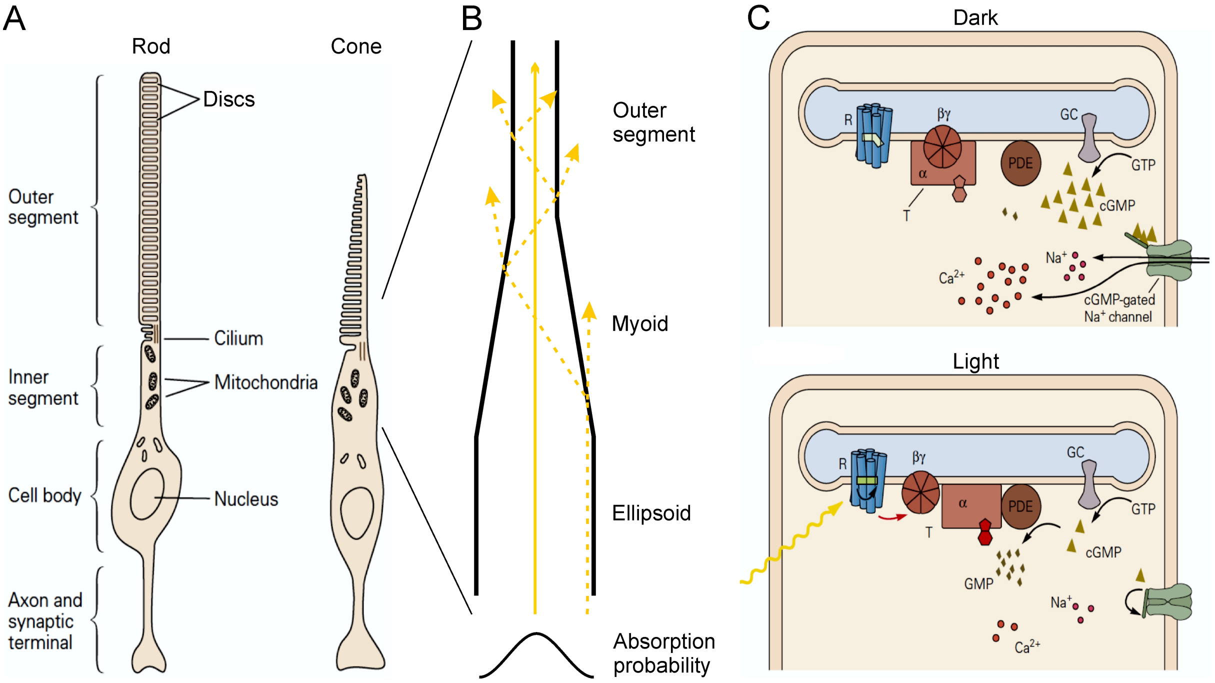

Figure 3: *Photoreceptor cells of the human retina. A) Anatomy of the rods and cones. B) Schematic illustration of the cones's wave guidance characteristics. C) Simple representation of the basic photo transduction in the discs of the outer segment. (c)GMP: (cyclic) guanosine monophosphate; GTP:guanosine triphosphate; GC: Guanylate cyclase; PDE: Phosphodiesterase; R: Rhodopsin; T: Transducin. Source: A&C) Meister and Tessier-Lavigne 2013.*

The photo transduction converts the light event into a neuron intrinsic voltage signal. Most of the molecules participating in the transduction cascade are located within or at the membrane of the outer segment discs (Figure 3C). The transduction starts with the photoisomerization of 11-cis retinal which is linked to the photopigment (iodopsin in cones, and rhodopsin in rods). The resulting change of 11-cis-retinal into all-trans retinal, changes the opsin into metarhodopsin II, which activates transducin. The alpha subunit of this G protein dissociates and activates a phosphodiesterase (PDE) called PDE6, which hydrolyzes cyclic guanosine monophosphate (cGMP) into GMP. Subsequently, the cGMP dependent sodium channels close causing a hyperpolarization of the photoreceptor cell, which results in a closure of the voltage-gated calcium channels. The decreased level of calcium lowers the number of glutamate containing vesicles that can dock and fuse with the cell membrane at the synapse. Finally, the reduction of the neurotransmitter results in a depolarization of the on-bipolar cells or a hyperpolarization of the off-bipolar cells [Meister and Tessier-Lavigne 2013].

The light induced voltage changes of the photoreceptor cell not only affect the downstream cells, but also the neighboring photoreceptor cells due to electric coupling via gap junctions [Hsu et al. 2000; DeVries et al. 2002; Hornstein et al. 2004].

Because the photopigment is associated with the outer segments disk membrane, the number of active photopigment molecules is directly correlated with the photoreceptor outer segment length [Baylor et al. 1979]. The longer the outer segment is, the higher is the probability for an incident photon to interact with the photopigment [Bowmaker et al. 1978; Baylor et al. 1979].

1.1.3 Light sensitivity

In general, light sensitivity describes the ability of an observer to detect intensity changes during visual stimulation. In terms of absolute sensitivity to light it is important to mention that, overall, the human visual system is functional across 14 log10 units of intensity (Figure 4A). On the one hand humans can view a sunny outdoor scene at midday, on the other hand it is possible to detect a single photon [Sakitt 1972; Tinsley et al. 2016].

One mechanism behind this is adaptation of the photoreceptor cells, which plays an important role when using stimuli against a background and testing so called increment thresholds. The Weber-Fechner-law, a fundamental law in psychophysics, implies that there is a constant proportion between increment thresholds and background intensity [Fechner 1860]. As a general rule, this statement was found to be true for the visual system across a large range of background intensities with a ratio of ten percent [Reeves et al. 1998]. It was shown, that this is possible due to adaptation of the photoreceptor cells: The individual dark-adapted photoreceptor cell is functional over an intensity range of about 3.5 log10 units and that this range is conserved when adapting to new background intensities [Normann and Perlman 1979]. As a side note, such range is reasonable, given the fact that the intensity values of a natural scene are typically spanning 2 log10 units [Hood and Finkelstein 1986]. For extremely bright background intensities the Weber-Fechner fraction rises, which can be explained by photopigment depletion [Burkhardt 1994].

The other one is that humans possess two different types of photoreceptor cells (Figure 3A). Firstly, the extremely light sensitive rods, which are visually active at scotopic conditions during the night. Secondly, the cones, which need a certain light level to become active and operate best at photopic conditions during daytime (Figure 4A). Therefore, depending on the actual light situation, humans have different locations of highest sensitivity. During photopic and mesopic conditions the rods are saturated and their response is getting inhibited by the increased activity of the cones [Eggers et al. 2013]. Thus, light sensitivity is best at the central fovea, where the cone outer segments are longest and the receptive field size is smallest with the highest density of ganglion cells [Watson 2014]. Under scotopic light conditions sensitivity is best at roughly 10 degree eccentricity [Tornow and Stilling 1998].

Additionally, to this absolute sensitivity to light, the photopigments of the different cone classes and rods are tuned differently to the spectrum of the visible light (Figure 4B). And in summation, a human observer is differently sensitive to light of different wavelengths. Meaning, that two stimuli containing the same number of photons but of different wavelengths are perceived differently bright. From Figure 4B it can be seen that humans at daylight are most sensitive to light with a wavelength of 543 nm as the photopigment of the L- and M-cones show an equally high absorbance probability.

Because of the retinal circuitry and the involved neurons not only intensity, eccentricity and wavelength influence the detection threshold, but also size and duration. These two factors are affected by summation, which was firstly reported for spatial pooling by Ricco 1877. He observed that the threshold in number of photons stayed at the same level for decreasing stimulus sizes. Therefore, this relationship is called Ricco's law. Ricco's area of complete summation varies across the visual field, as the number of ganglion cells decreases and their receptive field size increases. It also depends on the involved photoreceptor cells, for example at 10 degree eccentricity the diameter of Ricco's area for cones is about 40 arcminutes [Volbrecht et al. 2000] and for rods about 60 arcminutes [Scholtes and Bouman 1977]. For cones, Ricco's area is directly correlated with the dendritic field size of parasol ganglion cells [Volbrecht et al. 2000]. This linkage was not found in the foveola, as reported recently by Tuten et al. 2018, who assessed Ricco's area in the central fovea with adaptive optics scanning laser ophthalmoscope based microstimulation. They reported a diameter of 2.4 arcmin, which was bigger than the midget but smaller

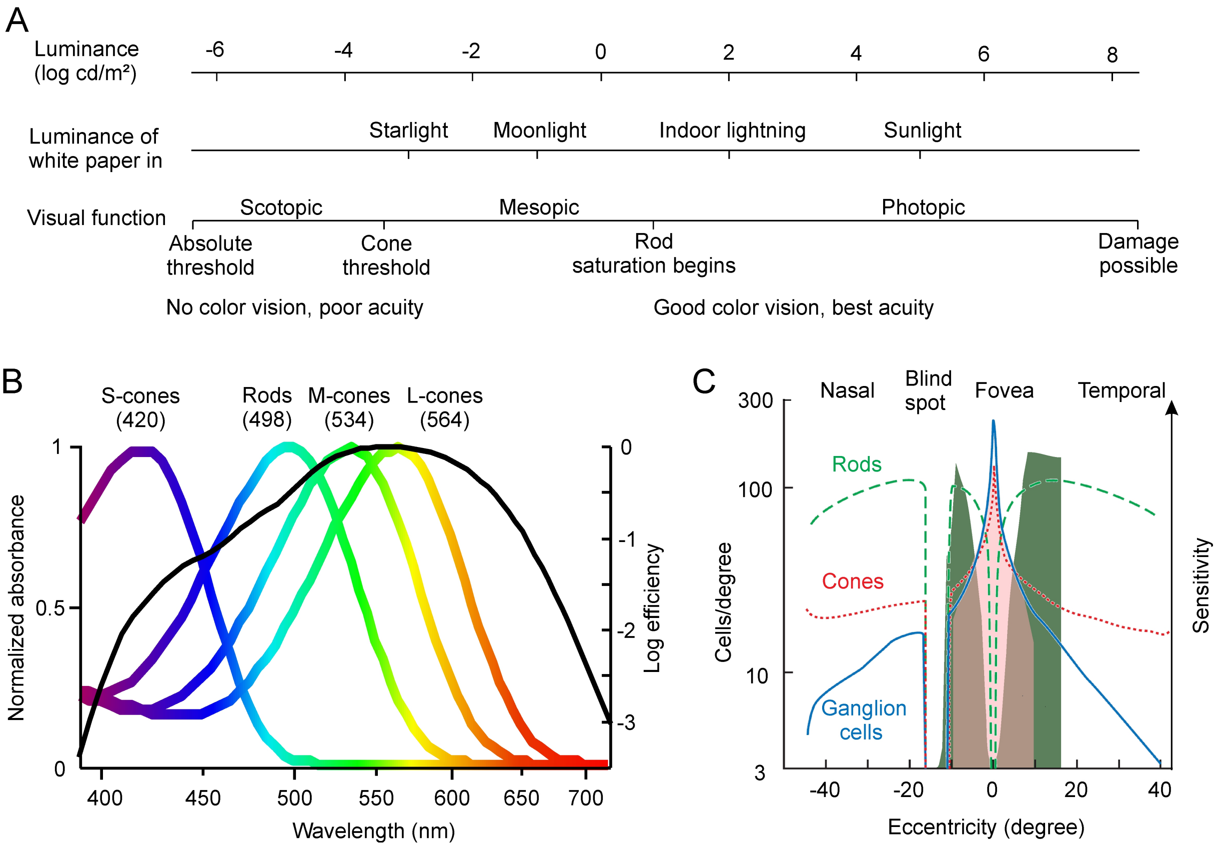

Figure 4: *The photoreceptor cells and light sensitivity. A) The dynamic range of the visual system. B) Absorbance of the individual photopigment in the different photoreceptor cell types. The number in brackets shows the absorbance optimum in nanometers. The luminous efficiency function shows the overall sensitivity to a photopic stimulus. It results from the combination of the eye's wavelength specific transmission and photopigment distribution. C) Distribution of photoreceptor and ganglion cells across the retina. The photopic and scotopic sensitivity (colored area) follows roughly the distribution of the mediating cell type. Source: A) Hood and Finkelstein 1986; B) based on data from Dartnall et al. 1983; Sharpe et al. 2005; C) Geisler and Banks 2010 with additional data from Tornow and Stilling 1998 and Choi et al. 2016*

than the parasol ganglion cell's dendritic field. They hypothesized that the thresholds were the result of a mixed activity of parasol and midget ganglion cells.

Comparable to Ricco's law for spatial summation, Bloch's law for temporal summation describes the phenomenon that the product of stimulus intensity and duration was constant for brief exposures [Bloch 1885]. Interestingly, the same relationship was reported earlier as the Bunsen-Roscoe law of photochemistry describing the process of light interactions with molecules [Bunsen and Roscoe 1863]. For rods temporal summation was found to be about 100 msec [Sperling and Jolliffe 1965]. For cones it was found that temporal summation is wavelength dependent, with longer summation times (about 100 msec) for the blue-light favoring S-cones, compared to L- and M-cones (about 50 msec)[Krauskopf and Mollon 1971]. For both, the rod and the cone system, it was reported that the threshold over intensity relation becomes more shallow with larger stimuli, which are several degrees in diameter [Graham and Margaria 1935; Karn 1936]. It was hypothesized that in this case the visual system benefits from pooling the information across several detectors Graham and Margaria 1935].

1.1.4 Fixational eye movements

Even during sustained fixation, small eye movements remain which are a major problem for retinal imaging and especially cell targeted microstimulation. The origin of these fixational eye movements (FEM) is still unclear. There are three superimposing types of FEM distinguished by amplitude and frequency, tremor, drift and microsaccades (Figure 5) [Martinez-Conde et al. 2004]. It is assumed, that tremor and drift on the one hand are caused by the noise and variability of motor neurons controlling the eyeball's movements [Eizenman et al. 1985]. Microsaccades on the other hand are supposed to counteract fixation errors [Engbert and Kliegl 2004; Nachmias 1959] resulting in an targeted eye movement directed towards the spatial locus of attention [Hafed and Clark 2002; Engbert and Kliegl 2003; Steinman 1965]. This hypothesis is supported by the recent finding in psychophysical experiments, that the motor program of microsaccades is modified, if the fixation target is displaced during a microsaccade [Havermann et al. 2014]. Overall, our visual system benefits from FEM, as visual acuity is better, if a stimulus moves across the retina, compared to a retinally stabilized stimulus [Ratnam et al. 2017].

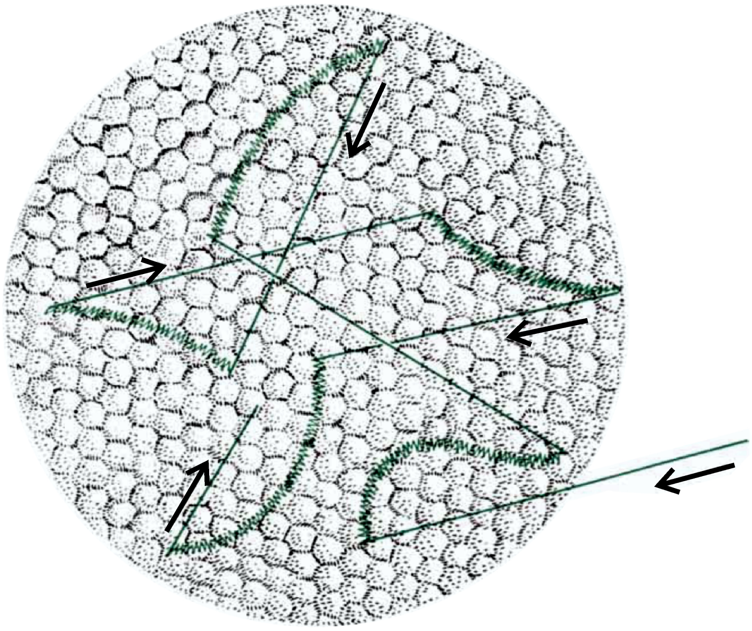

Figure 5: *Eye motion during fixation. While tremor and drift (curved lines) cause the image to move away from retinal locus of fixation, the fast microsaccades (straight lines) re-center the image on this locus of fixation. The patch diameter is about 0.05 mm. Source: Pritchard 1961.*

1.2 Optics of the eye

The cornea is the first surface of the eye an incident light beam has to pass. It contributes to two thirds of the eye's refractive power (43.1 D of 58.0 D, [Kiely et al. 1982]) due to its curvature and the change of the refractive index from air to water.

The light enters the eye through the pupil formed by the iris. The iris is connected to two opposing muscles, the sphincter pupillae and dilator pupillae, controlling the diameter of the pupil and therefore the size of the entering light beam, making the pupil the aperture of the eye. Typically the diameter of the pupil varies between 2 and 8 mm.

The entering light beam is focused by a flexible lens into the foveola. During accommodation, the refractive power of the lens is changed via contraction of the ciliary muscle. This relaxes the zonular fibers and allows the lens to contract thereby decreasing the curvature radius. The smaller curvature radius increases the refractive power of the lens and brings objects at close distances into focus.

In an optimal scenario, the eye's optics would provide a diffraction limited image on the retina. However, all surfaces are made of biological tissue which creates optical errors reducing the quality of the retinal image. These optical errors are wavefront aberrations, meaning that the rays of a point object are not perfectly focused into the same spot on the retina (Figure 6). The resulting image of a point source on the retina is described by the point spread function (PSF). Based on their wavelength dependency there are two groups of aberrations: the monochromatic and the chromatic aberrations.

This and the following two paragraphs are mainly based on [Collins et al. 2017; Marcos et al. 2017; Wilson 2017].

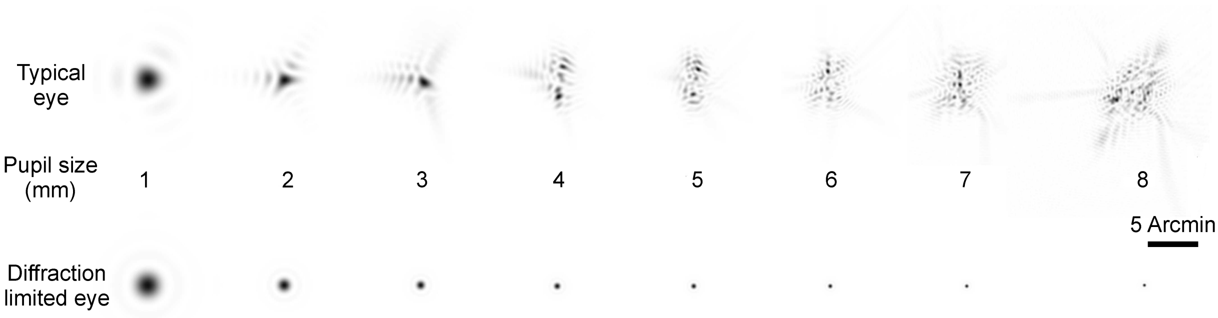

Figure 6: *Point spread functions for a diffraction limited and a typical eye, but with removed astigmatism. For a better visualization the aberrated PSFs were normalized. Source: Roorda 2011.*

1.2.1 Monochromatic aberrations

Monochromatic aberrations occur independently of the light's wavelength and can be further divided into the two subgroups of lower-order and higher-order aberrations. Of all aberrations in the eye, the lower-order aberrations (LOA) contribute 85 % and the higher-order aberrations (HOA) 15 % [Jayabalan and Bille 2019].

LOA are also called refractive errors since they displace the retinal image longitudinally. Optometrists measure the LOA traditionally via subjective refraction and correct these with spectacles or contact lenses. The lower-order aberrations include two types: defocus and astigmatism.

Defocus of the human eye is caused by a deficient relationship of the optic's refractive power and the eye length. Myopia, which is also called nearsightedness, is defined by a too high optical power of the cornea and lens, which displaces the image's focus before the retina. Therefore, only objects at a close distance can be seen sharply. Hyperopia, or farsightedness, is the opposite case of myopia and describes an optical power too low in relation to the actual eye length, displacing the focus point beyond the retina. Hyperopic humans are unable to see a sharp image of an object close to the eye. Similar but different case is presbyopia, which is an aging effect of the lens losing its flexibility, resulting in a diminished accommodation ability.

Astigmatism is more complex and describes a difference in refractive power along two perpendicular principal meridians. This results in two separate orthogonal focal planes of the eye's image. Astigmatism is mainly caused by a torodial shape of the cornea, where the curvature differs between the two meridians. Typically, corneal astigmatism can be described based on the cornea's principal meridians and is called "with-the-rule" if the steepest meridian is close to the vertical axis and "against-the-rule" if close to the horizontal axis.

HOA produce various focus points of the viewed object in dependency of the pupil part the individual ray passed. The three most important HOA to describe the refractive errors of the human eye are called coma, spherical aberration and trefoil. The spherical aberration is inherent in every normal eye because of the asphericity of the corneal surface. Thus, the closer to the pupil's edges the rays enter the eye the more they are refracted. Thereby, the amount of spherical aberrations is correlated with the current pupil size and affecting vision at night more than during daytime. Like the spherical aberration, coma is also inherent in every eye and results from the displacements of the cornea's apex and lens center from the optical axis. The third, trefoil, represents the non-rotational symmetric HOA.

A commonly used method to describe the eye's monochromatic aberrations is to use a set of Zernike polynomials (Figure 7). For this mathematical approach either the observed corneal surface or the actual measured wavefront (see 1.3.3) is fitted by the Zernike polynomials. The monochromatic aberration of healthy eyes can be sufficiently described by using Zernike polynomials up to the fourth order [Iskander et al. 2001].

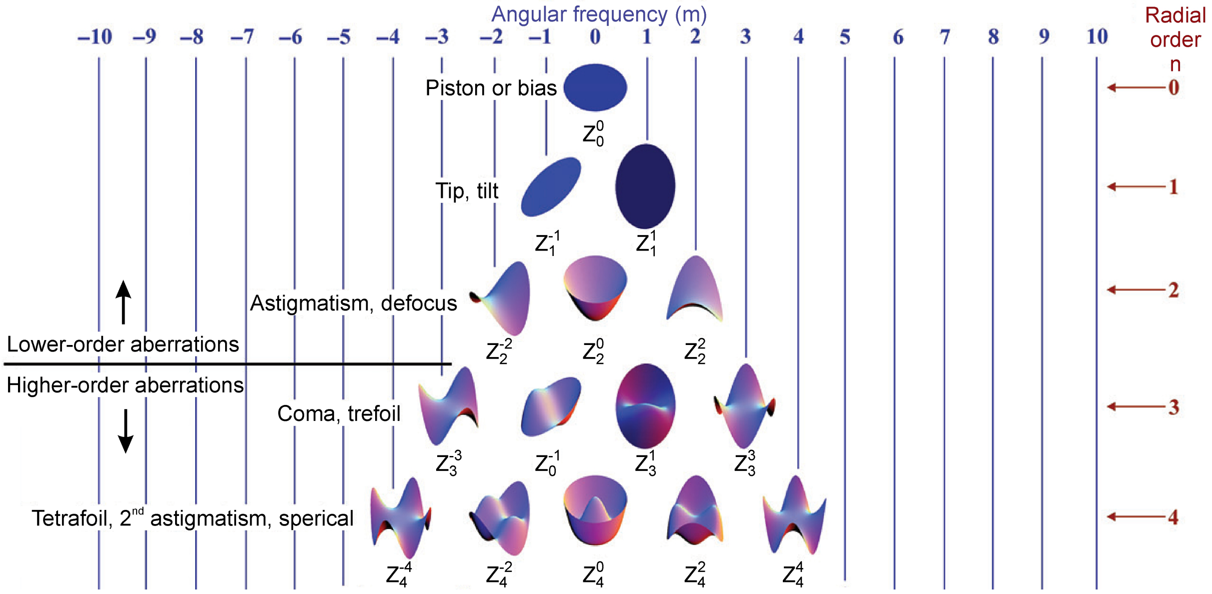

Figure 7: *Surface plots of the Zernike polynomials. Only the first 5 orders with the regarding classical naming are displayed. Source: Adapted from Lakshminarayanan and Fleck 2011.*

1.2.2 Chromatic aberrations

Chromatic aberrations are caused by dispersion, a physical phenomenon in which the refractive index and therefore the refractive power of a medium is based on the wavelength. The best known example of dispersion is the rainbow. A distinction is made between longitudinal and transversal (or lateral) chromatic aberrations.

Longitudinal chromatic aberrations (LCA) are comparable to spherical aberrations or defocus: shorter wavelengths are more refracted than longer wavelengths. Typically, accommodation focuses the green-yellow wavelengths (550 - 570 nm) on the photoreceptor layer [Kruger et al. 1993; Marcos et al. 1999], resulting in a focus point for longer reddish light beyond the retina and for shorter blueish light in front of the retina. Like spherical aberrations the amount of LCA depends on the actual pupil size.

These differences in refractive power have an additional effect on objects displaced from the optical axis described by the transversal chromatic aberrations. The principal ray - going from the object through the pupil's center - is refracted wavelength dependent, too. A small white light spot viewed off-axis will therefore appear on the retina as a line with a continuous spectrum where the blueish parts are closer to the fovea than the reddish. Additionally, the wavelength dependent refraction of the principal ray will magnify reddish light more than blue light.

1.3 Retinal imaging

The first direct ophthalmoscope was developed by Hermann von Helmholtz in the 1850s. This new device used the light of a candle to illuminate the retina through the pupil. The patient's lens and cornea are used to see a sharp and magnified image of the retina. With a focusing lens the aberrations of both the patient and examiner are corrected. This very simple design is still fundamental to all modern ophthalmoscopes [Helmholtz 1851].

In general, imaging of the retina is very helpful for ophthalmologists examining pathological eyes. Firstly, it is the only way to determine the patient's pathology (e.g. glaucoma, macular degeneration, etc.). Secondly, the progression of the disease or success of a treatment can be further examined. Therefore, a variety of instruments was developed to image the retina *in vivo* [Furlab 2017].

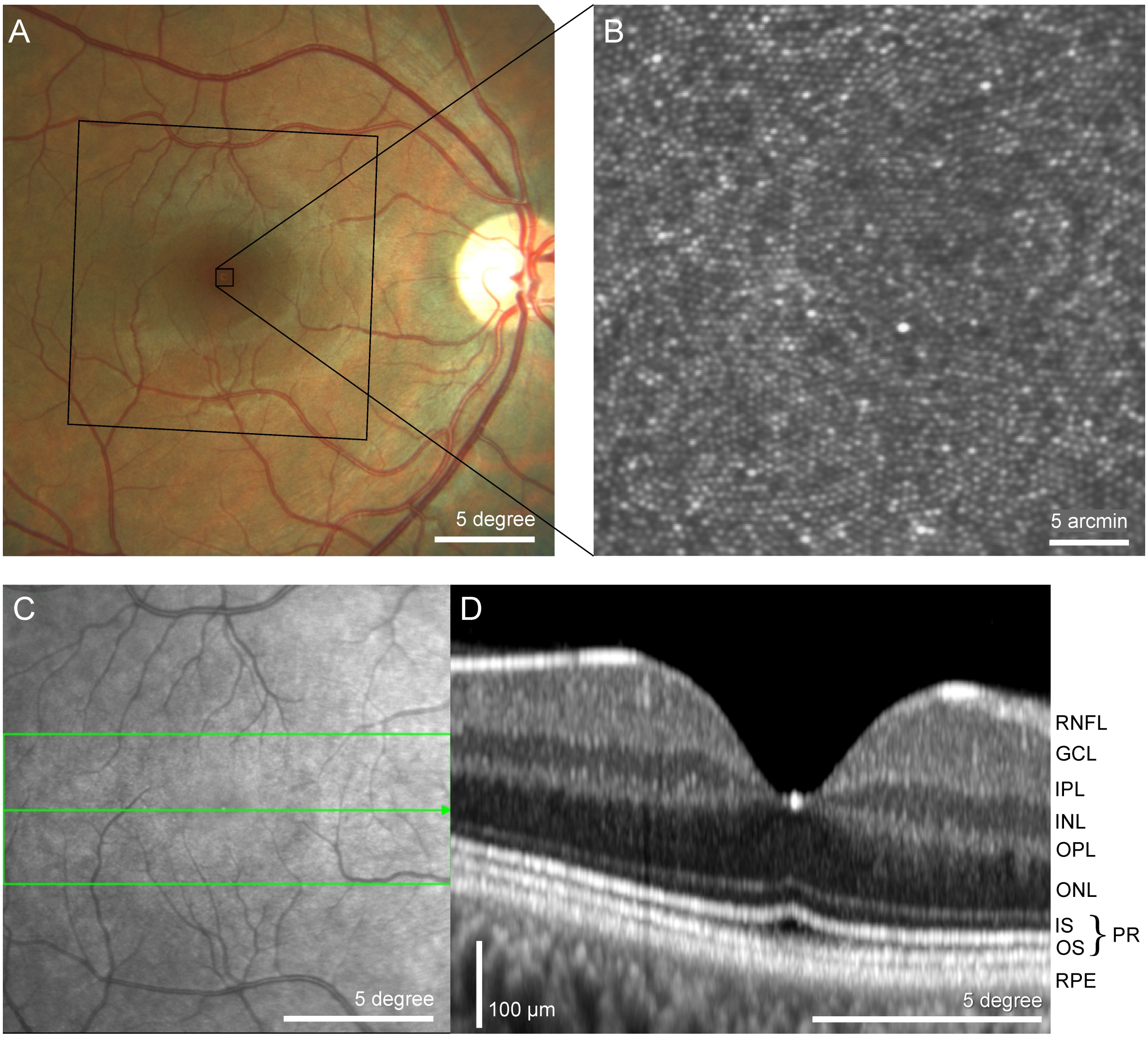

Figure 8: *Images of the same retina using different ophthalmic devices A) Color fundus photography of the retina (Visucam, Zeiss). The black boxes marking the imaging area of the adaptive optics scanning laser ophthalmoscope (AOSLO) in B and the Scanning laser ophthalmoscopy (SLO) of an Optical coherence tomography (OCT) in C. B) Retinal image recorded with an AOSLO revealing the foveal cone photoreceptor cell mosaic. C) Retinal image recorded with a SLO. D) B-Scan of an OCT recording revealing the individual layers of the retina: Retinal nerve fiber layer (RNFL), ganglion cell layer (GCL), inner plexiform layer (IPL), inner nuclear layer (INL), Outer plexiform layer (OPL), outer nuclear layer (ONL), photo receptor cells (PR) with inner segments or ellipsoid zone (IS), and outer segments (OS), and retinal pigmented epithelium (RPE). C+D) recorded with HRT Spectralis, Heidelberg Engineering.*

1.3.1 Fundus camera

The fundus camera (Figure 8A) is an indirect ophthalmoscope by picturing an inverted image of the retina instead of directly looking at the retina. Additionally to an infrared light source, which is used to set up the camera to get a sharp image of the retina, it uses a bright flash lamp. This flashlight flood illuminates the whole retina and allows it to capture the central 30 to 45 degree of the retina in one image [Furlab 2017]. An important advantage of a flood illumination system is that the image is captured within a few milliseconds and therefore the image is only minimally affected by artefacts due to fixational eye movements. The disadvantage is a lower contrast compared to for example scanning laser ophthalmoscopy because of capturing multiply scattered light from the retina and choroid, too [Elsner et al. 1996].

1.3.2 Scanning laser ophthalmoscope

The first scanning laser ophthalmoscope (SLO, Figure 8C) was built by Webb, Hughes and Pomerantzeff in 1980 and regarding its mode of operation it was termed “flying TV spot ophthalmoscope” [Webb et al. 1980]. A cathode ray tube and the SLO have in common that the single frame is generated continuously pixel by pixel and line by line during boustrophedon scanning of a light beam. Due to the continuous movement of the light there is no optical image of the retina at any single moment, like in fundus photography. Instead, a retinal image is assembled based on the temporal video signals of a photomultiplier tube (PMT) that is located in a retinal conjugate plane. One of the advantages of this technology is high light efficiency compared to conventional imaging systems [Webb and Hughes 1981], which also provides more comfort and safety for patients and participants.

To improve the imaging capability of this system, confocality was introduced to the SLO. By the use of a small pinhole in front of the PMT, most of the light is collected from the retinal area in focus, and scattered light from planes out of focus is rejected [Webb et al. 1987]. With the confocal SLO lateral resolution stays the same but the axial resolution is improved and therefore the image contrast significantly increases.

1.3.3 Adaptive Optics

A major improvement for retinal imaging came with the development of adaptive optics (AO) for ophthalmoscopy [Liang and Williams 1997; Liang et al. 1997]. Primarily, the idea to correct for wavefront errors by the use of AO was proposed by Babcock for astronomy [Babcock 1953] so that at first telescopes were tooled up with AO to overcome atmospheric turbulence [Buffington et al. 1977b; Buffington et al. 1977a; Hardy et al. 1977]. Because the eye’s optics are generally imperfect (see 1.2), lateral resolution of ophthalmoscopy was limited to the degree that those ocular aberrations impose. Using AO, a correction of higher-order aberrations of the human eye and therefore high resolution retinal imagery of microscopic structures such as single photoreceptor cells (see Figure 8B) and also diffraction limited stimulation became possible [Liang et al. 1997; Roorda and Williams 1999; Roorda et al. 2002; Yoon and Williams 2002].

In general, AO consist of two key elements, a wavefront detector and a wavefront corrector (see Figure 9A). The most commonly used detector is the Shack-Hartmann wavefront sensor [Liang et al. 1994]. In such setup, the lenslet array creates a range of focus spots from the reflected light beam, instead of one focus spot created by a regular lens. The current wavefront results from the offset of each individual focus spot from the respective centroid (Figure 9B). For example, a completely flat wavefront would show a perfect rectilinear spot pattern. The wavefront is then fitted with the Zernike polynomials and converted via an influence matrix into the according signal for the wavefront correcting element [Jayabalan and Bille 2019]. Such corrector can be a deformable mirror, which has numerous small actuators deflecting the surface [Dreher et al. 1989; Zhang et al. 2015a]. Typically, these two elements are operated in a closed loop to enable a continuous wavefront correction.

Due to the increase of computational power at affordable prices, sensorless AO become more important. Here, the wavefront and therefore the image is post-hoc corrected based on image intensity. On

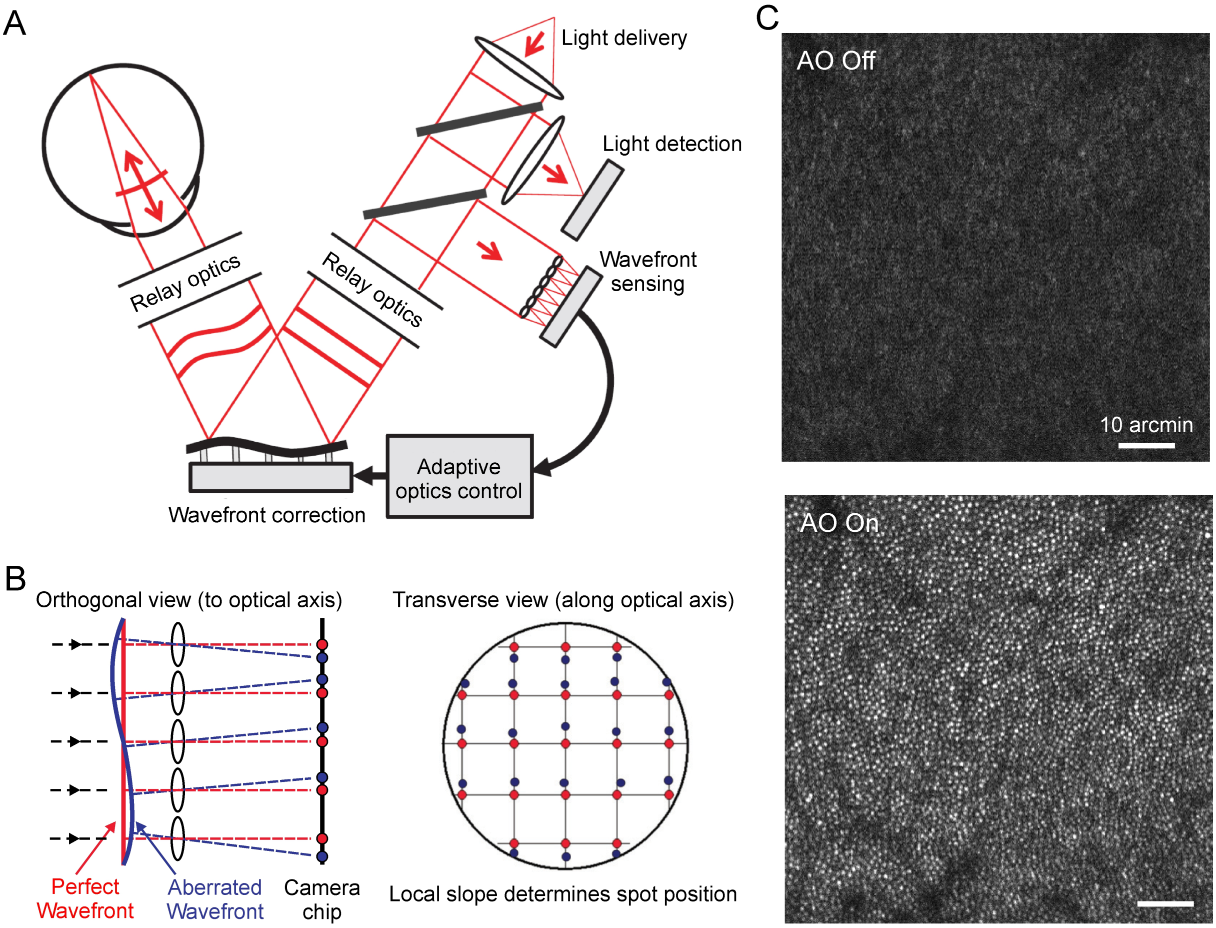

Figure 9: *Adaptive optics for ophthalmoscopy using a Shack-Hartmann wavefront sensor. A) Basic layout of an AO system for retinal imaging and visual psychophysics. B) The principle of a Shack-Hartmann wavefront sensor. The wavefront is subdivided into smaller wavefronts via a lenslet array, focusing on a camera chip. The deviation of the local slope represents the slope of the wavefront at this location. C) Imaging of the same retinal area with the AOs switched off (top) and closed AO control loop (bottom). Sources: A) Roorda 2011; B) modified from Lakshminarayanan and Fleck 2011.*

the one hand sensorless AO help to increase image quality for simple setups. On the other hand, the ongoing changes of the current aberrations (caused for example by tear film fluctuations), challenge these algorithms, leaving hardware based AO the only solution if optimal image quality is desired [Hofer et al. 2011].

The quality of the wavefront correction is given by the root-mean-square (RMS) value. The RMS is calculated as the square root of the sum of the individual Zernike coefficients. Another metric is the point spread function (PSF), which describes the image of a point light source formed by the analyzed optics in the form of a two-dimensional distribution [Jayabalan and Bille 2019]. Hermann von Helmholtz was the first who reported the observation of the PSF in the human eye, when he described the asymmetries of a light point he was looking at [Helmholtz 1867]. As the amount of monochromatic aberrations increases for larger pupil sizes (see 1.2.1), the PSF changes from a small spot into an idiosyncratic pattern based on the eye's aberrations.

AO can be combined with any of the above mentioned ophthalmoscopy systems. The most commonly used commercially available AO system is the rtx1 (Imagine Eyes, Orsay, France), an AO fundus camera [Reiniger et al. 2017; ImagineEyes 2021]. An AOSLO system is supplied by Boston Micromachines (The Apaeros AOSLO, Boston Micromachines, Cambridge, MA, USA) [BostonMicromachines 2020]). The AOSLO technology will be depicted in more detail in the following paragraph.

1.3.4 Adaptive Optics Scanning Laser Ophthalmoscopy

The first usage of AO in combination with SLO was reported in 2002 demonstrating its capability to image the human retina *in vivo* with a video-rate of 30 Hz for example by capturing the flow of individual white blood cells in the capillaries of the retina [Roorda et al. 2002]. Its enhanced axial resolution allowed for an optical sectioning of the retina and enabled to image for example either the nerve fiber layer or the photoreceptor layer (Figure 8B). Improvements in optical design like the reduction of system astigmatism and better wavefront correction with a new deformable mirror hardware renders possible *in vivo* studies of the smallest photoreceptor cells, the rods and foveal cones [Zhang and Roorda 2006; Dubra et al. 2011; Merino et al. 2011; Sulai and Dubra 2012].

The very basic design of the optical path is shown in Figure 10. The light is coupled into the system and is reflected by beam splitter into the front end. The front end consists of several curved mirrors setup in a 4f telescope configuration, thereby relaying conjugated planes of the retina and the pupil. The scanning mirrors and the deformable mirror are placed at the pupil planes. The reflected light takes the same path through the front end and enters the light detection part passing through the initial beam splitter. In the light detection arm, one proportion is used for the wavefront sensor, the rest is detected by a PMT.

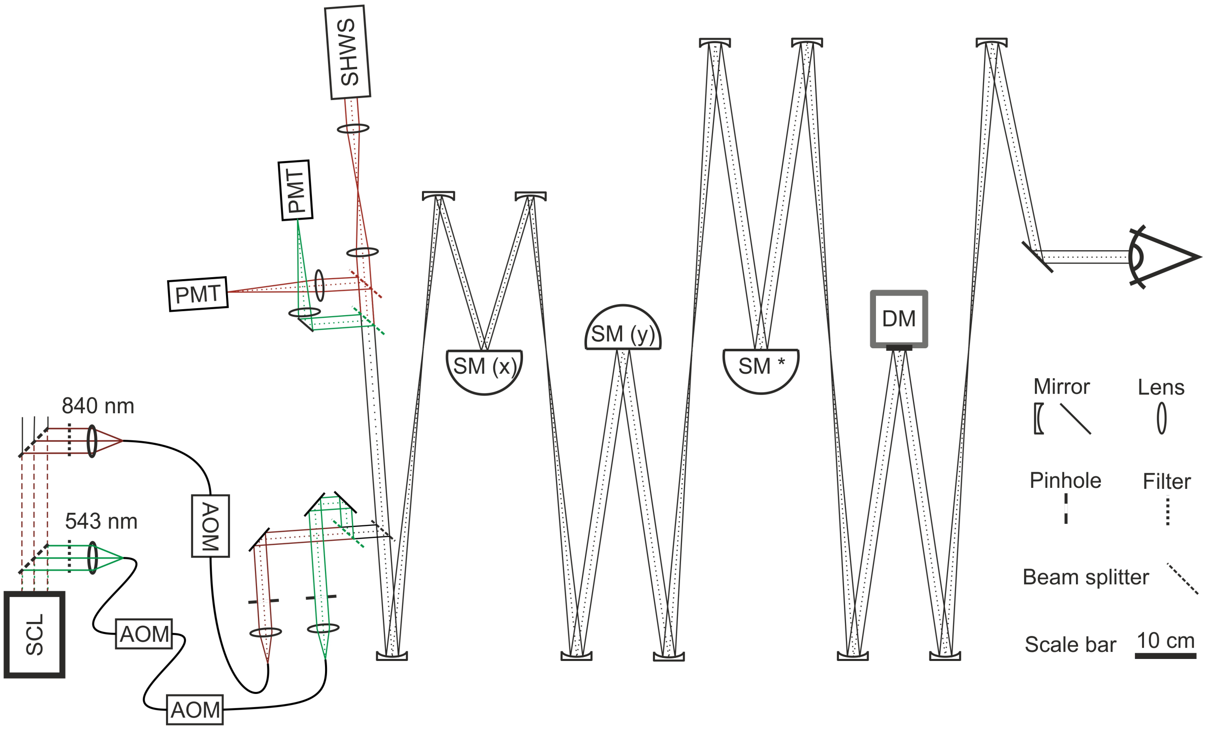

Figure 10: *Simplified optical path design of the AOSLO in Bonn. The light source is a super-continuums laser (SCL). The used light with specific wavelengths was band pass filtered from the SCL's output. The Acousto-optic modulator (AOMs) are fast light switches and needed to display stimuli. The scanning mirrors (SM) span the AOSLO's raster via boustrophedon motion pattern. The eye's wavefront aberrations are corrected with a Shack-Hartmann wavefront sensor (SHWS) and a deformable mirror (DM). SM* was planned to steer the beam regarding to detected eye motion, but this feature was not implemented and therefore SM* was just a flat mirror.*

The AOSLO is mostly used in a confocal configuration, which increases the contrast of the focus plane, because a pinhole in front of the detector blocks any light scatter and reflections from different layers. But this proportion of the reflected light can be used to image the weakly reflecting or translucent parts, too. For example the cells of the retinal pigment epithelium become visible with a so-called darkfield configuration, where the strong central part is blocked and only the stray light is used for imaging [Scoles et al. 2013]. The implementation of non-confocal split-detection, where the image is based on the contrast between the right and the left half of the PSF from the reflected light, enabled the imaging of the cone inner segments [Scoles et al. 2014]. Even the transparent ganglion cells could be imaged using a non-confocal detector arrangement [Rossi et al. 2017].

To this day, the AOSLO was used in a broad variety of clinical studies imaging the eye (see the following reviews for an overview: Roorda and Duncan 2015; Domdei et al. 2017; Burns et al. 2019). Its usage for functional imaging in fundamental research is discussed in more detail in 1.5.

1.3.5 Optical coherence tomography

A very important technological advance in ophthalmology since Helmholtz was the introduction of optical coherence tomography (OCT) in 1991 (Figure 8D). The fundamental basis of this technology is the low coherence interferometry which is used to determine the optical reflectivity profile of a sample tissue like the retina [Huang et al. 1991]. The image is based on the interference signal between the sample arm and the reference arm. During an individual A-scan the tissue is scanned axially by referencing the reflected light from the retina to a certain penetration depth via adjusting the length of the reference arm [Morgan 2016]. In contrast to this initially introduced method (time domain OCT), newer methods have a fixed reference arm length and estimate the depth of the tissue signal based on the wavelength and the fourier transform. In a spectral domain OCT, the light of a broadband light source is analyzed via spectroscopy to compute the tissue penetration of the reflected signal [Fercher et al. 1995]. And in a swept source OCT the emitted wavelength of the light source changes over time for each A-scan [Choma et al. 2003]. A series of laterally shifted A-scans forms the so called the B-scan, and a series of B-scans forms the C-scan which contains the whole volume information. Thus, it is very different from SLO and the fundus camera, which are capturing *en face* images of a certain retinal layer.

1.4 Psychophysics

Psychophysics describes an interdisciplinary field founded in 1860 by Gustav Fechner to study the impact of physical measurement parameters on human perception [Fechner 1860]. Typically, by determining a threshold of perception. For the human visual system, this can be done for any of its various sub functions like for example acuity, color vision, contrast sensitivity, or visual field sensitivity [Wilke et al. 2004]. But, psychophysics are not limited to vision science and apply for any sensory organ.

Threshold estimation in psychophysics relies on the participant's answer, therefore the questioning or task has a major effect on the outcome. One option is a forced-choice task in which the participant sees two or more stimuli simultaneously and has to decide which one matched the task best. The other option is a yes/no or seen/not seen task, which in turn can be rated a specialized form of a forced-choice task [Kingdom and Prins 2010].

1.4.1 The psychometric function

To estimate the threshold, it is important to quantify the relationship between the tested stimulus parameter (for example brightness or gap size) and the percept by generating the psychometric function. This psychometric function represents the percentage of correct answers (ordinate) in relation to the signal strength given by the properties of the stimulus (abscissa) (see Figure 11). In an optimal scenario the properties of the stimulus cover the full range from "undetectable" to "obvious", to ensure the best fit for example by a Logistic function of the s-shaped transition from "never detected" to "always detected". Other possible functions to fit the psychometric data are Cumulative Normal, Weibull, Gumbel, and Hyperbolic Secant [Kingdom and Prins 2010]. The optimal fit is determined by the two parameters Alpha and Beta underlying the sensory mechanism. Alpha marks the position of the reversal point and therefore the threshold. Beta is the slope of the curve. In addition to these, Gamma and Delta are related to the asymptotes at the lower and upper limit. Gamma describes the lower asymptote as the guess rate of giving a correct answer without any reliable percept. Given a 2-alternative forced-choice experiment, Gamma would be 50 %. Delta describes the lapse rate, the chance of an incorrect answer for an obvious stimulus, which defines the upper asymptote [Kingdom and Prins 2010].

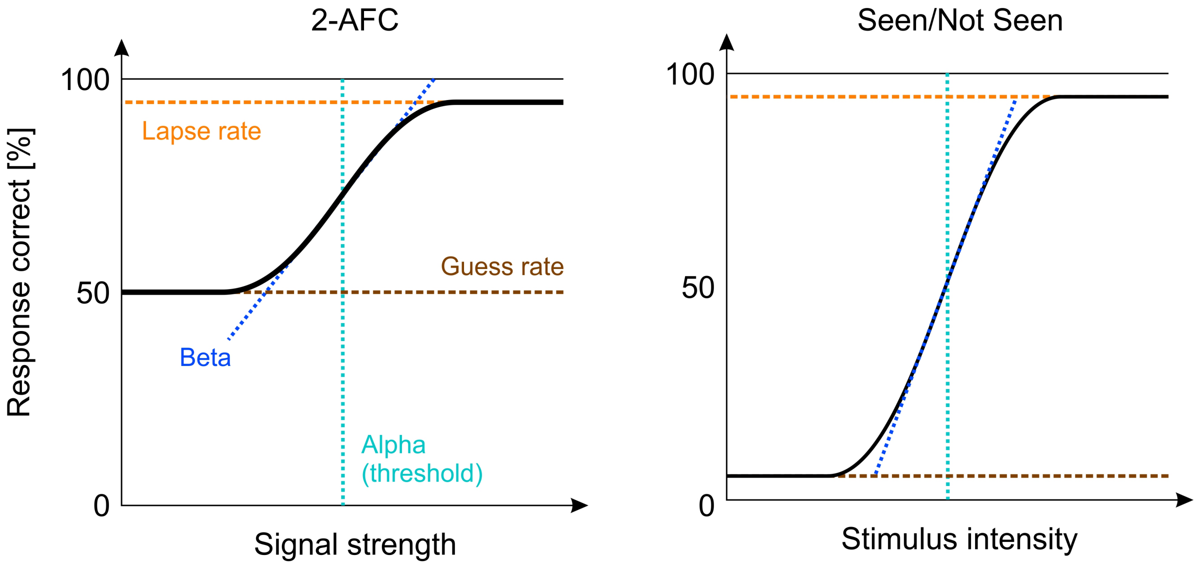

Figure 11: *Universal psychometric function. The psychometric function represents the percentage of correct answers (ordinate) in relation to the signal strength given by the properties of the stimulus (abscissa). Alpha marks the threshold, Beta the slope of the curve. Gamma and Delta are related to the asymptotes at the lower and upper limit. Gamma describes the guess and Delta the lapse rate. Left side: psychometric function for an 2-Alternative-Forced-Choice (2AFC) task. Right side: Seen/Not-Seen task.*

1.4.2 Psychophysical methods

Gustav Fechner described three different methods to determine a threshold, which are now called the classical psychophysical methods [Kingdom and Prins 2010; Treutwein 1995].

The first one is the method of constant stimuli. The examiner creates a set of stimuli, which vary in strength across the expected range from well below to well above threshold. This set is presented to the participant in randomized - or better pseudo-randomized - order and each strength is tested multiple times. A randomized order prevents learning effects. This procedure will provide a complete definition of the psychometric function, as the tested range covers both asymptotes. Thus, this procedure is the gold standard of psychophysics. The biggest disadvantage is that it is very time consuming, because even the obvious and impossible trials are tested with the same number of repetitions.

The second one, the method of limits, also uses a predefined set of stimuli covering the full range. But for this method, the stimuli are presented in descending (or ascending) order, starting with the upper (or lower) limit. Reaching the opposing limit, the sequence is presented in reverse order. The method of limits is typically used for subjective refraction, to estimate visual acuity by reading or specifying differently sized letters or optotypes. This method is the fastest of the three classical procedures, but it comes for the price that only the threshold but not the transition (Beta) zone is revealed.

The third one, called method of adjustment, transfers most of the responsibility to the participant. Instead of just responding to a presented stimulus, the participant controls the signal strength of the stimulus to find hers/his threshold. Hence, this is the only truly non-forced-choice task. The starting point of this procedure can be the upper or lower limit, or randomly set. This method is vulnerable to the participant's bias because the threshold position on the psychometric function is unknown. To minimize the impact of the individual bias, the final threshold is found by averaging the results of repeated runs and changing the starting point for each iteration.

The method of adjustment was used in chapter 4 and 5.

1.4.3 QUEST

New threshold estimation methods, the adaptive procedures, differ from the classical ones, as these prevent unnecessary trials at the lower and upper limit and focus on stimulus presentations at or close to the estimated threshold [Kingdom and Prins 2010; Treutwein 1995]. QUEST (QUick Estimate by Sequential Testing) is a very popular adaptive threshold estimation method [King-Smith et al. 1994] and was used before in various AOSLO psychophysical experiments [Tuten et al. 2012; Harmening et al. 2014; Bruce et al. 2015; Tuten et al. 2017; Tuten et al. 2018; Tuten et al. 2019]. Like other adaptive procedures it uses all available information and takes answers of previous trials into account. Its efficiency is based, firstly, on the assumption that the shape of the psychometric function is always the same and varies only in the threshold, hence, the position along the abscissa, which greatly simplifies the algorithm. In QUEST the psychometric function is fitted with the Weibull function. The second assumption was that the threshold does not change between trials. Therefore, all previous trials can be included into the threshold estimation. This assumption becomes invalid for example due to adaptation and may lead to a corrupted threshold estimate. The third assumption is commonly used and implies the statistical independence of the individual trials.

In practice, for the first trial the stimulus is set at the guessed threshold intensity. The current response (and later on all previous responses) are used to compute a likelihood function of the threshold following the Bayes' theorem (see Figure 12). The intensity of the next trial is set to the intensity of the most probable threshold estimate. The stop criterion can be a number of trials or a certain size of the confidence interval for the current threshold estimate [Watson and Pelli 1983; Treutwein 1995].

Threshold were estimated by using QUEST in chapter 4 and 6.

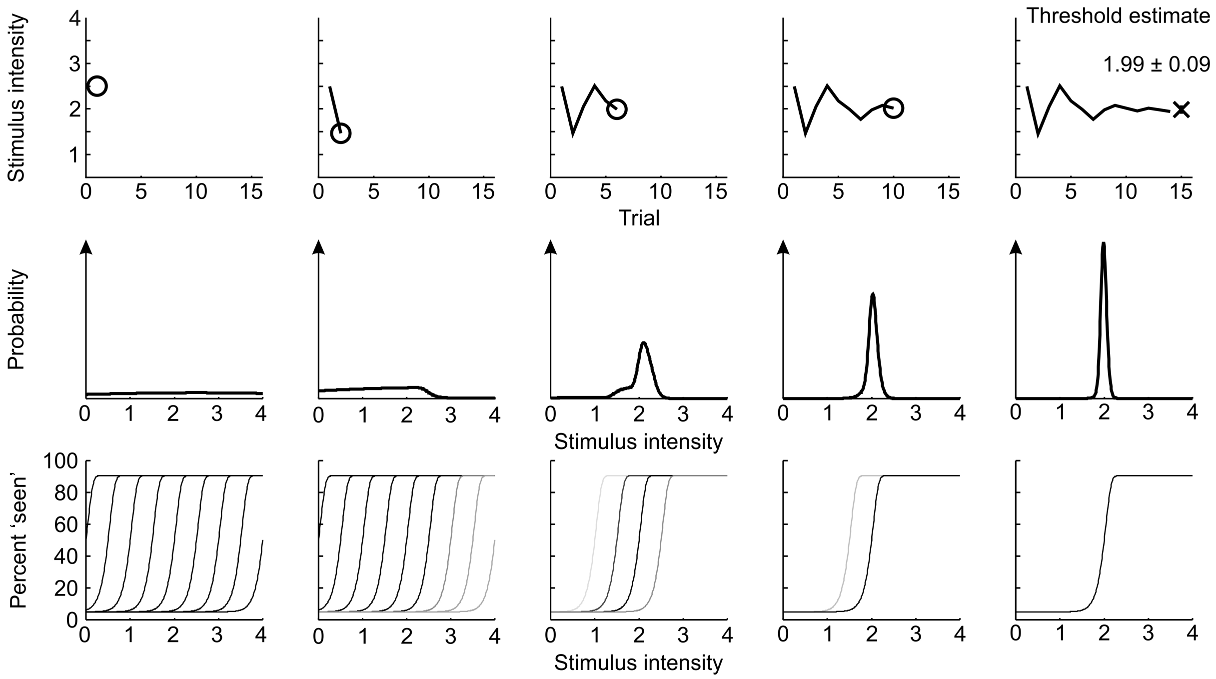

Figure 12: *Concept of threshold estimation with QUEST. Top row: Current threshold estimate and applied stimulus intensity. Middle row: probability density function (pdf) of the likelihood for a psychometric functions with a certain threshold. Bottom row: all possible psychometric functions. Unlikely psychometric functions are plotted with decreased contrast, based on the pdf. The fifth column shows the final threshold estimate after 14 trials.*

1.4.4 Single Cone Psychophysics

Over a long period of time the method of interference fringes was the only way to generate stimuli patterns that are small enough to drive isolated cones, investigate visual perception of cone sized stimuli and subsequently conclude on neural processing of vision [Le Grand 1935; Charman and Simonet 1997]. One of the great advantages is due to the fact that interference fringes were presented in Maxwellian view where the two interfering illumination patches are projected through a small pupil thereby reducing aberrations caused by the eye's optics to a minimum [Roorda 2011]. With an improved interferometric technique it was possible to generate interference fringes smaller than the inter cone distance. Using this new technique the spacing of foveal cones and the regularity of the foveal lattice was assessed by testing the contrast sensitivity at the human resolution limit [Williams 1985a; Williams 1985b].

After investigating how the light intensity of a stimulus viewed by a human eye distributes on the retina, researchers were aware that the smallest stimuli would show a two dimensional Gaussian light distribution on the retina, extending over multiple photoreceptors. Presumably, the first single cell psychophysical experiment was conducted based on the conclusion that by using small stimuli with a very low light intensity only the threshold of the center cones or cone would be exceeded [Krauskopf 1962; Krauskopf 1964]. One of these experiments tested the color perception triggered by stimulation of supposably an individual cone with brief light flashes (1 sec, 580 nm). During this experiment a contact lens with a mounted small mirror was used to compensate for eye motion [Riggs et al. 1953]. Hence, the evoked color perception during stabilized and unstabilized conditions was compared [Shortess and Krauskopf 1961]. Based on the observation that the participant's color response depends on the region that was stimulated, it was inferred that this finding supports the theory of spatially separated cone classes [Krauskopf 1964].

Another idea to drive a single cone was to utilize the sparse distribution of S-cones. By using a 420 nm test flash subtending a nominal visual angle of 1.1 arcmin (about 5 μm), Williams and colleagues demonstrated that there are discrete sensitivity peaks as a result to this stimulus, which confirms the physiological finding of sparsely distributed S-cones [Williams et al. 1981].

Furthermore, adaptive optics not only improved the imaging quality, but also the stimulus delivery as the wavefront of the incident and reflected light is corrected. This allowed to display stimuli with full widths at half maximum of 0.3 arcmin visual angle (about 1.5 μm on the retina) [Hofer et al. 2005]. With a stimulus as small as a foveal cone, the elicited color sensation when stimulating single cones was probed. One finding of this experiment was that the participants had to use at least eight color names to describe their sensations. This is inconsistent with the common theory at that time that hue sensation directly correlates with the excited cone class. On the basis of this finding a new hue sensation model was proposed in which the perceived color depends on the class of the center (excited) cone and its surrounding cones [Hofer et al. 2005].

But all these approaches lacked the possibility to trail the stimulus delivery, so the targeted cone remained unknown.

1.5 AOSLO based Microstimulation

Functional testing of targeted individual cones became possible by the use of a multi-wavelength AOSLO. The initial intention of building a multi-wavelength AOSLO was to increase the information content of the retinal images [Grieve et al. 2006] since the combination of three monochromatic SLO images improves the distinctness of the different retinal structures such as the nerve fiber layer, the blood vessels and the choroid [Reinholz et al. 1999]. But it soon became obvious that the biggest advantage lays in the possibility to image and stimulate photoreceptors simultaneously with different wavelengths [Grieve et al. 2006]. Using a single wavelength, the projection of a stimulus comes with the price of losing image information since the imaging beam has to be switched off to generate a stimulus. An acousto-optic modulator (AOM) acting as a fast light switch, projects letters and simple geometric forms on the retina by switching the incident light beam on and off [Webb and Hughes 1981; Mainster et al. 1982; Poonja et al. 2005]. This way it is possible to use the (AO)SLO as a display (see chapter 3 for details). For single cell psychophysics there are at least two reasons for adding a second wavelength into the AOSLO. First, the stimulation of a single photoreceptor with brief light pulses makes simultaneously imaging of the targeted retinal area with the same wavelength impossible, because the imaging system always captures the inverse of the displayed stimulus. Second, imaging the retina should be done at very low light levels to avoid damaging the photoreceptor cells, which is only possible with infrared light ($\lambda > 780$ nm, IR). However, the highest sensitivity of the human perception is at 560 nm (photopic) [Schnapf et al. 1987]. The eye's chromatic aberrations hamper the precise stimulus delivery with wavelengths differing from the imaging wavelength.

The chromatic dispersion within the eye brings light into different focus points depending on its wavelength (1.2.2). The displacement of the focus in the axial plane defined as the longitudinal chromatic aberration (LCA) is relatively consistent between individuals [Atchison and Smith 2005] and can easily be compensated by the adjustment of the light's path length [Harmening et al. 2012]. If the AOSLO is accurately corrected for LCA, images recorded with IR and for example green light are both in focus. The correction of transverse chromatic aberration (TCA) is more complicated, as direction and magnitude of TCA is idiosyncratic and additionally depends on the beam position on a participant's pupil. A sophisticated method allows to correct for TCA by recording interleaved images from the used light channels. The offsets of retinal structures between the captured frames correspond to the offset caused by TCA. This offset is used to shift a green light stimulus in relation to the IR light respectively. Psychophysical testing shows a good match between subjective and objective TCA measurements ([Harmening et al. 2012]; see also chapter 5).

Targeting an individual cone for repeated stimulation during psychophysical threshold assessment, is challenging because of the fixation eye movements (see 1.1.4). Online tracking of eye motion during retinal imaging with an AOSLO [Arathorn et al. 2007] helps to overcome this issue for trained human participants with normal vision [Yang et al. 2010; Tuten et al. 2012; Harmening et al. 2014] and anesthetized primates [Sincich et al. 2009]. This online tracking works by stripe-wise referencing each current frame to a reference frame. Therefore, it achieves a very high sampling rate (about 1 KHz) of the FEM, sufficiently fast enough to compensate for drifts and small microsaccades [Arathorn et al. 2007; Sheehy et al. 2012].

According to the wave-guiding properties of cones sensitivity should be best when a stimulus hits the center of a cone [Enoch 1964; MacLeod et al. 1992]. Harmening and colleagues compared the detection thresholds between targeting a cone's center and the space between cones using the AOSLO's smallest stimulus. The results of this psychophysical experiment showed that the thresholds were 1.5 times higher when the stimulus is targeted between cones proving that a multi-wavelength AOSLO renders possible single cell psychophysics [Harmening et al. 2014]. Recent studies including electrophysiological recordings from macaque monkey retina and the lateral geniculate nucleus show similar results [Sincich et al. 2009; Field et al. 2010].

AOSLO based microstimulation is a special form of microperimetry, because it provides fundus related perimetry, testing the sensitivity of the visual field on an extremely fine scale [Tuten et al. 2012]. Several fundamental research studies used the AOSLO to assess human visual perception on a single cell level. One of the first studies tested, if there is a functional difference between dark cones, which are not visible and normal reflecting cones [Bruce et al. 2015]. However, Bruce and colleagues reported no significant threshold differences between dark and normal cones. They concluded, that in dark cones destructive interference cause its dark appearance, due to the waveguidance characteristic and the specific length of such cone. The length of the individual photoreceptor cell is affected by the renewal of the outer segment's disk. During this process - called disk shedding - a stack of old disks with depleted photopigment is absorbed by the RPE cells, significantly changing the outer segment length length and thereby the cone's reflectivity, which could be shown recently *in vivo* with an AOOCT [Kocaoglu et al. 2016]. Therefore, dark cones should be called rather dysflective cones. Retinal summation was tested in the periphery, comparing thresholds of individual and pairwise stimulation, thereby revealing the cone's functional weighting [Bruce 2016; Sincich et al. 2016]. Tuten and colleagues probed the spatial summation of the foveola with differently sized stimuli and reported, that Ricco's area spanned about

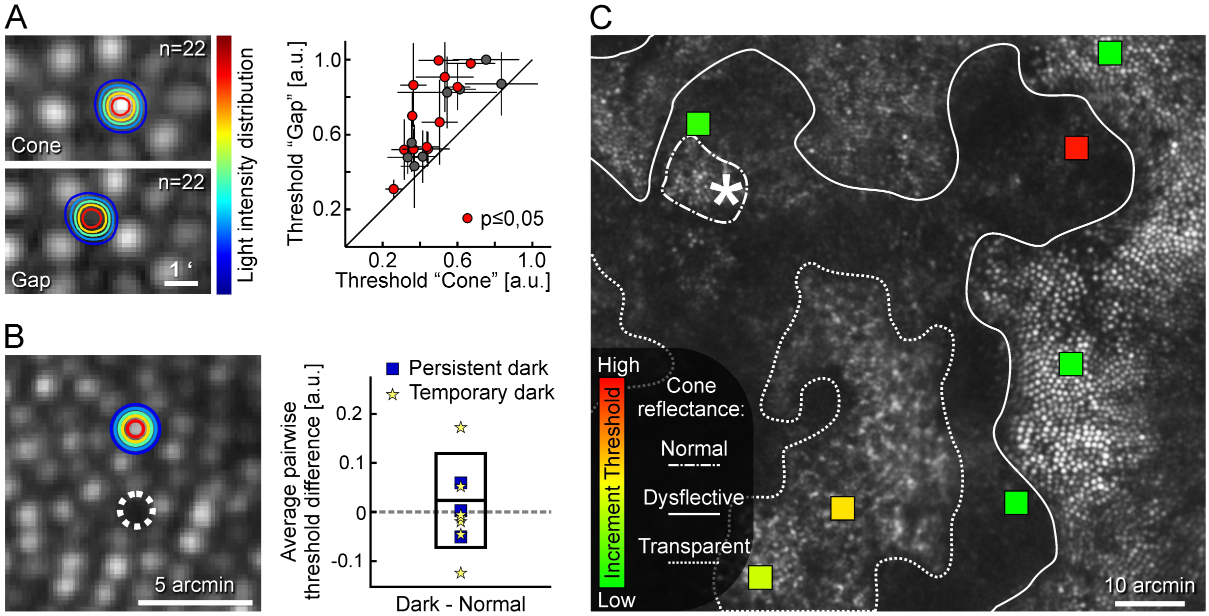

Figure 13: *Examples of AOSLO based microstimulation studies. A) Proof-of-principle at an retinal eccentricity of about 3 degree. The stimulus targeted either the center of a cone or a gap. The repeatedly determined psychophysical thresholds were significantly higher when targeting the gap between cones. B) Pairwise function testing in normal and so-called dark or dysflective cones (dashed). The detection thresholds were not distinguishable for both cases and dark cones showed normal visual function. Y-axis shows the threshold difference in arbitrary units. C) AO-microperimetry of a diseased retina (macular telangiectasia type 2). Squares show test site and stimulus size; the star marks the foveal center. Most detection thresholds were comparable and normal despite noticeable image differences. Sources: A) adapted from Harmening et al. 2014; B) adapted from Bruce et al. 2015; C) adapted from Wang et al. 2015.*

2.4 arcmin [Tuten et al. 2018]. When testing color perception on a single cell level, it was observed that most of the cones targeted did not elicit a perception of hue. The percept of hue seemed to be based on the surrounding cone classes. The highest probability of a chromatic sensation was produced by cones next to cones of different classes [Sabesan et al. 2016]. A followup study showed that individual M- and fewer L-cones elicit a blueish percept when stimulated against a blue background. The authors explained their finding that the activity of neighboring cones, controlled via the background, caused a favoring of the blue opponent pathway [Schmidt et al. 2018a]. In addition to this, sensitivity thresholds were significantly increased, if the target cone was neighbored by cones of an opposing cone class [Tuten et al. 2017].

The possibility to generate cone sized stimuli makes the AOSLO furthermore a useful tool for clinical research leading to a better understanding of different retinal pathologies. With AOSLO based microperimetry physicians are able to investigate the progress of retinal diseases or the therapeutic effect of new drug substances on the single cell level [Roorda 2010; Chen et al. 2011; Tuten et al. 2012; Wang et al. 2015; Tuten et al. 2019].

2 Aims of the project

The AOSLO has proven its enormous potential as an imaging system for researchers and physicians by providing real-time high resolution *in vivo* retinal images [Williams 2011]. In addition, the AOSLO can be used as a platform for psychophysical experiments by enabling the means to test individual photoreceptor cells (see 1.5). However, the central ±0.6 degree of the human retina - the foveola - was so far seldom included due to technological limitations. Hence, all recent AOSLO based psychophysical studies targeted individual cones of the fovea at about 1.5 degree eccentricity (Figure 14) with the exception of Tuten et al. 2018.

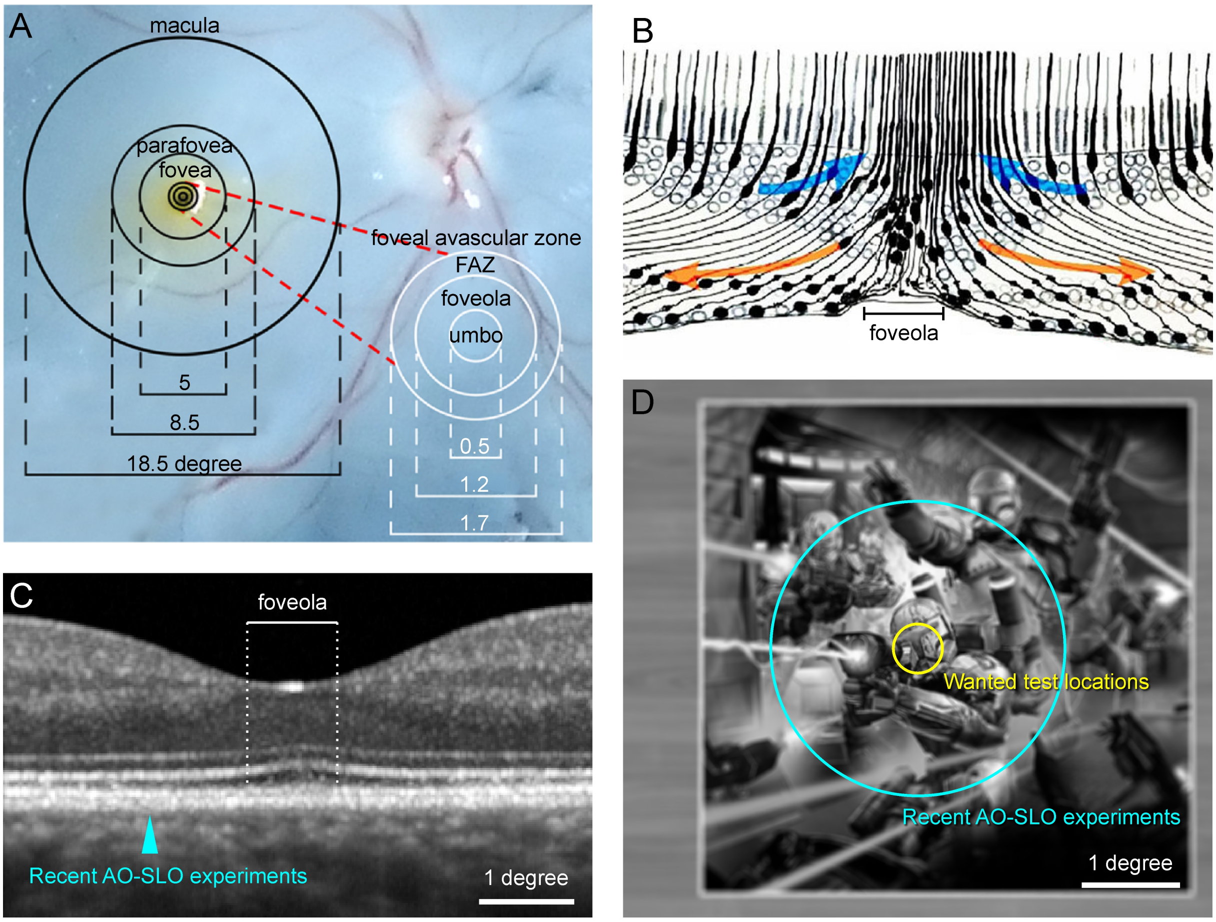

Figure 14: *The human fovea and its importance for AOSLO microstimulation experiments. Recent AOSLO experiments were conducted at roughly 1.5 degree eccentricity (cyan coloring in C and D). A) A map of the whole macular area to show the dimensions of the foveal pit, foveal avascular zone, parafovea, perifovea, and the limits of the macula. Inset shows the dimensions of the foveal avascular zone, foveola (defined by the absence of ganglion cells) and umbo (elongated OS). All measurements are stated in degree. B) Drawing to show the closely packed cones in the foveal pit. Blue arrows show the vertical squeezing and packing of the cones in the foveal pit and orange arrows show the displacement horizontally of the foveal cone axons. C) OCT image showing the foveola of a human* in vivo *with horizontal displacement of the foveal cone axons, and the elongation of the cone OS. D) Simulated retinal image when viewing at a printed drawing on a table based on the dendritic field sizes of midget ganglion cells. Sources: A) adapted from Cuenca et al. 2020; B) adapted from Kolb 1995; D) Image from Willging 2011; Formula to compute the dendritic field size from Watson 2014.*

The foveola is the most important location of the retina for human visual perception. Firstly, the second and third order neurons are displaced (Figure 14B) thereby exposing the cone photoreceptor cells and reducing the otherwise occurring scatter of the incident light [Goldsmith 1990; Agte et al. 2011].

Secondly, it is the area where the cone photoreceptor cells are tightest packed at their smallest diameter found anywhere in the retina (Curcio et al. 1990, see also Figure 4C). Thirdly, the outer segments are elongated thus maximizing the photon absorbance probability (Figure 14B, C) [Bowmaker et al. 1978; Baylor et al. 1979; Bassi and Powers 1990]. Fourthly, the midget ganglion cells in this area are connected with cones in a one-to-one circuitry [Kolb and Marshak 2003] enabling the highest possible spatial sampling (Figure 14D) [Rossi and Roorda 2010]. Finally, the importance of the foveola is also reflected by its representation in the primary visual cortex, where the central 1 degree (about 0.7 %) of the retina occupy approximately 12 % of the striate cortex [Daniel and Whitteridge 1961; Connolly and Van Essen 1984; Van Essen et al. 1984].

Therefore, it would be important to assess the human photoreceptor mosaic at the foveola on a cellular scale *in vivo*. To date this is, however, not possible due to technological limitations of the stimulus delivery. Consequently, the first aim of my dissertation encompasses the evaluation and optimization of the AOSLO as a display for single cell psychophysics at the foveola. The focus here will be on the stimulus light channel, for example probing of the complicated time-space-relationship of the AOSLO and its impact on the stimulus delivery. This detailed description should help to understand how hard- and software interoperate to display a stimulus on a participant's retina. Subsequently, this knowledge can be used to optimize the stimulus processing for example to display smaller stimuli, to increase the stimulus contrast, or to improve the accuracy of the stimulus delivery. The analysis of the AOSLO display will point out its benefits and its limits, ultimately narrowing down the smallest stimulus achievable with an AOSLO and thereby proving its usefulness for future psychophysical experiments.

The second aim takes advantage of the first aim, rendering possible a sufficiently small and precise stimulus delivery to move the single cone experiments from the parafovea into the foveola. Testing of human foveolar light sensitivity based on individual cone stimulation is going to be the major experiment here. This enables for example direct assessment of the long-standing hypothesis of foveal private lines for the first time in an *in vivo* experiment.

3 Characterization of an AOSLO as a display for psychophysics

Due to the scanning nature of the AOSLO, visual stimuli can be encoded into the system's beam with highspeed light modulation. In a simple case this modulation means switching the imaging light beam on and off to create trivial binary stimuli like letters [Mainster et al. 1982], thereby creating an acute visual display directly on a participant's retina (Figure 15A).

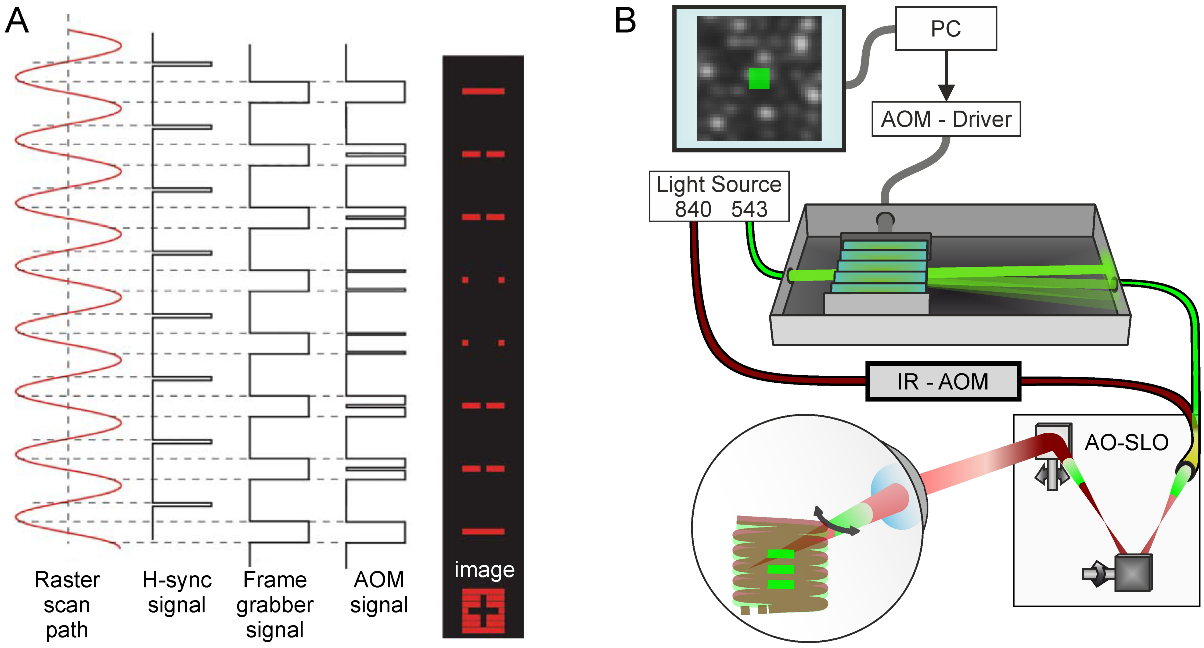

Figure 15: *AOSLO stimulus generation. A) Simplified sequence of signals that are used to generate cross stimulus. The left column shows the path of the focused spot in the raster scan. Each time the scan mirror crosses the midpoint on the backward direction, an horizontal pulse for synchronization (hsync) is generated, which serves as the master timer for the entire AOSLO system. The hsync signal is used to trigger the line-by-line acquisition of the image by the frame grabber and is shown as the third trace. The last column shows the light pattern falling on the retina for the corresponding line scan. B) Stimulus generation in a multi-wavelength AOSLO using an acousto-optic modulator (AOM). While the IR (840 nm) light is used for continuous scanning of the retina, the green (543 nm) stimulus is produced on top of the imaging raster. Source: A) adapted from Poonja et al. 2005.*

A more sophisticated method uses acousto-optic modulation (AOM), which allows to set stimulus intensities between full on and off. By implementing a second light channel for stimulation, the retina is scanned continuously without any information loss due to a light off switching event, and the stimulus is projected on top of the retina (Figure 15B). To activate the two cone classes of the foveola (the L- and M-cones) equally a wavelength of 543 nm was used for stimulation (see Figure 4B).

The contrast achieved with an AOM is about 4 log10 units, or 0.9999 Michelson contrast. The field programmable gate array (FPGA) board used for image acquisition and stimulus generation, operates the digital stimulus channel with 14 bit coding, allowing for 16,383 steps from off to full on. But the output of the AOM is linearized by using a look up table (LUT) with 1,000 steps. Therefore, the smallest increment is limited to the 10 bit signal coding of the LUT. A significant increase of the overall stimulus contrast and number of steps was achieved by cascading two AOMs (see also chapter 4).

In consequence of the fast scanner moving in an oscillation pattern, the laser beam is steered with various speeds across the retina: slowly moving at the scan field borders and fast moving in the center of the field (Figure 16). To dewarp the raw image a LUT is created containing the time window for each pixel. For example, a pixel at the raster's edge takes about 160 nsec to write, while a pixel in the center takes about 37 nsec.

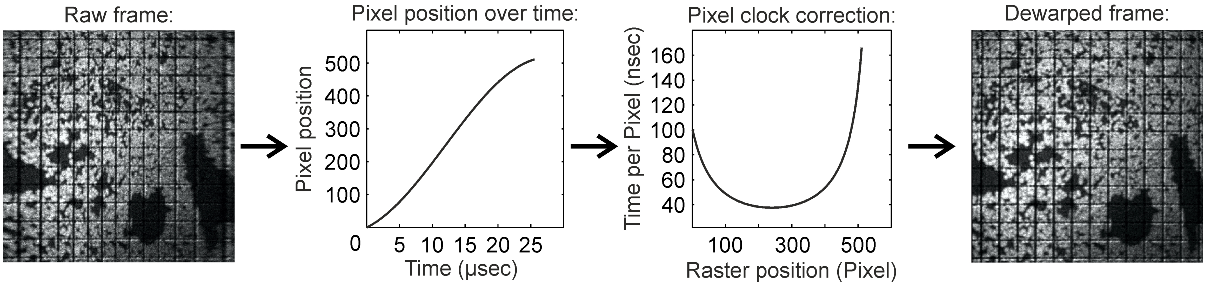

Figure 16: *Dewarping of the raw AOSLO image. Due to the sinusoidal movement speed of the resonant scanner, the stimulation laser is swept across the retina with variable speed, and thus the duration spent per display pixel changes. Therefore the captured frame is stretched at the edges and compressed in the center (left: raw image frame acquired from a perfectly orthogonal grid). For dewarping, pixel position over time is plotted and the inverse pixel position values are used to compute the pixel clock correction (right: same grid as left with pixel clock correction).*

Hence, stimuli with a constant size across the raster differ in light-on duration depending on their position in the scanning raster. This is a problem when testing sensitivity because the number of photons delivered per stimulus has to be the set intensity without changes due to the position in the scanning raster. Furthermore, the processor unit of the employed FPGA board is operating with 20 MHz meaning that the minimal time interval to process stimuli is 50 nsec. This produces jumps in light-on duration even for neighboring pixels (Figure 17A). For example, a typical 3-by-3 pixel stimulus is reduced to 2-by-3 pixel during the output computation and thereby suffers a decrease in light intensity by 33 %, which tremendously interferes with the threshold estimation algorithm. Optimally, the stimulus would be presented with a light-on duration of about 111 nsec (3 x 37 nsec). But the stimulus presentation jumps between 2 pixels (too short) and 3 pixels (too long) for neighboring pixels because of the minimum time step of 50 nsec, which is significantly longer than the real duration of 37 nsec in the center. On the plus side, this rounding is constant for each line in the raster and strictly tied to the currently used LUT. Therefore, one solution could have been to use the actual stimulus positions in the raster to recompute the QUEST threshold estimate, as the raster positions with divergent light-on times are known.

As a solution to this problem I implemented a constant power mode, where the stimulus is always displayed with the exact same number of pixels in terms of the minimal interval time, as set in the stimulus configuration (Figure 17B). For example a 3-by-3 pixel stimulus is always played out with 150 nsec light on per line. The drawback of this method is a decreased stimulus contrast close to the edges. Thus, stimuli should only be displayed in the central part of the imaging field orthogonal to the resonant (fast) scanner axis, to minimize the variation in stimulus contrast (Figure 17C). Additionally, we assessed the impact of diminished stimulus contrast at the raster's edges for stimulation using constant power mode. Thresholds were indeed increased for stimuli being displayed outside the central area. The observed threshold increase was similar to the dewarping LUT, which therefore could be applied to correct stimulus presentations (Figure 17D).

The pixel independence is mainly affected by the AOM operating with 100 MHz. Therefore, the AOM needs 10 nsec to change between two different values, which affects 20 % of a pixel in the center. On the plus side, pixels orthogonal to the fast scanning axis are completely independent.

3.1 Simulation of cone stimulation

To test, if stimulation of an individual photoreceptor cell in the foveola is possible with our AOSLO, I wrote a Matlab script, simulating the light spread of a stimulus on the retina and the light absorption in the individual photoreceptor cell (see Figure 18). In the first step, the point spread function (PSF) is computed. For the AOSLO I assumed the PSF to be diffraction limited with a small amount of residual defocus. A recent study estimated the amount of residual defocus to be about 0.03 D [Meadway and Sincich 2018]. The light spread on the retina is given by a convolution of the planned stimulus and the

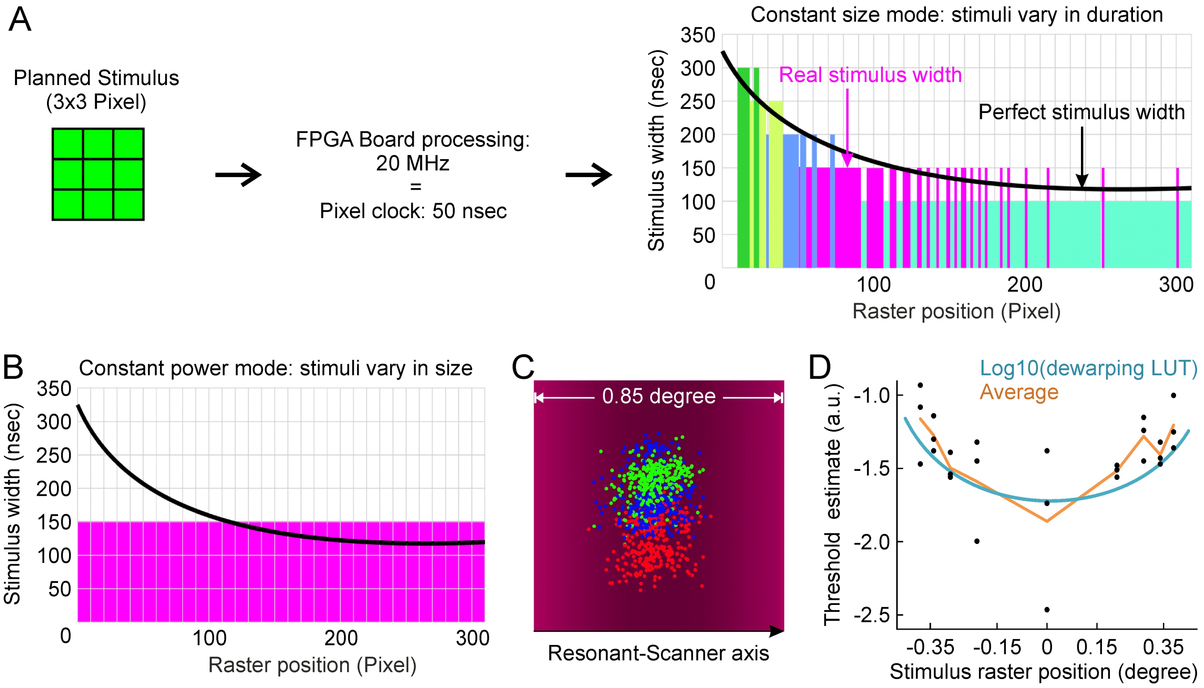

Figure 17: *Side effects of dewarping on stimulus presentation. A) To keep its size constant, a 3 pixel square stimulus will vary in light-on duration across the raster. Additionally, the stimulus processing FPGA board runs with 20 MHz and therefore the smallest time interval for changes is 50 nsec. As a result, the stimulus size jumps between the two possible time intervals for neighboring positions in the raster. B) Our solution to this problem was the implementation of a constant power mode where the stimulus is always displayed with the exact same number of pixels. C) To minimize the impact of the now varying stimulus contrast stimulus presentation should be limited to the central field of the raster. The intensity of the AOSLO raster as seen by a participant was simulated based on the LUT. D) Assessment of stimulus positions close to the raster edges confirmed a significant impact of decreased stimulus contrast on threshold estimation. The threshold change was similar to the LUT, with the result that the LUT can be used to correct threshold estimates based on the stimulus' raster position.*

PSF. Light absorption was computed for each cell, by applying a two dimensional Gaussian function with an aperture of 0.48 [MacLeod et al. 1992]. The cone size and cone spacing in this model is based on Curcio et al. 1990. This model neglects any contribution of light coupling effects of the cone inner segment [Meadway and Sincich 2018].

In theory, the smallest stimulus possible, is 1 pixel. Interestingly, this stimulus (in a field measuring 600 pixel per degree) would be smaller than the PSF and therefore making the PSF the limiting factor and not the stimulus delivery hardware. In an optimal scenario, with a 1 pixel stimulus and only 0.01 D residual defocus, we could achieve a cone contrast of about 7 for a cone in the central fovea. Meaning, that the targeted cone would absorb 7 times more photons than the direct neighbors combined, which would be sufficient to elicit a percept based on an individual photoreceptor cell being activated. A more realistic scenario would be a point spread function with 0.03 D residual defocus. Here, the cone contrast is diminished to 2.3. With a technically more reliable stimulus of 3-by-3 pixel, the cone contrast is only 1.6, which surely rules out activation of an individual cell in the central fovea. With a 3-by-3 pixel stimulus and a residual defocus of 0.03 D, cone contrast would be higher than 5 at an eccentricity of 0.35 degree, or a cone spacing of 0.69 arcmin (= 7,500 cones/degree^2) (see Figure 19). If residual defocus is further increased, the PSF becomes even larger. Hence, at 0.05 D residual defocus the actual size of the stimulus on the retina is almost the same for a 1 pixel stimulus and a three pixel square.

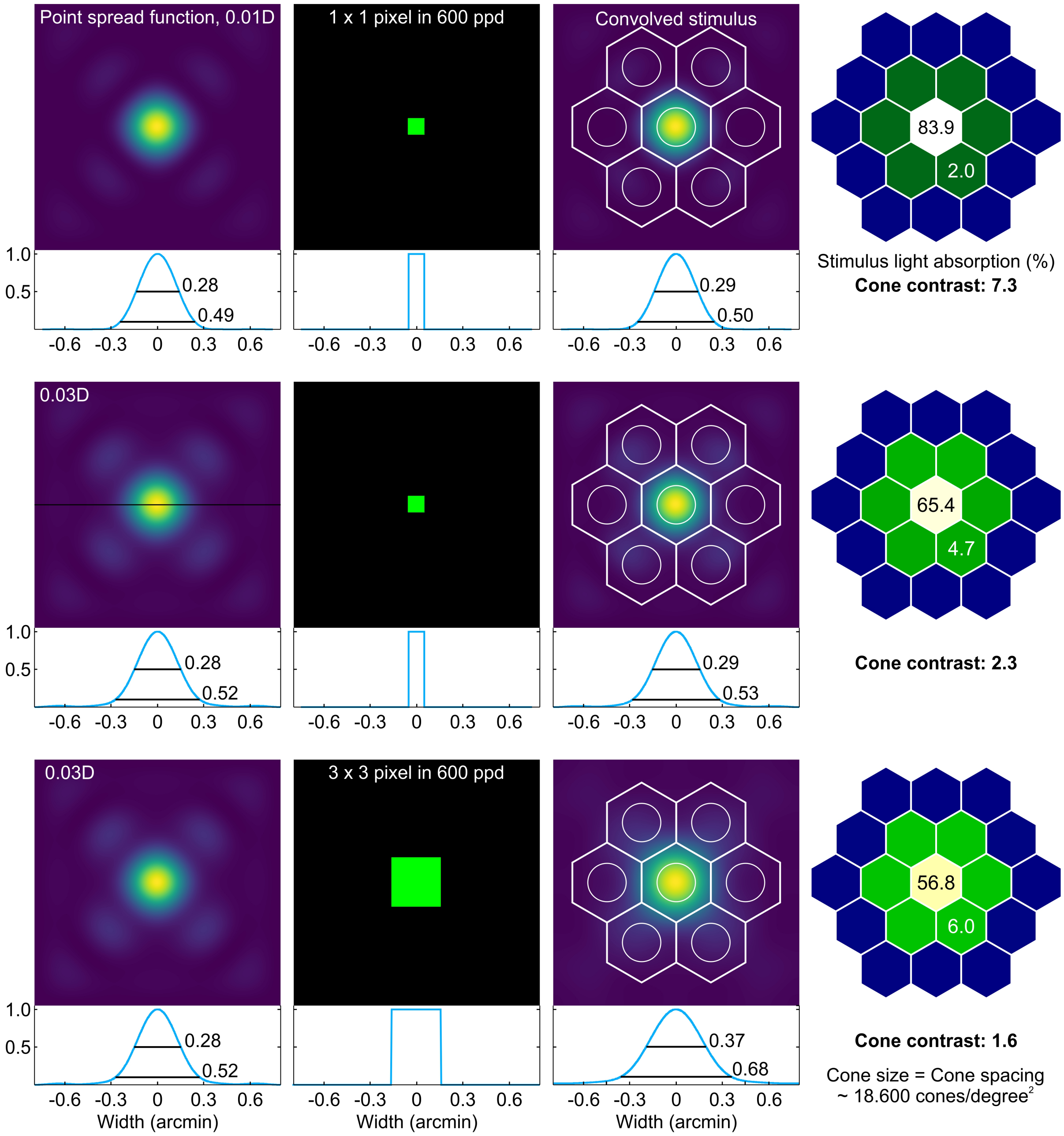

Figure 18: *Simulating the stimulus appearance on the retina and resulting photon catch in the underlying cone cells. The left column shows a two dimensional representation of the normalized PSF. The second column contains the planned stimulus. The convolution result of the stimulus with the PSF is shown in the third column. The cone inner segments are given by the hexagons and the aperture (48 %) is marked with a circle. The central profiles (marked by the black line) are shown below the 2D representations. The numbers state the full-width-at-half-maximum and the width at 10 % height. The right column shows the color coded light absorption modeling for each cone. For a realistic residual defocus of 0.03 D the stimulus size is defined by the size of PSF and cone contrast too low for excitation of an individual cone.*

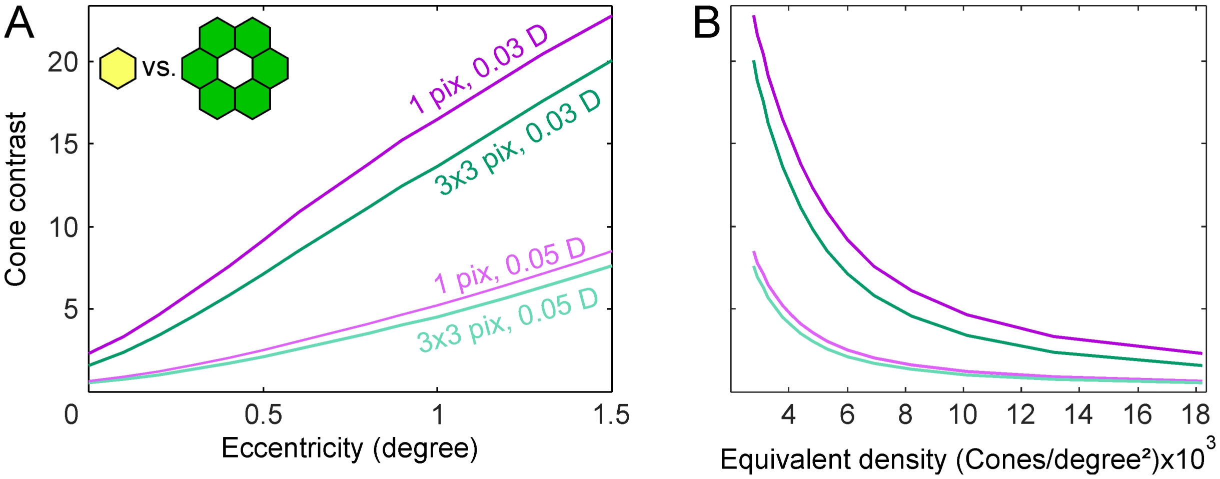

Figure 19: *Estimated stimulus contrast for a targeted cone-sized stimulus, summing across 6 surrounding cones. A cone contrast of at least 5:1 is reached for a 0.03 D PSF and a 3 pixel square at 0.35 degree retinal eccentricity, or for a cone density of about 7,500 cones/degree*^{2} *(cone spacing about 0.7 arcmin). With a residual defocus of 0.05 D cone contrast exceeds 5:1 at a retinal eccentricity of about 1 degree. Due to the size of the PSF, the planned stimulus size is secondary and the stimulus size on the retina is solely defined by the PSF. The relationship of eccentricity and cone density is based on [Curcio et al. 1990].*

4 Ultra-high contrast retinal display system for single photoreceptor psychophysics

The content of this chapter is based on:

Domdei N*,Domdei L*, Reiniger J, Linden M, Holz FG, Roorda A, Harmening WM (2018) Ultra-high contrast retinal display system for single photoreceptor psychophysics. *Biomedical Optics Express*, 9(1): 157-172. DOI: 10.1364/BOE.9.000157

*: denotes equal contribution

4.1 Introduction

Human vision starts in the mosaic of retinal photoreceptors, cones and rods, where the stream of incident photons is captured and converted into neurochemical signals which form the basis of visual perception. With recent advances in high-resolution ophthalmoscopy, the retinal photoreceptor mosaic can be resolved and imaged in the living participant, opening the door to assess the retina's structural as well as its functional architecture *in vivo* [Liang et al. 1997; Roorda 2011; Williams 2011]. In particular, the adaptive optics scanning laser ophthalmoscope (AOSLO) is an optical platform that can deliver light to targeted retinal areas with microscopic precision, enabling physiological and psychophysical visual function testing on a cellular scale [Sincich et al. 2009; Rossi and Roorda 2010; Harmening et al. 2014].

In a scanning system such as the AOSLO, spatially resolved visual stimuli are generated by temporal modulation of a visible laser beam swept across the retina of an observer, reminiscent of the temporal modulation of an electron beam in a cathode ray tube to create a visual display [Mainster et al. 1982]. For instance, a square stimulus with maximum visual contrast is rendered by turning on the stimulation light for the time the scanning beam needs to sweep across a retinal area that corresponds to the stimulus' visual features, and turning it off for the remaining time (Figure 20A). In such a display, visual contrast is governed by the temporal modulation characteristics of the light switch. Because AOSLO systems operate with scanning line rates in the Kilohertz range, light switching needs to be fast if stimuli of high spatial resolution (with their size usually being just a fraction of a complete line scan) are desired [Arathorn et al. 2007; Yang et al. 2010]. Acousto-optic modulators (AOMs) provide the necessary bandwidth (typically above 100 Megahertz) to achieve nanosecond-scale switching events independent of wavelength, and are therefore the method of choice for today's AOSLO imaging and stimulation devices.

Acousto-optic light modulation, however, comes at the cost of incomplete extinction: Even when an AOM is off, some amount of light "leaks" through its output due to imperfect optical isolation of the modulated diffraction pattern (Figure 20B). Commercially available AOMs are specified with maximum extinction ratios of around 40 dB, i.e. the radiant power ratio at their modulated output between OFF and ON, or simply their optical contrast, covering an illumination range of around 11 log units for cones and rods combined [Stockman and Sharpe 2006], the contrast of today's AOMs set a fundamental limit to stimulation capabilities. AOM leakage creates a constant background illumination, with an extent coinciding with the SLO scanning field. In consequence, measures of visual sensitivity, for instance, can only be performed as light increments against a visible background, with the stimulus and background being comprised of the same wavelength (Figure 20). If small visual stimuli are desired (e.g. when single cones are tested), stimulus light levels need to be high, and in turn, background levels will be high as well. At higher eccentricities, on the other hand, visual stimuli are not bright enough to trigger perception. Moreover, high background light intensities will saturate rods, making it impossible to assess them psychophysically [Harmening et al. 2014].

We describe a simple solution how to achieve background light elimination and greater dynamic range for the stimulus light for SLO-based psychophysics (Figure 20C). By cascading and temporally aligning two fiber-coupled AOMs, we demonstrate radiometrically and psychophysically that this approach extends current AOSLO testing regimes into the mesopic and full scotopic range. In general, AOM cascading may be useful in all fields requiring extremely high visual contrast ratios.

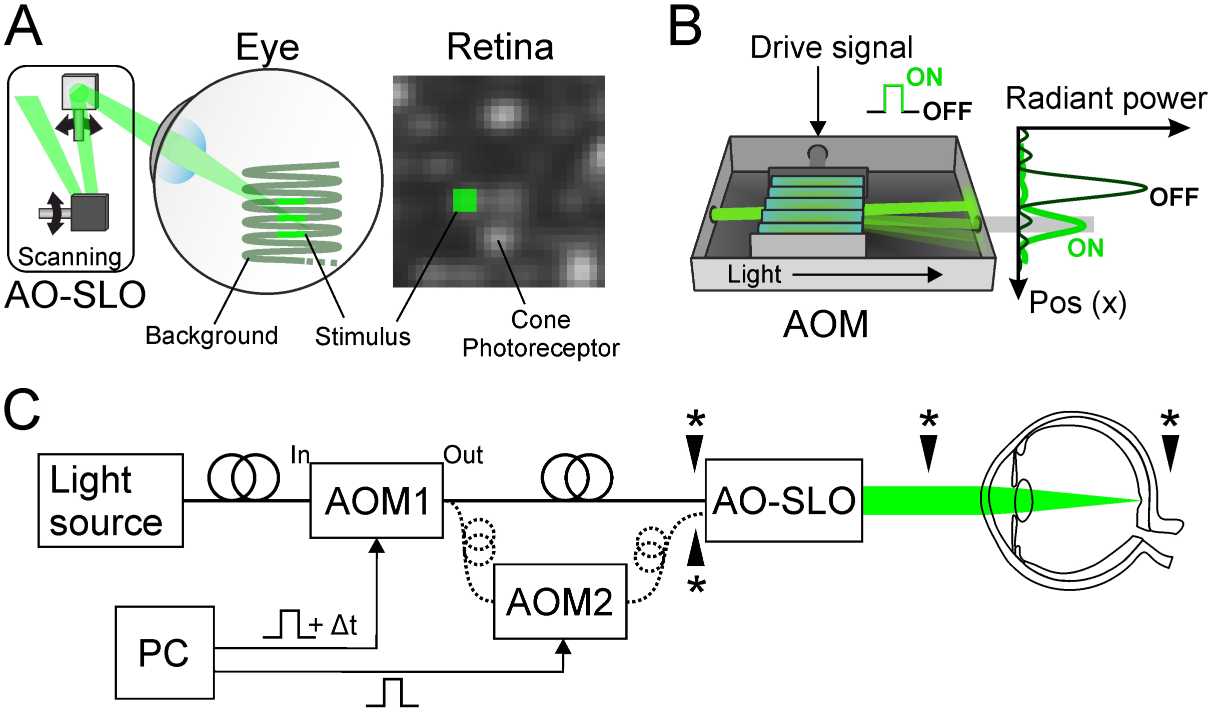

Figure 20: *High-contrast* in vivo *micro-stimulation for visual psychophysics. A) With AOSLO, single photoreceptors can be imaged and targeted for small spot stimulation. During scanning (horizontal and vertical arrows), incomplete extinction of stimulus light modulation will produce stimuli on the participant's retina that contain a visible background, limiting experimental options. B) Acousto-optic modulation exhibits finite extinction, i.e. the ratio of light transmitted during full ON and OFF is limited by light leak caused by incomplete optical isolation between the undiffracted (black) and the modulated diffracted beam (green, gray area in power plot, not to scale). C) AOM cascading schematic. Intensity of a visible stimulation light is controlled by fiber-coupled AOM in single (solid) or cascaded (dashed) configuration to produce diffraction limited spatially resolved stimuli on the retina of a human observer. Temporal alignment is realized by delaying drive signals (Δt) for AOM1. We analyzed visual contrast of the stimulus light either radiometrically or psychophysically at the locations marked with an asterisk. Cascading increased contrast multiplicatively and removed unwanted backgrounds.*

4.2 Materials and methods

To determine the limits of optical contrast produced with an acousto-optic switched retinal display, we first characterized the contrast of single and cascaded fiber-coupled AOMs by measuring their radiometric power outputs as a function of drive voltages. After identifying zero-point location and latency for each AOM individually, temporal alignment (i.e. concurrent switching times), was verified in an AOSLO system. For functional testing of single photoreceptors, we fitted a multi-wavelength AOSLO setup with a temporally aligned AOM cascade to produce small visual targets for psychophysical testing and measured background light visibility and small spot thresholds in two human observers.

4.2.1 Acousto-optic light modulation and radiometry

In AOMs, contrast limits arise due to their mode of operation. Briefly, light intensity modulation is achieved through light diffraction in an oscillating crystal. Piezo elements attached to one side of a photonic crystal (in our case: Tellurium dioxide) induce travelling ultrasonic waves within the crystal. The oscillating crystal forms a spatially resolved pattern of local density changes that acts as an optical lattice by which an incident optical beam is diffracted. While most light propagates through the lattice undiffracted, some light will be diffracted under a flat angle (the Bragg-angle), and can be collected at the AOM's output. In theory, the amplitude of that modulated portion and hence the radiant power output, P, of an AOM depends on the piezo drive voltage, U, following a $\sin^2$ - function [Saleh and Teich 1991]:

$$P(U) = P_{max} \cdot sin\left(\frac{U - U_{min}}{U_{max} - U_{min}} \cdot \frac{\pi}{2}\right)^2 + P_{min} \tag{1}$$

U_{max} is the drive voltage to generate the maximum output power P_{max}. Increasing drive voltage and thus increasing ultrasonic wave amplitude will cause higher efficiency of the optical lattice, which in turn leads to more power at the AOM output. P_{min} describes the minimum output power at U_{min}, which is non-zero and defines the amount of light leaked at this driving voltage. P_{min} being non-zero is due to the fact that light inevitably falls into the output path of the AOM. This occurs because of light scattering within the crystal and optical components. Moreover, because the Bragg angle is relatively flat, the first order maximum of the deflected light path and the Airy disc of the undiffracted light path overlap (Figure 20B). Since P_{max}, U_{max}, P_{min} and U_{min} are values inherent to the exact optomechanical setup, crystal medium and wavelength tuning of the AOM, they have to be determined empirically by direct measurement of radiant power at its output.

In the experiments two commercially available fiber-coupled AOMs with 250 MHz bandwidth and an optimized efficiency for a wavelength of 545 nm were used (Model TEM-250-50-10-2FP with high extinction option, Brimrose, Maryland, USA). Since each AOM device and driver unit are tuned individually by the manufacturer to achieve maximal extinction ratios, their modulation characteristics will be different and have to be measured individually. To that end, we first recorded each AOM's radiant output power at steady state drive voltages separately and combined (by cascading them). The cascade is setup by feeding the modulated output of one AOM into the input of a second AOM. The resulting radiant power was measured at the second AOM's fiber output with a silicon photodiode attached to a benchtop power meter (Standard probe: S121C, high sensitive probe: S130C, Power meter: PM320E, Thorlabs, Inc., Newton, New Jersey, USA). Steady-state drive voltages between 0 and 1000 mV with 25 mV steps were produced with a digital signal generator (Model 33500B, Keysight Technologies, Inc., Santa Rosa, California, USA). The results of each AOM were used to calculate a look-up-table (LUT) to linearize AOM output individually for further testing in our AOSLO setup. Mapping of AOM drive signals to the voltage needed to achieve a constant output power was expressed in arbitrary units. A drive signal of 1.0 produced maximum power at the AOM's output, a value of 0.0 produced minimum power. A drive signal of 0.5, for instance, produced half of the maximum output power. Light source for all experiments was a supercontinuum laser (SuperK Extreme EXR-15, NKT Photonics, Birkerød, Denmark), spectrally filtered to output light in two distinct fiber-coupled channels with center wavelengths of 543 nm (± 12 nm) for stimulus presentation and 840 nm (± 25 nm) for retinal imaging.

4.2.2 Temporal alignment and AOSLO micro stimulation

The AOSLO is an optical instrument that can resolve and target individual photoreceptor cells of the living retina for functional testing. The details of AOSLO stimulation procedures have been described elsewhere [Poonja et al. 2005; Grieve et al. 2006; Arathorn et al. 2007; Harmening et al. 2014]. Briefly, a focused beam scans across the retina creating a square field in which visible stimuli can be created (retinal display). Stimuli are rendered directly on the retina by temporal modulation of the beam's intensity. This is achieved either by reducing the intensity of the imaging wavelength to form spatially resolved stimuli with negative contrast polarity ('black' against a visible imaging field), or by modulation increments of a dedicated stimulation wavelength for positive contrast polarity stimuli (colored on same color background), or a combination thereof (Figure 20C).

In order to successfully cascade two AOMs for our experiments, each AOM had to be controlled via individual drive signals. This is due to differences in zero-point location (U_{min} of Eq. (1)) and signal latency, which are idiosyncratic to the AOM. Thus, both units had to be measured separately before they were integrated into the AOSLO system. Zero-point location was determined by adjusting the voltage of each AOM's drive input in 1 mV steps until the radiant power reached a minimum. AOM latency was measured as the elapsed time between the onset of a bar stimulus producing drive signal (comparable to a 5 MHz square-wave drive signal with 10 ns slopes formed by a digital signal generator) and the onset of a voltage change of a high-speed photodetector (Model FPD510-FV, Menlo Systems GmbH, Martinsried, Germany) placed at the AOM fiber output. Latency signals were recorded with a digital oscilloscope (Model MSO-X 3054A, Agilent Technologies, Inc., Santa Clara, California, USA) and analyzed with Matlab (R2014a, The Mathworks, Inc., Natick, MA, USA). Latency measurements are given as the mean of 7 repeated onset events.

After determining zero-point location and latency for each AOM individually, temporal alignment (i.e. concurrent switching times) was verified in the AOSLO system. Therefore, AOM drive signals were produced by a field programmable gate array (FPGA) board (Model ML-506, Xilinx, San Jose, USA) that ran in synchrony with the AOSLO's scanning mirrors [Yang et al. 2010]. This added spatial control to the stimulus geometry, enabling stimulus presentation by definition of pixel coordinates in reference to collected AOSLO images. Because the resonant scanner of the AOSLO operates at 16 KHz, one line of our imaging and stimulation system (512 x 512 pixels) was generated in 25 μs. Scan reversals were omitted, resulting in a 40 % duty cycle of the AOM driver signal. Due to the sinusoidal velocity profile of the resonant scanner during a cycle, laser sweep time across a retinal area corresponding to one image pixel was not constant. Close to the reversal points of the scan line, the area corresponding to one image pixel was traversed in about 160 ns, whereas in the center of the field travel time was considerably shorter (40 ns per pixel). Because the pixel clock of the employed signal generator for the AOSLO system (FPGA board) ran at 20 MHz, the resulting computational step size was 50 ns, limiting tests to larger (i.e. longer) stimuli: 2, 3 and 5 pixel squares were chosen.

AOM latency correction was verified in our AOSLO system by recording images of the square stimuli with a CCD camera (Model GS3-U3-15S5M-C, FLIR Integrated Imaging Solutions, Inc., Richmond, British Columbia, Canada), positioned in a retinal plane of the system's beam path. The camera's digital shutter was adjusted to capture a single AOSLO frame (~33 msec). For later analysis, 90 frames were captured and an averaged image was computed. We compared stimulus intensities in the average frame by calculating the sum of all pixel values within a cropped area of the whole frame around the stimulus location (Figure 22C).

4.2.3 Human psychophysics

We conducted psychophysical experiments in two volunteer participants (1 female, 1 male) with no known vision abnormalities. For scotopic viewing conditions, participants were dark adapted for at least 40 minutes. Mydriasis and cycloplegia were induced by instilling one drop of 1 % Tropicamide before dark adaptation started. Written informed consent was obtained from each participant and all experimental procedures adhered to the tenets of the Declaration of Helsinki and were in accordance with the guidelines of the independent ethics committee of the medical faculty at the Rheinische Friedrich-Wilhelms-Universität of Bonn.

Three psychophysical experiments were carried out with each participant. First, a foveal and peripheral detection threshold of the 543 nm background light was determined. The AOSLO scan field was set to comprise 600 pixels per degree of visual angle, resulting in a field size of 0.85 degree of visual angle, or ~247 μ m edge length on the retina (assuming an average retinal magnification of 290 μ m per degree of visual angle). The light source output power and hence AOM input intensity was held constant. Measured at the plane of the cornea, maximum incident power was 30 μ W for single AOM and 3 μ W for cascaded AOMs. Drive voltages were then set to yield minimum output power (about 10^4 and 10^{10} attenuation for single and cascaded AOMs, respectively) to produce the residual background light, calculated to carry $5.7 \cdot 10^{-10}$ W for single, and $2.5 \cdot 10^{-16}$ W of 543 nm light for cascaded AOMs. Neutral density filters were introduced into the AOSLO beam path until the scanning field became invisible during foveal and peripheral (10 degree nasally) inspection.

Second, having the individual attenuation for complete background elimination at the given retinal location in place, we tested small spot stimulus visibility under dark-adapted conditions. Square stimuli with edge lengths of 64, 32, 10, 5, 3 and 2 pixels were used. Stimuli were flashed at 3 Hz to minimize adaptation effects. Stimulus intensity was carefully adjusted by the operator by controlling FPGA drive signals to yield the minimum intensity detectable for each stimulus size. To avoid additional light from the 840 nm imaging and wavefront sensing channel during these two experiments, the best wavefront correction was measured before an experimental session and the deformable mirror was locked with a fixed correction until the end of the experiment. The 840 nm light was then turned off during detection experiments. Sufficient wavefront correction throughout a session was confirmed by inspecting the quality of the IR retinal image after completion of a session.

In a third experiment, we compared detection thresholds of single and cascaded AOM stimulation during typical micro-stimulation conditions. Infrared light (840 nm) was employed for imaging and closed-loop AOSLO operation, and it produced a visible background of around 3.14 cd/m^2 (~100 μ W of 840 nm light at the pupil plane). Light levels for single and cascaded AOM switching in the stimulus channel (543 nm) was set to produce similar maximum power as measured at the participant's pupil plane (~1-15 nW full field, 100 % duty cycle). Despite the different contrast ratios for single and cascaded AOM switching, the 543 nm background was not visible to the participants in both operating modes due to the brighter 840 nm imaging field. Stimulus presentation duration was set to a single frame of AOSLO image acquisition, habitual fixational eye movements were tolerated. The tested stimulus sizes were 3-by-3 pixel (stimulus duration: 62.6 μ sec, stimulus size on retina: 1.21 μ m or 0.25 arcmin) and 10-by-10 pixel (562.9 μ sec, 4.35 μ m or 0.9 arcmin). Detection thresholds were estimated using an adaptive Bayesian staircase method (QUEST Matlab toolbox from [Watson and Pelli 1983]), with 20 trials per run. Participants completed 4 to 7 repeat runs per retinal location (foveal center and 10 degree eccentricity). Threshold estimates were expressed in arbitrary units (a.u.). For example, a threshold of 0.5 a.u. corresponds to 50 % of maximum light intensity. To minimize variability in the light source output power, experiments commenced 20 minutes after the laser was turned on. To compensate for residual drift, we measured the AOM output power at maximum level at the beginning and after completion of all runs per test condition. We converted threshold estimates from arbitrary units into absolute stimulus power under the assumption of a linear power drift of the source during a single session using the exact time stamps for each test run. Linear power drift behavior of the light source was confirmed in previous measurements. Because temporal alignment of both AOMs was not perfect in our case (see results: Switching latency and temporal alignment, Figure 22B), a 3 x 3 pixel stimulus created in the cascade carried only 90 % of the total power of the same stimulus created with a single AOM at the same drive signal. For the 10x10 pixel stimulus, this value was 97 %. Threshold estimates for AOM cascading relative to single AOM switching were corrected for this difference.

Statistical threshold comparison was performed with Student's t-test for paired data after confirming normal distribution (Shapiro-Wilk test) and homoscedasticity (Levene test).

4.3 Results

4.3.1 Light modulation characteristics

To characterize the contrast of single and cascaded fiber-coupled AOMs, first their individual radiometric power outputs as a function of drive voltages was measured. For that purpose, a constant input light source with 55 mW at 543 nm center wavelength was used. Generally, both AOMs showed sine-power function characteristics, but with differing exponents (Figure 21A). The fit functions minimizing the sum of the residual errors were:

$$P_{AOM1}(U) = 5.5 \cdot sin\left(\frac{U+4.2}{1100+4.2} \cdot \frac{\pi}{2}\right)^2 + 1.0 \cdot 10^{-4} \tag{2}$$

$$P_{AOM2}(U) = 2.74 \cdot sin\left(\frac{U-38}{1050-38} \cdot \frac{\pi}{2}\right)^2 + 1.2 \cdot 10^{-5} \tag{3}$$

Insertion loss due to finite diffraction efficiency in each AOM was about 90 %. Zero point location (i.e. the drive voltage at which the radiant power output had its minimum) differed for each AOM. AOM1 had its minimum at -4.2 mV and AOM2 at 38.0 mV. These idiosyncratic differences are to be considered, as they would lead to a non-monotonic characteristic in the cascade if left unaccounted for. Minimum output power was $1.04 \cdot 10^{-4}$ mW and $1.20 \cdot 10^{-5}$ mW for AOM1 and AOM2, respectively.

In the cascade, feeding the modulated output of AOM1 into AOM2, the measured characteristic followed the multiplied single AOM measurements with a correlation of 99.99 % ($p = 4 \cdot 10^{-66}$, Pearson correlation) as expected (Figure 21A). Range limits of the used photodiode demanded cascade drive signals above 100 mV. Effectively, readings levelled off at around $5 \cdot 10^{-7}$ mW. The overall light loss due to AOM cascading (irrespective of AOM order) was about 90 % compared to single AOM operation.

In terms of light modulation contrast, the ratio of radiant output power between U_{min} and U_{max} is of interest. Single AOM characteristics were normalized to their maximum output power and corrected for zero point location by creating a look-up-table based on the measurements from Figure 21A. Individual and cascaded modulation contrast resulted in measurements shown in Figure 21B. Individual AOMs achieved maximum contrast ratios of $1{:}5.3 \cdot 10^4$ (AOM1) and $1{:}2.3 \cdot 10^5$ (AOM2). The overall cascaded AOM contrast ratio was calculated to be $1 :1.2 \cdot 10^{10}$. Ultimately, cascading two AOMs increased the displayable contrast by a factor between 10^5 and 10^6 compared to single AOM switching.

4.3.2 Switching latency and temporal alignment

In SLO-based applications where spatially resolved visual stimuli are rendered by temporal modulation of a scanning beam (see section 4.2), light switching timing is essential. If two AOMs are cascaded, both need to respond synchronously, especially if small stimuli are desired. Otherwise, uncontrolled size and intensity losses will occur. We measured single AOM latencies by detecting their optical output with a high-speed photodetector in response to repeated square-wave drive signals.

We found the latencies of our AOMs to be 245 ± 3 ns for AOM1 and 485 ± 3 ns for AOM2, resulting in an offset of 240 ± 6 ns between them (Figure 22A). This temporal offset needs to be taken into account for cascaded stimulation by adding a corresponding delay for the faster AOM (AOM1). We tested how far temporal delays of 200, 250 and 300 ns would impact stimulus geometry and intensity (Figure 22B), while using small squares with edge lengths of 2, 3 and 5 pixels as stimuli. We recorded images of these stimuli with a CCD-camera placed in a retinal plane of the AOSLO. A qualitative analysis yielded the optimal offset to be 250 ns (Figure 22C). Non-overlapping drive signals (300 ns delay) resulted in extremely low stimulus intensities. When drive signals overlapped, the stimulus spot was visible with increasing size and intensity closer to the optimal 240 ns delay. For a quantitative assessment of the optimal offset, we computed the mean stimulus intensity of the three different sized stimuli while varying the offset for AOM1 (Figure 22D). Again, an offset of 250 ns showed the best results, determined by the highest stimulus intensity. An x^2-fit to the three data points revealed an optimal offset of 236 ± 3 ns, which is in good accordance with the initially measured offset of 240 ± 6 ns.

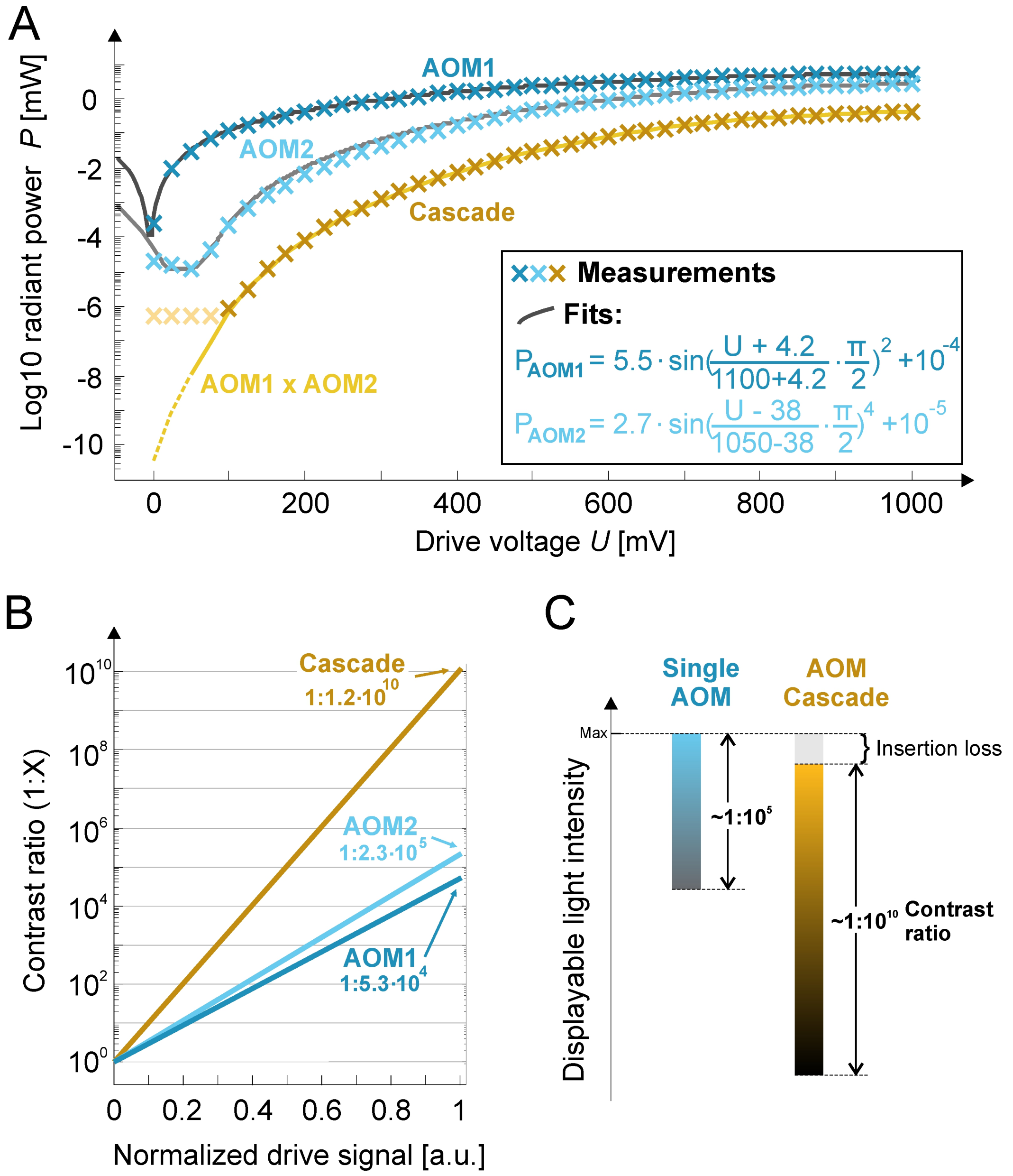

Figure 21: *Single and cascaded AOM optical contrast. A) Radiant output power as a function of drive voltage measured with individual AOMs (blue markers) were best fitted by a sin2 or sin4 function (grey lines, fit parameters given), respectively. Minimal power was found at non-zero drive signals. In the cascade, maximum absolute output power is lower (amber markers), and the characteristic closely follows multiplication of the single AOM measurement points (amber line). Our setup did not allow power measurements below* 10^{-6} *mW, resulting in a plateau at low drive voltages (lightly colored x's). B) AOM contrast ratios yielded by normalization and zero-point correction of data from A after drive signal linearization. A drive signal of 1.0 a.u. produces maximum output power for each AOM, a signal of 0 the minimum. The y-axis shows the contrast ratio relative to minimum output. C) Cascading two AOMs results in a superior contrast ratio relative to single AOMs. Due to about 90 % insertion loss of absolute output power in the cascade, the range of displayable light levels is shifted towards lower intensities. The effective contrast ratio of the AOM cascade was about* $1 : 10^{10}$.

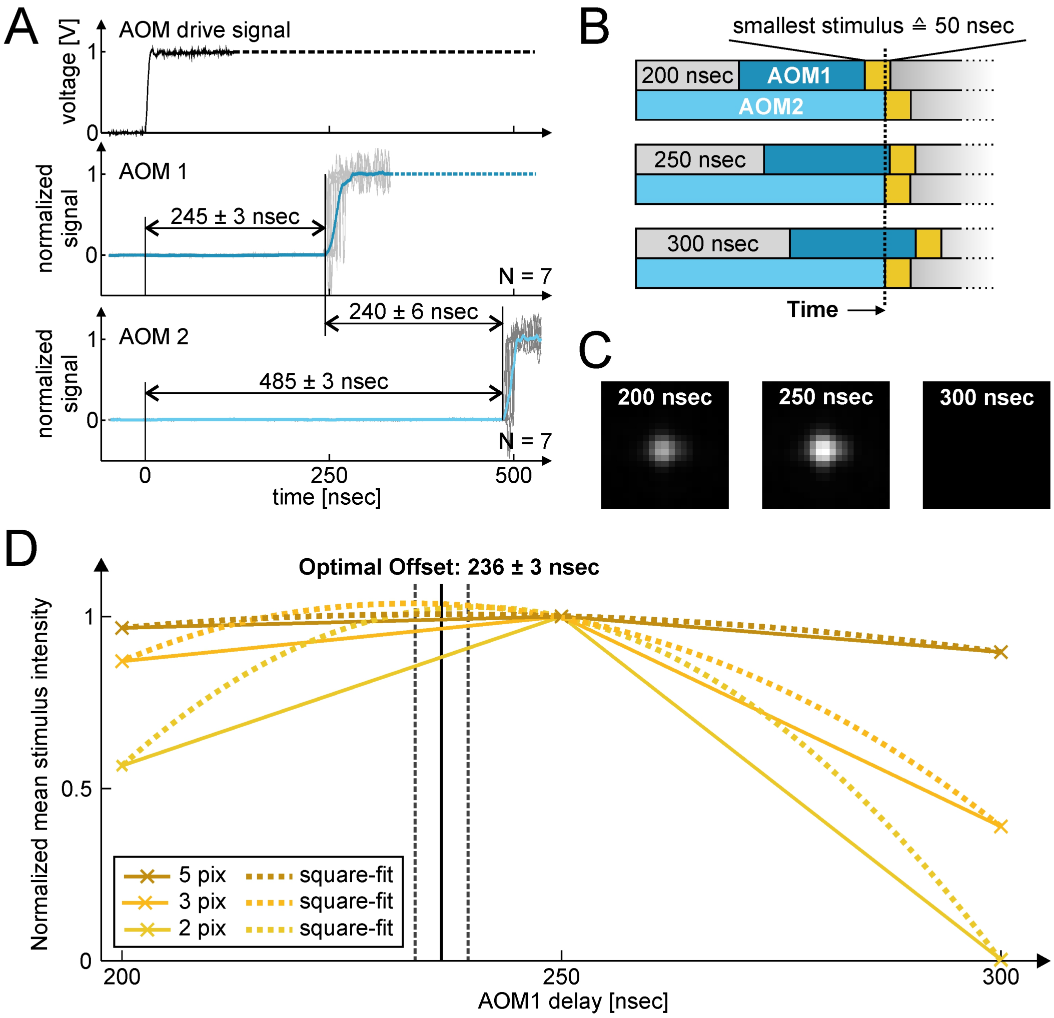

Figure 22: *AOM latency and temporal alignment. A) Single AOM response functions (middle and lower row, grey: single measurement, blue: average) measured after repeated (n = 7) square wave drive signal onsets (upper row). Mean latency (± STD) values are shown in the plot, latency difference between the two AOMs was 240 ± 6 ns. B) To temporally align AOM switching events for small visual stimuli, drive signals for AOM1 were delayed in 50 ns increments, to a close-to-optimal delay at around 250 ns. C) Average of 90 frames captured with a CCD-camera at a retinal plane of the AOSLO with varying AOM delays for a 50 ns stimulus (2 x 2 pixel). D) Optimal delay analysis with different stimulus sizes based on image intensity as in C. Cross markers are data points (connecting solid lines added for visibility), exponential fit functions (power of two, dotted lines) locate the optimal offset to be 236 ± 3 ns, in agreement with the measured delay from A.*

4.3.3 Psychophysics: background extinction and small spot sensitivity

To demonstrate that the increased optical contrast in the AOM cascade has measurable consequences for visual perception, we conducted three psychophysical experiments with two human participants. In the first experiment, participants determined the level of light attenuation (by adding neutral density (ND) filters into the beam path) necessary for complete AOM leak background elimination in the AOSLO retinal display after dark adaptation. With a single AOM, P1 required attenuation of $10^{5.5}$ at the fovea and an attenuation of 10^{7} at 10° eccentricity (P2: $10^{4.5}$ and $10^{6.6}$, respectively) (Figure 23A). With cascaded AOMs, combining high extinction and an additional insertion loss of one log unit, both participants were not able to perceive a background at the fovea, and an ND of $10^{0.6}$ (factor ~4) was sufficient to remove the background at eccentric fixation for both participants. Defining the minimal attenuation needed to remove the background as detection threshold, single AOM radiant powers incident at threshold were $1.8 \cdot 10^{-15}$ W (P1) and $1.8 \cdot 10^{-14}$ W (P2) at foveal inspection, and $5.7 \cdot 10^{-17}$ W (P1) and $1.4 \cdot 10^{-16}$ W (P2) at eccentric fixation. For cascaded AOMs, a foveal threshold remains undefined because the background was never visible. At eccentric fixation, thresholds were $6.3 \cdot 10^{-17}$ W for both participants. Converting the radiometric measurements to an equivalent photometric unit of luminous intensity (brightness) of the scan field (for a detailed calculation see Paper1), the resulting average background luminance threshold across participants and condition was $1.19 \cdot 10^{-3}$ cd/m^2 for foveal and $3.9 \cdot 10^{-6}$ cd/m^2 for eccentric fixation.

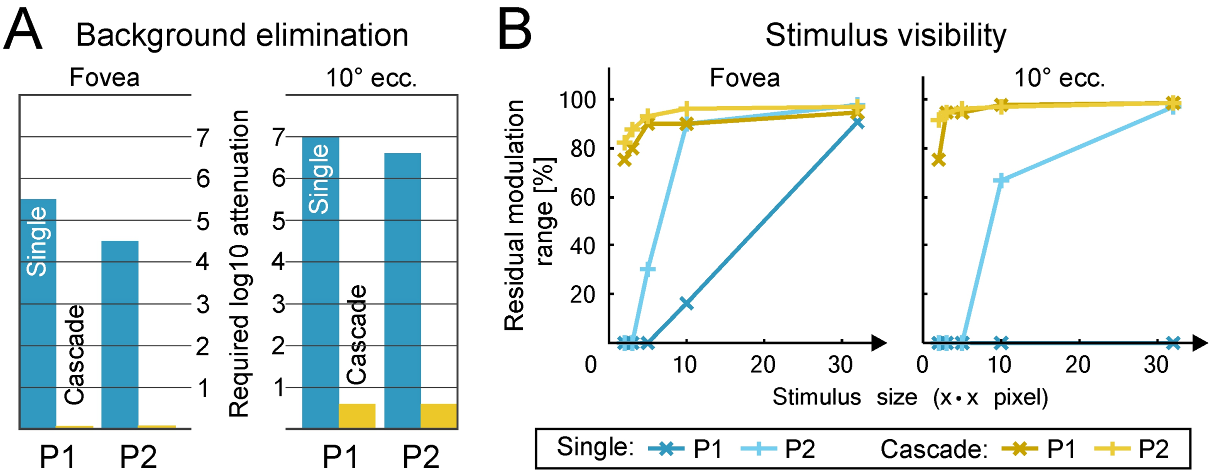

Figure 23: *Background elimination and stimulus visibility in AOSLO micro-stimulation. A) Light attenuation necessary to eliminate the AOM background leak for two dark adapted participants (P1, P2), inspected foveally and at 10 degree nasal eccentricity. With single AOM modulation (blue bars), light leak was removed with an attenuation of 4.5 - 5.5 log units at the fovea. The background was never visible with cascaded modulation. With eccentric fixation, attenuation of 6.6 - 7.0 log units was required to remove the background for single AOM, and 0.6 log units for cascaded AOM light modulation (amber bar). B) Residual modulation range for small visible stimuli with eliminated background (i.e. viewing conditions found in A). Different sized stimuli were flashed at 3 Hz, participants reported detection under foveal or eccentric fixation. With single AOM switching, stimuli had to be large to be visible, at both foveal and eccentric fixation (blue markers and lines). The smallest stimuli were not visible or required maximal modulation to be seen. With AOM cascading, even the smallest stimuli were easily seen, leaving a much greater dynamic range of stimulus modulation for psychophysical testing (amber markers and lines).*

We tested visibility of various sized stimuli in a second experiment, under conditions where the background was fully eliminated. With a single AOM, the smallest stimuli (2, 3 and 5 pixels) were either never visible or barely visible at maximum light modulation (Figure 23B). With cascaded AOMs, stimuli were visible at all sizes. Visibility was even preserved at low modulation levels (inter participant average detection threshold for the 2-by-2 pixel square: 0.21 a.u. at fovea, 0.09 a.u. at 10 degree eccentricity), leaving a large dynamic range for visual stimulation and threshold experiments. This was the case for both foveal and eccentric fixation (Figure 23B).

Finally, it was tested if cascaded AOM switching can produce small spot visual stimuli with light levels that can be directly compared to prior studies that used single AOM switching [Harmening et al. 2014; Bruce et al. 2015; Sabesan et al. 2016; Tuten et al. 2017]. Sensitivity thresholds were recorded for 3 and 10 pixel square stimuli (1.21 μ m and 4.35 μ m on the retina, respectively) against a visible 840 nm imaging raster, which effectively masked the 543 nm background. While the stimulus appeared at a fixed position relative to the imaging raster, natural fixational eye movements were allowed to occur (see example in Figure 24A). Averaged across both participants, more than 50 % of all stimuli presentations fell into a (roughly) circular area with a diameter of 5.58 arcmin, or 26.98 μ m on the retina (P1: 5.66/4.92 arcmin; P2: 5.75/6.00 arcmin; single/cascaded AOMs, respectively). Thresholds were determined using an adaptive Bayesian staircase method, and threshold progression was very similar for both single and cascaded AOM stimulus presentation (see example in Figure 24B). For threshold comparison between single and cascaded AOM switching, threshold estimates given in arbitrary units were converted into radiant stimulus power. Across both participants and stimulus sizes we found no differences between threshold power values for both single and cascaded AOM switching (Figure 24C). With a 3x3 pixel stimulus we found a mean threshold power (± STD) of 34.2 ± 5.0 fW (single) and 35.3 ± 7.7 fW (cascade) for P1 ($p = 0.77$), and 17.7 ± 2.1 fW (single) and 19.8 ± 3.6 fW (cascade) for P2 ($p = 0.29$). With the 10x10 pixel stimulus we found a mean threshold power of 35.1 ± 7.3 fW (single) and 39.8 ± 9.2 fW (cascade) for P1 ($p = 0.47$), and 108.7 ± 15.2 fW (single) and 117.2 ± 4.7 fW (cascade) for P2 ($p = 0.43$).

4.4 Discussion

By cascading and temporally aligning two acousto-optic modulators we demonstrate a substantial boost in optical contrast in an SLO-based retinal display, reaching a maximum contrast ratio of about $1:10^{10}$. Using the AOSLO as a retinal display, this superior contrast made it possible to create extremely small stimuli approaching the size of single foveal cones and rods without a visible background, while maintaining a large modulation range for psychophysical testing. We validated our method by recording comparable sensitivity thresholds for stimuli created by the cascade and by a single AOM. High visual contrast has implications for SLO-based displays in particular as well as light switching for high-contrast vision testing in general. Cascaded AOM light switching will extend single cone photoreceptor testing options, and enable single rod testing. These are fundamental applications for both basic and clinical research of retinal function.

Earlier studies reporting maximum contrast ratios in AOM-based displays of around 1:300 are likely to have underestimated the full range of single AOM extinction due to technical difficulties in accurately measuring the AOM's black level (P_{min} in Eq. (1)). Errors can be caused by the use of an unsuited photodiode, or because insufficient cancellation of spurious light sources in the test setup [Harmening et al. 2014; Rossi et al. 2013; Domdei et al. 2015]. In the current study, we took extra care to avoid both factors: a highly sensitive probe head was employed (see section 4.2), and outside light sources were eliminated by repeated visual inspection by a human observer after a longer period of dark adaptation. Due to the extremely high extinction ratio of the AOM cascade, we approached the physical limits of silicon photodiode sensitivity to radiant power levels ($\sim 10^{-7}$ mW) in our measurements. Thus, output levels at low drive voltages could only be reported indirectly. Because the attenuation of the cascade can be mathematically described by multiplying the attenuation of its single AOM elements over the full range of measurable output powers (see Figure 21A), we are confident that the maximum contrast values of the cascade reported here are accurate. Further support for this view is provided by the psychophysical results, confirming no difference between single or cascaded AOM operation when both modes are set up to produce comparable light levels (see Figure 24).

As a byproduct of combining two AOMs with independent drive signals into a single stimulation channel, the amount of displayable light levels (corresponding to the bit depth of the SLO display) increased as well. The system's current hard- and software design allowed single AOM drive signals to

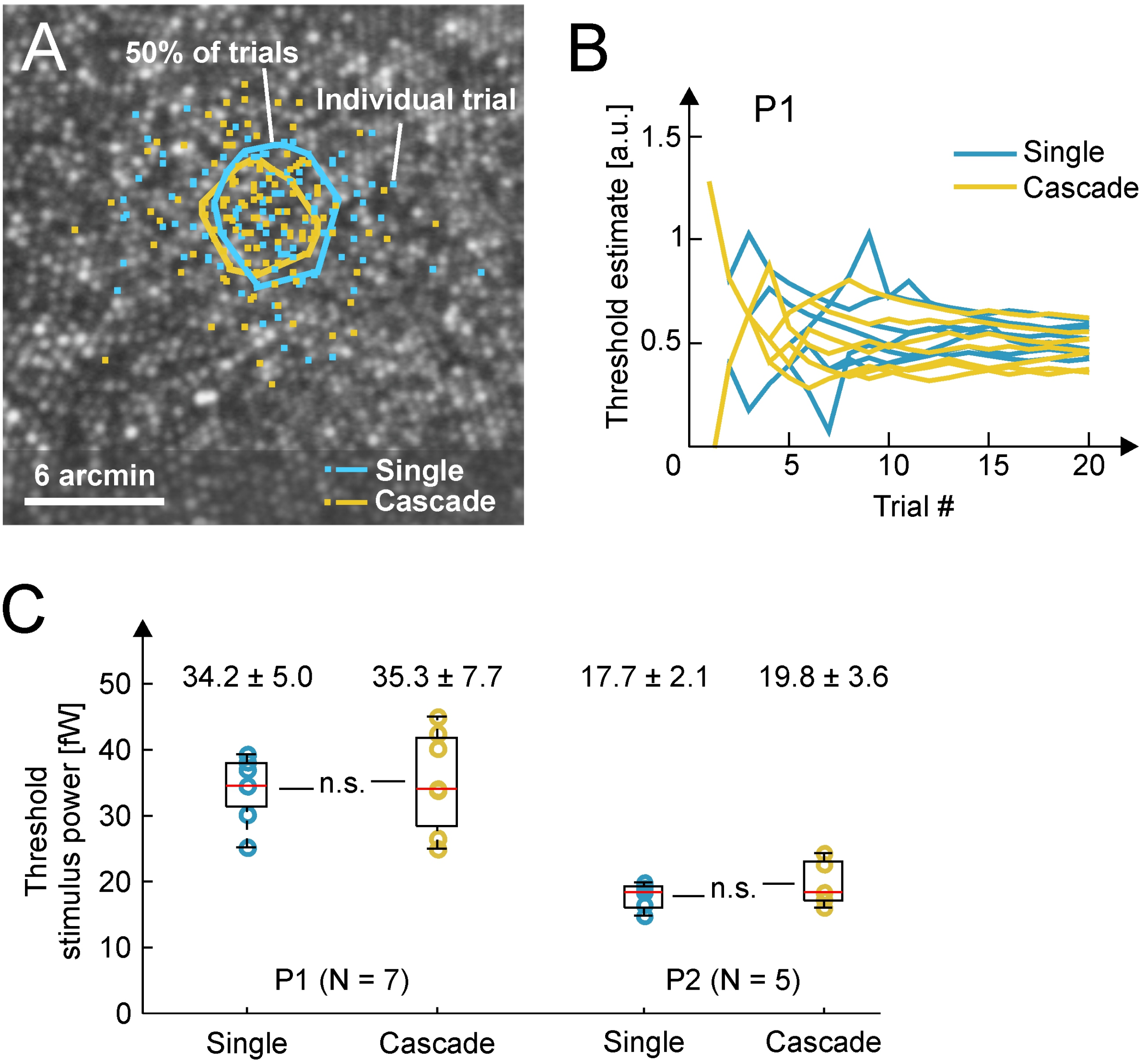

Figure 24: *Psychophysical detection thresholds using single and cascaded AOMs. A) Foveal stimulus locations plotted on P1's AOSLO retinal image in repeated increment sensitivity measurements. Square markers show the exact position and approximate size of the stimulus (3 x 3 image pixel) for a total of 280 trials. Polygons encompass the area where 50 % of all trials hit. Participants had little fixational eye motion, reflected here by the size of the 50 % area. B) Raw psychophysical threshold estimates from the example in A given in arbitrary units of power modulation after 20 trials using QUEST staircases for both single and cascaded AOM switching. Thresholds and variability are similar in both cases. C) Threshold comparison for both single and cascaded switching converted to absolute stimulus power at the cornea in two participants (P1, P2). We found no significant differences between conditions within participants (p = 0.77 and 0.29, t-test for paired data). Values indicate mean threshold power in fW ± standard deviation. For all panels, colors denote single (blue) and cascaded (amber) AOM switching, respectively.*

be represented in exactly 1,001 steps (~10 bit) between maximal and minimal output. In the cascade, a total of 248,084 unique steps (~18 bit) are theoretically possible to display. Put differently, the cascade expands the range of displayable light levels below the current minimum of 1 ‰ of the maximum intensity and additional light levels between 1 ‰ and 100 % can now be set. As a practical note, to display modulated stimuli with cascaded AOMs during threshold experiments, computation of necessary drive signals is simply based on the multiplicative behavior of the cascade (compare Figure 21). A look-up-table mapping single AOM drive signals to the desired cascade output can be easily established after each single AOM drive to output power relationship has been linearized: if $P_{cascade} = P_{AOM1} \cdot P_{AOM2}$, and $P_{AOM1} = P_{AOM2}$, then $P_{AOM} = \sqrt{P_{cascade}}$. For example, if the desired stimulus intensity is 30 % of the maximum intensity, each AOM driving signal is set to a voltage generating an output level of 55 % ($\sqrt{0.3}$ = 0.55) of the maximum intensity.

Luminance contrast is a key technological characteristic of visual displays which is continuously improving; not only in consumer products but in scientific applications as well. To probe visual function of the intact human visual system, the physical requirements for stimulation devices and displays are high and frequently unmet by off-the-shelf solutions. In most of today's psychophysical studies of human vision, cathode ray tubes (CRTs) are still the display of choice, because of their high temporal and spatial fidelity and custom control of their source electron guns [Bach et al. 1997]. CRTs can produce visual contrast ratios of up to 1:10^4, on par with liquid crystal displays (LCD) [Ghodrati et al. 2015]. Higher contrasts of up to 1:$10^{6.7}$ can be found in organic light emission diode (OLED) displays [Ito et al. 2013]. Similar high-contrast ratios of about 1:$10^{6.4}$ can be achieved in projector systems with two conjugate digital mirror device (DMD) units [Geissler et al. 2009]. For SLO-based displays, a few alternatives to AOM light intensity modulation exist. Bright light sources such as super luminescent laser diodes (SLDs, e.g. model iBeamsmart, TOPTICA Photonics AG, Munich, Germany) can be electronically modulated fast enough [Petermann 2012], but are bound to their diode's wavelength and options are (yet) too limited for psychophysical testing. For example, there is currently no laser diode with a central wavelength close to 550 nm, which would minimize sensitivity differences in M- and L-cone photoreceptors [Stockman et al. 1993]. Other fast optical switches can be established by electro-optical modulation (e.g. model EO-AM-NR-C4, Thorlabs GmbH, Dachau, Germany) or pockels cells (e.g. model EO-PC-550, Thorlabs), but both options have lower contrast ratios when compared to AOMs (EO-AM: 1:10^1, EO-PC: 1:$10^{2.4}$) [Roth et al. 2005].

As exemplified in the current study, an SLO-based display with AOM cascading can produce spatially resolved stimuli with visual contrast ratios up to 1:10^{10}. To the best of our knowledge, this is the highest visual contrast ever reported in any display device. With the added minute spatial and temporal control of a small visual stimulus, this system is well suited to stimulate individual cone and rod photoreceptors against a zero-luminance background. For instance, if source light levels are decreased appropriately (e.g. by neutral density filters), the AOM cascade described here can produce background light levels well below the detection threshold of cone and rod photoreceptors. The detection threshold for cones is about 200 incident photons with a wavelength λ = 490 nm at an integration time t = 100 ms [Koenig and Hofer 2011]. This is equivalent to 225 photons at 543 nm. With the Planck constant, $\hbar$ ($6.26 \cdot 10^{-34}$ Js), the speed of light, c ($3 \cdot 10^8$ m/s), number of photons, n_γ , wavelength, λ , and integration time, t, this equates, according to Eq. (4), to a radiant threshold power of $P_{cone} = 8.23 \cdot 10^{-16}$ W:

$$P_{cone} = \left(\frac{\hbar \cdot c \cdot n_\gamma}{t \cdot \lambda} \right), \tag{4}$$

This compares well to our foveal detection threshold estimate of the background light of about $1.8 \cdot 10^{-15}$ W. For rods, detection of single photons have been reported, and thresholds are likely to be somewhere around 50 incident photons [Koenig and Hofer 2011; Tinsley et al. 2016], thus around $6.76 \cdot 10^{-17}$ W. This is close to our estimated threshold at 10 degree eccentricity (where the density of rod photoreceptors is highest) of $6.3 \cdot 10^{-17}$ W in cascaded viewing condition. If the minimum output power of the cascade is attenuated with a 1 log unit ND filter to produce a background of $P_{min} = 8.4 \cdot 10^{-17}$ – an order of magnitude below the detection threshold of single cones – the maximum output power in this scenario would be $P_{max} = 1, \mu W$. The smallest square stimulus in the current AOSLO system (2 x 2 pixel) at 543 nm would result in a luminance of $L_v = 3.1 \cdot 10^{-2}$ cd/m^2, (~1 Troland at a 7 mm pupil) which is clearly visible. For rod photoreceptors, light levels can be adjusted accordingly.

A zero-background stimulation channel is an important step towards new experimental options, but for some applications, the concurrent imaging raster has to be invisible as well. In our case, using 840 nm as imaging wavelength (at power levels suited for imaging, ~0.1 mW at the cornea), the imaging field produces an equivalent scotopic luminance of ~3.14 cd/m^2. One solution would be to shift imaging towards longer, less visible wavelengths (in conjunction with appropriate detectors), or suspend imaging for experimentation times, and recover stimulus locations from external, invisible methods, such as high-resolution IR pupil trackers [Crane and Steele 1985]. A considerable drawback of the cascade is the overall light loss of 90 % compared to single AOM operation. This reduction of maximum radiant power output needs to be taken into account in applications where light levels are a limiting factor.

Single photoreceptor psychophysical testing has recently proven to offer new insights into retinal function on the elemental level of single cells. In previous experiments, this was realized by single AOM switching, creating small visual stimuli within a visible background. This background light set fundamental limits to experimental designs. For example, single cone sensitivity thresholds are necessarily reported as thresholds to light increments [Harmening et al. 2014; Bruce et al. 2015; Tuten et al. 2017]. In a study of single cone color appearance, background light options were limited, requiring high intensity fields to mask the residual background of the stimulus light [Sabesan et al. 2016]. By cascading two AOMs we can now extend experimental options enabling background-free, high-contrast (1:10^{10}) visual stimulation. In color vision applications, this approach will allow photoreceptor function tests with a greater freedom for custom adaptation lights, and a zero background situation will enable isolated stimulation of single cones for extended cone resolved models of color computation [Brainard et al. 2008]. In clinical applications, the higher dynamic range of stimulus lights will enable dark adapted vision, as well as rod function, testing. Rod function testing is of importance for clinically oriented visual testing [Bruce et al. 2015; Wang et al. 2015; Tuten et al. 2012], especially with regard to retinal diseases affecting mesopic and scotopic vision, where early signs of the disease is most likely found in reduced rod function [Massof and Finkelstein 1979; Fraser et al. 2016].

5 Eye tracking-based estimation and compensation of chromatic offsets for multi-wavelength retinal microstimulation with foveal cone precision

The content of this chapter is based on:

Domdei N, Linden M, Reiniger J, Holz FG, Harmening WM (2019) Eye tracking based estimation and compensation of chromatic offsets for multi wavelength retinal microstimulation with foveal cone precision. *Biomedical Optics Express*, 10(8): 4126–4141. DOI: 10.1364/BOE.10.004126

5.1 Introduction

AOSLO coupled with microstimulation techniques enables imaging and simultaneous functional testing of targeted human photoreceptors *in vivo*. This approach was recently employed to study single cone photoreceptor function [Harmening et al. 2014; Bruce et al. 2015], retinal circuitry [Tuten et al. 2017; Tuten et al. 2018], color vision [Sabesan et al. 2016; Schmidt et al. 2018b], and sensitivity changes during retinal disease [Tu et al. 2017; Wang et al. 2015].

The specific techniques employed in these studies, using two (or more) beams of light of different wavelengths for imaging and stimulation, are faced with a particular challenge arising from the chromatic dispersion characteristics of the human eye. Due to dispersion, light of different wavelengths will be focused axially displaced (termed longitudinal chromatic aberration, LCA) [Atchison and Smith 2005], and if incident at an oblique angle, focus points will also be laterally displaced (termed transverse chromatic aberration, TCA) [Howarth 1984].

The magnitude of LCA is relatively consistent across the population [Atchison and Smith 2005; Vinas et al. 2015] and across the field of view [Rynders et al. 1998; Jaeken et al. 2011], thus it can be corrected sufficiently for most eyes by adjusting the relative vergence between beams of different wavelength. In an AOSLO system, this is currently achieved by a coaxial displacement of the light sources' entry points.

By setting the light sources at different distances, transverse chromatic offset (TCO) is induced in the eye. These lateral offsets in focus position on the retina have two origins. One is the imperfect axial positioning of the two (or more) beams. The second is of ocular origin, and closely related to TCA. When the eye is moved laterally in front of the displaced beams, their focus location will move laterally on the retina as a linear function of eye position, akin to a chromatic parallax. The magnitude of this offset is identical to TCA [Harmening et al. 2012].

In an AOSLO, TCO can be directly measured by spatially registering simultaneously recorded retinal images with the two (or more) wavelengths. This method allows a determination of TCO of the order of arcseconds but requires high light intensities massively bleaching the photopigment and leading to strong fluctuations in retinal adaptation [Harmening et al. 2012]. Therefore, continuous or repeated measurements of TCO during psychophysical sessions are unfeasible.

In earlier studies, TCO was thus statically compensated by assuming no lateral eye motion between measurements before and after an experimental run. Residual head and eye movement were thought to displace the stimulus within the cone's inner segment diameter at the targeted eccentricities (about 1.2 arcmin at 2 degree eccentricity) [Harmening et al. 2014; Tuten et al. 2017; Sabesan et al. 2016; Schmidt et al. 2018b]. With our eye tracking setup, we observed residual head motion during experiments that would change TCO in the range of ± 0.65 arcmin up to ± 1.27 arcmin. Therefore, AOSLO based microperimetry would require an eye position monitor system, limiting stimulus delivery to a certain range of eye positions. For stimulation of the smallest cones at the foveal center or rods, however, such static approach is not practicable, because the range of allowed eye positions would be too small.

A chromatic eye model by Thibos et al. [Thibos et al. 1990; Thibos et al. 1992; Rynders et al. 1995] predicts a simple linear correlation between TCO and eye position offsets in front of the AOSLO beams, depending on the wavelengths, described by:

$$TCA \propto EyeDisplacement \cdot LCA \tag{5}$$

This relationship was experimentally confirmed in previous studies [Harmening et al. 2012; Privitera et al. 2016], and applied to a method to infer TCO from pupil position, yet without focusing on the precision necessary to target single cones [Boehm et al. 2019]. We here employ high-resolution eye tracking to demonstrate that transverse chromatic offsets can be compensated continuously and in real time to ensure cell sized precision during single cell stimulation of cones of the central fovea or rods.

5.2 Material and methods

To map lateral eye position changes to transverse chromatic offset changes, we employed an AOSLO to measure image-based retinal TCO [Harmening et al. 2012] during controlled movements of the head and simultaneous eye tracking. Following such calibration, eye tracking-based TCO estimates were validated in a psychophysical experiment. TCO calibrations were performed in fourteen participants (9 female, 5 male) with no known vision abnormalities. Three participants (1 female, 2 male) took part in the subjective experiments. Mydriasis and cycloplegia were induced by instilling one drop of 1 % Tropicamide 15 min before the beginning of a session. For each participant, a holder fixed to a custom dental impression (bite bar) was used to immobilize and control the position of the head during imaging. Written informed consent was obtained from each participant and all experimental procedures adhered to the tenets of the Declaration of Helsinki, in accordance with the guidelines of the independent ethics committee of the medical faculty at the Rheinische Friedrich-Wilhelms-Universität of Bonn.

5.2.1 Adaptive optics scanning laser ophthalmoscope (AOSLO)

A detailed description of the used multi-wavelength AOSLO system is given in [Domdei et al. 2018] with relevant details specified below.

The adaptive optics component consists of a Shack-Hartmann wavefront sensor (SHSCam AR-S-150-GE, Optocraft GmbH, Erlangen, Germany) and a deformable mirror (DM97, ALPAO, Montbonnot-Saint- Martin, France) and was operated in a closed-loop mode. The two wavelengths used (840 ± 12 nm and 543 ± 22 nm) were filtered from the spectrum of a supercontinuum light source (SuperK EXTREME, NKT Photonics, Birkerød, Denmark). 840 nm light was used for wavefront sensing and imaging. 543 nm (green) light was used for TCO determination and stimulation. Both channels were raster-scanned onto the retina with a beam size of about 7 mm at the pupil and generated a square field of 0.85 x 0.85 degrees of visual angle (corresponding to a sampling resolution of 0.10 arcmin per pixel). Backscattered light from the retina was detected in a confocal setup (pinhole sizes were 20 μ m (840) and 30 μ m (543)) with a photomultiplier tube (Photosensor module H7422, Hamamatsu Photonics, Hamamatsu, Japan).

5.2.2 Eye tracking camera

In order to accurately track the position of a participants's eye in front of the AOSLO beam, we mounted a video camera coaxially to the AOSLO imaging and stimulation beams by means of a cold mirror (DMLP900L, Thorlabs, Munich, Germany) (Figure 25). The camera was a 752 x 480 pixel CMOS sensor (DMK 23UV024, The Imaging Source, Bremen, Germany) with a 50 mm, f/1.26 objective lens (TCL 5026 5MP, The Imaging Source). A central 640 x 480 pixels subfield of the sensor was used in our custom eye tracking software. Camera focus was set to a fixed working distance of 350 mm. By judging the sharpness of the pupil image within the eye tracking user interface, eyes could be positioned at an approximate distance coinciding with a conjugate pupil plane of the AOSLO beam. Image magnification of the eye tracker was 0.030 mm per image pixel in the pupil plane. As a result of back-scattered light from the imaging beam (7.2 mm diameter), the camera captured an image of the retroilluminated pupil on an otherwise dark background (Figure 25C, D). The imaging beam also produced a bright visible reflection on the cornea front surface, the first Purkinje image, referred to as Purkinje image in the following. The bright image pixels of the Purkinje image were used to track the eye's lateral location. Because of the coaxiality between camera and illumination, we used the horizontal offset between the pupil's center and the Purkinje image to calculate the horizontal component of angle Kappa, κ, (the

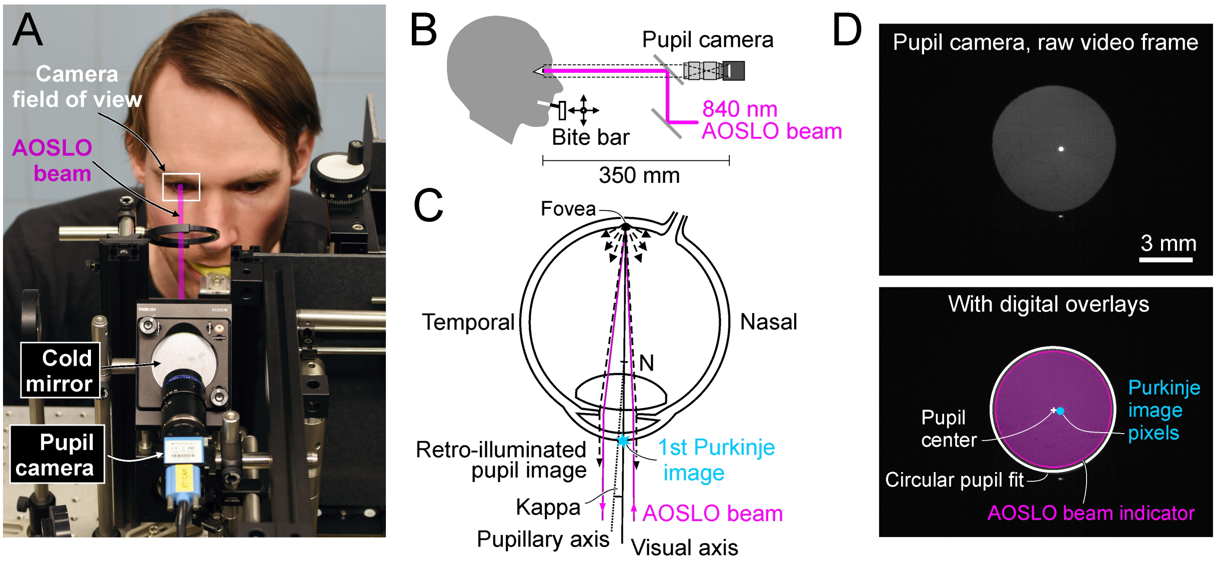

Figure 25: *On-axis eye tracker with AOSLO as light source. A) Photograph of the physical implementation from a top-oblique angle. The pink AOSLO beam is drawn for illustrative purposes and was not visible. B) Side-view, to scale. The participant's head could be moved via XYZ-microdrives attached to a bite bar. C) Using the 840 nm beam of the AOSLO as light source, retinally back-scattered light illuminates the pupil from within the eyeball. The first Purkinje image was used to track the eye's position relative to the AOSLO beam. "N" marks the first Nodal point of the eye and defines the intersection between pupillary and visual axes. Note that the camera is aligned with the visual axis. D) Pupil and Purkinje image could be tracked with high precision (1 image pixel equaled 30 µ m in the pupil plane). During operation, digital overlays could be displayed to aid positioning during calibration.*

angular subtense between visual and pupillary axis) as follows:

$$\kappa_x = arctan\left(\frac{PI_x - PC_x}{\overline{\mathrm{PN}}}\right) \tag{6}$$

PI_x defined as the horizontal Purkinje image coordinate, PC_x as the horizontal pupil center coordinate, and $\overline{\mathrm{PN}}$ as the distance from the entrance pupil to the Nodalpoint, which was assumed to be 4 mm [Atchison 2017]. The vertical component of Kappa was calculated in the same way. Additionally, we calculated the Hirschberg ratio (the inverse of the displacement of the Purkinje image from pupil center per degree of eye rotation) in four participants during controlled gaze shifts. The average Hirschberg ratio across four participants was 13.3 ± 0.7 degree/mm, which corresponds to an average $\overline{\mathrm{PN}}$ of 4.2 mm. The individual values of $\overline{\mathrm{PN}}$ were used to calculate the participant's Kappa more precisely and estimate TCO based on LCA and Kappa.

5.2.3 Eye tracking software

A custom C++ program based on previously described algorithms [Schaeffel 2002; Ivanchenko et al. 2018] was written to display, track, and measure certain image features visualized by the eye tracking camera (Figure 25D). Each of the following metrics was computed for every new frame with a refresh rate of 29.87 Hz. The pupil was fitted by a circle to determine its center and diameter. The Purkinje image coordinate was specified by the center of a second circle fit to the brightest pixels of the corneal reflection. Pixel detection thresholds for the circle fits were adjusted manually at the beginning of each session to ensure the best fits at the current image quality. To assist eye alignment, an AOSLO beam indicator marking the perimeter of the imaging beam was added. AOSLO beam position was captured at the beginning of every session based on the camera image of a white paper illuminated by the imaging beam in the pupil position. While running a TCO calibration sequence, all data was written to a log file containing frame number, time stamp, pupil center coordinates, Purkinje center coordinates, and pupil diameter.

5.2.4 TCO measurement

A detailed description of the method to objectively measure TCO with an AOSLO is given in [Harmening et al. 2012]. In short, a video is recorded containing interleaved information of both imaging and stimulation light channels (here, 840 nm and 543 nm) in a subfield of the imaging raster (192 x 128 pixel). Images recorded in both channels were spatially cross-correlated frame by frame to compute the positional shift between the imaging light and stimulation light on the retina. Because this method is image-based, it requires video footage with resolved retinal structure which can be a limiting factor at the central fovea. As a side note, we observed that image structure moved if the confocal pinhole in front of the light detector is moved. As a consequence, TCO readings will change, although no changes occurred on the retina with the result that an uncorrected displaced pinhole leads to an over- or underestimation of TCO. To control for this additional system-related chromatic offset, we centered the confocal pinhole position on the beam's point spread function by optimizing image brightness and contrast ahead of each session.

5.2.5 Calibration procedure

To correlate image-based measurements of TCO to eye position changes, a 20 sec dynamic calibration sequence was performed. During recording, the head (and therefore the eye) was moved in a somewhat random pattern with an extent of about ± 0.2 mm in each direction by manually turning the knobs of a XY-micrometer-stage attached to the bitebar. Meanwhile, the participant fixated on a target ensuring video acquisition of the same retinal location which was at ~0.4 degree eccentricity. Reminiscent of a clapperboard in film industry, we modulated the AOSLO beam through three quick full on and off cycles to flash the imaging beam at the beginning and at the end of the recording, a signal which could be accurately assigned to a single frame in both data streams. TCO video data and eye tracking data were processed offline with a custom Matlab (Mathworks, Inc., Natick, MA, USA) software in three steps (Figure 26):

1. Synchronization and interpolation: the two independent data streams were synchronized based on the flash-sequence flagging "start" and "end" by downsampling TCO data via linear interpolation - due to slightly differing framerates (TCO: 30.00 Hz, Eye tracker: 29.87 Hz) - to assign an individual TCO data sample to each Purkinje image position (Figure 26A).

2. Image noise removal: changes between consecutive TCO samples larger than 2 pixels (threshold determined empirically) were regarded as image noise and removed from further analysis (Figure 26B). Single samples with change rates below threshold that lay in immediate neighboring blocks of samples flagged as noise were also removed.

3. TCO-tracking correlation: the linear regression of TCO and eye tracking data for both horizontal and vertical component was computed and then used to estimate TCO from eye position. The linear regression (for horizontal eye shifts) was in the form of:

   $$TCO_x(PI_x) = m \cdot PI_x + b \tag{7}$$

   where PI_x is the Purkinje's image X-coordinate, m and b are the slope and a constant offset of the linear regression and TCO_x is the resulting retinal image offset (Figure 26C). The estimate for the vertical component was computed accordingly.

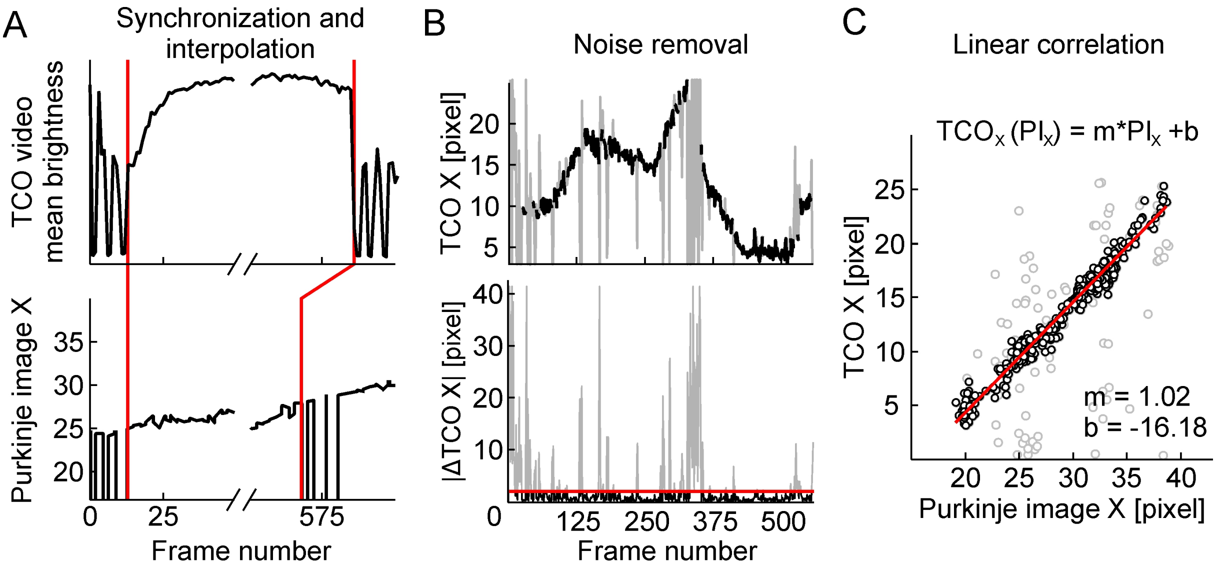

Figure 26: *Calibration processing steps. TCO and eye tracking data were recorded simultaneously while the operator moves the participant's eye in front of the system. A) For synchronization, three quick full on and off cycles flashed the imaging beam (before and after vertical red lines). Due to slight differences in sampling rate, TCO data was down-sampled via linear interpolation. B) Larger TCO data excursions (grey) were removed by thresholding for frame by frame TCO sample changes, Δ TCO (bottom graph, red line marks 2-pixel-threshold). C) Computation of the correlation between TCO and Purkinje image position by least-squares linear fit. The resulting function (shown as inset) was used to continuously estimate TCO based on eye tracking data.*

5.2.6 Experimental validation

For an objective validation of our eye tracking-based TCO estimation, we consecutively recorded 20 calibration sequences in one eye. We then used the linear regression function found in the first sequence and compared the measured TCO data at each eye position with the estimated TCO data by plugging in the eye position data in the calibration function for all following sequences. This was repeated for all 20 runs. Precision was estimated by using the x and y component of each frame's error as a coordinate in a two-dimensional displacement histogram. Repeatability of the procedure was measured by comparing the TCO coordinates across all 20 calibrations by solving Eq. (7) for a single (average) eye position.

We validated TCO estimation in a psychophysical experiment with three participants. The participant's task was to manually align their head in front of the AOSLO beam such that the features of a two-color centroiding stimulus produced in the AOSLO imaging raster were aligned. The stimulus feature offsets (a 2.3 arcmin dot of 543 nm light shown within a black target within the 840 nm imaging raster) were randomly chosen from sixteen offsets in a 4-by-4 grid with 0.4 arcmin spacing. Each offset was presented 6 times, for a total of 96 trials of subjective alignments. By the push of a button, the participant confirmed the correct alignment, the current Purkinje image location was stored, and a new stimulus offset presented. The predicted eye position based on the TCO calibration sequence and chromatic stimulus offsets were compared with the actual eye position at each trial.

5.3 Results

We performed TCO eye tracking calibrations in a total of 14 eyes, with multiple (3-20x) repetitions in all eyes, producing a total of 62 calibration sequences. We found that in order to collect sufficient data points (of both, image-based TCO and eye tracking data) during the 20 sec calibration, the most efficient head movement pattern resembled a square or circle. Figure 27 shows four example calibration sequences from three eyes with the produced raw data and subsequent regression analyses. To review calibration success, three different metrics were displayed after each calibration sequence, which also guided repeat decisions if a sequence had failed (e.g. due to insufficient image quality):

1. Percentage of clean data samples,
2. Eye movement extent in both horizontal and vertical direction given as distance of the center 80 % quantiles of all clean location samples (Q80),
3. Coefficient of determination of the linear regression to the data (R^2).

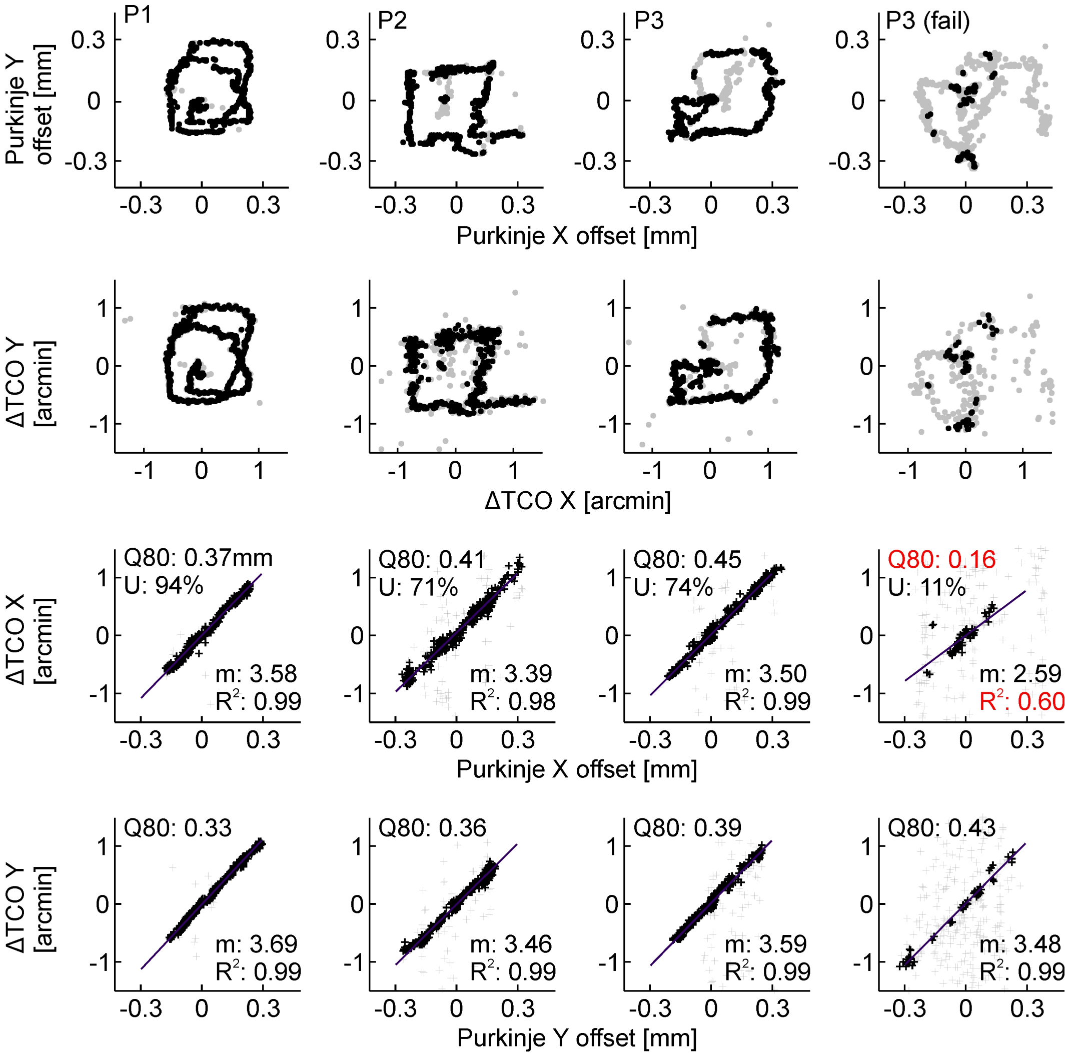

Figure 27: *Calibration sequences recorded in three participants (P1, P2, P3). Top row: Captured Purkinje image positions during calibration. 2nd row: TCO data of the same calibration sequence, based on video data recorded at 0.4 degree eccentricity. 3rd and 4th row: Linear regression for horizontal and vertical eye shifts, respectively. Percent samples used (U), range of data points (Q80) and goodness of fit (R^2) are metrics chosen to support the operator's decision whether a calibration has to be repeated (an example is shown in the 4th column). Black data points are the usable samples after interpolation and removing data noise, grey data points represent the data samples flagged as noise (see section 5.2 for details).*

When image quality decreased, the TCO computation algorithm produced an increasing number of noisy data (Figure 27, 4th column). We found that in order to ensure a reliable calibration, the percentage of used samples should exceed 33 %. The second metric, Q80, should exceed 0.3 mm in vertical and horizontal direction for a successful calibration (see an example of this metric taking effect in Figure

27, last column). The third metric, R^2, was mostly greater than 0.96 and calibration sequences with $R^2 > 0.90$ were considered to be sufficiently accurate. Based on a chromatic model eye describing the relationship between LCA, TCA and eye position [Rynders et al. 1995], the correlation between eye lateral position and TCO was expected to be linear (see Eq. (6)). The slope, m, of the linear regression was observed to be constant across eyes but different for horizontal and vertical shifts. Considering the median slope of three consecutively recorded calibrations in each eye, the mean slope for horizontal eye shifts was 3.55 ± 0.08 arcmin/mm and 3.43 ± 0.12 arcmin/mm for vertical eye shifts across participants (Figure 28A). By pairing horizontal and vertical data for each eye, this difference was significant ($p = 0.02$, Wilcoxon signed rank test). The absolute offset, b, of the linear regression was found to vary across participants, reflecting an idiosyncratic component of TCA (Figure 28B). Because the pupil's center was tracked simultaneously during calibration, the TCO values were also computed for a pupil computationally centered on the beam (Figure 28C).

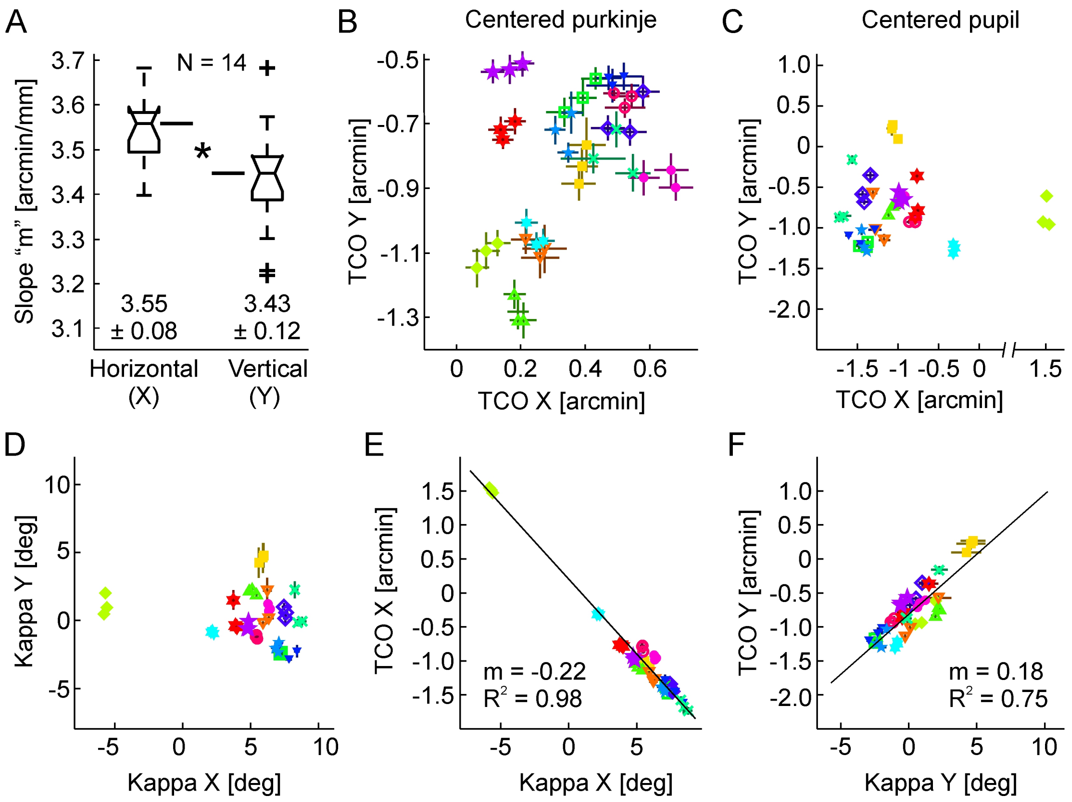

Figure 28: *TCO data across 14 eyes of 14 participants. A) Boxplot of the median calibration slope for each eye (3 repeats each). The average horizontal correlation slope across eyes was 3.55 ± 0.08 arcmin/mm, the average vertical correlation slope 3.43 ± 0.12 arcmin/mm. This difference between horizontal and vertical slope was significant (p = 0.02, Wilcoxon signed rank test). B) Calculated TCO for each run with a Purkinje position centered on the AOSLO beam. C) Calculated TCO for a centered pupil position. The one left eye included in this data set shows an absolute TCO with inversed sign (green diamonds). D) Angle Kappa for all eyes. E) Correlation of horizontal Kappa and horizontal TCO of the centered pupil. F) Correlation of vertical Kappa and vertical TCO of the centered pupil. For plots (B-F), vertical and horizontal bars mark the 0.5 quantile of the calibration function (TCO) and the standard deviation (Kappa). Different symbols mark different eyes. If no error bar is visible, the error is smaller than the symbol.*

For a centered Purkinje position, individual TCOs were positioned close to each other, with an extent of 0.8 arcmin from lowest to highest value for both dimensions. The range of individual TCO values broadened when calculated for a centered pupil: TCO values for the right eyes spread within a range of 1.5 arcmin. TCO for the one left eye tested had the opposite sign, as expected. Finally, we calculated angle κ for each participant (Figure 28D) and found a strong correlation between the TCO calculated for the centered pupil position and κ (Figure 28E, F). The linear regression of horizontal TCO with Kappa was defined by a slope of m = -0.22 arcmin/deg ($R^2 = 0.98$) and m = 0.18 arcmin/deg ($R^2 = 0.75$) for the vertical dimension.

To estimate measurement error of our eye tracking based method, we compared 20 consecutively recorded calibration sequences of one eye with each other (Figure 29). The 0.9 quantile of the framewise calculated difference between estimated and measured TCO was 1.04 pixel (0.10 arcmin) and 0.66 (0.07 arcmin) for horizontal and vertical axis, respectively (Figure 29A, B). Exceptions were single events - presumably due to eye blinks or bad image quality - which could be as high as 2 pixel (0.2 arcmin) (Figure 29B). By comparing each data set with each other in all possible pairwise combinations disallowing redundancy, 190 error sets containing a total of 88,266 error frames could be analyzed (Figure 29C). As an estimate of precision we calculated the area containing 95 % of all data points in a plot of positional error in both spatial dimensions between estimated and measured TCO. The extent of this area was ± 0.15 arcmin along the horizontal and ± 0.12 arcmin along the vertical axis. The area containing 50 % of all positional errors had a width of ± 0.07 arcmin and a height of ± 0.05 arcmin. To analyze the repeatability of measurement, we first determined the average eye position across all 20 calibrations. This value was plugged in for each calibration function to calculate the TCO estimate for this position (Figure 29D). The standard deviation for these 20 TCO estimates was 0.022 arcmin on the horizontal and 0.024 arcmin on the vertical axis. Across the three repeated calibrations in 14 participants we observed a median standard deviation for absolute TCO estimates with a centered Purkinje image of 0.029 arcmin (min = 0.012; max = 0.062) on the horizontal and 0.038 arcmin (min = 0.013; max = 0.070) on the vertical axis (Figure 28B).

Finally, a subjective validation experiment addressed the psychophysical component of the TCO estimation. Three participants were asked to adjust their head position in front of the AOSLO beams to align a centroid stimulus containing controlled chromatic offsets (Figure 30A). TCO estimation quality was assessed by comparing the applied chromatic stimulus offset with the resulting TCO estimated from the participant's self-adjusted eye position (Figure 30B). The average difference between calculated TCO from estimation and the actual applied offset was 2.49, 2.96, and 2.95 pixel (0.25, 0.30 and 0.30 arcmin) for P1, P2, and P3, respectively. Each participant showed an individual alignment strategy, resulting in clustering of certain displacement offsets. When pooling data across participants, no systematic direction for displacement errors was evident.

5.4 Discussion

Here, we present a video-based eye tracking approach to estimate transverse chromatic offsets (TCO) in an adaptive optics scanning laser ophthalmoscope (AOSLO) retinal microstimulator. The ultimate goal of this work was to compensate system- and eye-inherent chromatic offsets with a precision enabling targeting and stimulation of the smallest retinal photoreceptors, foveal cones and rods, without the need of direct and continuous TCO measurement, while at the same time allowing small head (and eye) movements to occur. By using a corneal reflection of the AOSLO beam as eye position beacon, we achieved TCO estimation with low noise, high repeatability and high spatial precision. We here discuss our principle of Purkinje image based positional tracking, the relationship between transverse chromatic aberrations (TCA), TCO, and the angle Kappa of the eye, and finally its usability and application for single photoreceptor stimulation.

Many eye trackers use pupil coordinates such as its center to report absolute eye position, and the pupil center has been shown to correlate with objective measures of TCA [Harmening et al. 2012; Privitera et al. 2016; Boehm et al. 2019]. For precise estimates of TCA, however, the location of the TCA-inducing beams relative to the eye's optics – and not its pupil – is more relevant [Simonet and Campbell 1990]. In general, correlations of pupil position with chromatic offsets were accurate enough to allow for TCO compensation. A direct comparison between pupil and Purkinje based TCO estimation over time (2h) revealed an average estimation error of up to 0.33 arcmin and 0.15 arcmin for pupil and Purkinje tracking respectively (data not shown). Such estimation error would be sufficient when targeting single

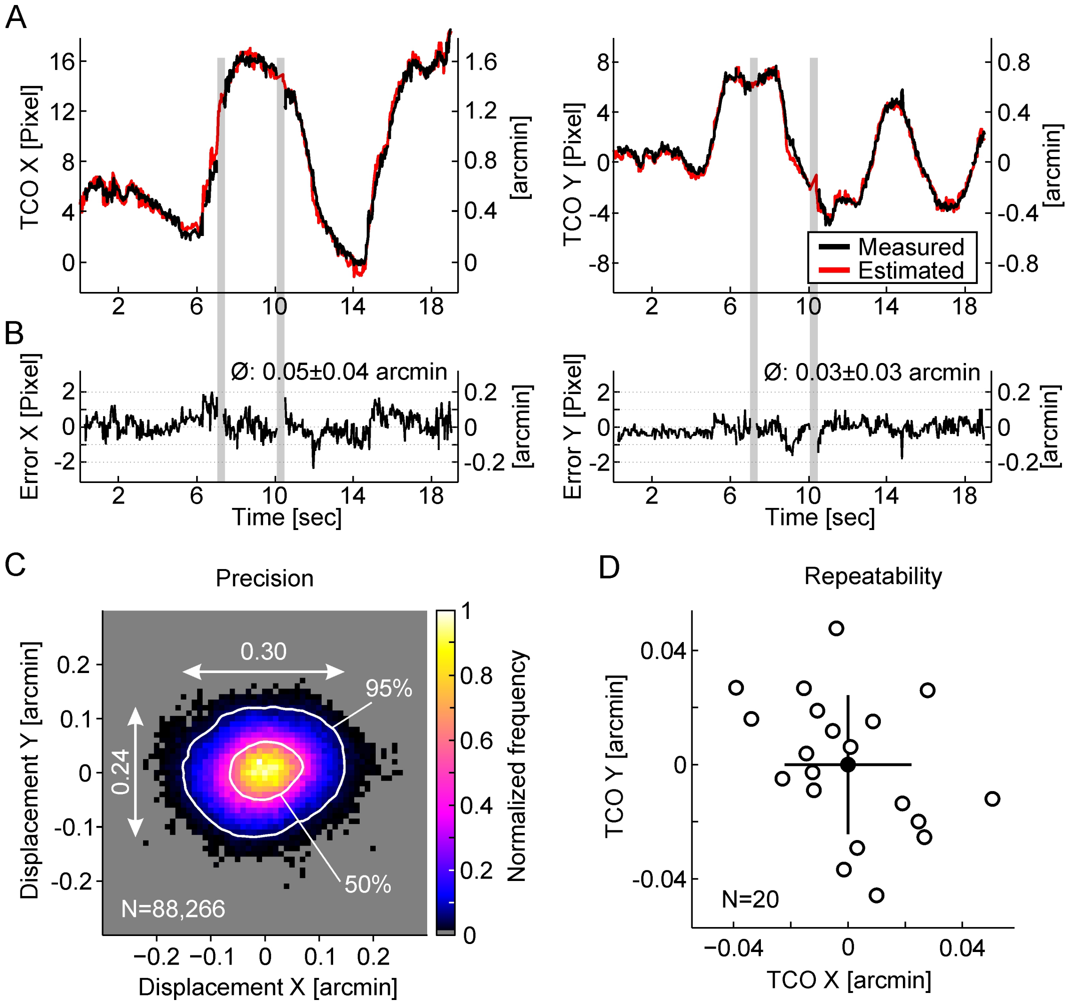

Figure 29: *Error estimation. A) Exemplary comparison between measured TCO (black) and estimated TCO (red) following a single calibration sequence. Grey areas mark examples where image quality did not allow TCO measurement. B) Error of TCO estimation over time. Average (± STD) estimation error was 0.05 ± 0.04 arcmin. Single events may exceed an estimation error of 1 pixel (1 pixel = 0.1 arcmin). C) To determine TCO estimation precision, 20 consecutive calibration sequences were validated against each other. The framewise displacement error was plotted in both spatial dimensions with one-tenth pixel resolution (1 block = 0.01 arcmin). 95 % of all displacement errors were within ± 0.15 arcmin (horizontal) and ± 0.12 arcmin (vertical). D) Repeatability was tested by using the average eye position in the 20 calibration functions (open circles). The standard deviation across all data is visualized via the extent of the horizontal and vertical bars (STDx = 0.022 arcmin/ STDy = 0.024 arcmin).*

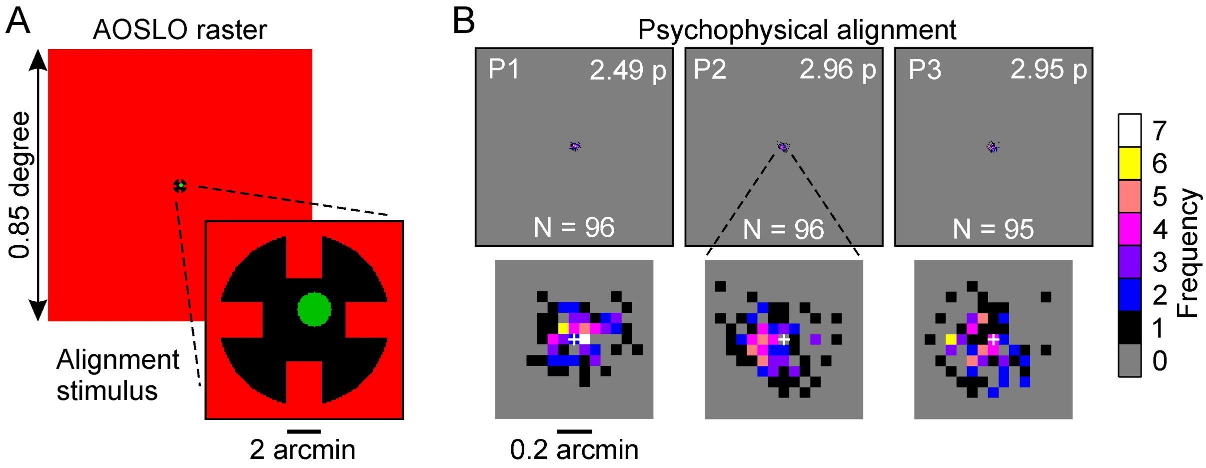

Figure 30: *Subjective validation of our eye tracking based TCO estimation approach. A) AOSLO raster with stimulus to scale. The task was to center the green circle within the red notches. B) Results from all 3 participants in the same scale as the zoomed stimulus in A (white scale bar = 2 arcmin). The mean difference between predicted position from estimation and subjective alignment was 2.49, 2.96, and 2.95 pixels (0.25, 0.30 and 0.30 arcmin) for P1, P2, and P3, respectively. There was no systematic direction for displacement errors. The enlargement below each panel in B displays the pixelwise TCO correction errors for each participant. The white cross marks the zero difference position.*

cones at an eccentricity of 2 degree or further on the human retina, but too high for foveal photoreceptor stimulation (cone aperture size = 0.25 arcmin). We assume that the observed increase of estimation error is due to the fact that the axis defined by the pupil center can shift with respect to the visual axis, e.g. during pupil constriction and dilation [Wildenmann and Schaeffel 2013]. Typical pupil trackers determine the pupil's center applying a circle fit, which is sensitive to errors because circularity of the pupil changes with pupil size. Even during drug induced mydriasis pupil size changes asymmetrically [Hoang et al. 2016], and is usually uncontrolled for during microstimulation experimentation. To overcome these deficiencies, we use in our approach the first Purkinje image, the reflection of the AS-OLO beam on the front surface of the cornea, as the tracking signal for eye translation changes. The location of this reflection depends on both the absolute position of the eye relative to the light source and camera as well as the rotational state of the eye. In relationship with the positional changes of the pupil center during eye rotation, it can therefore also be used as a gaze signal [Morimoto and Mimica 2005].

In our setup, with a static camera coaxially aligned to the light source, lateral head and eye shifts as well as rotation of the eye ball will move the Purkinje image. Purkinje image movement caused by gaze shifts could induce an error in our TCO estimation, because measures of TCO changes with retinal eccentricity [Winter et al. 2016]. Eye ball rotation occurs in two different cases and in both cases we used the Hirschberg ratio to estimate the magnitude of eye rotation induced errors. The individual Hirschberg ratios of four eyes measured with our eye tracker were 12.2 degree/mm, 13.5 degree/mm, 13.6 degree/mm, and 13.7 degree/mm (average 13.3 degree/mm), in good accordance with values found in the literature [Schaeffel 2002; Model et al. 2010]. In the first case, gaze changes occur due to the lateral head motion during calibration while the participant maintains visual fixation of a static visual target. Shifting the head by 0.4 mm in one direction will induce a rotation of the eyeball of 0.05 degree. This angle will move the Purkinje image about 0.0038 mm or 1/10 of a pixel in the camera image, and is thus negligible. In the second case, fixational eye movements during calibration or later compensation will shift the Purkinje image with a ratio of about 2.5 pixel per degree of gaze shift. Hence, to displace the Purkinje image by a full pixel the participant would have to rotate the eyeball by 0.4 degree. Typical fixational eye movements such as tremor and drift have an amplitude of about 0.01 degree, or 0.1 degree respectively [Martinez-Conde et al. 2004]. Thus, only microsaccades could move the Purkinje image with detectable amplitudes. Because of the AOSLO's inability to correct stimulus locations for the fast changes in retinal location during a microsaccade, however, TCO compensation would not be needed in that situation.

As hypothesized by a theoretical chromatic eye model, the relationship between ocular TCA and small displacements of eye position (< 2 mm) ought to be linear, and dependent on wavelength [Thibos et al. 1990; Thibos et al. 1992; Rynders et al. 1995]. We found an average slope of 3.55 arcmin horizontal TCO change per mm eye shift, and 3.43 arcmin/mm for vertical TCO. This finding is in accordance with earlier reports (3 arcmin/mm, 3.5 arcmin/mm, and 3.86 arcmin/mm [Harmening et al. 2012; Privitera et al. 2016; Boehm et al. 2019]), and matches the chromatic eye model, predicting a slope of 3.44 arcmin/mm for a LCA of 1.00 D when 840 nm and 543 nm light is used [Thibos et al. 1990; Thibos et al. 1992; Rynders et al. 1995]. The residual variations we observed might be caused by individual differences in LCA. In our group of 14 participants, the observed difference between slopes of horizontal and vertical direction was significant, an observation which was also found in a similar study [Boehm et al. 2019]. Following Eq. (5), such difference could be caused by differences in optical dispersion along the horizontal and vertical dimension of the eye. Although this kind of dispersion anisometry has not been reported before, it could be hypothesized that the dispersive characteristic of the eye also differs between horizontal and vertical meridians, because curvature and therefore refractive power of the cornea differs between those meridians [Kiely et al. 1982; Iyamu and Osuobeni 2012].

We determined absolute TCO values in 14 participants with a centered Purkinje image (due to the fact that our light source, visual axes and camera are all coaxially aligned), and found values ranging within 0.6 arcmin along the horizontal and 0.8 arcmin along the vertical dimension. These ranges are clearly smaller than the ranges of absolute foveal TCA estimation reported by previous studies: about 1 arcmin [Simonet and Campbell 1990; Winter et al. 2016], 2 arcmin [Thibos et al. 1990; Ogboso and Bedell 1987], 4 arcmin [Rynders et al. 1995] and 8 arcmin [Marcos et al. 2001]. In all these studies, TCA was determined with a centered pupil. The range of absolute TCO for a centered pupil position in our study spanned 1.4 arcmin and 1.6 arcmin for horizontal and vertical dimension, including only right eyes. The closer range of absolute TCO - including the single left eye - for a centered Purkinje position can be explained by the fact that the foveal achromatic axis and the visual axis are closely related [Atchison 2017], and that our eye tracking camera was aligned with the visual axis. The remaining scatter could be caused by individual differences of the eye's optics. The reason for our observation that the TCO values with a centered Purkinje do not vary around zero may be due to a minimal alignment difference between the imaging and stimulation light in the light delivery path, or - since the TCO measurement is image based - the IR and green detector positions.

To study the relationship between visual, pupillary and achromatic axes in more detail, we also measured individual Kappa angles in all eyes. The measured TCO values for a centered pupil where linearly correlated with Kappa (R^2 = 0.98 for horizontal, R^2 = 0.75 for vertical Kappa). This finding supports the chromatic eye model, where TCA is correlated with the angle Psi Ψ (defined by pupil displacement and nodal point distance from the entrance pupil, like Kappa, here) [Thibos et al. 1990; Rynders et al. 1995]. This experimental confirmation has important implications for all ophthalmic applications where TCA is wished to be measured or corrected. First, we confirmed that the slope, m, of TCA per pupil displacement can be directly derived from individual LCA values of the eye. Second, if beams are centered in the pupil, a precise measurement of Kappa can be a direct measure for foveal TCA, once their relationship has been established in the system used, determining the offset b (see Eq. (7)). We tested this in four participants, by recalculating Kappa for the individual Nodalpoint distance obtained from the participant's Hirschberg ratio. In that situation, where the TCO estimation function based solely on Purkinje image and pupil center data, we would have made an average error of 0.13 ± 0.04 arcmin for horizontal TCO and 0.14 ± 0.07 arcmin for vertical TCO. Thus, only if a spatial precision on the order of single cones of the central fovea and rods is desired, a direct calibration as presented here would be required. Other applications like functional testing of pathologic areas of the retina in patients where direct TCO measure is unfeasible or unsuitable due to the high light intensities could utilize real time TCO compensation, simply by determining Kappa [Tu et al. 2017; Wang et al. 2015].

One of the important goals of the eye tracking based estimation of TCO was to increase estimation precision up to single foveal cone level. The cones of the central fovea are the smallest photoreceptor cells of the retina with an inner segment diameter of about 30 arcsec [Curcio et al. 1990] comparable to the diameter of rods. With larger eccentricity, cones increase in diameter with the result that positional errors caused by a participant's residual head movements become more negligible (Figure 31). Typically, participants show individual amounts of residual head shifts. We determined in a few observers that, during experiments with a static TCO compensation method, where TCO is measured before and after an experiment without any ongoing monitoring, stimuli can be displaced up to 2 arcmin (Figure 31, top row). To visualize the impact of our proposed TCO compensation method, the precision of ± 0.15 arcmin determined here for our system was used to exemplary shift the target position on a retinal image due to noise of the ongoing compensation. For an experiment targeting individual cones of the central retina or rods, a maximal positional error of a single pixel, or 6 arcsec, is tolerable - a requirement that is met by about 75 % of the TCO compensated positions. At 0.4 degree eccentricity, positional errors up to 12 arcsec would be acceptable. This criterion was met for all (100 %) estimated TCO values in our study. Additionally, variability across three consecutively recorded calibrations in 14 tested participants fell well within 0.1 arcmin, which was lower than the observed single frame measurement noise (Figure 28B and 29).

In the subjective validation experiment, participants made an average error of 0.30 arcmin, corresponding to twice the objectively determined precision, and smaller than the expected Nyquist limit of 0.43 arcmin for a foveal cone density of 200,000 cells/mm^2 [Williams and Coletta 1987], but slightly higher than the typically found average Vernier acuity of 0.19 arcmin [Reiniger et al. 2019b] and 0.25 arcmin [Abbud and Cruz 2002]. Because we did not observe any systematic displacements across the three participants, we conclude that the subjective validation confirmed the current calibration process. However, comparable to other eye tracker setups, we plan to include a brief subjective validation routine of the calibration before running single cell stimulation experiments to detect systematic mismatches between subjective and estimated TCO. These small chromatic offsets could occur, for example, due to alignment changes in the AOSLO setup.

As a practical note, for compensation of TCO during microstimulation experiments, we currently implemented a per-trial approach. The stimulus was shifted according to the current TCO by converting the current offset into a temporal signal, switching the light on and off at the according scanning raster positions (see [Poonja et al. 2005] for more details). Because our eye tracking software is a standalone solution, its data has to be transmitted to our stimulation software, which is run in a Matlab environment. Purkinje image coordinates were sent from the eye tracker software to Matlab on request, triggered by the participant's keystroke that also triggers stimulation presentation. The delay of this communication was measured by means of timestamps, and did not exceed 30 msec. Based on the calculations shown above, we disregard the amount of gaze shifts for this period of time. The average head shift within a 30 msec window across all our calibration sequences was 0.006 mm, resulting in a TCO glitch of 0.02 arcmin due to transmission delays introduced by the software interface.

In summary, the demonstrated eye tracking method seems a viable solution to estimate and compensate chromatic offset in real time within a fraction of arcmin, necessary for adaptive optics microstimulation of the smallest photoreceptors of the retina. Furthermore, we experimentally confirmed the fundamental relationship between angle Kappa and TCA, which could be a convenient implementation in applications where TCA is wished to be compensated but cannot be directly measured.

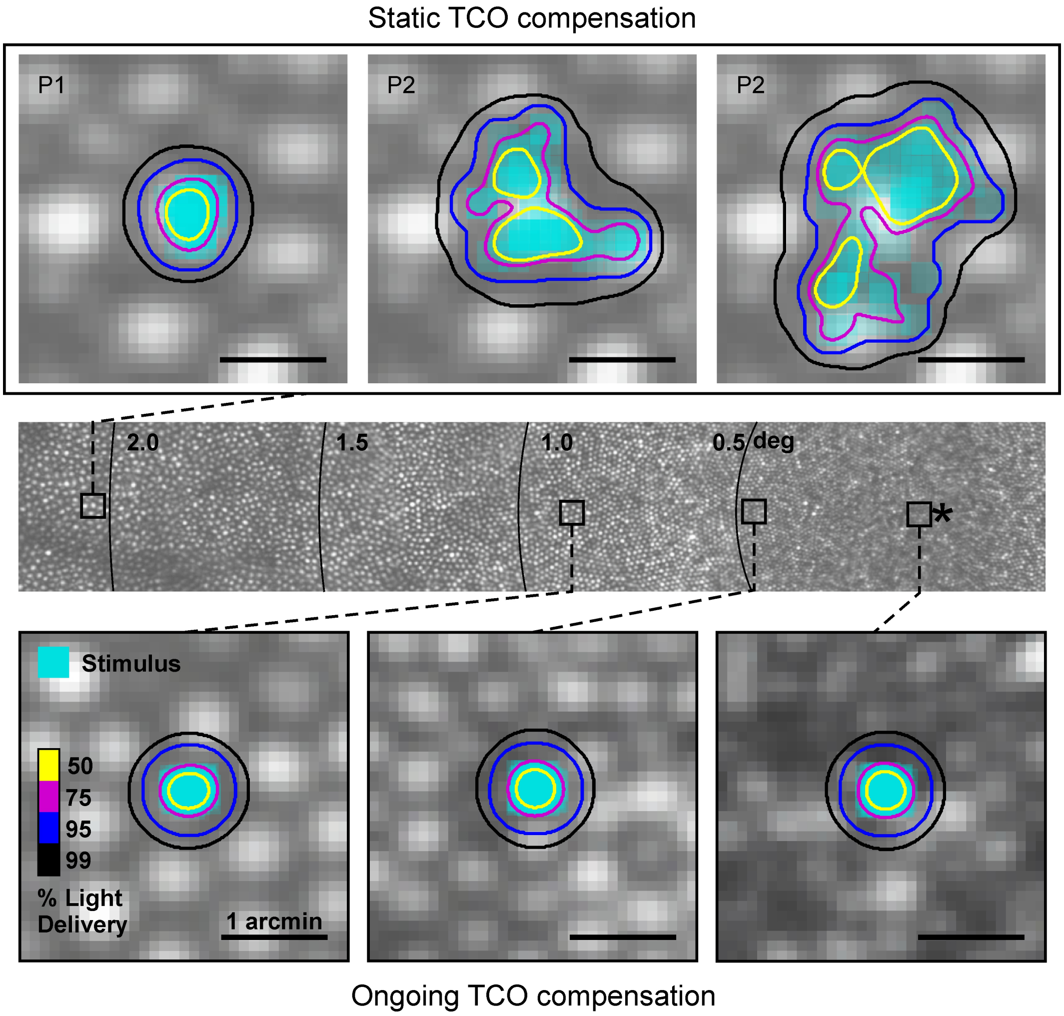

Figure 31: *Demonstration of TCO compensation error at different retinal eccentricities. Top: Enlarged view of a typical stimulation site in AOSLO based experiments with current static TCO compensation. Overlay shows actual light delivery based on minimal head shifts in front of the system recorded by our eye tracking system during experiments in three participants (P1-3). Middle: AOSLO image montage encompassing the central fovea, asterisk marks the preferred retinal location of fixation, rings denote eccentricity. Cone size increases rapidly with increasing eccentricity. Bottom: Enlarged view of the smallest cones in the central fovea, 0.4 degree and 0.9 degree eccentricity. Overlays display theoretical stimulus delivery with ongoing TCO compensation as presented in this study. Our typical cell sized square-stimulus expands 3 pixels (diffraction limited FWHM, 0.3 arcmin).*

6 Retinal factors of visual sensitivity in the human foveola

The content of this chapter is based on:

Domdei N, Reiniger J, Holz FG, Harmening WM (2021) The Relationship Between Visual Sensitivity and Eccentricity, Cone Density and Outer Segment Length in the Human Foveola. *Investigative Ophthalmology and Visual Science*, 62(9): 31. DOI: 10.1167/iovs.62.9.31

6.1 Introduction

The presence of a fovea in the retina of some birds, fish, reptiles and primates like humans [Slonaker 1897], provides an outstanding opportunity to study the linkage between a sensory system's cellular architecture and its function. In humans, the fovea features several morphologic specializations as a result of a complex series of events that are initiated during gestation and completed in childhood [Yuodelis and Hendrickson 1986; Zhang et al. 2020]. The network of retinal blood vessels organizes itself around an avascular zone concentric within the fovea [Provis et al. 2013] and the foveal pit emerges as post-receptoral neurons migrate laterally. As a consequence, the foveola, the central 0.6 degree diameter of the fovea [Cuenca et al. 2020], is completely free of overlying neural tissue, favoring undisturbed light catch. Cone photoreceptors migrate inwards to form a lattice of tightly packed receptors at their smallest diameter found anywhere in the retina [Curcio et al. 1990], and simultaneously, the pigment-laden cone outer segments elongate [Yuodelis and Hendrickson 1986], leading to a peak in optical density at the foveola [Elsner et al. 1993; Marcos et al. 1997]. Psychophysically, photopic light sensitivity drops rapidly outside of the foveola [Choi et al. 2016].

At close inspection, the topography and density of cone photoreceptors within the foveola is highly variable between individuals [Wang et al. 2019] and it is not known, to what extent the individual cellular mosaic and the exact foveal topography is related to visual sensitivity. In patients with inherited retinal degeneration, for example, light sensitivity in the fovea was similar to a healthy control group and showed declined sensitivity only when peak cone density was reduced to less than 60 % of the average [Foote et al. 2018]. Sensitivity to light is assumed to be conveyed primarily by parasol ganglion cells [Takeshita et al. 2017], supported by the observation that spatial summation is correlated with the receptive field size of parasol ganglion cells [Volbrecht et al. 2000]. In the foveola, however, the spatial summation area is less than 5 arcmin^2, between the dendritic field size of parasol and midget ganglion cells [Tuten et al. 2018]. Thus, a visual stimulus smaller than the spatial summation area might reveal an otherwise obscured relationship between the peaking topography of the detector array in the foveal center and its visual sensitivity.

Concomitant to the peaking spatial sampling capacity at the fovea, motor circuits of the brain stem generate eye and head movements to bring the retinal images of objects of interest detected in the periphery into the foveola [Goldberg and Walker 2013; Poletti et al. 2013], where they fall on a distinct bouquet of only a handful cones, the preferred retinal location of fixation (PRL or "optimal locus") [Nachmias 1959; Steinman 1965; Putnam et al. 2005]. Previous studies showed that the PRL does not colocalize with structural features such as peak cone density [Putnam et al. 2005] or the center of the foveal pit volume [Wilk et al. 2017a]. The subset of cones at the PRL may thus have functional preeminence, as fixational eye movements re-center the object of interest on this location with extreme precision [Pritchard 1961; Reiniger et al. 2021].

With recent optical tools, the mosaic of even the smallest cone photoreceptors in the foveola can now be resolved in the living human eye and visual function such as visual sensitivity can be simultaneously probed psychophysically with cellular precision [Harmening et al. 2014]. In a first attempt to better understand how the specific mosaic of cone photoreceptors within the foveal center has functional consequences to vision, we here use this experimental access to study the direct relationship between the cellular makeup of the foveal center and sensitivity to cell-targeted light in four human participants.

6.2 Material and Methods

In four human participants (1 female, 3 males; 35 ± 6 years), the cellular topography of the fovea, light sensitivity to cone-sized stimuli, and the preferred retinal locus of fixation where mapped with cellular precision using an adaptive optics scanning laser ophthalmoscope (AOSLO) microstimulator. The participants were three of the authors (P1= ND, P2 = JLR, P3 = WMH), and one lab member (P4). Pupil dilation and cycloplegia were induced by instilling one drop of 1 % Tropicamide 15 minutes before the beginning of an experimental session. For each participant, a custom dental impression (bite bar) was used to immobilize and control the position of the head during imaging and stimulation. Written informed consent was obtained from each participant and all experimental procedures adhered to the tenets of the Declaration of Helsinki, in accordance with the guidelines of the independent ethics committee of the medical faculty at the Rheinische Friedrich-Wilhelms-Universität of Bonn, Germany.

6.2.1 Adaptive optics scanning laser ophthalmoscope microstimulator

The central ~1 degree of the right eye of each participant was imaged and targeted test sites were simultaneously stimulated with a custom multi-wavelength AOSLO (for details of the system see (Poonja et al., 2005; Grieve et al., 2006; Domdei et al., 2018, 2019)). In brief, the output of a supercontinuum light source (SuperK Extreme EXR-15, NKT Photonics, Birkerød, Denmark) was split into two light channels by serial dichroic and bandpass filtering: one near infrared (IR) light channel was used for imaging and wavefront sensing (840 ± 12 nm, FF01-840/12-25, Semrock, Rochester, USA), and a visible green light channel for microstimulation (543 ± 22 nm, FF01-543/22-25, Semrock). Adaptive optics correction, run in closed loop operation at about 25 Hz, consisted of a Shack-Hartmann wavefront sensor (SHSCam AR-S-150-GE, Optocraft GmbH, Erlangen, Germany) and a magnetic 97-actuator deformable mirror (DM97-08, ALPAO, Montbonnot-Saint-Martin, France) placed at a pupil conjugate. Imaging and stimulation beams, traversing the system coaxilly, were point-scanned across the retina, spanning a square field of 0.85 x 0.85 degrees of visual angle. The light reflected from the retina was detected in photomultiplier tubes (PMT, Photosensor module H7422-40 and -50 Hamamatsu Photonics, Hamamatsu, Japan) individually for each channel, placed behind a confocal pinhole (pinhole diameter = 20 μm, equaling 0.47 (840 nm) and 0.71 (543 nm) Airy disk diameters). The PMT signals were continuously sampled by an FPGA board (ML506, Xilinx, San Jose, USA), producing video frames with 512 x 512 pixel (spatial resolution = 0.1 arcmin of visual angle per pixel) at 30 Hz by combining the PMT's voltage output with the positional data of the scanners. To increase dynamic range and contrast, the 543 nm stimulus light was modulated by two cascaded acousto-optic modulators (see chapter 4). The stimulation light was attenuated by 3 log units using a neutral density filter before coupling light into the AOMs, ensuring an optimal operating range of the AOMs. The combined effects of chromatic aberrations of the human eye were minimized as follows: longitudinal chromatic aberration, LCA, was compensated by a static relative vergence difference of 1 diopters between the 840 nm and 543 nm lights [Atchison and Smith 2005], and an individual adjustment of defocus of the DM for each eye, prioritizing image quality in the visible channel. Transverse chromatic offsets were compensated dynamically with every stimulus presentation by lateral stimulus location offsets driven by correction signals from Purkinje-based pupil monitoring (see chapter 5).

6.2.2 Cone density maps and cone density centroid

Continuous maps of cone photoreceptor density were generated by recording a 10 second AOSLO video with an imaging wavelength of 543 nm (P1 and P2) or 788 nm (P3 and P4) while the participant was asked to fixate on a small flashing target in the center of the imaging raster. High signal-to-noise ratio images were then generated by strip-wise image registration and averaging of individual frames of those videos, while manually excluding single frames with failed registration. In these normalized images, one human grader marked the location of each cone, assisted by convolutional neural network custom software [Cunefare et al. 2017; Reiniger et al. 2019a]. Matlab's Voronoi function (*voronoiDiagram*, Mathworks, Inc., Natick, MA, USA) was used to compute each cone's area. Cone density at each pixel of this image was then calculated by first identifying the nearest 150 cones around each pixel in the image. Cone density was then defined by dividing the number of cones by their summed area. The cone density centroid (CDC) was the retinal location found as the weighted centroid (Matlab function *regionprops(Image,'weightedcentroid')*) of the area containing the highest 20 % cone density values.

6.2.3 Determination of cone outer segment length

Spectral-domain optical coherence tomography (OCT) images were acquired for all 4 participants in a 5 x 15 degree field, centered on the fovea with a B-scan spacing of 11 μm with a clinical OCT device (HRA-OCT Spectralis, Heidelberg Engineering, Heidelberg, Germany). For further processing, the central 45 B-scans around the foveal pit were selected. Cone outer segment (OS) length was defined as the space between visible bands 2 and 3 in each B-scan, thus is the space between the ellipsoid zone and the interdigitation zone, respectively [Spaide and Curcio 2011]. In a first step, these two bands were segmented by manually adjusting a brightness-based automated detection algorithm (Figure 36A). Because the retinal pigment epithelium is thought to have a relatively uniform thickness and flat layout, a two-dimensional area fit across all B-scans for the third band was computed, reducing artifacts of the individual band marking. The width of both bands was modelled with a 1D Gaussian profile, centered on the band marking. The OS length was defined as the linear space between the steepest parts of the second band's declining and the third band's rising slope (see also [Spaide and Curcio 2011]). In the final step, the two-dimensional OS length map was smoothed along the orthogonal B-scan axis with a Savitzky-Golay filter to remove residual artifacts of individual band markings between the single B-scans and then rescaled to obtain equal increment per pixel values in all directions. These 2D maps of OS length were registered with retinal AOSLO imagery by centering their maximum value at the CDC.

6.2.4 PRL determination

The preferred retinal locus of fixation (PRL) was determined by recording the exact retinal location at which a small, flashing visual stimulus landed during attempted fixation. The fixation stimulus was created by modulating the imaging channel of the AOSLO to turn off in a central region of the raster, creating a small visible black square, 1.6 × 1.6 arcmin nominal size, shown against the visible 840 nm, 51 × 51 arcmin scanning background. The stimulus flashed continuously at 3 Hz and its retinal landing positions were recorded in three consecutive 10 second AOSLO videos. Retinal fixation locations were then found by, (1) automatically registering each frame strip-by-strip to a common reference frame of a single video [Arathorn et al. 2007], (2) manual deletion of incorrectly registered frames (usually due to microsaccades, insufficient image quality or eye blinks), (3) tabulating all stimulus locations within the remaining, co-registered frames (Figure 32A). The final PRL estimate for each eye was the median stimulus location across all three videos, equaling on average 387 frames (Figure 32B). This location was defined as 0 eccentricity.

6.2.5 Increment sensitivity thresholds

After PRL determination, participants underwent small spot sensitivity testing at multiple sites within their foveola, with the PRL as a spatial anchor at the center of the test locations. Sixteen additional test locations were selected manually around the PRL, close to the intersections of two concentric perimeters (spaced 6 and 12 arcmin) around the PRL with the horizontal, vertical, and diagonal meridians (Figure 33A and B). At each of the 17 test locations, sensitivity thresholds were determined as the median of 3-5 repeat measurements per location. In each experimental run, three out of the 17 locations that were oriented closely along a vertical axis were tested as a group, with the individual locations tested pseudo-randomly interleaved within the group. This approach minimized participant fatigue, allowed for more regular breaks between runs, and also minimized background intensity changes that are present towards the horizontal edges of the imaging raster (± 0.05 contrast change), because stimuli could be presented in the central part of the imaging raster at all times. Sensitivity thresholds at each test location were esti-

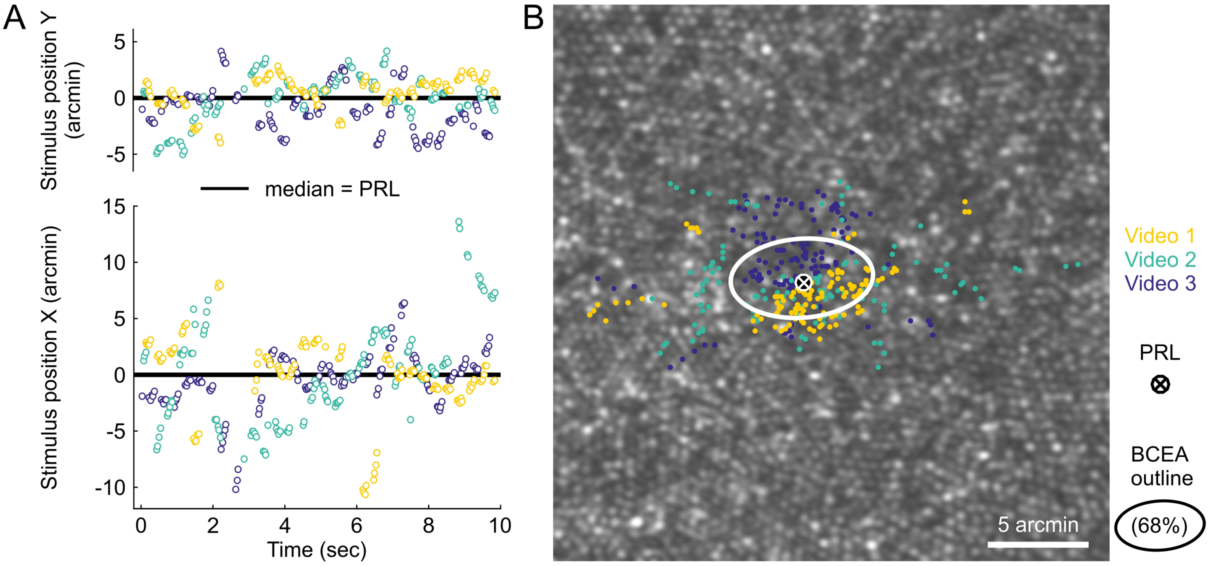

Figure 32: *Preferred retinal locus (PRL) determination from three 10 sec videos. A) The nominal fixation target was a 1.6 × 1.6 arcmin square presented at a fixed position in the center of the AOSLO raster flashing with 3 Hz. High resolution eye motion traces were recorded in three 10 second epochs, tracking the position of the target's center in retinal coordinates. Single dots represent frame-by-frame derived retinal coordinates of the target, colors indicate repeats. B) Stimulus positions in relationship to the foveal cone photoreceptor mosaic. The bivariate contour ellipse was set to contain 68 % of all stimulus locations. The participant's PRL (white ellipse and marker) was computed as the median data point, pooling all locations of the three consecutively recorded videos.*

mated with QUEST, an adaptive staircase method (Watson and Pelli, 1983), adjusting stimulus intensity following a Yes/No-test paradigm with logarithmic step sizes (King-Smith et al., 1994). Because of the visible IR imaging raster, stimuli were presented against a reddish background (about 5 cd/m^2 photopic luminance), rendering our sensitivity testing paradigm to yield increment sensitivity thresholds (see also [Harmening et al. 2014; Tuten et al. 2017]). Test stimulus was a green square with 7 pixels edge length in scanning raster coordinates, equaling a diffraction limited full width at half maximum of 0.8 arcmin, or 3.9 μm on the retina. Due to the scanning nature of the AOSLO, where visual stimuli are rendered pixel-by-pixel while the illumination beam traverses the retina, the presentation time spanned 350 μsec from the first to the last pixel of the stimulus. This equals a net illumination time per stimulus of 2.5 μsec. Stimulus presentation progression was self-paced and successful deliveries were accompanied by an auditory cue. Stimulus delivery was blocked if either the online stabilization algorithm or the eye tracking for TCO compensation failed, and the participant had to repeat the trial (~32.4 % of all 5674 stimulus presentations). Threshold estimation was completed after 12 trials if the standard deviation (STD) value of QUEST was lower or equaled 0.10 log arbitrary AOM voltage drive units (Figure 33D). If STD was higher, the run was extended by additional trials until the STD criterion was met. The run was terminated and had to be repeated if the STD criterion was not met after 18 trials. Runs were repeated until a minimum of three valid threshold estimates per test location were recorded.

Real-time image stabilization enabled retinal tracking and repeated stimulation of the targeted test sites [Arathorn et al. 2007]. In a subsequent offline analysis, trials with suboptimal delivery (more than 0.6 arcmin deviance from median delivery location, equaling about 1.2 cone diameters) were excluded from further analysis. The non-linear swing speed of the resonant scanner produced a non-uniform IR background across the field, with increasing brightness close to the vertical edges of the field. For compensation, the individual trial intensity was corrected based on the position in the imaging raster and the resulting stimulus contrast, with compensation factors ranging between 0.95 and 1.00. After trial rejection and intensity correction, QUEST was computationally re-run with the updated stimulus intensities to recompute the final threshold estimate. Trial deletions on account of stabilization errors

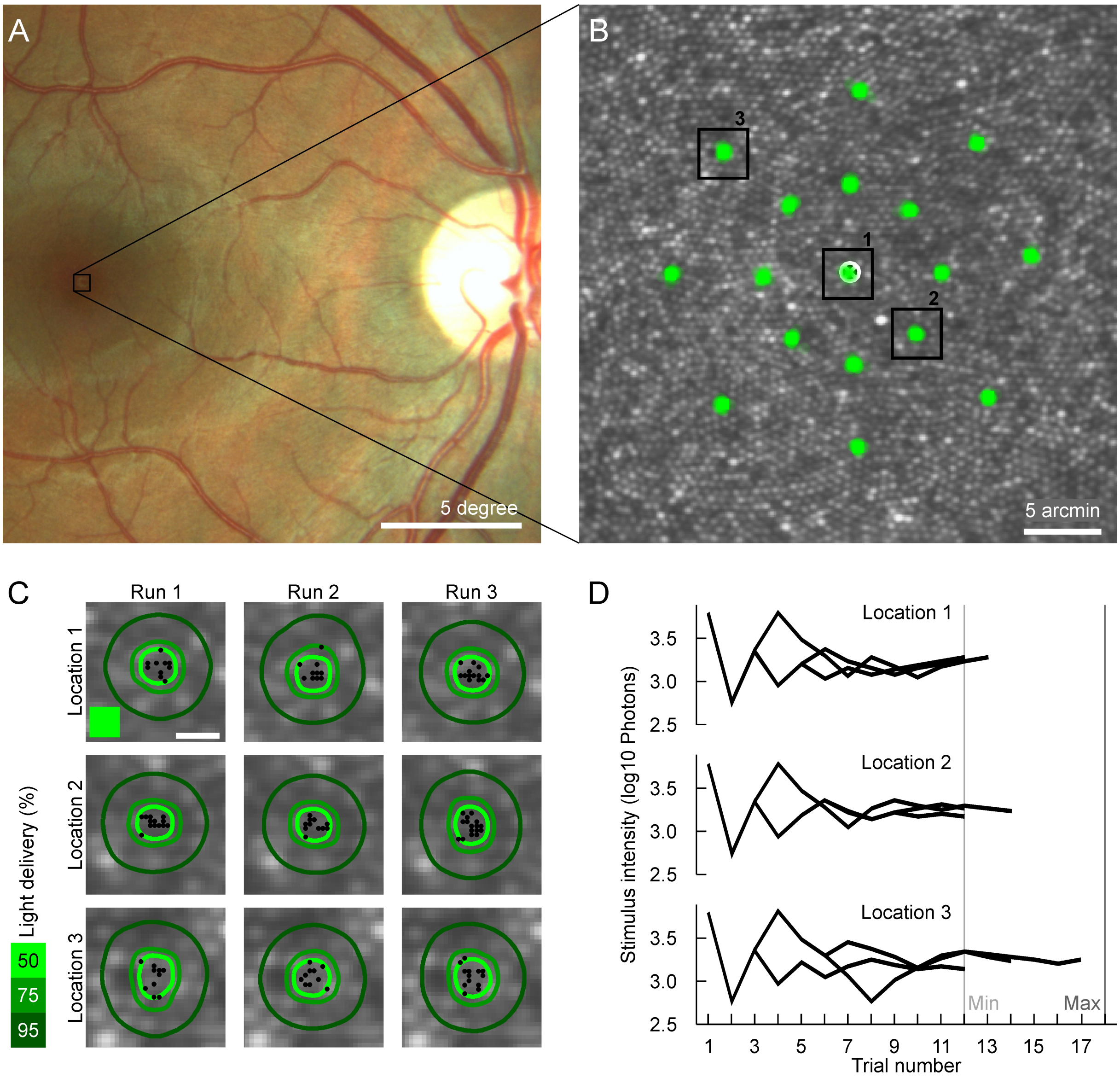

Figure 33: *AOSLO-based microstimulation. A) Color fundus image of one participant. The grey square shows the size and position of the AOSLO imaging and stimulation raster on the retina, positioned at the center of the fovea. B) Cropped view of an averaged frame showing the AOSLO image of the central fovea. Retinal stimulation sites are marked by transparent green markers, three sites are highlighted by black boxes to be further analyzed in the next panels. C) Zoomed-in view of selected target sites. Markers indicate individual stimulus locations during repeated stimulation for threshold estimation. The green square represents the stimulus in raster pixel size. The contour lines mark 50 %, 75 %, and 95 % of the summed light delivery for each run. The scale bar is 1 arcmin. D) Exemplary progression of stimulus intensity based on the current threshold estimation via QUEST with three runs per test site. The individual run was completed, when the standard deviation of the estimated threshold was less or equal 0.10, resulting in a varying number of trials per test site and run.*

produced higher QUEST STDs. In a second step, thresholds with an STD higher than 0.15 log a.u. were excluded from the following analysis. Sensitivity thresholds are finally computed and reported as the number of photons incident at the cornea at the threshold intensity (see next chapter).

6.2.6 Conversion of arbitrary power units to number of photons at the cornea

Before and after each experimental run, maximum output power of the AOSLO stimulation light channel was measured at maximum AOM drive voltage with a silicon photodiode and power meter (S130C and PM320E, Thorlabs GmbH, Bergkirchen, Germany) in the transmitted portion of the stimulation beam after a 90/10 (Transmisson/Reflection) beam splitter placed in the light delivery arm of the AOSLO. The average of these two measurements was used for actual stimulus power calculation of a given run. Typically, laser power fluctuated by less than 1 % between measurements. With this, the QUEST threshold estimate (ThreshEst.), so far given in log10 arbitrary AOM drive units, could be converted into a number of photons at the cornea using formula (1):

$$Photons_{Thresh.} = \frac{P_{Max} \cdot Trans_{AOSLO}}{E_{Photon}} \cdot t_{Stim} \cdot 10^{ThreshEst}. \tag{8}$$

with P(Max) being the maximum AOM output power measured, Trans(AOSLO) being the relationship of maximum power fed into the AOSLO and the power detected at the eye's pupil position (determined earlier to be 0.065), and t(Stim) being the stimulus duration during a single presentation (2.45 μsec). E(Photon), the photon's energy, was calculated as:

$$E_{Photon} = \frac{\hbar \cdot c}{\lambda} \tag{9}$$

with $\hbar$, Planck's constant, c, the speed of light, and λ stimulus light wavelength (543 nm).

6.2.7 Modelling of cone light capture and ISETBio

To assess the impact of the exact stimulus location relative to the individual cone mosaic, a custom spatial model of quantal catch in the targeted cones was implemented in Matlab, similar to [Harmening et al. 2014]. First, all stimulation trials were registered to a high-signal-to-noise image of the foveal center used to create the cone density map. Second, cone center locations were used to compute a complete Voronoi tessellation of the mosaic defining the inner segment area of the individual cones. Third, the actual absorption characteristic across this inner segment area was modelled by a two dimensional Gaussian with a sigma value creating an aperture of 0.48 of the equivalent diameter [MacLeod et al. 1992]. The retinal stimulus was a two-dimensional convolution of the initial 7 x 7 AOSLO raster pixel stimulus and a diffraction limited point spread function with a residual defocus of 0.03 D [Meadway and Sincich 2018]. In the final step, the convolved stimulus was multiplied by the cone absorption matrix to arrive at the amount of stimulus light that was absorbed by each cone. The reported value of percent of light per cone is based on the total light distribution given by the convolved stimulus matrix.

But this model lacked a more generalized testing of the impact on thresholds by variations in the OS length or cone density. To test the hypothesis that the cone's biophysical properties such as cone density, cone diameter and cone outer segment length had an impact on sensitivity thresholds, the Image Systems Engineering Toolbox for Biology (ISETBio) for Matlab [Cottaris et al. 2019; Cottaris et al. 2020], was used. This computational-observer model simulates the cone photoreceptor isomerizations and photo currents based on physiological constraints. To set up ISETBio, the following parameters were used: the 'scene' was a 511 x 511 pixel image with the central 7 x 7 pixel containing the stimulus. The field of view was set to 0.85 degree and the background luminance set to 0.1 cd/m^2. The wavefront was set to be diffraction limited, with a varying residual defocus of 0.01, 0.03, and 0.05 diopters and zero LCA. The hexagonal mosaic function was used with a custom cone spacing and optical density. The optical density was calculated as the product of the OS length and an average absorbance of 0.014 μm^{-1} (L-cones = 0.013 ± 0.002 μm^{-1} and M-cones = 0.015 ± 0.004 μm^{-1}, [Bowmaker et al. 1978]). Each condition (varying cone density, optical density and both coupled) was repeated 10 times taking simulated neural noise of the photoreceptor cells into account. To model different stimulus positions relative to the mosaic, the stimulus was shifted in steps of 0.6 arcsec. The test site's cone class composition was controlled by adjusting the L- and M-cone spatial density parameter for each cone class and carefully checking the center surround configuration of the generated mosaic. These two simulations were both run with a residual defocus of 0.03 and repeated 33 times per condition. For Figure 41, the average of these data sets was plotted with the error bars reflecting one standard deviation.

The slopes found by the ISETBio model for each parameter were used to calculate the threshold difference for each of the test site's factors from the respective average value with the following formula:

$$\Delta T_i = \left(X_i - \overline{X}_i\right) \cdot m_i \tag{10}$$

With X_i being the test site's value of the factor i (e.g. OS length), $\overline{X}$ the factor's average (31.4 μm) and m_i the factor specific slope. The sum of all three ΔX_i values yielded the test site's threshold offset from the average threshold. This way it was possible to compare the observed thresholds with an expected threshold based on the models without knowing the intercept of the factor specific function.

6.3 Results

6.3.1 Retinal topography and the PRL

With AOSLO imaging, the foveal mosaics of all four observers could be resolved, and all cone photoreceptors could be identified and marked to create continuous topographical maps of cone density. Participant numbering, P1-P4, was ordered for all following analysis according to their peak cone density values (13733, 15230, 18023, and 18406 cones/degree^2 for P1, P2, P3, and P4 respectively). At the location of the cone density centroid (CDC, see Methods) the density values were slightly lower P1: 13460, P2: 15199, P3: 16956, P4: 16914 cones/deg^2. Cone density dropped rapidly with increasing eccentricity. Across participants, cone density dropped on average to 66 % of the peak cone density at a distance of about 20 arcmin from the CDC. However, there were marked differences in topographical profiles between participants. For instance, P1 had a rather plateau like cone density distribution, while P4 showed a steep decline with a two-pronged cone density profile. The other participants had a similar slope in cone density profiles.

The two-dimensional map of cone outer segment (OS) length as determined by high-resolution OCT imaging was found to show a similar topography as cone density in each eye. P1, the participant with the lowest peak cone density, also had the lowest maximum OS length of 28 μm. For P2, P3, and P4 the maximum OS length was 28, 32, and 40 μm, respectively. The range of OS length was 3 μm (25 to 28 μm) for P1, 4 μm (28 to 32 μm) for P2, 4 μm (29 to 33 μm) for P3, and 7 μm (32 to 40 μm) for P4 within the central 12 arcmin radius around the CDC. The PRL was found to be offset from the CDC and the location of highest OS length in all eyes. It was shifted away from a nasal-inferior quadrant of the retina with respect to the CDC with an average offset of about 3 arcmin. For each participant, the offset, as well as the angle, were different, ranging from 1 arcmin and 15 degree (P1) to 3 arcmin and 178 degree (P4) with a good repeatability of about 1 arcmin (Figure 3A). PRL ellipses were found to be small in all participants (BCEA: P1 = 50; P2 = 67; P3 = 16; P4 = 30 arcmin^2), indicative of high fixation stability, a prerequisite for the following cone-targeted sensitivity testing.

6.3.2 Small spot sensitivity

Small spot sensitivity thresholds across participants were found to lie between 2.97 and 3.67 log10 photons, spanning an overall range of 0.7 log10 photons. The combined median of all thresholds across retinal locations and participants was 3.25 log10 photons at the cornea and the average 3.27 ± 0.16 log10 photons. While the range of thresholds across the four participants was similar (3.04 to 3.59, 2.99 to 3.53, 3.02 to 3.67, and 2.97 to 3.51 log10 photons for P1, P2, P3, and P4 respectively; see Figure 34B), there was a continuous shift of the median, 1st, and 3rd quartile of thresholds from P1 to P4. The median

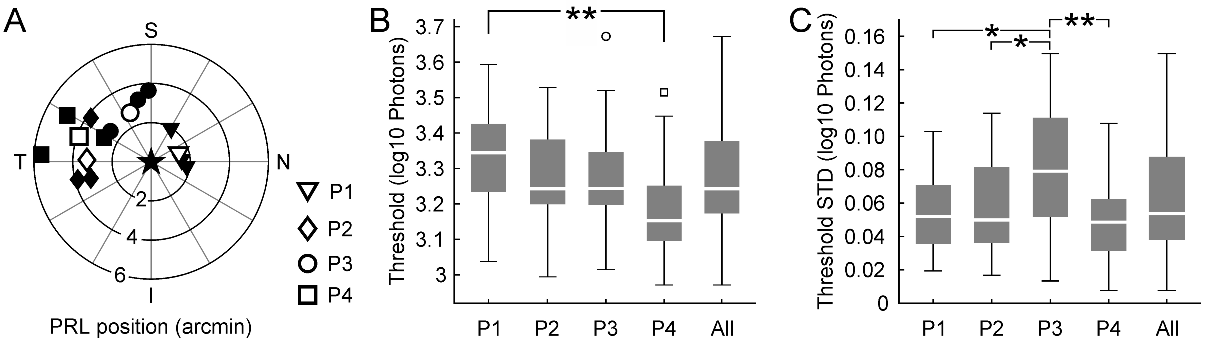

Figure 34: *Fixation behavior and foveal increment sensitivity. A) The PRL of each participant (P1-4) is plotted relative to the location of the cone density centroid (plot origin, 'star' marker). Filled markers represent single measurements, open markers are the final PRL based on three repeat measurements. Letters marking Nasal, Temporal, Inferior, and Superior. B) Pooled sensitivity thresholds across all test sites for each participant separately (P1-P4), and combined ("All"). While the range (~0.5 log10 units, whiskers) was very similar across the four tested participants as well as the highest and lowest threshold, the median, 1st, and 3rd quartile differed. C) The observed standard deviation of repeated threshold estimations at the same test site was similar for three participants. Variability for P3 was higher than for the other three. 85 % of all observed STDs were lower or equaled 0.10 log10 (Photons).*

thresholds shifted by 0.2 log10 photons from 3.35 for P1 towards 3.15 for P4 (3.24 for P2 and P3). For P2 and P3 the 1st and 3rd quartile of thresholds were lower than for P1, but higher than for P4, this difference was not significant (Q1: 3.23, 3.20, 3.20, and 3.10; Q3: 3.43, 3.38, 3.34, and 3.25). The repeatability for each test site, computed across three to five reruns, was high, with an average standard deviation of 0.06 ± 0.03 log10 photons (Figure 34C). The standard deviation across reruns was higher for P3 (average = 0.08 log10 photons) compared to the other three participants (0.05 log10 photons).

6.3.3 Correlation between retinal structure and function

To bring sensitivity thresholds into spatial correspondence with the structural data and fixation behavior, averaged retinal images derived from all four independent analysis steps (cone density maps, OS length map, PRL determination, and microstimulation target sites) were carefully aligned with each other (see Figures 35 and 36), to allow a pointwise and cellular resolved comparison between retinal structure and function.

As a first observation, for none of the participants, the target site with the lowest threshold and therefore highest sensitivity was at the PRL or fell within the fixation ellipse (5.7, 6.5, 6.5, and 6.0 arcmin distance). The average distance between the test site with lowest threshold and highest cone density was 7.3 arcmin. In P1 and P2 the CDC was closer to the target site with the lowest threshold than the PRL (CDC distances: 4.5, 3.3, 7.8, 9.8 arcmin).

The range of cone densities at the test sites differed clearly within and between participants, with a difference from minimum to maximum of 2300 cones/deg^2 (11215 to 13198 cones/deg^2) for P1, 3400 cones/deg^2 (12564 to 14971 cones/deg^2) for P2, 6100 cones/deg^2 (11786 to 17881 cones/deg^2) for P3, and 3800 cones/deg^2 (14364 to 18132 cones/deg^2) for P4. While the highest cone density of P4 was about one third higher than the peak cone density of P1, sensitivity thresholds were similar at those locations. However, a general trend was noticeable that most of the sensitivity thresholds observed in P1 were higher than most of the thresholds of P4.

For further correlation analysis, we used the median threshold of repeated threshold estimations at the same test location. The difference between individual sensitivity thresholds and their median can be seen comparing Figure 37A with 37B. While there was no general significant correlation between the distance from PRL and sensitivity thresholds (Figure 37B), the lowest thresholds were observed at 6 arcmin PRL distance for all participants, and the median threshold at this eccentricity was almost

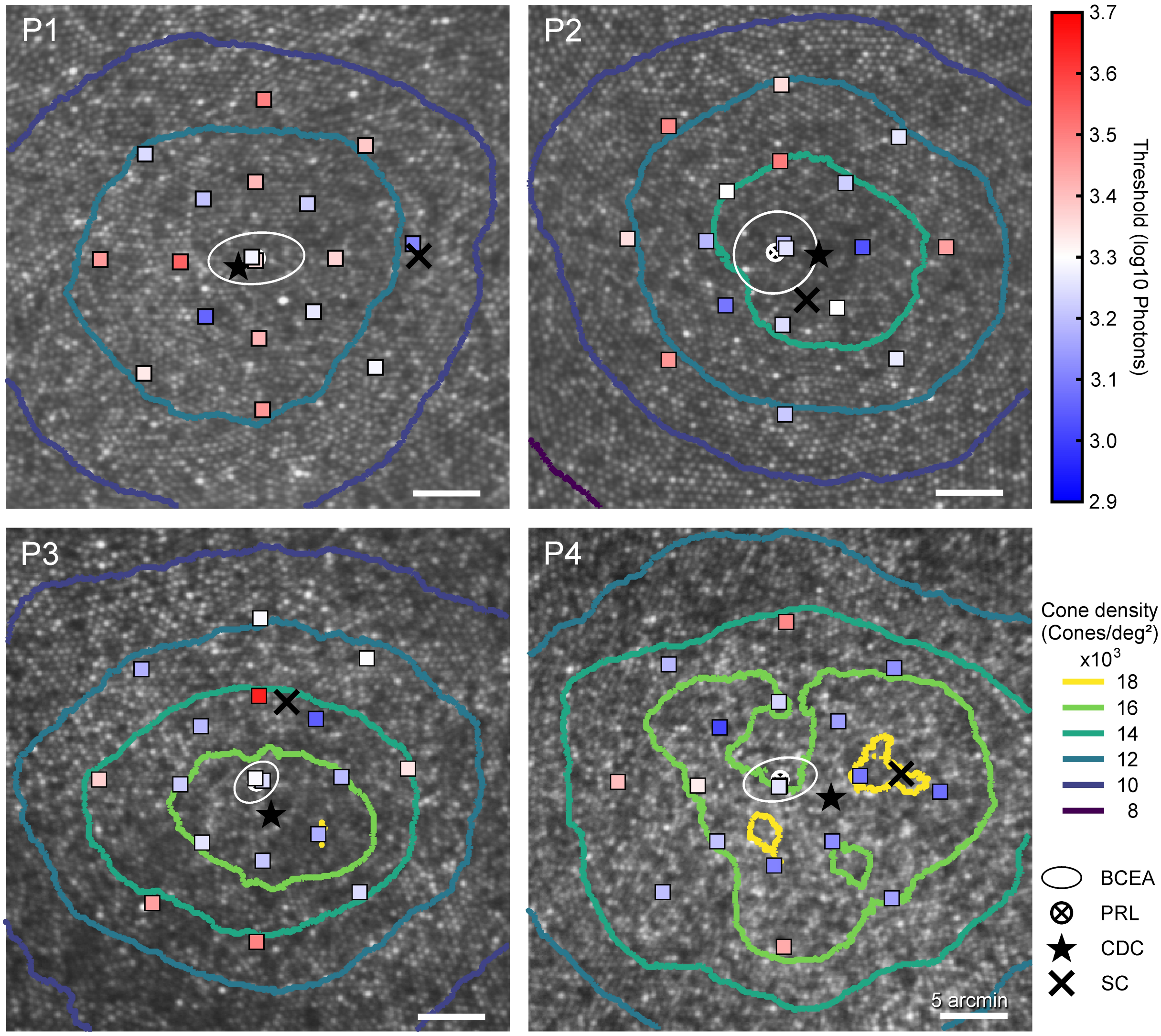

Figure 35: *Sensitivity in relationship to cone topography and fixation behavior in all participants. Squares mark the average stimulus location for each test site, coloring reflects the median sensitivity threshold in log10 photons. Marker area is four times the actual stimulus area on the retina and equals the average 95 % outline of the summed light delivery (see Figure 32C). Cone density is indicated by colored contour lines. The PRL (white circle and crosshair), the location of the cone density centroid (star) and an estimated location of the sensitivity centroid (SC, cross) are shown as well.*

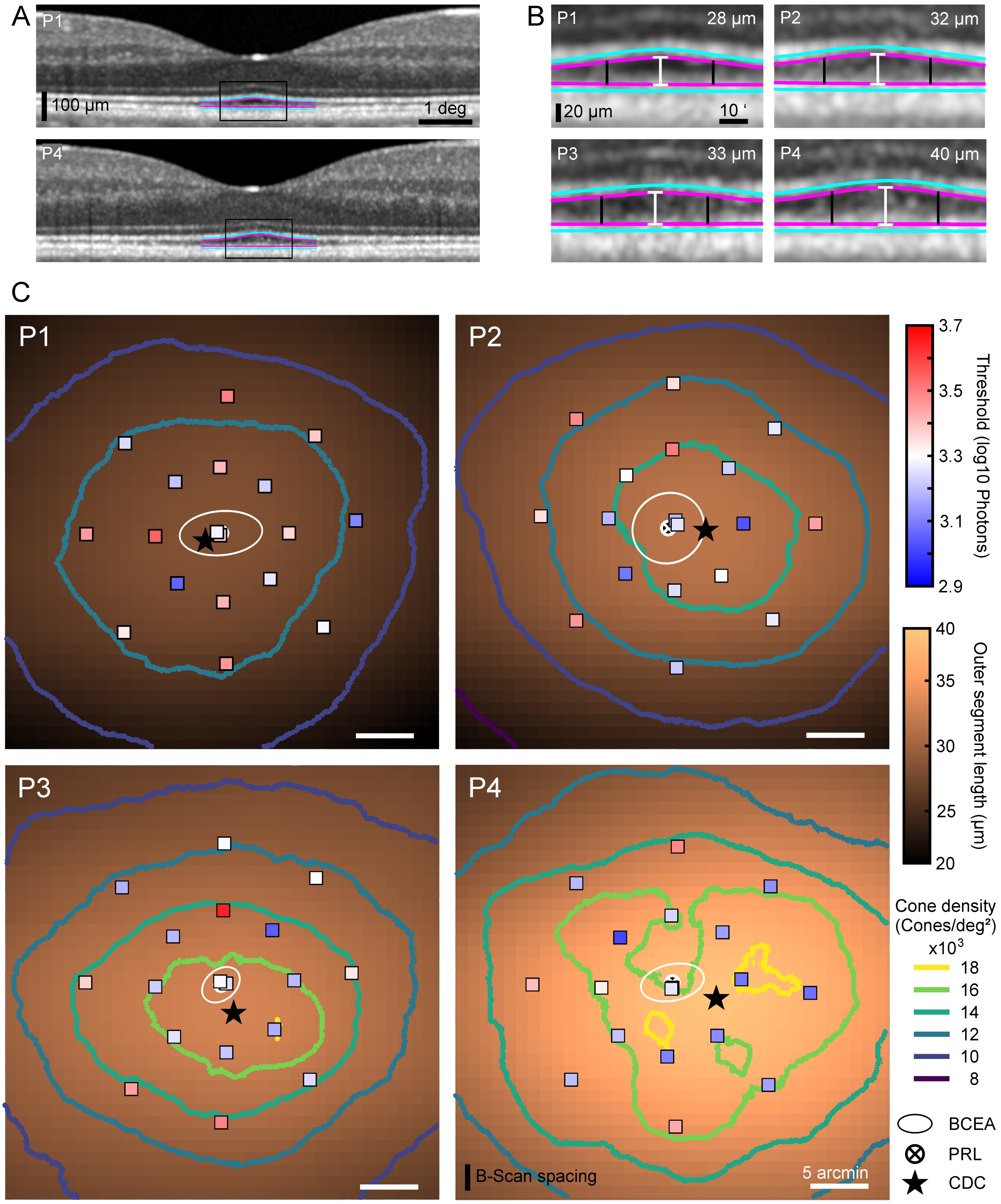

Figure 36: *Cone outer segment length topography. A) Foveal OCT B-scans from P1 and P4, and a zoomed-in view of the OS in the central fovea. B) Further zoomed-in view of central OS and measurement demonstration for all 4 participants. The band's center (cyan line) was semi-automatically marked. The OS start and end (magenta) was found by fitting a 1D Gaussian centered on the 2nd and 3rd band. The estimated maximum OS length is stated in the upper right corner. C) Interpolated 2D map of cone OS length in the central fovea for each participant. The black vertical lines in (B) indicate the region of the 2D presentation in (C).*

identical (P1 and P2) or even lower (P3 and P4) than the median threshold at the PRL. For the 12 arcmin eccentricity, we observed a similar or higher median threshold compared to the median PRL threshold. In P3 we observed an extremely high threshold at one location that was 0.3 log10 photons higher than the second highest threshold.

Plotting the individual thresholds as a function of the test site's cone density revealed a tendency towards lower thresholds for higher cone densities (Figure 37C), with a correlation coefficient of ρ = -0.09 for P1, ρ = -0.49 for P2, ρ = -0.32 for P3 and ρ = -0.52 for P4. The slope showed a tendency to be steeper for higher correlation coefficients: m = -0.02, -0.06, -0.03, and -0.07 log10 photons per 10^3 cones/degree^2 for P1, P2. P3, and P4 respectively).

Correlating thresholds with foveal cone OS length revealed a similar trend: thresholds were generally lower at sites with higher OS length (Figure 37D). Correlation coefficients were ρ = -0.18 for P1, ρ = -0.45 for P2, ρ = -0.31 for P3 and ρ = -0.52 for P4. The slope was almost the same across the four participants (m=-0.03, -0.05, -0.04, and -0.04 log10 photons per micron for P1, P2, P3, and P4 respectively).

When data was pooled across participants, the correlation between the thresholds and the distance from the PRL was given by a slope of 0.65 log10 photons per degree (ρ=0.27, Figure 38A). The observed decrease of thresholds at 6 arcmin distance from the PRL remained in the combined dataset. Thresholds as a function of cone density had a negative slope of -0.04 log10 photons per 10^3 cones/degree^2 (ρ= -0.45, Figure 38B). The correlation between thresholds and OS length indicated an average decrease of thresholds by -0.02 log10 photons per micron in the pooled data set (ρ= -0.43, Figure 38C).

Because the individual factors, distance from PRL, cone density and OS length are all highly significantly correlated with each other ($p < 0.001$, data not shown), a physiological model of cone light capture (ISETBio) was employed to model the impact of two of the three factors independently.

6.3.4 Modelling the impact of cone density, OS length and distance from PRL on sensitivity

The first hypothesis tested with ISETBio modelling was if the highly significant correlation between detection thresholds and cone density could be caused by spatial summation effects. The stimulus used in sensitivity testing was about 1.5 times the average foveal cone diameter (see methods) and therefore the average distance to the surrounding neighbors could have played an important role. Using the cone spacing according to the individual cone densities of our participants, the model showed a correlation of about -0.01 log10 photons per 10^3 cones/degree^2, roughly four times lower than the observation in the behavioral data (Figure 39A).

ISETBio was also used to test the influence of outer segment length and therefore optical density on sensitivity. The outer segment length was estimated for each participant from foveal OCT B-scans (see Figure 36), with a range of 25 μm to 40 μm, and fed into the model. A strong impact of outer segment lengths on thresholds was predicted (ρ = -0.99), with a slope of -0.008 log10 photons per μm OS length (Figure 39B).

In the following step, the slopes derived for 0.03 D residual defocus [Meadway and Sincich 2018] were used to remove the estimated proportional influence of cone density and OS length from the observed thresholds. The corrected thresholds were supposed to vary only due to retinal eccentricity. These thresholds were then used to compute the location of the sensitivity centroid (SC) for each participant (Figure 34) by finding the retinal coordinate yielding the highest value of ρ for corrected thresholds against distance from this coordinate (Figure 39C). The SC was always offset from the PRL (11.7, 3.8, 4.8, and 7.5 arcmin distance) or CDC (13.1, 2.2, 6.8, and 3.7 arcmin distance). When all rescaled thresholds were plotted as a function of distance to the SC, a linear fit with a slope of 0.69 log10 photons per degree eccentricity or 0.012 log10 photons per arcmin (ρ = 0.46) emerged.

Finally, we applied these three slopes to model the expected shift from the average observed threshold, due to the test site's cone density, OS length and SC distance (Figure 40). Because the y-intercept b was unknown, the expected shift was calculated for each of the three factors based on the difference from its average. The estimated thresholds were best fitted by a linear regression with a slope of 1.03 (ρ= 0.38, R^2 = 0.37), confirming that the interaction of cone spacing, OS length and eccentricity yielded

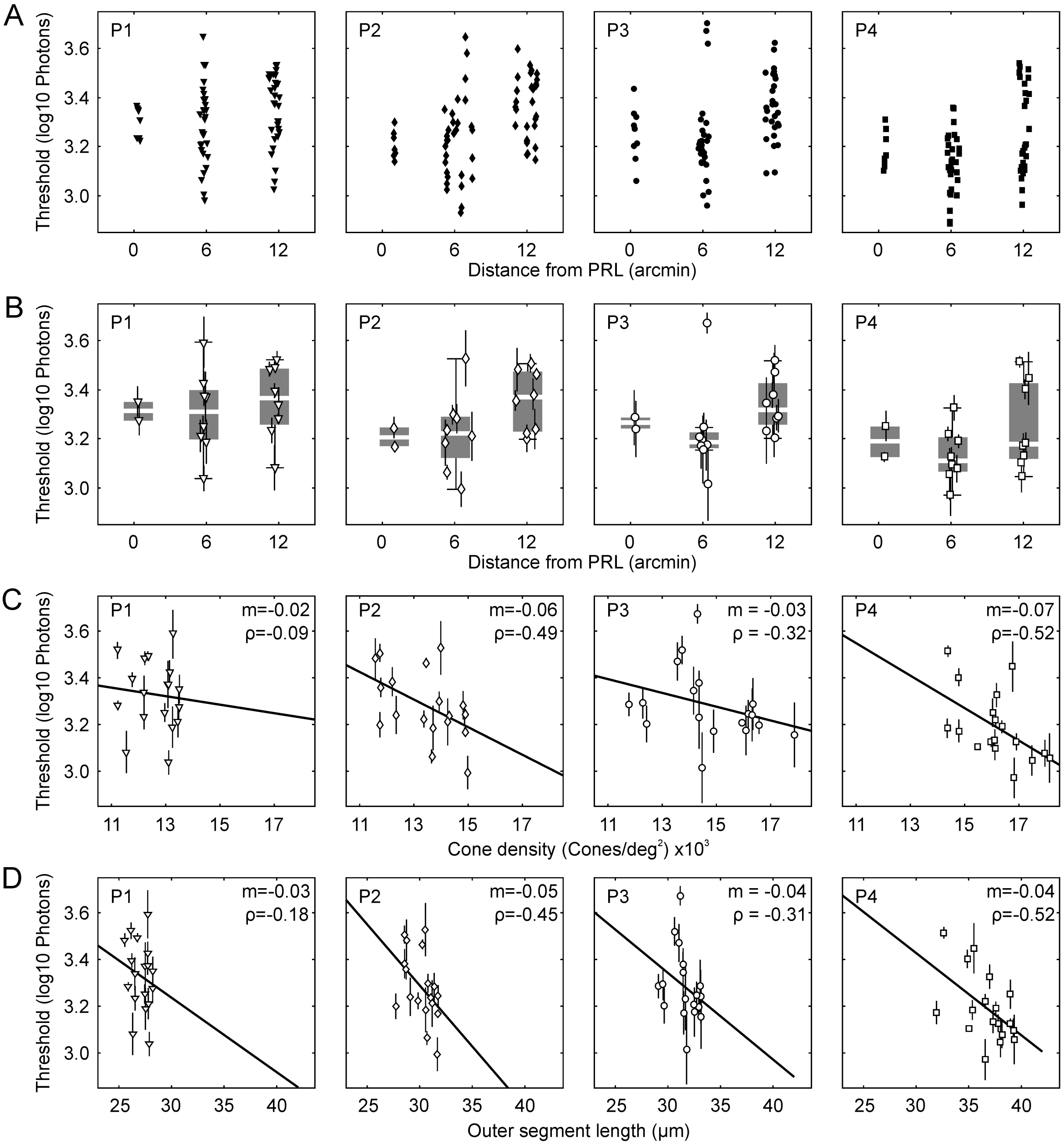

Figure 37: *Sensitivity thresholds for each participant in relation to distance from PRL, cone density and outer segment length. A) Individual thresholds for each test site's distance from the PRL are marked with filled symbols. B) For each test site we used the median threshold (open symbols) of repeated testing (3-5), and reported this value as the test site's sensitivity. Boxplots show median (white line), first and third quartile (box), whiskers extend to 1.5 fold the distance between the first and third quartile. C) Median thresholds in relation to the test site's cone density. D) Median thresholds in relation to the outer segment length at the test site as obtained from the 2-D map shown in Figure 36. Vertical lines in B, C, and D show the standard deviation across repeated runs, thick black lines are linear fits to the data.*

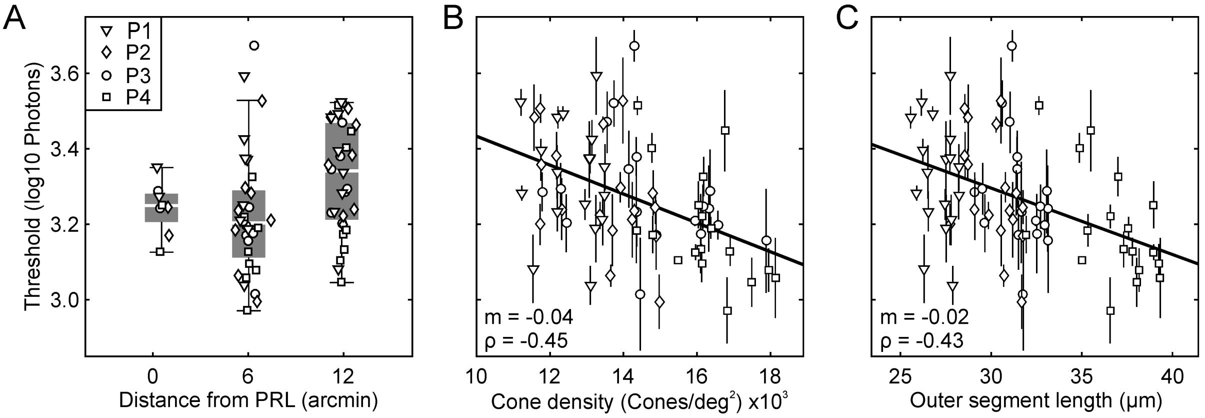

Figure 38: *Pooling threshold data across participants. A) Sensitivity thresholds of all participants as a function of test site distance from PRL, given as median (white line), first and third quartile (box). Whiskers extend to 1.5 fold the distance between the first and third quartile. For the pooled data set, a bend towards lower thresholds at 6 arcmin was observed. B) Thresholds as a function of local cone density at the test site, vertical lines show the standard deviation of threshold estimates for repeated testing. Thresholds and cone densities showed a moderate correlation (ρ = -0.45). C) Thresholds as a function of cone outer segment lengths showing a moderate correlation (ρ = -0.43). All independent variables (Distance, Density, OS length) were pairwise significantly correlated with each other (p < 0.001, data not shown).*

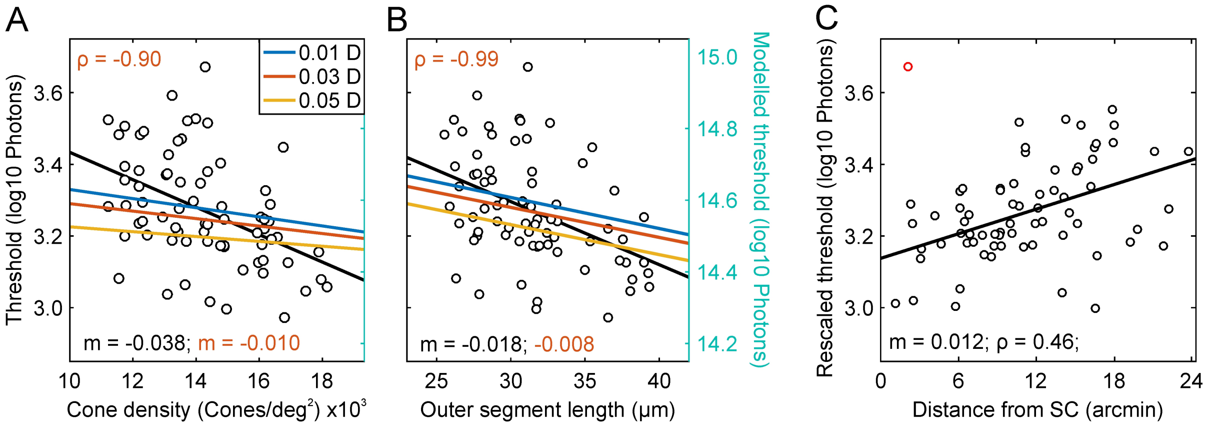

Figure 39: *ISETBio model testing the impact of cone density and outer segment (OS) length. A) The ISETBio model evaluating the threshold photons to elicit a certain number of isomerizations, revealed only a small influence of cone density and therefore spacing on sensitivity thresholds, too small to explain the observations. The curves are fitted for 0.01 D, 0.03 D, and 0.05 D residual defocus. B) Testing the influence of outer segment length and therefore optical density on sensitivity. We fed the observed range of outer segment lengths (25 μm to 40 μm) in our ISETBio model, which predicted a strong impact of different outer segment lengths on thresholds. C) The pooled data of the rescaled thresholds, which had the OS length and density influence removed, against the distance from the participant's sensitivity centroid (see Figure 3). The red marked threshold was ignored in this analysis due to its uncertain nature.*

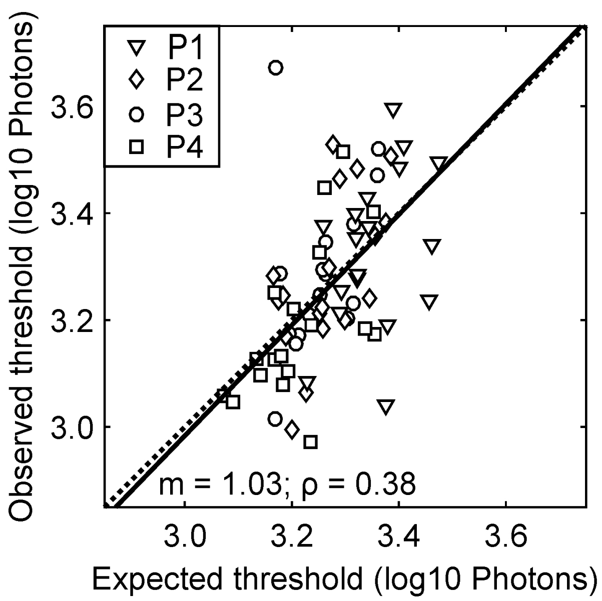

Figure 40: *Predicting sensitivity thresholds from retinal factors. The expected threshold was derived from the test site's cone density, OS length and distance from the sensitivity centroid (Figure 35). Each parameter was converted into a threshold offset from the average. The solid line is the linear fit to the data, the dotted line shows the 1:1 relationship.*

a good predictor for sensitivity thresholds. Given a residual variability of ±0.15 log10 photons from the prediction, we also looked at the variability that is possibly due to the exact stimulus position on the cone mosaic. As our stimulus was roughly 1.5 foveal cone diameters in size, the number of isomerizations elicited could have depended on the stimulus being centered on a single cone or in the middle between three cones.

6.3.5 Modelling the impact of stimulus position and cone class composition

To test the hypothesis that the exact placement of the test stimulus relative to the cone mosaic bears on sensitivity at that site, photon catch of each cone for the average stimulus location during each threshold experiment was modelled. The exact cone locations relative to the stimulus location were determined by registering the experiment's video data with the high signal-to-noise image used for cone annotation. An example of the result of that model is shown in Figure 41A for two different cases. The first case shows two different target sites in the retina of P2. At both target sites, the actual stimulus location on the cone mosaic was similar, but thresholds differed significantly by 0.36 log10 photons (p=0.03, Mann-Whitney U-test, n = 4). In the second example from P4, the stimulus placement differed, the first one was centered on a single cone while the second one was placed in the middle of three cones. For this case we found similar sensitivity thresholds, with a non-significant difference (p=0.49, Mann-Whitney U-test, n = 4). When all thresholds were plotted against light catch in the nearest cone, no significant correlation emerged (Figure 41B). The ISETBio model, creating a generalized perfect hexagonal retinal mosaic, supported this observation, when shifting the stimulus systematically from a cone-centered position to a position in the middle between cones (Figure 41C). For such shifts, the resulting change given by the number of isomerizations was 0.1 in log10 space. There was no difference if the center cone was a L- or M-cone. Such small changes could not explain the observed variability of ±0.3 log10 photons, but could be one reason for the observed intra-run variability of 0.06 log10 photons due to small stimulus displacements caused by residual errors of the real-time stabilization (Figure 32C).

Another reason causing such variability could be the composition of cone classes at the stimulus location. Again, ISETBio modelling showed only minor changes in the sum of isomerization for different cone mosaic compositions (Fig 41D). The maximum difference was 0.02 log10 isomerizations for a

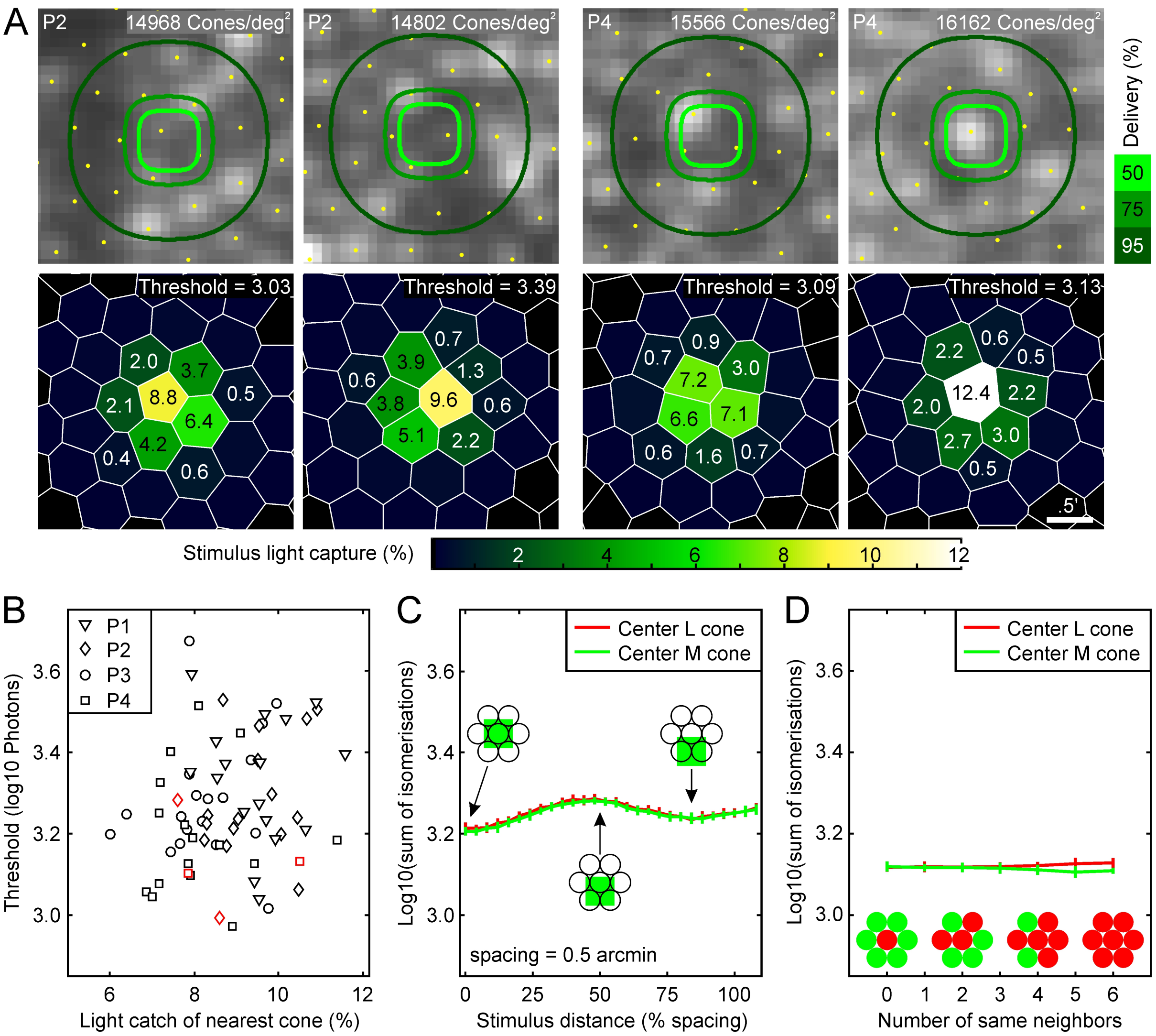

Figure 41: *Possible sources of threshold variability. A) We used the cone maps to model the light catch for each cone at the target site. The left two panels show two different test sites of P2, with a similar light catch situation. The observed thresholds for these test sites differed significantly (p=0.03, Mann-Whitney U-test, n = 4). The right two panels show two different test sites of P4, with different light catch situations. In the first condition three cones are supposed to catch the same number of photons, while in the second condition the major portion of stimulus photons are being caught by a single cone. The observed thresholds for these test sites differ insignificantly (p=0.49, Mann-Whitney U-test, n = 4). B) Pooling the data across all participants. Small light catch numbers indicate a 3-cone position, high numbers a single cone center position. Example data sets shown in A were highlighted with a red marker outline. There was no significant correlation between observed thresholds and stimulus delivery condition. C) This observation was confirmed by an ISETBio model testing the influence of stimulus position on the number of isomerizations. The model showed a maximum change of 0.1 log10 isomerizations for different stimulus positions. D) ISETBio model to test the influence of different cone class compositions at the test site. This model does not contain any inter cone class inhibition and therefore shows only a slight increase of isomerizations if solely L-cones were activated. The error bars in C and D indicate the ISETBio simulated retinal noise.*

stimulus location consisting of only L-cones versus only M-cones. As the actual composition of the cone mosaic in our four participants was unknown, this model did not contain any specific L-M-cone interactions and only used the cone class specific spectral sensitivity.

6.4 Discussion

The human fovea is the result of morphologic specializations culminating in tight photoreceptor packing and elongation of the photopigment containing OS. Eye movements constantly align fixated objects of interest to a distinct group of cones in the fovea, the PRL. The PRL and the retinal location where anatomical features peak are known to be offset from each other. By using an AOSLO as high-resolution imaging and microstimulation platform, the functional profile of the foveola was further investigated. In four observers, increment sensitivity thresholds at a number of target sites around the PRL were correlated with retinal factors such as cone density, photoreceptor OS length, and the distance from the PRL. Generally a plateau-like sensitivity profile was found within the central 6-arcmin radius around the PRL with a declined sensitivity at about 12 arcmin eccentricity, resulting in a much flatter slope than the anatomical topography of cone density and OS length changes in the same region. However, about 37 % of the variability in thresholds could be explained by a combined model of the impact of cone density, OS length and distance from the PRL on thresholds, indicating that the exact makeup of the foveal cone mosaic and fixation behavior are indeed factors of visual function at cellular scale.

The average threshold for detecting a cone-sized visual stimulus against a dim red background (5 cd/m^2 at 840 nm) was 3.27 ± 0.16 log10 photons at the cornea (Figure 35). While rods enable the detection of individual photons [Sakitt 1972; Tinsley et al. 2016], the absolute detection threshold at the fovea, and therefore based on cone vision only, was reported to be about 2.8 log10 photons [Marriott 1963; Geisler and Davila 1985] or 2.3 log10 photons [Koenig and Hofer 2011]. Because the here reported thresholds are increments against the IR scanning background, the cones are adapted to the background resulting in elevated thresholds. The best comparison is given by a previous AOSLO microstimulation study on the foveal cone summation area, reporting an average increment threshold of 4.4 log10 photons [Tuten et al. 2018]. Because they used a 795 nm wavelength background, their increment thresholds are more elevated. Based on Lamb's equation [Lamb 1995] in combination with the cone's specific spectral absorbance [Schnapf et al. 1987] the sensitivity difference between 840 nm and 795 nm is about 1.1 log10 units, which is very close to the observed difference of the here reported thresholds compared to Tuten et al. 2018.

6.4.1 The factor "Distance from PRL"

Early studies investigating fixational eye movements reported an "optimal locus", a small group of cones that is mainly used to resolve any object of interest [Barlow 1952; Cornsweet 1956; Steinman 1965]. It was assumed that this retinal location colocalizes with the location of peak cone density. Scanning laser ophthalmoscopy enabled a direct study of the retinal locus used, for example during reading [Mainster et al. 1982]. In combination with adaptive optics, it was observed that this optimal locus - now termed "preferred retinal locus", PRL - was displaced from the location of peak cone density [Putnam et al. 2005]. Continuing investigation of the PRL showed that it furthermore did not colocalize with the bottom of the foveal pit or the center of the foveal avascular zone [Bedell 1980; Zeffren et al. 1990; Wilk et al. 2017b].

In clinical research, the term PRL refers to a newly formed stable location on the retina used for fixation [Crossland 2011], due to a central scotoma [Noorden and Mackensen 1962; Timberlake et al. 1986; Timberlake et al. 1987; Whittaker et al. 1988] caused by macular diseases [Crossland et al. 2005], such as age-related macular degeneration [Rees et al. 2005]. As well as for healthy eyes, the underlying processes of PRL formation are yet unknown and the newly formed PRL is usually a suboptimal retinal location, given the fact that other intact locations of the retina would have provided better acuity [Bernard and Chung 2018] or higher contrast sensitivity [Rees et al. 2005].

One of the hypotheses assessed here, was that visual sensitivity contributes to the formation of the

PRL. The overall observed fixation stability, given by the BCEA, ranged between 16 arcmin^2 and 67 arcmin^2 in our study. This is smaller than previously reported BCEA values between 110 arcmin^2 and 630 arcmin^2 measured with SLO [Crossland and Rubin 2002], presumably due to the increased measurement accuracy with an AOSLO.

We found that, in all eyes, the location of the individual best sensitivity did not coincide with the PRL. Additionally, for two participants (P3 and P4) a drop of the sensitivity at the 6 arcmin eccentricity locations was observed, while P1 and P2 showed similar median thresholds for the PRL location and at the 6 arcmin locations.

In all eyes, the location of the individual best sensitivity, as well as the empirically determined SC was offset from the PRL (Figure 34 and 36). However, the distance between the PRL and the SC was small, about 7 arcmin on average, and given the observation that thresholds at the PRL and the 6 arcmin eccentricity were similar, it is likely that during natural viewing and the typical blur induced by the eye's optics, the visual system is insensitive to such subtle offsets, leading to a PRL formation as close as possible to the location with the highest cone density [Putnam et al. 2005], or at a location favoring binocular fixation [Reiniger et al. 2021].

6.4.2 The factor "Cone density"

There was a moderate correlation between sensitivity thresholds and cone densities at the tested retinal locations within the fovea. Recent research on light propagation in cone photoreceptors would predict a similar outcome, but more clinically oriented small spot sensitivity testing comes to different conclusions. Modelling light propagation in cone inner and outer segments revealed that a smaller cone aperture is beneficial for increased quantum catch due to the cone's waveguiding properties (Meadway and Sincich, 2018). Thus, if everything else was held equal, a more densely packed cone mosaic would result in smaller foveal cones and therefore increased sensitivity. In our experiments, the diffraction limited stimulus diameter (0.8 arcmin FWHM) was larger than the individual foveal cone aperture (about 0.5 arcmin), favoring additional summation effects between cones straddling the incident light patch.

In general, spatial summation is closely related to the field size of parasol ganglion cells [Volbrecht et al. 2000]. Only within the foveola, spatial summation was found to be smaller than the field size of parasol ganglion cells, but still larger than the field size of midget ganglion cells, with a diameter of Ricco's area of 2.5 arcmin [Tuten et al. 2018]. While the private line forming midget ganglion cells [Polyak 1941; Boycott and Dowling 1969] show a relatively stable dendritic field size up to an eccentricity of 4 degrees [Dacey 1993], the dendritic field size of parasol ganglion cells enlarges rapidly, especially within the 5 degree eccentricity diameter[Dacey and Petersen 1992]. Because the detection of small dim stimuli seemed to rely on parasol ganglion cells, showing a steep increase of summation based on their dendritic field size and the cone's inner diameter [Curcio et al. 1990; Scoles et al. 2014], and the improved light absorption of smaller cones, a sharp peak of sensitivity within the foveola, centered on the cone density distribution should be expected.

Early light sensitivity testing in a perimetry apparatus revealed such a light sensitivity peak for cone vision at the foveola [Sloan 1939; Sloan 1950], even with a coarse testing method, with no tracking of the retinal locus and a stimulus about 1 degree in diameter. Using a smaller stimulus (10 arcmin) and testing with 0.25 degree spacing between test sites, Stiles observed a more distinct sensitivity peak within the central 1 degree radius with a slope of 2.5 dB/degree, surrounded by a plateau [Stiles 1949]. Further testing with clinical perimetry or fundus-controlled perimetry (so-called microperimetry) devices showed that the foveal sensitivity peak sharpens when stimulus size is further reduced to 6 arcmin (Goldman I size), demonstrating that sensitivity testing is prone to summation [Johnson et al. 1981; Khuu and Kalloniatis 2015; Choi et al. 2016]. Clinicians typically use a Goldmann III stimulus (24 arcmin diameter), which activates about 2500 central cones and was shown to be unable to pick up the steep foveolar sensitivity peak [Choi et al. 2016]. However, recent microperimetry studies using a Goldman I stimulus reported a slope of about 1.4 dB/degree [Tuten et al. 2012; Khuu and Kalloniatis 2015; Choi et al. 2016]. In this study, the stimulus was much smaller than Ricco's area of the foveola. Thus, an even steeper slope due to the rapid increase of cone and parasol field size would have been expected. Indeed, a 5 times steeper slope of about 7 dB/degree within the central 0.2 degree was observed, but with a sensitivity plateau for the central 0.1 degree radius.

An ISETBio model simulating cone activation with different cone spacings was applied to assess the effect of spatial summation. This model predicted a small influence of spacing on sensitivity thresholds due to the size of our stimulus, but did not include any effects due to different light propagation in differently sized cones as proposed by Meadway and Sincich 2018 or increased summation due to an increased ganglion field size.

Furthermore, we found a correlation for the median foveal sensitivity threshold and the participant's peak cone density. Using a clinical Humphrey field perimeter to assess sensitivity lacking fundus controlled delivery, no correlation between foveolar sensitivity and the minimum cone spacing and therefore maximum cone density with sensitivity in healthy participants was found [Foote et al. 2018; Bensinger et al. 2019]. However, assessing sensitivity with a commercial microperimetry system, a significant correlation of sensitivity and density was observed across the central ± 5 degree eccentricity [Agarwal et al. 2015; Supriya et al. 2015; Foote et al. 2019].

6.4.3 The factor "Outer segment length"

Another factor influencing light sensitivity is the cone OS. Because the photopigment is stored in the OS, its length is directly linked with optical density [Bowmaker et al. 1978; Baylor et al. 1979], and therefore associated with the isomerizations and biochemical transduction cascade. The estimation of the foveal cone's OS length from a clinical grade OCT device is still part of an ongoing discussion. At first it was reported, that the functional OS is to be found in between the 2nd and 3rd band, since the 2nd band was not the IS/OS junction but the ellipsoid zone of the IS (see also [Lu et al. 2012]) and the 3rd band was not the OS tip, but the contact cylinder [Spaide and Curcio 2011].

Contradicting these findings it was demonstrated with an AO-OCT that the origin of these two bands are more likely to be the IS/OS junction and OS tips [Jonnal et al. 2014; Jonnal et al. 2017]. Their theory is supported by a computational model simulating the light reflectivity of cones [Meadway and Sincich 2019]. But, there are still uncertainties (see Jonnal et al. 2015; Spaide 2015), since band 2 and band 3 look very different in AO-OCT and conventional OCT. It was later stated that the thickness of band 3 may be overestimated in a conventional OCT resulting in an overestimation of OS length [Jonnal et al. 2017]. Recent findings support the initial report that in conventional OCT band 2 origins from the IS ellipsoids and band 3 from the phagosome zone [Cuenca et al. 2018; Cuenca et al. 2020; Xie et al. 2018]. That is why I here decided to follow the findings reported in Spaide and Curcio 2011.

Applying these approaches to our OS length estimation we found maximum OS lengths between 28 and 40 μm, which is much smaller compared to other OS length reports for healthy participants from conventional OCT (~41 μm (N = 43) [Srinivasan et al. 2008]; ~47 μm (N = 23) [Wilk et al. 2017b]; ~52 μm (N = 97) [Maden et al. 2017]; average values), but closer to histological reports (35 μm [Polyak 1941]; >45 μm [Yamada 1969]; 30 μm [Hoang et al. 2002]).

The shortening of the cone OS is accompanied with a decrease of photopigment density over eccentricity [Elsner et al. 1993]. In accordance we found that thresholds were well correlated with foveal cone OS length, which was recently observed by Foote et al. 2019, too, but not by Bensinger et al. 2019. Studies examining this relationship of OS length and sensitivity in diseased eyes (Age-related Macular degeneration [Acton et al. 2012; Wu et al. 2014]; Glaucoma [Asaoka et al. 2017]; retinitis pigmentosa (but IS/OS length) [Mitamura et al. 2009], reported a significant correlation, too.

The ISETBio model confirmed this relationship, based on the assumption that the amount of photopigment per cone is relatively constant [Marcos et al. 1997]. Thus, with increasing cone diameter and decreasing outer segment length over eccentricity the resulting optical density decreases.

For the four participants tested herein, we furthermore observed a direct coupling of maximum OS length and the average or peak cone density. Recent publications presented varying results about a correlation of foveal cone density and OS length: While some publications reported a significant correlation for healthy participants [Wilk et al. 2017b; Bensinger et al. 2019; Foote et al. 2019], others found no correlation between maximum cone density and OS lengths [Foote et al. 2018; Allphin et al. 2020].

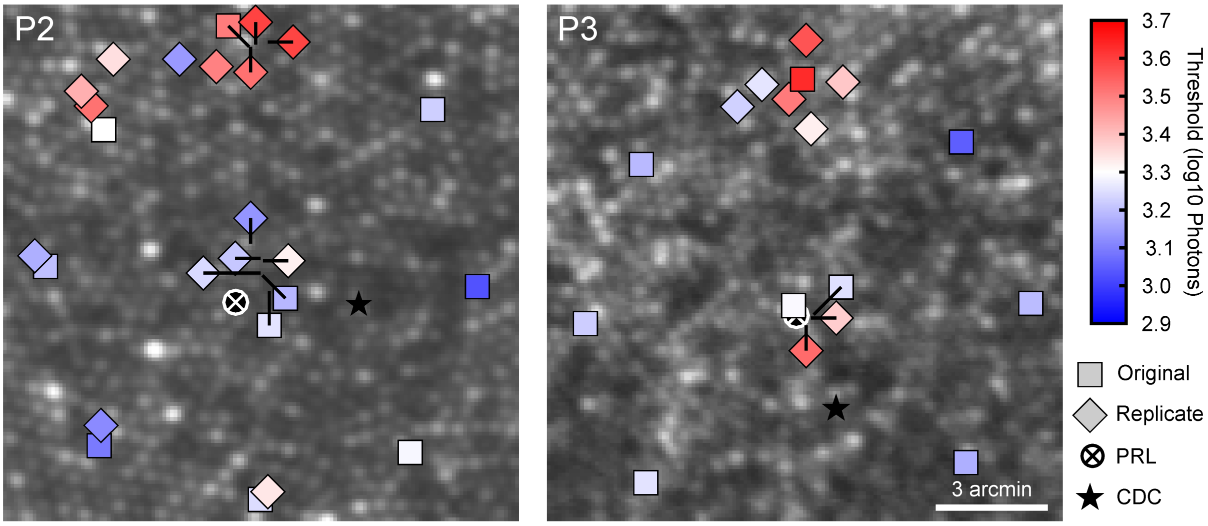

Figure 42: *Replicate testing of test sites with conspicuous high thresholds. Squares mark the formerly shown original test sites (Figure 35), while diamonds mark additionally collected data. The markers match the nominal size of the stimulus. To reduce overlapping, markers were shifted and the tip of a black line indicates the center of the retinal location. For P2 the replicate data points were collected 2 days earlier during a piloting experiment. In P3, the additional locations were tested on the same day, due to the suspiciously high threshold. The PRL is marked with the white circle and crosshair, the cone density centroid by a black star.*

6.4.4 Variability of threshold estimates

Taking all these observations together, we developed a model which predicted the shift of a threshold from the average threshold based on the test site's spacing, OS length and distance from the SC. This model confirmed that all these three factors are important considering sensitivity within the same retina and across different participants. However, this model showed a residual variability of ±0.2 log photons for the expected thresholds which could also not be explained by our ISETBio model for different cone activation patterns or cone classes spectral sensitivity. Also, this variability was more than three times higher than the average variability given by the standard deviation of 0.06 log10 photons we observed during repeated testing (Figure 34C). For further investigation of this phenomenon, we analyzed replicate testings from a piloting experiment in P2 and extended stimulation of the surrounding retinal area of a cone with conspicuous high thresholds in P3 (Figure 42). Based on the intra run variability (STD = ± 0.1 log10 photons), threshold differences up to 0.2 log10 photons are not significant. Here, we observed a maximum threshold difference of 0.4 log10 photons between test sites spaced only 1 arcmin apart. These additional data points reveal a very strong dependency between retinal location and small spot sensitivity, presumably caused by different weighting of individual cones. Furthermore, the replicate testing in P2 from another day confirmed that these fluctuations in sensitivity are not only on a small local scale, but also stable for a few days and can be assessed repeatable via AOSLO microstimulation.

This finding of distinct threshold variations between neighboring test sites is consistent with recent work by [Sincich et al. 2016]: Using a cone sized stimulus, thresholds changed up to 100 % between neighboring cones (about 0.3 log units). The author's conclusion was that such unexpected observations might be caused by the individual weighting of each cone.

One possible source of variability could be minimal variations of the photopigment in the individual cones from the same retina [Schnapf et al. 1987; Schnapf et al. 1990]. But this alone cannot explain such high differences between neighboring cones. A more likely explanation could be given by the observation that the individual cone input to ganglion cells varies, due to functional weighting [Chichilnisky and Baylor 1999; Field et al. 2010; Li et al. 2014]. Such functional weighting could happen at the cone-bipolar- or bipolar-ganglion-synapse. So far, in vitro studies reported linear and non-linear interaction between cones due to subunits within receptive fields of a ganglion cell [Freeman et al. 2015]. Such subunits in the ganglion cell's field were reported to align directly with the bipolar cells [Liu et al. 2017].

A recent study using AOSLO-based microstimulation found that the actual test site's cone class composition has a significant influence on sensitivity thresholds [Tuten et al. 2017]. The authors reported threshold changes of up to 100 % between test sites with the same cone class composition and the target cone in a surround of a different cone class. They ruled out a simple coupling mechanism through gap junctions [Hsu et al. 2000] and propose a key role of H1 and H2 horizontal cells, mediating an elevated activation level of L-cones due to the 840 nm imaging background thereby inhibiting weak M-cone responses to the stimulus connected to the same horizontal cell [Thoreson and Mangel 2012]. Furthermore, they showed that neighboring S-cones had a suppressing effect on thresholds. The influence of S-cones on this retinal level of modulation during our experiment in the central fovea has to be considered for the following reasons: firstly, histology showed that scattered S-cones can be found within the central 0.15 degrees [Curcio et al. 1991; Bumsted and Hendrickson 1999], and for individual cases even within the foveola [Ahnelt 1998]. Secondly, our pulsed light source (pulse durations of about 25 psec and a frequency of 100 Mhz) could give rise to activate S-cones via a two photon effect [Palczewska et al. 2014]. In the unlikely event of a stimulus being placed centered on an S-cone, the expected threshold would have been elevated by 0.3 log10 photons, based on our stimulation simulation shown in Figure 41A. Therefore, the conspicuously high threshold found in P3 could be due to an S-cone situated at that location.

On the other hand, sensitivity to small spots could be modulated during post receptor processing in the lateral geniculate nucleus [Jiang et al. 2015; Alitto et al. 2019] or at later cortical stages such as V1 [Gandhi et al. 1999; Smith et al. 2006]. The observed high variability between individual test sites might be also an explanation for the reported increase of rerun variability for smaller stimuli (Goldmann V versus Goldmann I) during perimetry, lacking the possibility to stabilize the stimulus on a certain retinal location [Gilpin et al. 1990; Vislisel et al. 2011].

6.4.5 Estimation of the number of isomerizations at threshold

Given the overall transmission for 543 nm light through the ocular media is 41 % [Boettner and Wolter 1962], the average threshold was 2.9 log10 photons at the cone inner segments. The two-dimensional model of cone capture showed that the central cones at the target site catch between 55 photons (7 % of the stimulus light on the retina) and 95 photons (12 %). With an optical density of about 0.5 [Bowmaker and Dartnall 1980] this corresponds to 27 or 45 isomerizations in either L- or M-cones. The 840 imaging light had a radiant power of about 14.8 log10 photons per second at the cornea (170 μW). With an overall ocular transmission factor of 0.55 [840 nm; [Boettner and Wolter 1962]] and a field size of 0.85 degree, the estimated photon rate at an individual inner segment was 10.7 log10 photons per second. If a fraction of 33 % was transferred into the outer segments, due to a Gaussian absorption model [MacLeod et al. 1992] and assuming a cone integration time (cit) of 100 msec [Sperling and Jolliffe 1965; Krauskopf and Mollon 1971], we yield roughly 250 R*/cit per L-cone and 22 R*/cit per M-cone. Therefore, increment thresholds found here followed Weber's law [Reeves et al. 1998] comparing the L-cones isomerizations, but not for M-cones. In other words, we would have expected thresholds to vary by about 1 log unit comparing the isomerizations due to the background, but this was not the case. An explanation could be that even in the central fovea, sensitivity is not transmitted in a 1:1 circuitry but spatially summed across several cones and processed by parasol ganglion cells of the magnocellular pathway [Tuten et al. 2018].

7 Discussion

With a multi-wavelength adaptive optics scanning laser ophthalmoscope (AOSLO) it is nowadays possible to image and stimulate the human photoreceptor cells *in vivo*. By probing the individual cone cells researchers are able to study the relationship between structure and function of the central nervous system in the living tissue. To date, such experiments are conducted outside the foveola at about 1.5 degree. However, the foveola as the very center (± 0.6 degree) of the retina is a highly specialized area with the highest density of photoreceptor cells. Additionally, this area is characterized by an elongation of the cone outer segments, a displacement of the bipolar and ganglion cells as well as the absence of retinal blood vessels. It is the area of the retina that is steered via (micro-)saccades to any object of interest in order to obtain the best image available. Thus, the overall motive of this thesis was the extension of AOSLO based microstimulation towards the foveola.

7.1 AOSLO microstimulation

The first aim of my doctoral thesis was to assess the AOSLO's display characteristics and its suitability for visual psychophysics on a single cell level in the foveola. The first improvement was the elimination of the stimulus light background caused by the AOM's light leakage. This was achieved by cascading two AOM's, thereby increasing the stimulus contrast by 4 log10 units to an effective test range of 6 log10 units. The thresholds are still incremental because they are tested against the remaining background of the infrared (IR) imaging light. To test absolute thresholds the imaging wavelength could be increased to about 1100 nm which would have a similar transmittance as the 543 nm stimulus light [Boettner and Wolter 1962; Boettner 1967]. Additionally, the visibility would be greatly reduced by 5 log10 units compared to 840 nm light based on the photopigment's absorption probability ([Dartnall et al. 1983] in combination with Lamb's photopigment template [Lamb 1995]).

The image based method introduced by Harmening et al. 2012 allows for an objective correction of transversal chromatic aberrations (TCA) in an AOSLO. This technique is mandatory for probing individual photoreceptor cells with a dedicated light channel differing in wavelength from the imaging light. So far, it was common to measure TCO (TCA + system offsets) ahead of an experiment and afterwards, assuming that the TCO would be stable during the experiment (see chapter 5). However, this approach is insufficient for foveolar microstimulation due to the small size of the target cone and thus a high susceptibility to positional errors. With our purkinje-based TCO compensation method, we enabled the ongoing monitoring of TCO with an accuracy of less than 0.1 arcmin. The resulting stimulus delivery is sufficiently precise to target the smallest cones in the foveola (aperture 0.25 armcin) or rods.

A simulation of the stimulus delivery revealed that the stimulus size is limited by the physical laws as the point spread function is larger than the smallest stimulus possible. Currently, the residual defocus is unknown and can only be estimated. Meadway and Sincich 2018 proposed a residual defocus of 0.026 D for their AOSLO system. The simulation showed that a residual defocus of 0.01 D would be necessary in combination with a single pixel stimulus to stimulate an isolated cone photoreceptor cell of the foveola. Such small residual defocus seems impossible to achieve due to ongoing rapid changes for example of the tear film or the orientation of the human eye's optics caused by fixational eye motion and microscopic head displacements.

A recent study tested the minimum area of spatial summation and found that Ricco's area at the preferred retinal locus of fixation spanned 2.4 arcmin in diameter, summing the signal of about 24 cones [Tuten et al. 2018]. Therefore, it is not necessary to limit the stimulus size to an individual cone when testing sensitivity. Knowing this finding, we increased the stimulus size to test sensitivity across the foveola. In the beginning a 3x3 pixel stimulus was used (about 0.7 arcmin on the retina, see Figure 18), which was then changed to 7x7 pixel (about 0.9 arcmin), because it falls safely within Ricco's area of complete summation and at the same time is more robust for presentation.

Of course, to test cone-cone-interactions the stimulus size has to be sufficiently small to drive individual cones independently. Thus, AO correction and stimulus delivery have to run perfectly to guarantee stimulation of an individual cone in the foveola. Another approach could be the application of two-photon microperimetry [Ruminski et al. 2019; Łabuz et al. 2020; Marzejon et al. 2021]. The overall principle of this technique is, that the energy of two IR photons (e.g. 1080 nm) sums up during simultaneous absorption of the photopigment, equalling the energy of one photon of half the wavelength (e.g. 540 nm) [Dmitriev et al. 1979; Palczewska et al. 2014]. To achieve a high probability for simultaneous absorption, photons have to accumulate in a very short period of time (laser pulse duration and pulse frequency) as well as in a very small location. Accordingly, the probability of two photon events will be highest in the center of the stimulus light distribution with very steep shoulders following a squared relationship between probability and the number of photons [Schwarz et al. 2018].

7.2 Rod psychophysics

The successful elimination of the stimulus light background and extension of the available test range due to cascading of two AOMs theoretically enables probing of individual rod photoreceptor cells. Expanding the capabilities of AOSLO microstimulation towards rod psychophysics would be of interest for basic research as well as in clinical research. Basic research could assess the rod-cone interactions during mesopic light conditions on an individual cell level *in vivo*, providing psychophysical data to the great number of electrophysiogical observations [Grimes et al. 2018]. For clinical research such psychphysical probing of individual rods could lead to a better understanding of several eye diseases which effect the rods such as age-related macular degeneration [Curcio et al. 1996; Owsley et al. 2000; Jackson et al. 2002; Steinberg et al. 2015], retinitis pigmentosa [Arden et al. 1983], cone-rod dystrophies [Lorenz et al. 2000], or macular telangiectasia [Schmitz-Valckenberg et al. 2009], eventually revealing sensitive precursors helping to prevent loss of vision at a very early stage.

We conducted a few piloting experiments, aiming to pick up threshold differences between individual cones and rods after 45 minutes of dark adaptation. Test sites were chosen at about 7 degree eccentricity to ensure optimal scotopic sensitivity [Tornow and Stilling 1998]. However, we did not find a significant threshold difference between rod and cone target sites (See Figure 43A). The maximum sensitivity difference between cones and rods for a 543 nm stimulus in the dark adapted retina was expected to be about 2 log units [Wald 1945].

There are several possible reasons that may have played a role in impeding a successful outcome. Firstly, due to summation across at least several thousand rods [Schefrin et al. 1998; Taylor and Smith 2004] it is not possible to perceive the activation of an individual rod photoreceptor. Yet, it is possible to see a night sky's star with an airy disk diameter of 0.8 arcmin on the retina in the periphery, which cannot be seen with the fovea consisting of cones only [Lodriguss 2014; Hood and Finkelstein 1986; Field et al. 2005]. Secondly, rods and cones interact at various sites with each other (electric coupling [Nelson 1977; Schneeweis and Schnapf 1995], horizontal cells [Kolb and Famiglietti 1974; Boycott et al. 1987], scattered bipolar cells [Tsukamoto and Omi 2014; Tsukamoto and Omi 2016], and amacrine cells [Nelson and Kolb 1984; Völgyi et al. 2004]), ultimately sharing the same ganglion cells [Enroth-Cugell et al. 1977; Rodieck and Rushton 1976] (see Figure 43B). At mesopic light conditions, rod mediated signals will be increasingly inhibited based on the current level of cone activation [Makous and Boothe 1974; Yang and Wu 1989; Keizaj 2000; McLaughlin et al. 2020]. The IR imaging light background has a luminance of about 5 cd/m^2, which falls in the transition zone between mesopic and photopic light condition (see Figure 4A). Additionally, psychophysical testing of increment thresholds showed, that rod thresholds are more effected by small cone backgrounds (< 1 degree) than large backgrounds (> 5 degree) and more by long- than short wavelengths [Frumkes and Temme 1977; Latch and Lennie 1977; Sharpe et al. 1989]. Thirdly, our supercontinuum laser is a pulsed light source with a pulse duration of about 20 psec and a frequency of 100 MHz while the AOs focus the light in a nearly diffraction limited airy disk, thereby creating optimal conditions for two photons events. We estimated the rate of two-photon events to be about 1:1000 in our setup (personal communications with Christina Schwarz). Following this, the IR imaging field would create an additional blue background with a luminance of 0.7 cd/m^2, which falls in the range of rod saturation. An estimation of the amount of isomerizations per rod yielded a number of about 20 R*/sec due to the 840 nm light and 10^5 R*/sec due to two-photon events. Hence, the rods would be completely saturated, as they are supposed to enter saturation at about 10^4 R*/sec [Tamura

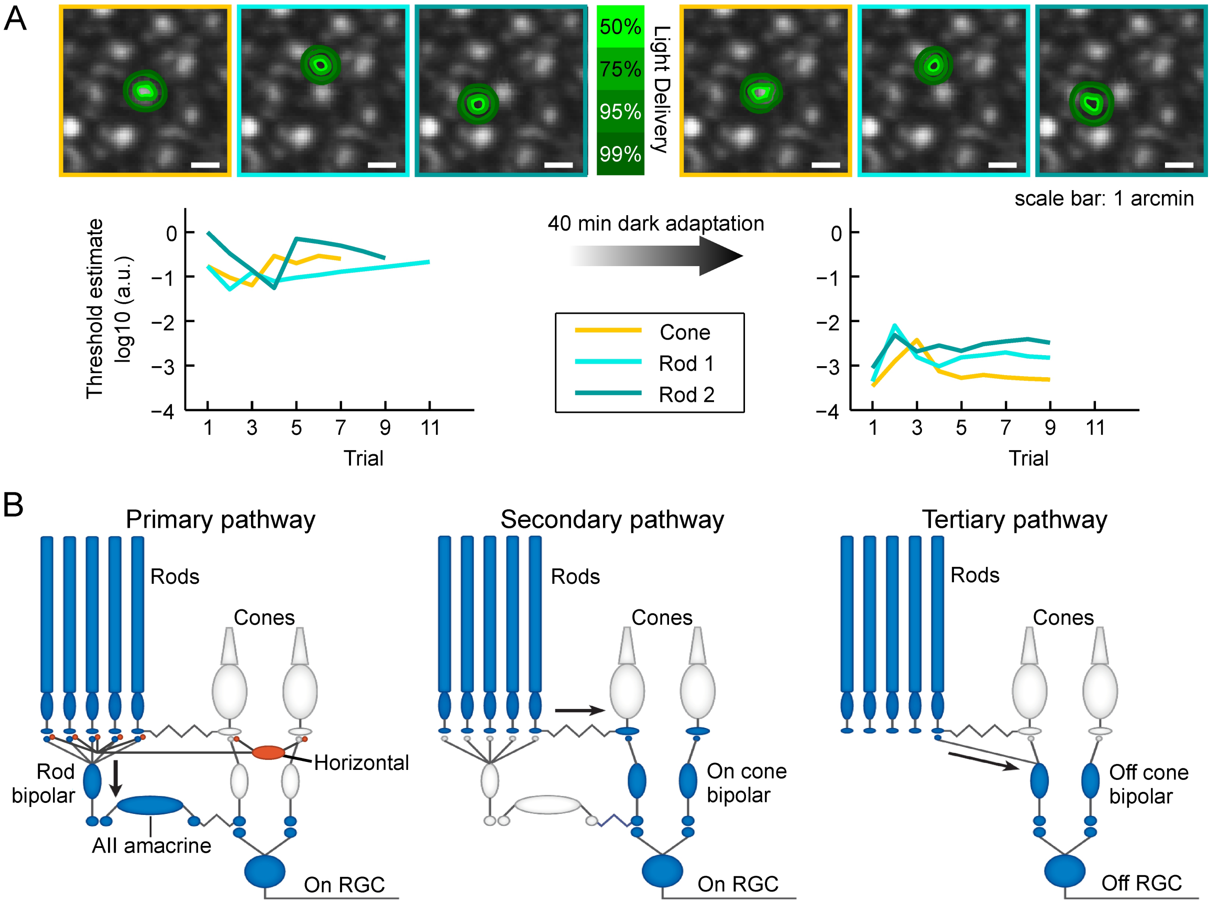

Figure 43: *Exemplary data of rod psychophysics and the rod pathways. A) Testsites and the regarding threshold estimate in log10 arbitrary units (a.u.) before and after 40 minutes dark adaptation. Cone and rod thresholds decreased by the same amount, presumably caused by cone-rod interactions inhibiting rod signal transmission and/or two-photons events saturating rods. B) Pathways conveying rod signals through the retina. In the primary pathway rod signals are transmitted through the dedicated rod bipolar cell and AII amacrine cell to the retinal ganglion cell (RGC). Horizontal cells receive input from cones and provide feedback to rods and cones. Through the secondary pathway rod signals are conveyed to cones via gap junctions. In the tertiary pathway rods provide direct input to a subset of cone bipolar cells, such as the Off cone bipolar cell depicted here. Source: B) modified from Grimes et al. 2018*

et al. 1989; Völgyi et al. 2004; Tikidji-Hamburyan et al. 2017]. Taken together, the most likely current scenario is, that cones are activated by the IR imaging background thereby inhibiting rod signals while the rods are saturated by two-photon events, making it impossible to elicit a rod based perception. To overcome this issue, an unpulsed light source like a super-luminescent diode would be needed to prevent any two photon related rod saturation. Ideally, the emitted light would be in the far IR range (about 1100 nm) to minimize any cone activation mediated rod inhibition.

7.3 Psychophysics: subjective function testing

AOSLO based microstimulation provides an unique tool to study human visual perception *in vivo* based on activation of individual photoreceptor cells. For example enabled single cell visual psychophysics to study cone-cone interactions of color perception, revealing that the perception of color depends on the surrounding cones. Stimulation of a target cone surrounded by a majority of opposing cones (e.g. L-cone center, 4 M-cones surrounding) led to a perception of color according to the target cone class (e.g. reddish for L-cone) [Sabesan et al. 2016]. If the surround consists mostly of cones of the same class, the stimulus was perceived as white. Additionally, the hue sensation could be predicted from the targeted cone type [Schmidt et al. 2018b] and M-cones contributed more to the sensation of a blue stimulus than L-cones [Schmidt et al. 2018a]. Another example for cone-cone interactions are the experiments from Kady Bruce, conducted during her PhD project [Bruce 2016; Sincich et al. 2016]. She tested the summation of neighboring cones revealing their network of signal integration, with directly neighboring cones showing a linear integration and two-detector summation for cones further apart.

A major drawback is that these experiments depend extremely on the involved participant. Firstly, the participant has to have sufficient optics to ensure optimal imaging and therefore stimulus delivery quality. Therefore, a screening prior to the actual experiment is mandatory. Secondly, the participant has to get comfortable with an unpleasant experiment environment. To reduce any head motion and holding the eye at the same location one has to bite on a bite bar during the experiment (see Figure 25). Furthermore, accommodation and miosis are inhibited by administration of eye drops. Thirdly, a good fixation is required, to minimize out-of-frame errors and to ensure a precise stimulus delivery at the target location due to the used online stabilization [Arathorn et al. 2007; Sheehy et al. 2012].

The participant's tear film plays an important role for the optical qualities of the eye and thus has a large impact for optical imaging [Rieger 1992]. The generally accepted theory is that the tear film reduces higher order aberrations (HOA) by smoothing the corneal surface [Jaeger 1981; Rieger 1992]. Therefore, irregularities of the tear film induce a significant amount of additional HOA hence reducing the optical quality [Montés-Micó et al. 2010]. To circumvent this issue and ensuring optimal imaging as well as stimulus quality, the operator or experimentalist remind the participant to blink often and ahead of each video or trial. A recent study underlines the importance of this procedure due to the reported observation that eye blinks additionally refresh the participant's attention [Ang and Maus 2020]. According to this study, a significant performance boost was observed during the first 300 msec after an eye blink. This is the equivalent of 10 frames in our AOSLO system and in good accordance with the current procedure, presenting the stimulus in the 8th frame, which would be ideally 240 msec after an eye blink.

Especially threshold estimation tasks are rated to be demanding and therefore prone to vigilance [See et al. 1995]. Additionally, the accompanying circumstances, like waiting for stimulus delivery, maintaining a precise fixation, and sitting in an uncomfortable position are exhausting, too. To prevent vigilance from affecting threshold estimations, small breaks in between individual runs are necessary, as vigilance decrements can occur after five minutes already [Nuechterlein et al. 1983; Maniscalco et al. 2017]. Such breaks are furthermore important to prevent any disruption of the ocular balance. It was reported that monocular deprivation of 2.5 hours, which is about the length of a typical experiment session, leads to an up-regulation in visual perception of the deprived eye [Lunghi et al. 2011; Wang et al. 2020; Steinwurzel et al. 2020]. Thus, during breaks the eye patch, typically used to cover the non-tested eye, covers the opposite eye, thereby maintaining dark adaptation of the test eye. Finally, younger participants (< 30 years) are not only preferred due to better optics, but are also less affected by vigilance decrements in threshold tasks than elderly (> 60 years) [Parasuraman et al. 1989].

7.4 Objective function testing

Instead of relying on the collaboration of the participant, an objective method gathers information to relate retinal structure and function more reliable and reproducible. Recent studies, using AO-OCT or AOSLO reported to detect the intrinsic signals of photoreceptor cells in response to stimulation [Hunter et al. 2019].

The first publication on objective functional testing described a significant change of photoreceptor reflectance in AOSLO images during stimulation [Grieve and Roorda 2008]. The stimulus was a 2x2 checkerboard with a wavelength of 658 nm and a luminance of 12,000 cd/m^2, eliciting an increase of light backscatter at the bright checkerboard patches due to photopigment depletion and visible by a brighter retinal image in this area. Such light dependent change of reflectance was observed for individual cone photoreceptor cells only a few years later during imaging with an AO flood illumination system [Bedggood and Metha 2013] and subsequently also with an AOSLO, which is shown in Figure 44A [Cooper et al. 2017].

Optical coherence tomography (OCT) provides axial imaging of the retina and therefore measuring variations of the optical path length. This renders possible to record a so called optoretinogram, reflecting the cone's response to a light stimulus and thereby its presumed functionality [Zhang et al. 2015b]. The optoretinogram is based on subtle morphological changes of the cones elicited by a bright light stimulus. These transient intrinsic optical signals are thought to be due to osmotic swelling as a result of the photo transduction induced hyperpolarization of the photoreceptor cells changing the optical path length [Zhang et al. 2017; Lu et al. 2018]. Combining a full-field swept-source OCT with a high-speed camera capturing up to 75,000 frames/sec, it was possible to measure the morphologic changes of the human photoreceptor cells with an extremely high temporal resolution [Hillmann et al. 2016]. This approach revealed two phases of the cone's light response. Within the first five milliseconds the optical path length shortens about a few nanometers and elongates by more then 100 nm (depending on the light level) during the following 300 msec as reported. Moreover, using the same system it was possible to detect morphologic changes of the ganglion cells [Pfäffle et al. 2019]. Latest publications using an AO-OCT system reported the recording of an optoretinogram with individually resolved photoreceptor cells [Azimipour et al. 2019; Azimipour et al. 2020; Pandiyan et al. 2020].

The major disadvantages of these objective function testing methods are, that (i) extremely high light levels are needed during stimulation with large stimuli, thereby activating thousands of photoreceptor cells, and (ii) single cell resolution can only be achieved in the parafovea due to the increased cone size at this eccentricity. Additionally, the objective methods capture only the changing signal due to activation from the photoreceptor or ganglion cells, thereby neglecting further downstream processing and the final percept. Therefore, AOSLO microstimulation experiments are the gold-standard for fundamental research to relate structure to function on an individual cell level and to assess the role of cone-cone or rod-cone and rod-rod interaction on perception (like spatial summation, or color vision).

7.5 Clinical relevance

AO imaging is of growing importance in the clinical research and as a side project of my doctorate I compiled a list which contains to this date 371 publications about clinical research project using AO imaging devices [Harmening 2021]. Additionally, fundus-controlled perimetry, or microperimetry, became an extremely helpful tool not only for fundamental researchers, but also clinicians, studying retinal pathologies. Since the stimuli are delivered to a tracked target site, a microperimeter visual sensitivity can be mapped directly to certain points of interest on the retina. This in turn enables clinicians to examine the residual photoreceptor function at the boarder of a progressing retinal disease or under photopic and scotopic light condition [Pfau et al. 2018; Pfau et al. 2021; Emde et al. 2019](for a comprehensive review see Pfau et al. 2020). Typically, these clinical microperimetry systems use relatively large stimuli like a Goldmann III stimulus (24 arcmin diameter), which activates about 2500 foveolar cones. Thus, the application of AOSLO based microperimetry could help to study the structure-function relationship in the pathological retina on the photoreceptor level. But the limitations described in 7.3 make it difficult to use AOSLO microstimulation with patients in clinical routine. The major problems are that the patient's eye optics have to be sufficiently good for imaging and the patient has to maintain a stable fixation. In many eye diseases (e.g. age-related macular degeneration) the fovea is affected first, thereby drastically decreasing the patient's fixation stability. During the last years only three studies have been published using AOSLO microstimulation on suitable patients.

The first study focused on macular telangiectasia type 2 patients and revealed that light sensitivity was almost normal in cones with waveguiding characteristics [Wang et al. 2015]. The authors' explanation for this observation was that the external limiting membrane is the important structure maintaining functional cones. For the second study visual function in choroideremia was assessed at the atrophic lesion border and the outer retinal tubulations [Tuten et al. 2019]. Here, visual sensitivity was mostly correlated to the structure observed during retinal imaging. Because the AOSLO stimulus (3.5 arcmin diameter) was much smaller than the typically used Goldman III stimulus (25.7 arcmin), precise testing along the outer retinal tubulations showed that sensitivity was completely lost within sharp borders, although remnant cone inner segments were still visible. The latest study assessed functional differences in patients with different forms of retinitis pigmentosa [Foote et al. 2020]. Patients with *RPGR* mutation showed a lower

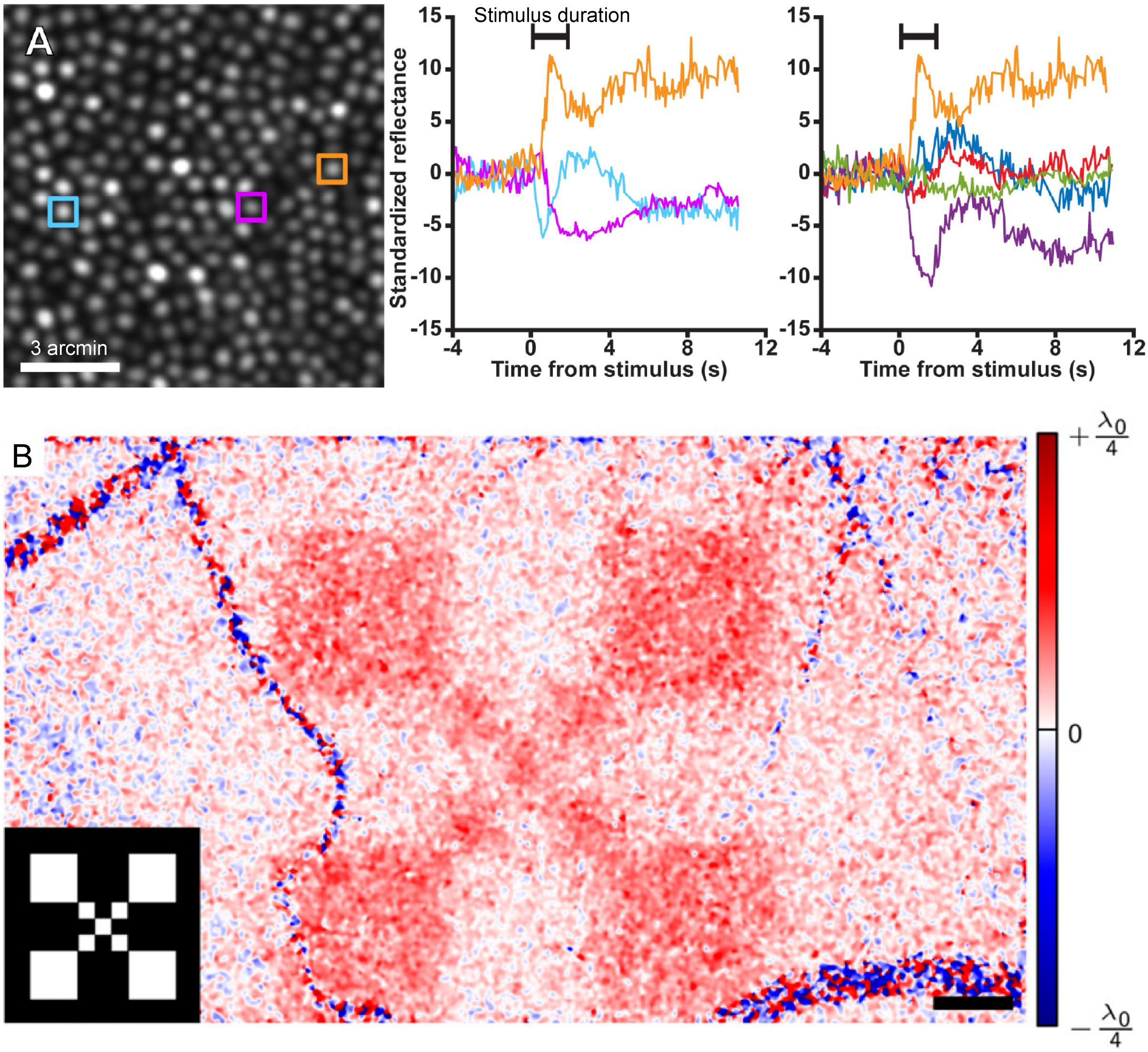

Figure 44: *Objective functional testing methods of photoreceptor cells. A) Individual infrared cone reflectance responds idiosyncratically to visible light stimulation. The cone mosaic was exposed to a two-second, 550 nm stimulus with a luminance of 22,000 cd/m*^{2}*. Cones' reflectance signals responded to the stimulus in a highly variable manner. The reflectance response of a single cone was also heterogeneous across trials (shown for the orange profile). B) Spatially resolved change of the optical path length* Δl*, 247 ms after switching off the stimulus pattern (lower left corner). Response is high in the stimulated region and random in blood vessels. Noise was reduced by a lateral Gaussian filter. Scale bar is 200 μm. Source: A) adopted from Cooper et al. 2017; B) adopted from Hillmann et al. 2016*

sensitivity compared to patients with *RHO*. Presumably this dicrepancy is caused by the order in which mutations disrupt the photoreceptor cells. The *RPGR* mutation affects the cones first, while the *RHO* mutation results firstly in rod and only later in cone degeneration.

In summary, these results show a non-trivial relationship between high-resolution AO imaging and cellular functional analysis, and a clinical application of functional imaging allowed new insights into retinal pathologies. But the size of the stimuli was, compared to other AOSLO experiments, relatively large (3.5 arcmin versus < 1 arcmin), thereby testing several cones. Testing of individual cones in the pathological retina benefits from the improvements described here (e.g. background elimination, increased delivery precision), too, as they are meant to increase the overall feasibility and reliability of single cell psychophysics. For example, one could study not only the loss, but also the restoration of photoreceptor cell function following gene therapy [Miraldi Utz et al. 2018; Ziccardi et al. 2019]. Additionally, the real-time TCO compensation project yielded a direct correlation of TCO and the angle κ, which enables an indirect compensation of TCO by measuring κ when image quality does not allow to determine the actual TCO objectively. Finally, the microstimulation experiments in the foveola revealed, that the cone outer segment length has a significant impact on light sensitivity even in the healthy retina. This will help to interpret the observations in future studies.

7.6 Conclusions and Outlook

This thesis focuses on improvements of an AOSLO system to enable human visual psychophysics in the foveola on an individual cell level. Overall, I developed new methodologies allowing for the stimulation of the smallest photoreceptor cells, the rods and foveal cones. These refinements were applied to conduct the first study testing sensitivity in the foveola by individual cell stimulation. My optimizations, including the findings about foveal sensitivity, will be beneficial for future fundamental research assessing the foveal cone-cone interactions, as well as for clinical research studying retinal pathologies and their treatment.

Together with Lennart Domdei, I realized a simple solution to eliminate the visible background of the stimulus light channel, which would otherwise limit the number of experimental options (chapter 4). By cascading two AOMs the radiant power contrasts was boosted up to $1{:}10^{10}$. This is the highest visual contrast reported for any display system so far. A psychophysical experiment confirmed that this contrast ratio is sufficient to stimulate single foveal photoreceptor cells with small and bright enough visible targets that do not contain a detectable background. Background-free stimulation will enable photoreceptor testing with custom adaptation lights. Furthermore, a larger dynamic range in displayable light levels can drive photoreceptor responses in cones as well as in rods.

Small shifts in eye position occurring during *in vivo* testing displace a stimulus by a significant amount when the TCO is only statically compensated, thus ruling out reliable testing of an individual foveolar cone or rod. Here, I developed a method that requires only a single measurement of the TCO during controlled movements of the eye to map retinal chromatic image shifts to the image space of a pupil camera (chapter 5). After such calibration, the TCO was compensated for by continuously monitoring the eye position during an experiment and by interpolating correction vectors from a linear fit to the calibration data. My solution enables continuous compensation of TCO with high spatial precision necessary for foveal cone-targeted psychophysical experimentation.

With the improvements mentioned above in place, I tested how far the special cellular organization at the very center of human vision is reflected in the sensitivity to light (chapter 6). Cone size, outer segment length, as well as distance from a computational estimated location of peak sensitivity had a significant influence. Interestingly, this location did neither coincide with the cone density centroid, nor with the preferred retinal locus of fixation. Overall, variability between individual test sites (0.6 log10 photons) was much higher compared to intra test site variability (0.1 log10 photons). Replicate testings showed that thresholds are reproducible across days. Therefore, the observed inter test site variability is assumed to be related to individual cone weighting.

The following future project ideas result from these observations:

1. To date, it was not possible to successfully conduct single rod psychophysics, since there was no significant difference between cone and rod thresholds as it would have been expected. One possible explanation is the saturation of the rods resulting from a significant number of two-photon events triggered by the pulsed laser light source and the AO correction. Furthermore, the rods could be inhibited through cone-rod interactions as the IR imaging light was clearly visible to the L- and M-cones. Hence, a light source with a continuous output would eliminate two-photon events. Ideally, the output wavelength should be at 1100 nm to ensure good transmission through the ocular media while significantly reducing visibility to L- and M-cones, as well as cone mediated inhibition of rod signals.

2. Currently, the two-photon absorption cross section (TPXS) is unsettled and roughly estimated by the order of two magnitudes. In a cooperation with Christina Schwarz a psychophysical pilot experiment was conducted to determine a better estimate of the TPXS.

3. The simulation of AOSLO microstimulation revealed, that it is almost impossible to activate an isolated cone in the foveola due to the physical limits in terms of diffraction. Here, the two-photon events could help to overcome this issue. By setting up a new stimulation light channel with a pulsed laser source at 1100 nm, the effective stimulus would be shrunken to a size smaller then a foveolar cone.

4. Due to the observed distinct threshold changes for neighboring cones, presumably caused by individual cone weighting, it would be interesting to assess cone-cone interactions of the foveola directly. For example, individual cones could be stimulated in pairs to analyze whether the two targeted cones sum their signal or feed into different detectors, comparable to an experiment already conducted by Kady Bruce [Bruce 2016].

References

Abbud, C. M. M. and Cruz, A. A. V. (2002). “Variability of Vernier acuity measurements in untrained subjects of different ages.” *Brazilian journal of medical and biological research* 35 (2), pp. 223–7.

Acton, J. H., Theodore Smith, R., Hood, D. C., and Greenstein, V. C. (2012). “Relationship between retinal layer thickness and the visual field in early age-related macular degeneration”. *Investigative Ophthalmology and Visual Science* 53 (12), pp. 7618–7624.

Agarwal, A., Soliman, M. K., Hanout, M., Sadiq, M. A., Sarwar, S., Jack, L. S., Do, D. V., Nguyen, Q. D., and Sepah, Y. J. (2015). “Adaptive Optics Imaging of Retinal Photoreceptors Overlying Lesions in White Dot Syndrome and its Functional Correlation.” *American journal of ophthalmology* 160 (4), 806–16.e2.

Agte, S., Junek, S., Matthias, S., Ulbricht, E., Erdmann, I., Wurm, A., Schild, D., Käs, J. A., and Reichenbach, A. (2011). “Müller glial cell-provided cellular light guidance through the vital guinea-pig retina.” *Biophysical journal* 101 (11), pp. 2611–9.

Ahnelt, P. K. (1998). “The photoreceptor mosaic”. *Eye (Basingstoke)* 12 (3), pp. 531–540.

Alitto, H. J., Rathbun, D. L., Fisher, T. G., Alexander, P. C., and Usrey, W. M. (2019). “Contrast gain control and retinogeniculate communication”. *European Journal of Neuroscience* 49 (8), pp. 1061–1068.

Allphin, M., Cava, J., Cooper, R. F., and Carroll, J. (2020). “Reevaluating Outer Segment Length as a Surrogate for Peak Cone Density”. *Investigative Ophthalmology and Visual Science* 61 (7), p. 204.

Ang, J. W. A. and Maus, G. W. (2020). “Boosted visual performance after eye blinks.” *Journal of vision* 20 (10), p. 2.

Arathorn, D. W., Yang, Q., Vogel, C. R., Zhang, Y., Tiruveedhula, P., and Roorda, A. (2007). “Retinally stabilized cone-targeted stimulus delivery.” *Optics express* 15 (21), pp. 13731–13744.

Arden, G. B., Carter, R. M., Hogg, C. R., Powell, D. J., Ernst, W. J., Clover, G. M., Lyness, A. L., and Quinlan, M. P. (1983). “Rod and cone activity in patients with dominantly inherited retinitis pigmentosa: comparisons between psychophysical and electroretinographic measurements.” *The British journal of ophthalmology* 67 (7), pp. 405–18.

Asaoka, R., Murata, H., Yanagisawa, M., Fujino, Y., Matsuura, M., Inoue, T., Inoue, K., and Yamagami, J. (2017). “The association between photoreceptor layer thickness measured by optical coherence tomography and visual sensitivity in glaucomatous eyes”. *PLoS ONE* 12 (10), pp. 1–12.

Atchison, D. A. (2017). “Axes and angles of the eye”. In: *Handbook of Visual Optics: Fundamentals and Eye Optics, Volume One*. Ed. by P. Artal. Taylor & Francis Group. Chap. 17, pp. 249–255.

Atchison, D. A. and Smith, G. (2005). “Chromatic dispersions of the ocular media of human eyes.” *Journal of the Optical Society of America. A, Optics, image science, and vision* 22 (1), pp. 29–37.

Azimipour, M., Migacz, J. V., Zawadzki, R. J., Werner, J. S., and Jonnal, R. S. (2019). “Functional retinal imaging using adaptive optics swept-source OCT at 16 MHz”. *Optica* 6 (3), p. 300.

Azimipour, M., Valente, D., Vienola, K. V., Werner, J. S., Zawadzki, R. J., and Jonnal, R. S. (2020). “Optoretinogram: optical measurement of human cone and rod photoreceptor responses to light”. *Optics Letters* 45 (17), pp. 4658–4661.

Babcock, H. W. (1953). “The Possibility of Compensating Astronomical Seeing”. *Publications of the Astronomical Society of the Pacific* 65 (12), pp. 229–236.

Bach, M., Meigen, T., and Strasburger, H. (1997). “Raster-scan cathode-ray tubes for vision research–limits of resolution in space, time and intensity, and some solutions.” *Spatial vision* 10 (4), pp. 403–414.

Barlow, H. B. (1952). "Eye movements during fixation". *The Journal of physiology* 116, pp. 290–306.

Bassi, C. J. and Powers, M. K. (1990). "Rod outer segment length and visual sensitivity". *Investigative Ophthalmology and Visual Science* 31 (11), pp. 2320–2325.

Baylor, D. A., Lamb, T. D., and Yau, K. W. (1979). "The membrane current of single rod outer segments." *The Journal of Physiology* 288 (1), pp. 589–611.

Bedell, H. E. (1980). "A functional test of foveal fixation based upon differential cone directional sensitivity". *Vision Research* 20 (6), pp. 557–560.

Bedggood, P. and Metha, A. (2013). "Optical imaging of human cone photoreceptors directly following the capture of light." *PloS one* 8 (11), e79251.

Bensinger, E., Rinella, N., Saud, A., Loumou, P., Ratnam, K., Griffin, S., Qin, J., Porco, T. C., Roorda, A., and Duncan, J. L. (2019). "Loss of Foveal Cone Structure Precedes Loss of Visual Acuity in Patients With Rod-Cone Degeneration." *Investigative ophthalmology & visual science* 60 (8), pp. 3187–3196.

Bernard, J.-b. B. and Chung, S. T. L. (2018). "Visual Acuity Is Not the Best at the Preferred Retinal Locus in People with Macular Disease." *Optometry and Vision Science* 95 (9), pp. 829–836.

Bloch, A.-M. (1885). "Experiences sur la vision". *Comptes Rendus de la Societé de Biologie* 37 (493).

Boehm, A. E., Privitera, C. M., Schmidt, B. P., and Roorda, A. (2019). "Transverse chromatic offsets with pupil displacements in the human eye: sources of variability and methods for real-time correction". *Biomedical Optics Express* 10 (4), pp. 1691–1706.

Boettner, E. a. (1967). "Spectral transmission of the eye". *Contract AF41(609)-2966. USAF School of Aerospace Medicine. Aerospace Medical Division (AFSC). Brooks Air Force Base*.

Boettner, E. A. and Wolter, J. R. (1962). "Transmission of the Ocular Media". *Invest. Ophthalmol. Vis. Sci.* 1 (6), pp. 776–783.

BostonMicromachines (2020). *Adaptive Optics Instruments The Apaeros AOSLO*. URL: `https://bostonmicromachines.com/apaeros-retinal-imaging-system-aoslo/` (visited on 01/15/2021).

Bowmaker, J. K. and Dartnall, H. J. (1980). "Visual pigments of rods and cones in a human retina." *The Journal of physiology* 298 (2), pp. 501–11.

Bowmaker, J. K., Dartnall, H. J., Lythgoe, J. N., and Mollon, J. D. (1978). "The visual pigments of rods and cones in the rhesus monkey, Macaca mulatta." *The Journal of Physiology* 274 (1), pp. 329–348.

Boycott, B. B., Hopkins, J. M., and Sperling, H. G. (1987). "Cone connections of the horizontal cells of the rhesus monkey's retina." *Proceedings of the Royal Society of London. Series B, Biological sciences* 229 (1257), pp. 345–79.

Boycott, B. B. and Dowling, J. E. (1969). "Organization of the primate retina: Light microscopy, with an appendix: A second type of midget bipolar cell in the primate retina". *Philosophical Transactions of the Royal Society of London. Series B, Biological Sciences* 255 (799), pp. 109–184.

Brainard, D. H., Williams, D. R., and Hofer, H. (2008). "Trichromatic reconstruction from the interleaved cone mosaic: Bayesian model and the color appearance of small spots." *Journal of vision* 8 (5), pp. 15.1–23.

Bruce, K. S., Harmening, W. M., Langston, B. R., Tuten, W. S., Roorda, A., and Sincich, L. C. (2015). "Normal Perceptual Sensitivity Arising From Weakly Reflective Cone Photoreceptors." *Investigative ophthalmology & visual science* 56 (8), pp. 4431–8.

Bruce, K. S. (2016). "Elementary photoreceptor signaling in human vision". PhD thesis. University of Alabama at Birmingham.

Buffington, A., Crawford, F. S., Muller, R. a., and Orth, C. D. (1977a). "First observatory results with an image-sharpening telescope". *Journal of the Optical Society of America* 67 (3), pp. 304–305.

Buffington, A., Crawford, F. S., Muller, R. a., Schwemin, a. J., and Smits, R. G. (1977b). “Correction of atmospheric distortion with an image-sharpening telescope”. *Journal of the Optical Society of America* 67 (3), pp. 298–303.

Bumsted, K. and Hendrickson, A. (1999). “Distribution and development of short-wavelength cones differ between Macaca monkey and human fovea”. *Journal of Comparative Neurology* 403 (4), pp. 502–516.

Bunsen, R. W. and Roscoe, H. E. (1863). “III. Photochemical researches.—Part V. On the measurement of the chemical action of direct and diffuse sunlight”. *Proceedings of the Royal Society of London* 12, pp. 306–312.

Burkhardt, D. A. (1994). “Light adaptation and photopigment bleaching in cone photoreceptors in situ in the retina of the turtle”. *Journal of Neuroscience* 14 (3 I), pp. 1091–1105.

Burns, S. A., Elsner, A. E., Sapoznik, K. A., Warner, R. L., and Gast, T. J. (2019). “Adaptive optics imaging of the human retina.” *Progress in retinal and eye research* 68 (June 2018), pp. 1–30.

Charman, W. N. and Simonet, P (1997). “Yves Le Grand and the assessment of retinal acuity using interference fringes.” *Ophthalmic & physiological optics : the journal of the British College of Ophthalmic Opticians (Optometrists)* 17 (2), pp. 164–8.

Chen, Y., Ratnam, K., Sundquist, S. M., Lujan, B., Ayyagari, R., Gudiseva, V. H., Roorda, A., and Duncan, J. L. (2011). “Cone photoreceptor abnormalities correlate with vision loss in patients with Stargardt disease.” *Investigative ophthalmology & visual science* 52 (6), pp. 3281–3292.

Chichilnisky, E. J. and Baylor, D. A. (1999). “Receptive-field microstructure of blue-yellow ganglion cells in primate retina”. *Nature Neuroscience* 2 (10), pp. 889–893.

Choi, A. Y. J., Nivison-Smith, L., Khuu, S. K., and Kalloniatis, M. (2016). “Determining Spatial Summation and Its Effect on Contrast Sensitivity across the Central 20 Degrees of Visual Field.” *PloS one* 11 (7), e0158263.

Choma, M., Sarunic, M., Yang, C., and Izatt, J. (2003). “Sensitivity advantage of swept source and Fourier domain optical coherence tomography.” *Optics express* 11 (18), pp. 2183–9.

Collins, M., Vincent, S., and Read, S. (2017). “The cornea”. In: *Handbook of Visual Optics: Fundamentals and Eye Optics, Volume One*. Ed. by P. Artal. Taylor & Francis Group. Chap. 14, pp. 189–210.

Connolly, M. and Van Essen, D. (1984). “The representation of the visual field in parvicellular and magnocellular layers of the lateral geniculate nucleus in the macaque monkey”. *Journal of Comparative Neurology* 226 (4), pp. 544–564.

Cooper, R. F., Tuten, W. S., Dubra, A., Brainard, D. H., and Morgan, J. I. W. (2017). “Non-invasive assessment of human cone photoreceptor function.” *Biomedical optics express* 8 (11), pp. 5098–5112.

Cornsweet, T. N. (1956). “Determination of the Stimuli for Involuntary Drifts and Saccadic Eye Movements”. *Journal of the Optical Society of America* 46 (11), p. 987.

Cottaris, N. P., Jiang, H., Ding, X., Wandell, B. A., and Brainard, D. H. (2019). “A computational-observer model of spatial contrast sensitivity: Effects of wave-front-based optics, cone-mosaic structure, and inference engine.” *Journal of vision* 19 (4), p. 8.

Cottaris, N. P., Wandell, B. A., Rieke, F., and Brainard, D. H. (2020). “A computational observer model of spatial contrast sensitivity: Effects of photocurrent encoding, fixational eye movements, and inference engine.” *Journal of vision* 20 (7), p. 17.

Crane, H. D. and Steele, C. M. (1985). “Generation-V dual-Purkinje-image eyetracker.” *Applied optics* 24 (4), pp. 527–537.

Crossland, M. D. (2011). “THE PREFERRED RETINAL LOCUS IN Toward A Consensus Definition”. *the Journal of Retinal and Vitreous Diseases*, pp. 2109–2114.

Crossland, M. D., Culham, L. E., Kabanarou, S. A., and Rubin, G. S. (2005). “Preferred retinal locus development in patients with macular disease”. *Ophthalmology* 112 (9), pp. 1579–1585.

Crossland, M. D. and Rubin, G. S. (2002). “The use of an infrared eyetracker to measure fixation stability”. *Optometry and Vision Science* 79 (11), pp. 735–739.

Cuenca, N., Ortuño-Lizarán, I., and Pinilla, I. (2018). “Cellular Characterization of OCT and Outer Retinal Bands Using Specific Immunohistochemistry Markers and Clinical Implications”. *Ophthalmology* 125 (3), pp. 407–422.

Cuenca, N., Ortuño-Lizarán, I., Sánchez-Sáez, X., Kutsyr, O., Albertos-Arranz, H., Fernández-Sánchez, L., Martínez-Gil, N., Noailles, A., López-Garrido, J. A., López-Gálvez, M., Lax, P., Maneu, V., and Pinilla, I. (2020). “Interpretation of OCT and OCTA images from a histological approach: Clinical and experimental implications”. *Progress in Retinal and Eye Research* 77 (January), p. 100828.

Cunefare, D., Fang, L., Cooper, R. F., Dubra, A., and Carroll, J. (2017). “Open source software for automatic detection of cone photoreceptors in adaptive optics ophthalmoscopy using convolutional neural networks”. *Scientific Reports* (April), pp. 1–11.

Curcio, C. A., Medeiros, N. E., and Millican, C. L. (1996). “Photoreceptor loss in age-related macular degeneration.” *Investigative ophthalmology and visual science* 37 (7), pp. 1236–49.

Curcio, C. A., Sloan, K. R., Kalina, R. E., and Hendrickson, A. E. (1990). “Human photoreceptor topography.” *The Journal of comparative neurology* 292 (4), pp. 497–523.

Curcio, C. A. and Allen, K. A. (1990). “Topography of ganglion cells in human retina.” *The Journal of comparative neurology* 300 (1), pp. 5–25.

Curcio, C. A., Allen, K. A., Sloan, K. R., Lerea, C. L., Hurley, J. B., Klock, I. B., and Milam, A. H. (1991). “Distribution and morphology of human cone photoreceptors stained with anti-blue opsin.” *The Journal of comparative neurology* 312 (4), pp. 610–24.

Dacey, D. M. (1993). “The mosaic of midget ganglion cells in the human retina”. *Journal of Neuroscience* 13 (12), pp. 5334–5355.

Dacey, D. M. and Petersen, M. R. (1992). “Dendritic field size and morphology of midget and parasol ganglion cells of the human retina”. *Proceedings of the National Academy of Sciences of the United States of America* 89 (20), pp. 9666–9670.

Daniel, P. M. and Whitteridge, D (1961). “The representation of the visual field on the cerebral cortex in monkeys.” *The Journal of physiology* 159, pp. 203–21.

Dartnall, H. J., Bowmaker, J. K., and Mollon, J. D. (1983). “Human visual pigments: microspectrophotometric results from the eyes of seven persons.” *Proceedings of the Royal Society of London. Series B, Biological sciences* 220 (1218), pp. 115–30.

DeVries, S. H., Qi, X., Smith, R., Makous, W., and Sterling, P. (2002). “Electrical coupling between mammalian cones.” *Current biology : CB* 12 (22), pp. 1900–1907.

Dmitriev, V. G., Emel’yanov, V. N., Kashintsev, M. A., Kulikov, V. V., Solov’ev, A. A., Stel’makh, M. F., and Cherednichenko, O. B. (1979). “Nonlinear perception of infrared radiation in the 800–1355 nm range with human eye”. *Soviet Journal of Quantum Electronics* 9 (4), pp. 475–479.

Domdei, N., Reiniger, J., Pfau, M., Charbel Issa, P., Holz, F., and Harmening, W. (2017). “[Histology of the living eye : Noninvasive microscopic structure and functional analysis of the retina with adaptive optics].” *Der Ophthalmologe : Zeitschrift der Deutschen Ophthalmologischen Gesellschaft* 114 (3), pp. 206–214.

Domdei, N., Domdei, L., Reiniger, J. L., Linden, M., Holz, F. G., Roorda, A., and Harmening, W. M. (2018). “Ultra-high contrast retinal display system for single photoreceptor psychophysics.” *Biomedical optics express* 9 (1), pp. 157–172.

Domdei, N., Holz, F. G., Roorda, A. J., Sincich, L. C., and Harmening, W. M. (2015). “Characterization of an adaptive optics SLO based retinal display for cellular level visual psychophysics”. In: *Perception*. Vol. 44. 1_suppl, pp. 1–415.

Dreher, A. W., Bille, J. F., and Weinreb, R. N. (1989). “Active optical depth resolution improvement of the laser tomographic scanner.” *Applied optics* 28 (4), pp. 804–8.

Dubra, A., Sulai, Y., Norris, J. L., Cooper, R. F., Dubis, A. M., Williams, D. R., and Carroll, J. (2011). “Noninvasive imaging of the human rod photoreceptor mosaic using a confocal adaptive optics scanning ophthalmoscope.” *Biomedical Optics Express* 2 (7), pp. 1864–76.

Eggers, E. D., Mazade, R. E., and Klein, J. S. (2013). “Inhibition to retinal rod bipolar cells is regulated by light levels”. *Journal of Neurophysiology* 110 (1), pp. 153–161.

Eizenman, M., Hallett, P. E., and Frecker, R. C. (1985). “Power spectra for ocular drift and tremor.” *Vision research* 25 (11), pp. 1635–40.

Elsner, A. E., Burns, S. A., and Webb, R. H. (1993). “Mapping cone photopigment optical density”. *Journal of the Optical Society of America A* 10 (1), p. 52.

Elsner, A. E., Burns, S. A., Weiter, J. J., and Delori, F. C. (1996). “Infrared imaging of sub-retinal structures in the human ocular fundus”. *Vision Research* 36 (1), pp. 191–205.

Emde, L. von der, Pfau, M., Thiele, S., Möller, P. T., Hassenrik, R., Fleckenstein, M., Holz, F. G., and Schmitz-Valckenberg, S. (2019). “Mesopic and Dark-Adapted Two-Color Fundus-Controlled Perimetry in Choroidal Neovascularization Secondary to Age-Related Macular Degeneration.” *Translational vision science & technology* 8 (1), p. 7.

Engbert, R. and Kliegl, R. (2003). “Microsaccades uncover the orientation of covert attention”. *Vision Research* 43 (9), pp. 1035–1045.

Engbert, R. and Kliegl, R. (2004). “Microsaccades keep the eyes’ balance during fixation”. *Psychological Science* 15 (6), pp. 431–436.

Enoch, J. M. (1963). “Optical Properties of the Retinal Receptors”. *Journal of the Optical Society of America* 53 (1), pp. 71–85.

Enoch, J. M. (1964). “Physical properties of the retinal receptor and response of retinal receptors.” *Psychological bulletin* 61 (4), pp. 242–251.

Enroth-Cugell, C, Hertz, B. G., and Lennie, P (1977). “Convergence of rod and cone signals in the cat’s retina.” *The Journal of physiology* 269 (2), pp. 297–318.

Fechner, G. T. (1860). *Elemente der psychophysik*. Breitkopf u. Härtel.

Fercher, A., Hitzenberger, C., Kamp, G., and El-Zaiat, S. (1995). “Measurement of intraocular distances by backscattering spectral interferometry”. *Optics Communications* 117 (1-2), pp. 43–48.

Field, G. D., Gauthier, J. L., Sher, A., Greschner, M., Machado, T. A., Jepson, L. H., Shlens, J., Gunning, D. E., Mathieson, K., Dabrowski, W., Paninski, L., Litke, A. M., and Chichilnisky, E. J. (2010). “Functional connectivity in the retina at the resolution of photoreceptors.” *Nature* 467 (7316), pp. 673–7.

Field, G. D., Sampath, A. P., and Rieke, F. (2005). “Retinal processing near absolute threshold: From behavior to mechanism”. *Annual Review of Physiology* 67, pp. 491–514.

Foote, K. G., Huerta, I. de la, Gustafson, K., Baldwin, A., Zayit-Soudry, S., Rinella, N., Porco, T. C., Roorda, A., and Duncan, J. L. (2019). “Cone spacing correlates with retinal thickness and microperimetry in patients with inherited retinal degenerations". *Investigative Ophthalmology and Visual Science* 60 (4), pp. 1234–1243.

Foote, K. G., Loumou, P., Griffin, S., Qin, J., Ratnam, K., Porco, T. C., Roorda, A., and Duncan, J. L. (2018). "Relationship Between Foveal Cone Structure and Visual Acuity Measured With Adaptive Optics Scanning Laser Ophthalmoscopy in Retinal Degeneration." *Investigative ophthalmology & visual science* 59 (8), pp. 3385–3393.

Foote, K. G., Wong, J. J., Boehm, A. E., Bensinger, E., Porco, T. C., Roorda, A., and Duncan, J. L. (2020). "Comparing cone structure and function in Rho- And RPGR-associated retinitis pigmentosa". *Investigative Ophthalmology and Visual Science* 61 (4).

Fraser, R. G., Tan, R., Ayton, L. N., Caruso, E., Guymer, R. H., and Luu, C. D. (2016). "Assessment of retinotopic rod photoreceptor function using a dark-adapted chromatic perimeter in intermediate age-related macular degeneration". *Investigative Ophthalmology and Visual Science* 57 (13), pp. 5436–5442.

Freeman, J., Field, G. D., Li, P. H., Greschner, M., Gunning, D. E., Mathieson, K., Sher, A., Litke, A. M., Paninski, L., Simoncelli, E. P., and Chichilnisky, E. J. (2015). "Mapping nonlinear receptive field structure in primate retina at single cone resolution." *eLife* 4, pp. 1–21.

Frumkes, T. E. and Temme, L. A. (1977). "Rod-cone interaction in human scotopic vision—II: Cones influence rod increment thresholds". *Vision Research* 17 (6), pp. 673–679.

Furlab, W. D. (2017). "Basic ophthalmic instruments". In: *Handbook of Visual Optics: Fundamentals and Eye Optics, Volume One2*. Ed. by P. Artal. Taylor & Francis Group. Chap. 8, pp. 103–120.

Gandhi, S. P., Heeger, D. J., and Boynton, G. M. (1999). "Spatial attention affects brain activity in human primary visual cortex". *Proceedings of the National Academy of Sciences of the United States of America* 96 (6), pp. 3314–3319.

Geisler, W. S. and Banks, M. S. (2010). "Visual Performance". In: *Handbook of Optics, Volume III*. Ed. by M. Bass. 3rd editio. New York: McGraw-Hill. Chap. 2, pp. 2.1–2.51.

Geisler, W. S. and Davila, K. D. (1985). "Ideal discriminators in spatial vision:two-point stimuli". *Journal of the Optical Society of America A* 2 (9), p. 1483.

Geissler, E, Nieten, C, Rudolph, G, and Pretorius, M (2009). *Projektionssystem*. Germany.

Ghodrati, M., Morris, A. P., and Price, N. S. C. (2015). "The (un)suitability of modern liquid crystal displays (LCDs) for vision research". *Frontiers in Psychology* 6 (MAR), pp. 1–11.

Gilbert, C. D. (2013). "The Constructive Nature of Visual Processing". In: *Principles of Neural Science*. Ed. by E. R. Kandel, J. H. Schwartz, T. M. Jessell, S. A. Siegelbaum, and A. J. Hudspeth. 5th Editio. New York: McGraw-Hill. Chap. 25, pp. 556–576.

Gilpin, L. B., Stewart, W. C., Hunt, H. H., and Broom, C. D. (1990). "Threshold variability using different Goldmann stimulus sizes". *Acta Ophthalmologica* 68 (6), pp. 674–676.

Goldberg, M. E. and Walker, M. F. (2013). "The control of Gaze". In: *Principles of Neural Science*. Ed. by E. R. Kandel, J. H. Schwartz, T. M. Jessell, S. A. Siegelbaum, and A. J. Hudspeth. 5th. New York: McGraw-Hill. Chap. 39, pp. 894–916.

Goldsmith, T. H. (1990). "Optimization, constraint, and history in the evolution of eyes." *The Quarterly review of biology* 65 (3), pp. 281–322.

Graham, C. H. and Margaria, R. (1935). "Area and the intensity-time relation in the peripheral retina". *American Journal of Physiology-Legacy Content* 113 (2), pp. 299–305.

Grieve, K. and Roorda, A. (2008). "Intrinsic signals from human cone photoreceptors." *Investigative ophthalmology & visual science* 49 (2), pp. 713–9.

Grieve, K., Tiruveedhula, P., Zhang, Y., and Roorda, A. (2006). “Multi-wavelength imaging with the adaptive optics scanning laser Ophthalmoscope.” *Optics express* 14 (25), pp. 12230–12242.

Grimes, W. N., Songco-Aguas, A., and Rieke, F. (2018). “Parallel processing of rod and cone signals: Retinal function and human perception”. *Annual Review of Vision Science* 4, pp. 123–141.

Hafed, Z. M. and Clark, J. J. (2002). “Microsaccades as an overt measure of covert attention shifts”. *Vision Research* 42 (22), pp. 2533–2545.

Hardy, J. W., Lefebvre, J. E., and Koliopoulos, C. L. (1977). “Real-time atmospheric compensation”. *Journal of the Optical Society of America* 67 (3), p. 360.

Harmening, W. (2021). *AO Vision Lab Bonn*. URL: `http://ao.ukbonn.de/index.html` (visited on 04/13/2021).

Harmening, W. M., Tiruveedhula, P., Roorda, A., and Sincich, L. C. (2012). “Measurement and correction of transverse chromatic offsets for multi-wavelength retinal microscopy in the living eye.” *Biomedical optics express* 3 (9), pp. 2066–2077.

Harmening, W. M., Tuten, W. S., Roorda, A., and Sincich, L. C. (2014). “Mapping the perceptual grain of the human retina.” *The Journal of neuroscience : the official journal of the Society for Neuroscience* 34 (16), pp. 5667–77.

Havermann, K., Cherici, C., Rucci, M., and Lappe, M. (2014). “Fine-Scale Plasticity of Microscopic Saccades”. *Journal of Neuroscience* 34 (35), pp. 11665–11672.

Helmholtz, H. (1851). *Beschreibung eines Augen-Spiegels: zur Untersuchung der Netzhaut im lebenden Auge*. Berlin: A. Förstner’sche Verlagsbuchhandlung (P. Jeanrenaud).

Helmholtz, H. (1867). “§ 14. Monochromatische Abweichungen (Astigmatismus)”. In: *Handbuch der Physiologischen Optik*. Leipzig: Leopold Voss, pp. 137–147.

Hillmann, D., Spahr, H., Pfäffle, C., Sudkamp, H., Franke, G., and Hüttmann, G. (2016). “In vivo optical imaging of physiological responses to photostimulation in human photoreceptors.” *Proceedings of the National Academy of Sciences of the United States of America* 113 (46), pp. 13138–13143.

Hoang, Q. V., Linsenmeier, R. A., Chung, C. K., and Curcio, C. A. (2002). “Photoreceptor inner segments in monkey and human retina: Mitochondrial density, optics, and regional variation”. *Visual Neuroscience* 19 (4), pp. 395–407.

Hoang, T. A., Macdonnell, J. E., Mangan, M. C., Monsour, C. S., Polwattage, B. L., Wilson, S. F., Suheimat, M., and Atchison, D. A. (2016). “Time Course of Pupil Center Location after Ocular Drug Application.” *Optometry and vision science : official publication of the American Academy of Optometry* 93 (6), pp. 594–9.

Hofer, H., Singer, B., and Williams, D. R. (2005). “Different sensations from cones with the same photopigment”. *Journal of Vision* 5, pp. 444–454.

Hofer, H., Sredar, N., Queener, H., Li, C., and Porter, J. (2011). “Wavefront sensorless adaptive optics ophthalmoscopy in the human eye.” *Optics express* 19 (15), pp. 14160–71.

Hood, D. C. and Finkelstein, M. A. (1986). “Sensitivity to Light”. In: *Handbook of Perception in Human Performance, vol. 1*. Ed. by K. Boff, L. Kaufman, and J. Thomas. Chap. 5, pp. 5–25.

Hornstein, E. P., Verweij, J., and Schnapf, J. L. (2004). “Electrical coupling between red and green cones in primate retina.” *Nature neuroscience* 7 (7), pp. 745–50.

Howarth, P. A. (1984). “The lateral chromatic aberration of the eye.” *Ophthalmic & physiological optics : the journal of the British College of Ophthalmic Opticians (Optometrists)* 4 (3), pp. 223–6.

Hsu, A, Smith, R. G., Buchsbaum, G, and Sterling, P (2000). “Cost of cone coupling to trichromacy in primate fovea.” *Journal of the Optical Society of America. A, Optics, image science, and vision* 17 (3), pp. 635–40.

Huang, D, Swanson, E. A., Lin, C. P., Schuman, J. S., Stinson, W. G., Chang, W, Hee, M. R., Flotte, T, Gregory, K, and Puliafito, C. A. (1991). “Optical coherence tomography.” *Science (New York, N.Y.)* 254 (5035). Ed. by W. Drexler and J. G. Fujimoto, pp. 1178–81.

Hunter, J. J., Merigan, W. H., and Schallek, J. B. (2019). “Imaging Retinal Activity in the Living Eye.” *Annual review of vision science* 5, pp. 15–45.

ImagineEyes (2021). *rtx1 Adaptive Optics Retinal Camera*. URL: `https://www.imagine-eyes.com/products/rtx1/` (visited on 01/15/2021).

Iskander, D. R., Collins, M. J., and Davis, B. (2001). “Optimal modeling of corneal surfaces with Zernike polynomials”. *IEEE Transactions on Biomedical Engineering* 48 (1), pp. 87–95.

Ito, H., Ogawa, M., and Sunaga, S. (2013). “Evaluation of an organic light-emitting diode display for precise visual stimulation.” *Journal of vision* 13 (7), pp. 1–21.

Ivanchenko, D., Hafed, Z. M., and Schaeffel, F. (2018). “How correlated are drifts in both eyes during fixational eye movements?” *Investigative Ophthalmology & Visual Science* 59 (9), p. 5792.

Iyamu, E. and Osuobeni, E. (2012). “Age, gender, corneal diameter, corneal curvature and central corneal thickness in Nigerians with normal intra ocular pressure”. *Journal of Optometry* 5 (2), pp. 87–97.

Jackson, G. R., Owsley, C., and Curcio, C. A. (2002). “Photoreceptor degeneration and dysfunction in aging and age-related maculopathy.” *Ageing research reviews* 1 (3), pp. 381–96.

Jaeger, W (1981). “Der präkorneale Film und seine Bedeutung für die Therapie des „trockenen Auges“”. In: *Neue Erkenntnisse über Erkrankungen der Tränenwege*. Ed. by H. Hanselmayer. Stuttgart: Enke, pp. 40–51.

Jaeken, B., Lundström, L., and Artal, P. (2011). “Peripheral aberrations in the human eye for different wavelengths: off-axis chromatic aberration”. *Journal of the Optical Society of America A* 28 (9), p. 1871.

Jayabalan, G. S. and Bille, J. F. (2019). “The Development of Adaptive Optics and Its Application in Ophthalmology”. In: *High Resolution Imaging in Microscopy and Ophthalmology*. Ed. by J. F. Bille. Cham: Springer International Publishing, pp. 339–358.

Jiang, Y., Yampolsky, D., Purushothaman, G., and Casagrande, V. A. (2015). “Perceptual decision related activity in the lateral geniculate nucleus”. *Journal of Neurophysiology* 114 (1), pp. 717–735.

Johnson, C. A., Keltner, J. L., and Balestrery, F. G. (1981). “Static and acuity profile perimetry at various adaptation levels.” *Documenta ophthalmologica. Advances in ophthalmology* 50 (2), pp. 371–88.

Jonnal, R. S., Gorczynska, I., Migacz, J. V., Azimipour, M., Zawadzki, R. J., and Werner, J. S. (2017). “The properties of outer retinal band three investigated with adaptive-optics optical coherence tomography”. *Investigative Ophthalmology and Visual Science* 58 (11), pp. 4559–4568.

Jonnal, R. S., Kocaoglu, O. P., Zawadzki, R. J., Lee, S.-H., Werner, J. S., and Miller, D. T. (2014). “The cellular origins of the outer retinal bands in optical coherence tomography images.” *Investigative ophthalmology & visual science* 55 (12), pp. 7904–18.

Jonnal, R. S., Kocaoglu, O. P., Zawadzki, R. J., Lee, S.-H., Werner, J. S., and Miller, D. T. (2015). “Author Response: Outer Retinal Bands”. *Investigative Opthalmology & Visual Science* 56 (4), p. 2507.

Karn, H. W. (1936). “Area and the Intensity-Time Relation in the Fovea”. *The Journal of General Psychology* 14 (2), pp. 360–369.

Keizaj, D. (2000). “Mesopic state: Cellular mechanisms involved in pre- and post-synaptic mixing of rod and cone signals”. *Microscopy Research and Technique* 50 (5), pp. 347–359.

Khuu, S. K. and Kalloniatis, M. (2015). “Standard Automated Perimetry: Determining Spatial Summation and Its Effect on Contrast Sensitivity Across the Visual Field.” *Investigative ophthalmology & visual science* 56 (6), pp. 3565–76.

Kiely, P., Smith, G., and Carney, L. (1982). “The Mean Shape of the Human Cornea”. *Optica Acta: International Journal of Optics* 29 (8), pp. 1027–1040.

King-Smith, P. E., Grigsby, S. S., Vingrys, A. J., Benes, S. C., and Supowit, A. (1994). “Efficient and unbiased modifications of the QUEST threshold method: Theory, simulations, experimental evaluation and practical implementation”. *Vision Research* 34 (7), pp. 885–912.

Kingdom, F. A. A. and Prins, N (2010). *Psychophysics: A Practical Introduction*. First edit. London: Academic Press.

Kocaoglu, O. P., Liu, Z., Zhang, F., Kurokawa, K., Jonnal, R. S., and Miller, D. T. (2016). “Photoreceptor disc shedding in the living human eye.” *Biomedical optics express* 7 (11), pp. 4554–4568.

Koenig, D. and Hofer, H. (2011). “The absolute threshold of cone vision.” *Journal of vision* 11 (1), pp. 1–24.

Kolb, H and Famiglietti, E. V. (1974). “Rod and cone pathways in the inner plexiform layer of cat retina.” *Science* 186 (4158), pp. 47–9.

Kolb, H. (1995). *Webvision: The Organization of the Retina and Visual System [Internet]*. Ed. by H. Kolb, E Fernandez, and N. R. URL: `https://webvision.med.utah.edu/` (visited on 11/03/2020).

Kolb, H. and Marshak, D. (2003). “The midget pathways of the primate retina”. *Documenta Ophthalmologica* 106 (1), pp. 67–81.

Krauskopf, J and Mollon, J. D. (1971). “The independence of the temporal integration properties of individual chromatic mechanisms in the human eye.” *The Journal of physiology* 219 (3), pp. 611–23.

Krauskopf, J. (1962). “Light Distribution in Human Retinal Images”. *Journal of the Optical Society of America* 52 (9), pp. 1046–1050.

Krauskopf, J. (1964). “Color Appearance of Small Stimuli and the Spatial Distribution of Color Receptors”. *Journal of the Optical Society of America* 54 (9), p. 1171.

Kruger, P. B., Mathews, S, Aggarwala, K. R., and Sanchez, N (1993). “Chromatic aberration and ocular focus: Fincham revisited.” *Vision research* 33 (10), pp. 1397–411.

Łabuz, G., Rayamajhi, A., Usinger, J., Komar, K., Merz, P., Khoramnia, R., Palczewska, G., Palczewski, K., and Auffarth, G. U. (2020). “Clinical application of infrared-light microperimetry in the assessment of scotopic-eye sensitivity”. *Translational Vision Science and Technology* 9 (8), pp. 1–9.

Lakshminarayanan, V. and Fleck, A. (2011). “Zernike polynomials: a guide”. *Journal of Modern Optics* 58 (7), pp. 545–561.

Lamb, T. D. (1995). “Photoreceptor spectral sensitivities: Common shape in the long-wavelength region”. *Vision Research* 35 (22), pp. 3083–3091.

Latch, M and Lennie, P (1977). “Rod-cone interaction in light adaptation.” *The Journal of physiology* 269 (3), pp. 517–34.

Le Grand, Y. (1935). “Sur la mesure de l’acuité visuelle au moyen de franges d’interférence”. *Compte Rendus De L’Académie Des Sci* 200, pp. 490–491.

Li, P. H., Field, G. D., Greschner, M., Ahn, D., Gunning, D. E., Mathieson, K., Sher, A., Litke, A. M., and Chichilnisky, E. J. (2014). “Retinal Representation of the Elementary Visual Signal”. *Neuron* 81 (1), pp. 130–139.

Liang, J and Williams, D. R. (1997). “Aberrations and retinal image quality of the normal human eye.” *Journal of the Optical Society of America. A, Optics, image science, and vision* 14 (11), pp. 2873–2883.

Liang, J, Williams, D. R., and Miller, D. T. (1997). “Supernormal vision and high-resolution retinal imaging through adaptive optics.” *Journal of the Optical Society of America. A, Optics, image science, and vision* 14 (11), pp. 2884–2892.

Liang, J., Grimm, B., Goelz, S., and Bille, J. F. (1994). “Objective measurement of wave aberrations of the human eye with the use of a Hartmann-Shack wave-front sensor”. *Journal of the Optical Society of America A: Optics and Image Science, and Vision* 11 (7), pp. 1949–1957.

Liu, J. K., Schreyer, H. M., Onken, A., Rozenblit, F., Khani, M. H., Krishnamoorthy, V., Panzeri, S., and Gollisch, T. (2017). “Inference of neuronal functional circuitry with spike-triggered non-negative matrix factorization”. *Nature Communications* 8 (1).

Liu, Z., Kocaoglu, O. P., Turner, T. L., and Miller, D. T. (2015). “Modal content of living human cone photoreceptors”. *Biomedical Optics Express* 6 (9), pp. 3378–3404.

Lodriguss, J. (2014). *20 Fun Naked Eye Doubles*. URL: `https://www.astropix.com/html/observing/20_fun_naked_eye_doubles.html` (visited on 12/12/2020).

Lorenz, B, Gyürüs, P, Preising, M, Bremser, D, Gu, S, Andrassi, M, Gerth, C, and Gal, A (2000). “Early-onset severe rod-cone dystrophy in young children with RPE65 mutations.” *Investigative ophthalmology and visual science* 41 (9), pp. 2735–42.

Lu, R.-W., Curcio, C. A., Zhang, Y., Zhang, Q.-X., Pittler, S. J., Deretic, D., and Yao, X.-C. (2012). “Investigation of the hyper-reflective inner/outer segment band in optical coherence tomography of living frog retina”. *Journal of Biomedical Optics* 17 (6), p. 060504.

Lu, Y., Benedetti, J., and Yao, X. (2018). “Light-Induced Length Shrinkage of Rod Photoreceptor Outer Segments.” *Translational vision science & technology* 7 (6), p. 29.

Lunghi, C., Burr, D. C., and Morrone, C. (2011). “Brief periods of monocular deprivation disrupt ocular balance in human adult visual cortex”. *Current Biology* 21 (14), R538–R539.

MacLeod, D. I., Williams, D. R., and Makous, W. (1992). “A visual nonlinearity fed by single cones.” *Vision research* 32 (2), pp. 347–63.

Maden, G., Cakir, A., Icar, D., Erden, B., Bolukbasi, S., and Elcioglu, M. (2017). “The Distribution of the Photoreceptor Outer Segment Length in a Healthy Population”. *Journal of Ophthalmology* 2017.

Mainster, M. A., Timberlake, G. T., Webb, R. H., and Hughes, G. W. (1982). “Scanning laser ophthalmoscopy. Clinical applications.” *Ophthalmology* 89 (7), pp. 852–7.

Makous, W. and Boothe, R. (1974). “Cones block signals from rods”. *Vision Research* 14 (4), pp. 285–294.

Maniscalco, B., McCurdy, L. Y., Odegaard, B., and Lau, H. (2017). “Limited cognitive resources explain a trade-off between perceptual and metacognitive vigilance”. *Journal of Neuroscience* 37 (5), pp. 1213–1224.

Marcos, S., Burns, S. A., Moreno-Barriusop, E., and Navarro, R. (1999). “A new approach to the study of ocular chromatic aberrations.” *Vision research* 39 (26), pp. 4309–23.

Marcos, S., Burns, S. A., Prieto, P. M., Navarro, R., and Baraibar, B. (2001). “Investigating sources of variability of monochromatic and transverse chromatic aberrations across eyes”. *Vision Research* 41 (28), pp. 3861–3871.

Marcos, S., Perez-Merino, P., and Dorronsoro, C. (2017). “Peripheral aberrations”. In: *Handbook of Visual Optics: Fundamentals and Eye Optics, Volume One*. Ed. by P. Artal. Taylor and Francis Group. Chap. 21, pp. 313–336.

Marcos, S., Tornow, R. P., Elsner, A. E., and Navarro, R. (1997). “Foveal cone spacing and cone photopigment density difference: Objective measurements in the same subjects”. *Vision Research* 37 (14), pp. 1909–1915.

Marriott, F. H. C. (1963). “The foveal absolute visual threshold for short flashes and small fields”. *The Journal of Physiology* 169 (2), pp. 416–423.

Martinez-Conde, S., Macknik, S. L., and Hubel, D. H. (2004). “The role of fixational eye movements in visual perception.” *Nature reviews. Neuroscience* 5 (3), pp. 229–240.

Marzejon, M. J., Kornaszewski, Ł., Bogusławski, J., Ciąćka, P., Martynow, M., Palczewska, G., Maćkowski, S., Palczewski, K., Wojtkowski, M., and Komar, K. (2021). “Two-photon microperimetry with picosecond pulses”. *Biomedical Optics Express* 12 (1), p. 462.

Massof, R. W. and Finkelstein, D. (1979). “Rod sensitivity relative to cone sensitivity in retinitis pigmentosa”. *Investigative Ophthalmology and Visual Science* 18 (3), pp. 263–272.

McLaughlin, A. J., Percival, K. A., Gayet-Primo, J., and Puthussery, T. (2020). “Glycinergic Inhibition Targets Specific Off Cone Bipolar Cells In Primate Retina”. *Eneuro*, ENEURO.0432–20.2020.

Meadway, A. and Sincich, L. C. (2018). “Light propagation and capture in cone photoreceptors”. *Biomedical Optics Express* 9 (11), p. 5543.

Meadway, A. and Sincich, L. C. (2019). “Light reflectivity and interference in cone photoreceptors”. *Biomedical Optics Express* 10 (12), p. 6531.

Meister, M. and Tessier-Lavigne, M. (2013). “Low-Level Visual Processing: The Retina”. In: *Principles of Neural Science*. Ed. by E. R. Kandel, J. H. Schwartz, T. M. Jessell, S. A. Siegelbaum, and A. J. Hudspeth. 5th Editio. New York: McGraw-Hill. Chap. 26, pp. 577–601.

Merino, D., Duncan, J. L., Tiruveedhula, P., and Roorda, A. (2011). “Observation of cone and rod photoreceptors in normal subjects and patients using a new generation adaptive optics scanning laser ophthalmoscope.” *Biomedical optics express* 2 (8), pp. 2189–201.

Miraldi Utz, V., Coussa, R. G., Antaki, F., and Traboulsi, E. I. (2018). “Gene therapy for RPE65-related retinal disease”. *Ophthalmic Genetics* 39 (6), pp. 671–677.

Mitamura, Y, Aizawa, S, Baba, T, Hagiwara, A, and Yamamoto, S (2009). “Correlation between retinal sensitivity and photoreceptor inner/outer segment junction in patients with retinitis pigmentosa”. *British Journal of Ophthalmology* 93 (1), pp. 126–127.

Model, D., Eizenman, M., and Sturm, V. (2010). “Fixation-free assessment of the Hirschberg ratio.” *Investigative ophthalmology & visual science* 51 (8), pp. 4035–9.

Montés-Micó, R., Cerviño, A., Ferrer-Blasco, T., García-Lázaro, S., and Madrid-Costa, D. (2010). “The tear film and the optical quality of the eye.” *The ocular surface* 8 (4), pp. 185–92.

Morgan, J. I. W. (2016). “The fundus photo has met its match: optical coherence tomography and adaptive optics ophthalmoscopy are here to stay”. *Ophthalmic and Physiological Optics* 36 (3), pp. 218–239.

Morimoto, C. H. and Mimica, M. R. (2005). “Eye gaze tracking techniques for interactive applications”. *Computer Vision and Image Understanding* 98 (1), pp. 4–24.

Nachmias, J (1959). “Two-dimensional motion of the retinal image during monocular fixation.” *Journal of the Optical Society of America* 49 (9), pp. 901–8.

Nelson, R (1977). “Cat cones have rod input: a comparison of the response properties of cones and horizontal cell bodies in the retina of the cat.” *The Journal of comparative neurology* 172 (1), pp. 109–35.

Nelson, R and Kolb, H (1984). “Amacrine cells in scotopic vision.” *Ophthalmic research* 16 (1-2), pp. 21–6.

Noorden, G. K. von and Mackensen, G. (1962). “Phenomenology of eccentric fixation”. *American Journal of Ophthalmology* 53 (4), pp. 642–661.

Normann, R. A. and Perlman, I (1979). “The effects of background illumination on the photoresponses of red and green cones.” *The Journal of physiology* 286, pp. 491–507.

Nuechterlein, K. H., Parasuraman, R, and Jiang, Q (1983). “Visual sustained attention: image degradation produces rapid sensitivity decrement over time.” *Science (New York, N.Y.)* 220 (4594), pp. 327–9.

Ogboso, Y. U. and Bedell, H. E. (1987). “Magnitude of lateral chromatic aberration across the retina of the human eye.” *Journal of the Optical Society of America. A, Optics and image science* 4 (8), pp. 1666–72.

Owsley, C., Jackson, G. R., Cideciyan, A. V., Huang, Y., Fine, S. L., Ho, A. C., Maguire, M. G., Lolley, V., and Jacobson, S. G. (2000). “Psychophysical evidence for rod vulnerability in age-related macular degeneration.” *Investigative ophthalmology & visual science* 41 (1), pp. 267–73.

Palczewska, G., Vinberg, F., Stremplewski, P., Bircher, M. P., Salom, D., Komar, K., Zhang, J., Cascella, M., Wojtkowski, M., Kefalov, V. J., and Palczewski, K. (2014). “Human infrared vision is triggered by two-photon chromophore isomerization.” *Proceedings of the National Academy of Sciences of the United States of America* 111 (50), E5445–5454.

Pandiyan, V. P., Maloney-Bertelli, A., Kuchenbecker, J. A., Boyle, K. C., Ling, T., Chen, Z. C., Hyle Park, B., Roorda, A., Palanker, D., and Sabesan, R. (2020). “The optoretinogram reveals the primary steps of phototransduction in the living human eye”. *Science Advances* 6 (37), pp. 1–12.

Parasuraman, R., Nestor, P., and Greenwood, P. (1989). “Sustained-attention capacity in young and older adults.” *Psychology and aging* 4 (3), pp. 339–45.

Petermann, K. (2012). “Laser diode modulation and noise”. In: *Advances in Optoelectronics*. Dordrecht: Kluwer Academic Publishers. Chap. Intensity-, pp. 78–114.

Pfäffle, C., Spahr, H., Kutzner, L., Burhan, S., Hilge, F., Miura, Y., Hüttmann, G., and Hillmann, D. (2019). “Simultaneous functional imaging of neuronal and photoreceptor layers in living human retina”. *Optics Letters* 44 (23), p. 5671.

Pfau, M., Holz, F. G., and Müller, P. L. (2021). “Retinal light sensitivity as outcome measure in recessive Stargardt disease.” *The British journal of ophthalmology* 105 (2), pp. 258–264.

Pfau, M., Jolly, J. K., Wu, Z., Denniss, J., Lad, E. M., Guymer, R. H., Fleckenstein, M., Holz, F. G., and Schmitz-Valckenberg, S. (2020). “Fundus-controlled perimetry (microperimetry): Application as outcome measure in clinical trials”. *Progress in Retinal and Eye Research*, p. 100907.

Pfau, M., Lindner, M., Steinberg, J. S., Thiele, S., Brinkmann, C. K., Fleckenstein, M., Holz, F. G., and Schmitz-Valckenberg, S. (2018). “Visual field indices and patterns of visual field deficits in mesopic and dark-adapted two-colour fundus-controlled perimetry in macular diseases.” *The British journal of ophthalmology* 102 (8), pp. 1054–1059.

Poletti, M., Listorti, C., and Rucci, M. (2013). “Microscopic eye movements compensate for nonhomogeneous vision within the fovea”. *Current Biology* 23 (17), pp. 1691–1695.

Polyak, S. L. (1941). *The Retina*. Chicago: University of Chicago Press.

Poonja, S., Patel, S., Henry, L., and Roorda, A. (2005). “Dynamic visual stimulus presentation in an adaptive optics scanning laser ophthalmoscope.” *Journal of refractive surgery (Thorofare, N.J. : 1995)* 21 (5), S575–S580.

Pritchard, R. M. (1961). “Stabilized images on the retina.” *Scientific American* 204, pp. 72–8.

Privitera, C. M., Sabesan, R., Winter, S., Tiruveedhula, P., and Roorda, A. (2016). “Eye-tracking technology for real-time monitoring of transverse chromatic aberration.” *Optics letters* 41 (8), pp. 1728–31.

Provis, J. M., Dubis, A. M., Maddess, T., and Carroll, J. (2013). “Adaptation of the central retina for high acuity vision: Cones, the fovea and the a vascular zone”. *Progress in Retinal and Eye Research* 35, pp. 63–81.

Putnam, N. M., Hofer, H. J., Doble, N., Chen, L., Carroll, J., and Williams, D. R. (2005). “The locus of fixation and the foveal cone mosaic.” *Journal of vision* 5 (7), pp. 632–9.

Ratnam, K., Domdei, N., Harmening, W. M., and Roorda, A. (2017). “Benefits of retinal image motion at the limits of spatial vision.” *Journal of vision* 17 (1), p. 30.

Rees, A., Kabanarou, S., Culham, L., and Rubin, G. (2005). “Can retinal eccentricity predict visual acuity and contrast sensitivity at the PRL in AMD patients?” *International Congress Series* 1282, pp. 694–698.

Reeves, A., Wu, S., and Schirillo, J. (1998). “The effect of photon noise on the detection of white flashes”. *Vision Research* 38 (5), pp. 691–703.

Reinholz, F., Ashman, R. A., and Eikelboom, R. H. (1999). “Simultaneous three wavelength imaging with a scanning laser ophthalmoscope.” *Cytometry* 37 (3), pp. 165–70.

Reiniger, J. L., Domdei, N., Holz, F. G., and Harmening, W. M. (2021). “Human gaze is precisely aligned with the foveolar cone topography of both eyes”. *bioRxiv doi:10.1101/2021.03.19.436115*.

Reiniger, J. L., Domdei, N., Linden, M., Holz, F. G., and Harmening, W. M. (2019a). “Relationship between the foveal photoreceptor mosaic and adaptive optics corrected visual acuity”. *Investigative Ophthalmology and Visual Science* 60 (9), p. 1777.

Reiniger, J. L., Lobecke, A. C., Sabesan, R., Bach, M., Verbakel, F., Brabander, J. de, Holz, F. G., Berendschot, T. T. J. M., and Harmening, W. M. (2019b). “Habitual higher order aberrations affect Landolt but not Vernier acuity.” *Journal of vision* 19 (5), p. 11.

Reiniger, J., Domdei, N., Holz, F., and Harmening, W. (2017). “[Technical principles of adaptive optics in ophthalmology].” *Der Ophthalmologe : Zeitschrift der Deutschen Ophthalmologischen Gesellschaft* 114 (3), pp. 198–205.

Ricco, A. (1877). “Relazione fra il minimo angolo visuale e l’intensit‘a luminosa”. *Memorie della Societa Degli Spettroscopisti Italiani* 6, B29–B58.

Rieger, G. (1992). “The importance of the precorneal tear film for the quality of optical imaging”. *British Journal of Ophthalmology* 76 (3), pp. 157–158.

Riggs, L. a., Ratliff, F, Cornsweet, J. C., and Cornsweet, T. N. (1953). “The disappearance of steadily fixated visual test objects.” *Journal of the Optical Society of America* 43 (6), pp. 495–501.

Rodieck, R. W. and Rushton, W. A. (1976). “Cancellation of rod signals by cones, and cone signals by rods in the cat retina.” *The Journal of physiology* 254 (3), pp. 775–85.

Rodieck, R. W. (1998). *The First Steps in Seeing*. Ed. by R. W. Rodieck. Sunderland: Sinauer Associates.

Roorda, A. (2010). “Applications of adaptive optics scanning laser ophthalmoscopy.” *Optometry and vision science : official publication of the American Academy of Optometry* 87 (4), pp. 260–268.

Roorda, A. (2011). “Adaptive optics for studying visual function: A comprehensive review”. *Journal of vision* 11 (5), pp. 1–21.

Roorda, A. and Duncan, J. L. (2015). *Adaptive optics ophthalmoscopy.* Vol. 1. Sec 3, pp. 19–50.

Roorda, A., Romero-Borja, F., Donnelly, III, W., Queener, H., Hebert, T., and Campbell, M. (2002). “Adaptive optics scanning laser ophthalmoscopy”. *Optics Express* 10 (9), pp. 405–412.

Roorda, A. and Williams, D. R. (1999). “The arrangement of the three cone classes in the living human eye.” *Nature* 397 (6719), pp. 520–522.

Roorda, A. and Williams, D. R. (2002). “Optical fiber properties of individual human cones.” *Journal of vision* 2 (5), pp. 404–412.

Rossi, E. A., Achtman, R. L., Guidon, A., Williams, D. R., Roorda, A., Bavelier, D., and Carroll, J. (2013). “Visual Function and Cortical Organization in Carriers of Blue Cone Monochromacy”. *PLoS ONE* 8 (2), pp. 9–11.

Rossi, E. A., Granger, C. E., Sharma, R., Yang, Q., Saito, K., Schwarz, C., Walters, S., Nozato, K., Zhang, J., Kawakami, T., Fischer, W., Latchney, L. R., Hunter, J. J., Chung, M. M., and Williams, D. R. (2017). “Imaging individual neurons in the retinal ganglion cell layer of the living eye.” *Proceedings of the National Academy of Sciences of the United States of America* 114 (3), pp. 586–591.

Rossi, E. a. and Roorda, A. (2010). “The relationship between visual resolution and cone spacing in the human fovea.” *Nature neuroscience* 13 (2), pp. 156–157.

Roth, M, Tseitlin, M, and Angert, N (2005). “Oxide Crystals for Electro-Optic Q -Switching of Lasers”. *Glass Physics and Chemistry* 31 (1), pp. 86–95.

Ruminski, D., Palczewska, G., Nowakowski, M., Zielińska, A., Kefalov, V. J., Komar, K., Palczewski, K., and Wojtkowski, M. (2019). “Two-photon microperimetry: sensitivity of human photoreceptors to infrared light”. *Biomedical Optics Express* 10 (9), p. 4551.

Rynders, M. C., Navarro, R., and Losada, M. A. (1998). “Objective measurement of the off-axis longitudinal chromatic aberration in the human eye.” *Vision research* 38 (4), pp. 513–22.

Rynders, M., Lidkea, B., Chisholm, W., and Thibos, L. N. (1995). “Statistical distribution of foveal transverse chromatic aberration, pupil centration, and angle psi in a population of young adult eyes.” *Journal of the Optical Society of America. A, Optics, image science, and vision* 12 (10), pp. 2348–57.

Sabesan, R., Schmidt, B. P., Tuten, W. S., and Roorda, A. (2016). “The elementary representation of spatial and color vision in the human retina.” *Science advances* 2 (9), e1600797.

Sakitt, B (1972). “Counting every quantum.” *The Journal of physiology* 223 (1), pp. 131–50.

Saleh, B. E. A. and Teich, M. C. (1991). “Acousto-optics”. In: *Fundamentals of Photonics*. John Wiley & Sons, Inc. Chap. 20.

Schaeffel, F. (2002). “Kappa and Hirschberg ratio measured with an automated video gaze tracker.” *Optometry and vision science : official publication of the American Academy of Optometry* 79 (5), pp. 329–34.

Schefrin, B. E., Bieber, M. L., McLean, R., and Werner, J. S. (1998). “The area of complete scotopic spatial summation enlarges with age.” *Journal of the Optical Society of America. A, Optics, image science, and vision* 15 (2), pp. 340–8.

Schmidt, B. P., Boehm, A. E., Foote, K. G., and Roorda, A. (2018a). “The spectral identity of foveal cones is preserved in hue perception.” *Journal of vision* 18 (11), p. 19.

Schmidt, B. P., Boehm, A. E., Foote, K. G., and Roorda, A. (2018b). “The spectral identity of foveal cones is preserved in hue perception.” *Journal of vision* 18 (11), p. 19.

Schmitz-Valckenberg, S., Ong, E. E. L., Rubin, G. S., Peto, T., Tufail, A., Egan, C. A., Bird, A. C., and Fitzke, F. W. (2009). “Structural and functional changes over time in MacTel patients.” *Retina (Philadelphia, Pa.)* 29 (9), pp. 1314–20.

Schnapf, J. L., Kraft, T. W., and Baylor, D. a. (1987). “Spectral sensitivity of human cone photoreceptors.” *Nature* 325 (6103), pp. 439–441.

Schnapf, J. L., Nunn, B. J., Meister, M, and Baylor, D. A. (1990). “Visual transduction in cones of the monkey Macaca fascicularis.” *The Journal of physiology* 427, pp. 681–713.

Schneeweis, D. M. and Schnapf, J. L. (1995). “Photovoltage of rods and cones in the macaque retina”. *Science* 268 (5213), pp. 1053–1056.

Scholtes, A. M. and Bouman, M. A. (1977). “Psychophysical experiments on spatial summation at threshold level of the human peripheral retina.” *Vision research* 17 (7), pp. 867–73.

Schwarz, C., Sharma, R., Cheong, S. K., Keller, M., Williams, D. R., and Hunter, J. J. (2018). “Selective S Cone Damage and Retinal Remodeling Following Intense Ultrashort Pulse Laser Exposures in the Near-Infrared.” *Investigative ophthalmology & visual science* 59 (15), pp. 5973–5984.

Scoles, D., Sulai, Y. N., and Dubra, A. (2013). “In vivo dark-field imaging of the retinal pigment epithelium cell mosaic.” *Biomedical optics express* 4 (9), pp. 1710–23.

Scoles, D., Sulai, Y. N., Langlo, C. S., Fishman, G. A., Curcio, C. A., Carroll, J., and Dubra, A. (2014). “In vivo imaging of human cone photoreceptor inner segments.” *Investigative ophthalmology and visual science* 55 (7), pp. 4244–51.

See, J. E., Howe, S. R., Warm, J. S., and Dember, W. N. (1995). “Meta-analysis of the sensitivity decrement in vigilance”. *Psychological Bulletin* 117 (2), pp. 230–249.

Sharpe, L. T., Fach, C., Nordby, K., and Stockman, A. (1989). “The incremental threshold of the rod visual system and Weber’s law”. *Science* 244 (4902), pp. 354–356.

Sharpe, L. T., Stockman, A., Jagla, W., and Jägle, H. (2005). “A luminous efficiency function, V*(lambda), for daylight adaptation.” *Journal of vision* 5 (11), pp. 948–968.

Sheehy, C. K., Yang, Q., Arathorn, D. W., Tiruveedhula, P., Boer, J. F. de, and Roorda, A. (2012). “High-speed, image-based eye tracking with a scanning laser ophthalmoscope.” *Biomedical optics express* 3 (10), pp. 2611–22.

Shortess, G. K. and Krauskopf, J. (1961). “Role of Involuntary Eye Movements in Stereoscopic Acuity”. *Journal of the Optical Society of America* 51 (5), p. 555.

Simonet, P and Campbell, M. C. (1990). “The optical transverse chromatic aberration on the fovea of the human eye.” *Vision research* 30 (2), pp. 187–206.

Sincich, L. C., Sabesan, R., Tuten, W. S., Roorda, A., and Harmening, W. M. (2016). “Functional Imaging of Cone Photoreceptors”. In: *Human Color Vision*. Ed. by J. Kremers, R. C. Baraas, and N. J. Marshall. Cham: Springer International Publishing, pp. 71–104.

Sincich, L. C., Zhang, Y., Tiruveedhula, P., Horton, J. C., and Roorda, A. (2009). “Resolving single cone inputs to visual receptive fields”. *Nature Neuroscience* 12 (8), pp. 967–969.

Sloan, L. L. (1939). “Instruments and Technics for The Clinical Testing of Light Sense”. *Archives of Ophthalmology* 21 (6), pp. 913–934.

Sloan, L. L. (1950). “The threshold gradients of the rods and the cones: In the dark-adapted and in the partially light-adapted eye”. *American Journal of Ophthalmology* 33 (7), pp. 1077–1089.

Slonaker, J. R. (1897). “A comparative study of the area of acute vision in vertebrates”. *Journal of Morphology* 13 (3), pp. 445–502.

Smith, A. T., Cotillon-Williams, N. M., and Williams, A. L. (2006). “Attentional modulation in the human visual cortex: The time-course of the BOLD response and its implications”. *NeuroImage* 29 (1), pp. 328–334.

Spaide, R. F. (2015). “Outer retinal bands”. *Investigative Ophthalmology and Visual Science* 56 (4), pp. 2505–2506.

Spaide, R. F. and Curcio, C. A. (2011). “Anatomical correlates to the bands seen in the outer retina by optical coherence tomography: Literature review and model”. *Retina* 31 (8), pp. 1609–1619.

Sperling, H. G. and Jolliffe, C. L. (1965). “Intensity–Time Relationship at Threshold for Spectral Stimuli in Human Vision*”. *Journal of the Optical Society of America* 55 (2), p. 191.

Srinivasan, V. J., Monson, B. K., Wojtkowski, M., Bilonick, R. A., Gorczynska, I., Chen, R., Duker, J. S., Schuman, J. S., and Fujimoto, J. G. (2008). “Characterization of outer retinal morphology with high-speed, ultrahigh-resolution optical coherence tomography”. *Investigative Ophthalmology and Visual Science* 49 (4), pp. 1571–1579.

Steinberg, J. S., Fitzke, F. W., Fimmers, R., Fleckenstein, M., Holz, F. G., and Schmitz-Valckenberg, S. (2015). “Scotopic and Photopic Microperimetry in Patients With Reticular Drusen and Age-Related Macular Degeneration.” *JAMA ophthalmology* 133 (6), pp. 690–7.

Steinman, R. M. (1965). “Effect of Target Size, Luminance, and Color on Monocular Fixation”. *Journal of the Optical Society of America* 55 (9), p. 1158.

Steinwurzel, C., Animali, S., Cicchini, G. M., Morrone, M. C., and Binda, P. (2020). “Using psychophysical performance to predict short-term ocular dominance plasticity in human adults”. *Journal of Vision* 20 (7), pp. 1–13.

Stiles, W. S. (1949). “Increment thresholds and the mechanisms of colour vision”. *Documenta Ophthalmologica* 3 (1), pp. 138–165.

Stockman, A., MacLeod, D. I. A., and Johnson, N. E. (1993). “Spectral sensitivities of the human cones”. *Journal of the Optical Society of America A* 10 (12), p. 2491.

Stockman, A. and Sharpe, L. T. (2006). “Into the twilight zone: the complexities of mesopic vision and luminous efficiency.” *Ophthalmic & physiological optics : the journal of the British College of Ophthalmic Opticians (Optometrists)* 26 (3), pp. 225–39.

Stoerig, P. and Cowey, A. (2007). “Blindsight”. *Current Biology* 17 (19), pp. 822–824.

Sulai, Y. N. and Dubra, A. (2012). “Adaptive optics scanning ophthalmoscopy with annular pupils.” *Biomedical optics express* 3 (7), pp. 1647–61.

Supriya, D., Shwetha, M., Kiran Anupama, K., Kummelil Mathew, K., Berendschot, T. T., Schouten, J. S., Bharamshetter, R., Naresh, Y. K., Rohit, S., and Hegde, B. (2015). “Structural and function correlation of cone packing utilizing adaptive optics and microperimetry”. *BioMed Research International* 2015.

Takeshita, D., Smeds, L., and Ala-Laurila, P. (2017). “Processing of single-photon responses in the mammalian On and Off retinal pathways at the sensitivity limit of vision.” *Philosophical transactions of the Royal Society of London. Series B, Biological sciences* 372 (1717).

Tamura, T, Nakatani, K, and Yau, K. W. (1989). “Light adaptation in cat retinal rods.” *Science (New York, N.Y.)* 245 (4919), pp. 755–758.

Taylor, W. R. and Smith, R. G. (2004). “Transmission of scotopic signals from the rod to rod-bipolar cell in the mammalian retina.” *Vision research* 44 (28), pp. 3269–76.

Thibos, L. N., Bradley, A., Still, D. L., Zhang, X., and Howarth, P. A. (1990). “Theory and measurement of ocular chromatic aberration”. *Vision Research* 30 (1), pp. 33–49.

Thibos, L. N., Ye, M., Zhang, X., and Bradley, A. (1992). “The chromatic eye: a new reduced-eye model of ocular chromatic aberration in humans.” *Applied optics* 31 (19), pp. 3594–600.

Thoreson, W. B. and Mangel, S. C. (2012). “Lateral interactions in the outer retina”. *Progress in Retinal and Eye Research* 31 (5), pp. 407–441.

Tikidji-Hamburyan, A., Reinhard, K., Storchi, R., Dietter, J., Seitter, H., Davis, K. E., Idrees, S., Mutter, M., Walmsley, L., Bedford, R. A., Ueffing, M., Ala-Laurila, P., Brown, T. M., Lucas, R. J., and Münch, T. A. (2017). “Rods progressively escape saturation to drive visual responses in daylight conditions”. *Nature Communications* 8 (1).

Timberlake, G. T., Mainster, M. A., Peli, E., Augliere, R. A., Essock, E. A., and Arend, L. E. (1986). “Reading with a macular scotoma. I. Retinal location of scotoma and fixation area”. *Investigative Ophthalmology and Visual Science* 27 (7), pp. 1137–1147.

Timberlake, G. T., Peli, E., Essock, E. A., and Augliere, R. A. (1987). “Reading with a macular scotoma. II. Retinal locus for scanning text”. *Investigative Ophthalmology and Visual Science* 28 (8), pp. 1268–1274.

Tinsley, J. N., Molodtsov, M. I., Prevedel, R., Wartmann, D., Espigulé-Pons, J., Lauwers, M., and Vaziri, A. (2016). “Direct detection of a single photon by humans”. *Nature Communications* 7, p. 12172.

Tornow, R. P. and Stilling, R (1998). “Variation in sensitivity, absorption and density of the central rod distribution with eccentricity.” *Acta anatomica* 162 (2-3), pp. 163–168.

Treutwein, B. (1995). “Adaptive psychophysical procedures.” *Vision research* 35 (17), pp. 2503–22.

Tsukamoto, Y. and Omi, N. (2014). “Some OFF bipolar cell types make contact with both rods and cones in macaque and mouse retinas.” *Frontiers in neuroanatomy* 8, p. 105.

Tsukamoto, Y. and Omi, N. (2016). “ON Bipolar Cells in Macaque Retina: Type-Specific Synaptic Connectivity with Special Reference to OFF Counterparts.” *Frontiers in neuroanatomy* 10, p. 104.

Tu, J. H., Foote, K. G., Lujan, B. J., Ratnam, K., Qin, J., Gorin, M. B., Cunningham, E. T., Tuten, W. S., Duncan, J. L., and Roorda, A. (2017). “Dysflective cones: Visual function and cone reflectivity in long-term follow-up of acute bilateral foveolitis.” *American journal of ophthalmology case reports* 7, pp. 14–19.

Tuten, W. S., Cooper, R. F., Tiruveedhula, P., Dubra, A., Roorda, A., Cottaris, N. P., Brainard, D. H., and Morgan, J. I. W. (2018). “Spatial summation in the human fovea: Do normal optical aberrations and fixational eye movements have an effect?” *Journal of vision* 18 (8), p. 6.

Tuten, W. S., Harmening, W. M., Sabesan, R., Roorda, A., and Sincich, L. C. (2017). “Spatiochromatic Interactions between Individual Cone Photoreceptors in the Human Retina.” *The Journal of neuroscience : the official journal of the Society for Neuroscience* 37 (39), pp. 9498–9509.

Tuten, W. S., Tiruveedhula, P., and Roorda, A. (2012). “Adaptive optics scanning laser ophthalmoscope-based microperimetry.” *Optometry and vision science : official publication of the American Academy of Optometry* 89 (5), pp. 563–74.

Tuten, W. S., Vergilio, G. K., Young, G. J., Bennett, J., Maguire, A. M., Aleman, T. S., Brainard, D. H., and Morgan, J. I. (2019). “Visual Function at the Atrophic Border in Choroideremia Assessed with Adaptive Optics Microperimetry”. *Ophthalmology Retina*, pp. 1–12.

Van Essen, D. C. (2004). “Organization of Visual Areas in Macaque and Human Cerebral Cortex”. *The Visual Neurosciences* 1, pp. 507–521.

Van Essen, D. C. and Drury, H. A. (1997). “Structural and functional analyses of human cerebral cortex using a surface-based atlas.” *The Journal of neuroscience : the official journal of the Society for Neuroscience* 17 (18), pp. 7079–102.

Van Essen, D. C., Newsome, W. T., and Maunsell, J. H. (1984). “The visual field representation in striate cortex of the macaque monkey: asymmetries, anisotropies, and individual variability.” *Vision research* 24 (5), pp. 429–48.

Vinas, M., Dorronsoro, C., Cortes, D., Pascual, D., and Marcos, S. (2015). “Longitudinal chromatic aberration of the human eye in the visible and near infrared from wavefront sensing, double-pass and psychophysics.” *Biomedical optics express* 6 (3), pp. 948–62.

Vislisel, J. M., Doyle, C. K., Johnson, C. A., and Wall, M. (2011). “Variability of rarebit and standard perimetry sizes i and III in normals”. *Optometry and Vision Science* 88 (5), pp. 635–639.

Vohnsen, B., Iglesias, I., and Artal, P. (2005). “Guided light and diffraction model of human-eye photoreceptors.” *Journal of the Optical Society of America. A, Optics, image science, and vision* 22 (11), pp. 2318–28.

Volbrecht, V. J., Shrago, E. E., Schefrin, B. E., and Werner, J. S. (2000). “Spatial summation in human cone mechanisms from 0 degrees to 20 degrees in the superior retina.” *Journal of the Optical Society of America. A, Optics, image science, and vision* 17 (3), pp. 641–50.

Völgyi, B., Deans, M. R., Paul, D. L., and Bloomfield, S. A. (2004). “Convergence and segregation of the multiple rod pathways in mammalian retina”. *Journal of Neuroscience* 24 (49), pp. 11182–11192.

Wald, G. (1945). “Human vision and the spectrum”. *Science* 101 (2635), pp. 653–658.

Wang, M., McGraw, P., and Ledgeway, T. (2020). “Short-term monocular deprivation reduces inter-ocular suppression of the deprived eye”. *Vision Research* 173 (May), pp. 29–40.

Wang, Q., Tuten, W. S., Lujan, B. J., Holland, J., Bernstein, P. S., Schwartz, S. D., Duncan, J. L., and Roorda, A. (2015). “Adaptive optics microperimetry and OCT images show preserved function and recovery of cone visibility in macular telangiectasia type 2 retinal lesions.” *Investigative ophthalmology & visual science* 56 (2), pp. 778–86.

Wang, Y., Bensaid, N., Tiruveedhula, P., Ma, J., Ravikumar, S., and Roorda, A. (2019). “Human foveal cone photoreceptor topography and its dependence on eye length.” *eLife* 8.

Watson, A. B. (2014). “A formula for human retinal ganglion cell receptive field density as a function of visual field location.” *Journal of vision* 14 (7), pp. 1–17.

Watson, A. B. and Pelli, D. G. (1983). “QUEST: a Bayesian adaptive psychometric method.” *Perception & psychophysics* 33 (2), pp. 113–20.

Webb, R. H. and Hughes, G. W. (1981). “Scanning laser ophthalmoscope.” *IEEE transactions on biomedical engineering* 28 (7), pp. 488–492.

Webb, R. H., Hughes, G. W., and Delori, F. C. (1987). “Confocal scanning laser ophthalmoscope.” *Applied optics* 26 (8), pp. 1492–1499.

Webb, R. H., Hughes, G. W., and Pomerantzeff, O (1980). “Flying spot TV ophthalmoscope.” *Applied optics* 19 (17), pp. 2991–2997.

Whittaker, S. G., Budd, J., and Cummings, R. W. (1988). “Eccentric fixation with macular scotoma”. *Investigative Ophthalmology and Visual Science* 29 (2), pp. 268–278.

Wildenmann, U. and Schaeffel, F. (2013). “Variations of pupil centration and their effects on video eye tracking.” *Ophthalmic & physiological optics : the journal of the British College of Ophthalmic Opticians (Optometrists)* 33 (6), pp. 634–41.

Wilk, M. A., Dubis, A. M., Cooper, R. F., Summerfelt, P., Dubra, A., and Carroll, J. (2017a). “Assessing the spatial relationship between fixation and foveal specializations”. *Vision Research* 132, pp. 53–61.

Wilk, M. A., Wilk, B. M., Langlo, C. S., Cooper, R. F., and Carroll, J. (2017b). “Evaluating outer segment length as a surrogate measure of peak foveal cone density”. *Vision Research* 130, pp. 57–66.

Wilke, R., Bach, M., Wilhelm, B., Durst, W., Trauzettel-Klosinski, S., and Zrenner, E. (2004). “Testing Visual Functions in Patients with Visual Prostheses”. In: *Artificial Sight*. June. New York, NY: Springer New York, pp. 91–110.

Willging, A. (2011). *Grit Vs. Gears In A Galaxy Far, Far Away: Star Wars: Republic Commando*. URL: `https://rhapsodistreviews.files.wordpress.com/2010/11/republic-commando-promo.jpg` (visited on 11/18/2020).

Williams, D. R., MacLeod, D. I., and Hayhoe, M. M. (1981). “Punctate sensitivity of the blue-sensitive mechanism.” *Vision research* 21 (9), pp. 1357–75.

Williams, D. R. (1985a). “Aliasing in human foveal vision”. *Vision Research* 25 (2), pp. 195–205.

Williams, D. R. (1985b). “Visibility of interference fringes near the resolution limit.” *Journal of the Optical Society of America. A, Optics and image science* 2 (7), pp. 1087–1093.

Williams, D. R. (2011). “Imaging single cells in the living retina.” *Vision research* 51 (13), pp. 1379–96.

Williams, D. R. and Coletta, N. J. (1987). “Cone spacing and the visual resolution limit.” *Journal of the Optical Society of America. A, Optics and image science* 4 (8), pp. 1514–1523.

Wilson, D. A. (2017). “Refractive errors”. In: *Handbook of Visual Optics: Fundamentals and Eye Optics, Volume One*. Ed. by P. Artal. Taylor & Francis Group. Chap. 19, pp. 277–292.

Winter, S., Sabesan, R., Tiruveedhula, P., Privitera, C., Unsbo, P., Lundström, L., and Roorda, A. (2016). “Transverse chromatic aberration across the visual field of the human eye.” *Journal of vision* 16 (14), p. 9.

Wu, Z., Ayton, L. N., Luu, C. D., and Guymer, R. H. (2014). “Relationship between retinal microstructures on optical coherence tomography and microperimetry in age-related macular degeneration”. *Ophthalmology* 121 (7), pp. 1445–1452.

Xie, W., Zhao, M., Tsai, S. H., Burkes, W. L., Potts, L. B., Xu, W., Payne, H. R., Hein, T. W., Kuo, L., and Rosa, R. H. (2018). “Correlation of spectral domain optical coherence tomography with histology and electron microscopy in the porcine retina”. *Experimental Eye Research* 177 (April), pp. 181–190.

Yamada, E. (1969). “Some structural features of the fovea centralis in the human retina”. *Archives of Ophthalmology* 82 (2), pp. 151–159.

Yang, Q., Arathorn, D. W., Tiruveedhula, P., Vogel, C. R., and Roorda, A. (2010). “Design of an integrated hardware interface for AOSLO image capture and cone-targeted stimulus delivery.” *Optics express* 18 (17), pp. 17841–58.

Yang, X. L. and Wu, S. M. (1989). “Modulation of rod-cone coupling by light.” *Science (New York, N.Y.)* 244 (4902), pp. 352–4.

Yoon, G.-Y. and Williams, D. R. (2002). “Visual performance after correcting the monochromatic and chromatic aberrations of the eye.” *Journal of the Optical Society of America. A, Optics, image science, and vision* 19 (2), pp. 266–275.

Yuodelis, C. and Hendrickson, A. (1986). “A qualitative and quantitative analysis of the human fovea during development.” *Vision research* 26 (6), pp. 847–55.

Zeffren, B. S., Applegate, R. A., Bradley, A., and Heuven, W. A. van (1990). “Retinal fixation point location in the foveal avascular zone.” *Investigative ophthalmology and visual science* 31 (10), pp. 2099–105.

Zhang, C., Kim, Y. J., Silverstein, A. R., Hoshino, A., Reh, T. A., Dacey, D. M., and Wong, R. O. (2020). “Circuit Reorganization Shapes the Developing Human Foveal Midget Connectome toward Single-Cone Resolution”. *Neuron* 108 (5), 905–918.e3.

Zhang, J., Yang, Q., Saito, K., Nozato, K., Williams, D. R., and Rossi, E. A. (2015a). “An adaptive optics imaging system designed for clinical use”. *Biomedical Optics Express* 6 (6), pp. 2120–2137.

Zhang, P., Zawadzki, R. J., Goswami, M., Nguyen, P. T., Yarov-Yarovoy, V., Burns, M. E., and Pugh, E. N. (2017). “In vivo optophysiology reveals that G-protein activation triggers osmotic swelling and increased light scattering of rod photoreceptors”. *Proceedings of the National Academy of Sciences* 114 (14), E2937–E2946.

Zhang, Q., Lu, R., Wang, B., Messinger, J. D., Curcio, C. a., and Yao, X. (2015b). “Functional optical coherence tomography enables in vivo physiological assessment of retinal rod and cone photoreceptors.” *Scientific reports* 5, p. 9595.

Zhang, Y. and Roorda, A. (2006). “Evaluating the lateral resolution of the adaptive optics scanning laser ophthalmoscope.” *Journal of biomedical optics* 11 (1), p. 014002.

Ziccardi, L., Cordeddu, V., Gaddini, L., Matteucci, A., Parravano, M., Malchiodi-Albedi, F., and Varano, M. (2019). “Gene therapy in retinal dystrophies”. *International Journal of Molecular Sciences* 20 (22).

List of Abbreviations and Units

2AFC	Two-alternative-forced-choice
AO	Adaptive optics
AOSLO	Adaptive optics scanning laser ophthalmoscope
AOM	Acousto-optic modulator
arcmin	Minutes of arc (1/60 degree)
arcsec	Seconds of arc (1/3600 degree)
BCEA	Bivariate contour ellipse area
cd	Candela
CRT	Cathode ray tube
D	Diopter
FEM	Fixational eye movements
HOA	Higher-order aberrations
IR	Infrared
KHz	Kilohertz
LCA	Longitudinal chromatic aberration
LOA	Lower-order aberrations
LUT	Look up table
MHz	Megahertz
μm	Micrometer
ND	Neutral density
nm	Nanometer
OCT	Optical coherence tomography
OS	Outer segment
PMT	Photomultiplier tube
PSF	Point spread function
QUEST	Quick estimate by sequential testing
RMS	Root-mean-square
RPE	Retinal pigment epithelium
SLO	Scanning laser ophthalmoscope
STD	Standard deviation
TCA	Transverse (or lateral) chromatic aberration
TCO	Transverse chromatic offset
TPXS	two-photon absorption cross section

Publications in peer-reviewed journals (*denotes equal contribution)

Domdei N, Reiniger JL, Holz FG, Harmening WM (2021) The Relationship Between Visual Sensitivity and Eccentricity, Cone Density and Outer Segment Length in the Human Foveola. *Investigative Ophthalmology and Visual Science,* 62(9): 31

Reiniger JL, **Domdei N**, Holz FG, Harmening WM (2021) Human gaze is precisely aligned with the foveolar cone topography of both eyes. *Under Review (Current Biology)*

Domdei N, Linden M, Reiniger J, Holz FG, Harmening WM (2019) Eye tracking based estimation and compensation of chromatic offsets for multi wavelength retinal microstimulation with foveal cone precision. *Biomedical Optics Express,* 10(8): 4126-4141

Domdei N*,Domdei L*, Reiniger J, Linden M, Holz FG, Roorda A, Harmening WM (2018) Ultra-high contrast retinal display system for single photoreceptor psychophysics. *Biomedical Optics Express,* 9(1): 157-172

Reiniger JL*, **Domdei N***, Pfau M, Issa PC, Holz FG, Harmening WM (2017) Potential of Adaptive Optics for the Diagnostic Evaluation of Hereditary Retinal Diseases. *Klinische Monatsblätter,* 234(03): 311-319

Domdei N, Reiniger JL, Pfau M, Issa PC, Holz FG, Harmening WM (2017) Histology of the living eye. Noninvasive microscopic structure and functional analysis of the retina with adaptive optics. *Der Ophthalmologe,* 114(3):206-214

Neitz A, Jian X, Kuchenbecker JA, **Domdei N**, Harmening WM, Yan H, Yeonan-Kim J, Patterson SS, Neitz M, Neitz J, Coates D, Sabesan R (2020) Effect of cone spectral topography on chromatic detection sensitivity. *Journal of the Optical Society of America A*, 37 (4): A244-A254

Fang P, **Domdei N**, Herrmann P, Schmitz-Valckenberg S, Holz F, Harmening W, Krohne T (2019) Minimal optical coherence tomography B-scan density for reliable detection of intra- and subretinal fluid in macular diseases. *Retina,* 39(1):150-156

Reiniger JL, **Domdei N**, Holz FG, Harmening WM (2017) Technical principles of adaptive optics in ophthalmology. *Der Ophthalmologe,* 114(3):198-205

Ratnam K, **Domdei N**, Harmening WM, Roorda AJ (2017) Benefits of retinal image motion at the limits of spatial vision. *Journal of Vision,* 17(30):1-11

Lindner M, Fang P, Steinberg J, **Domdei N**, Pfau M, Krohne T, Schmitz-Valckenberg S, Holz FG, Fleckenstein M (2016) OCT-Angiography-based detection and quantification of the neovascular network in exudative AMD. *Investigative Ophthalmology & Visual Science,* 57: 6342-6348

Conference presentations (Talks)

Domdei N, Harmening WM (2020) Retinal factors of foveal sensitivity. e-meeting *i2Eye2020*

Domdei N, Holz F, Harmening WM (2019) Photoreceptor-targeted psychophysics with adaptive optics scanning laser ophthalmoscopy. *Young Researcher Vision Camp*, Leibertingen, Germany

Domdei N, Reiniger JL, Linden M, Holz FG, Harmening WM (2019) Mapping the sensitivity of the central fovea with cone-targeted microstimulation. *ARVO*, Vancouver, Canada

Domdei N, Harmening WM (2018) Funktioniert Psychophysik auf Einzelzellniveau auch mit Stäbchen-Photorezeptoren?. *AOO*, Lübeck, Germany

Domdei N, Domdei L, Reiniger JL, Holz FG, Harmening WM (2018) Funktionelle Untersuchung einzelner Stäbchen-Photorezeptoren in vivo. *DOG*, Bonn, Germany

Domdei N, Holz F, Harmening WM (2016) Functional imaging of single photoreceptor cells in the living human eye. *Young Researcher Vision Camp*, Leibertingen, Germany

Domdei N, Sheehy C, Roorda A, Holz FG, Harmening WM (2014) Yes, we (s)can: Ein Ophthalmoskop zur Stimulation einzelner Rezeptorzellen. *Jahrestreffen des Arbeitskreises Ophthalmische Optik (AOO)*, Ilmenau, Germany.

Conference presentations (Poster)

Domdei N, Domdei L, Reiniger JL, Holz FG, Görlitz A, Harmening WM (2017) High contrast stimulation with an optimized adaptive optics SLO for cellular level visual psychophysics. *ECVP*, Berlin, Germany

Reiniger JL, Sheehy C, **Domdei N**, Holz FG, Roorda A, Harmening WM (2017) Photoreceptor-resolved visual psychophysics with and without adaptive optics. *ECVP*, Berlin, Germany

Fang P, **Domdei N**, Herrmann P, Harmening WM, Schmitz-Valckenberg S, Holz FG, Krohne TU (2017) Effect of optical coherence tomography B-scan density on the identification of intra- and subretinal fluid in patients with macular diseases. *DOG*, Berlin, German

Domdei N, Tellers P, Wagner H (2016) Rate variability analysis of auditory pathway units in barn owls. *Young Researcher Vision Camp*, Leibertingen, Germany

Herrmann P, **Domdei N**, Krohne TU, Harmening WM, Issa PC, Holz FG (2016) Analysis of retinal damage after use of high powered, handheld laser pointer in five children. *Annual Meeting of the German Ophthalmology Society (DOG)*, Berlin, Germany

Domdei N, Holz FG, Roorda S, Sincich L, Harmening WM (2015) Characterization of an adaptive optics SLO based retinal display for cellular level visual psychophysics. *ECVP*, Liverpool, United Kingdom

Harmening WM, Ratnam K, Roorda A, **Domdei N** (2015) Limits of spatial vision in the presence and absence of fixational eye movements. *European Conference on Visual Perception (ECVP)*, Liverpool, United Kingdom

Domdei N, Holz FG, Sincich LC, Harmening WM (2015) In vivo imaging and stimulation of human cone photoreceptors with adaptive optics scanning laser ophthalmoscopy. *Young Researcher Vision Camp*, Leibertingen, Germany

Domdei N, Holz FG, Sincich LC, Harmening WM (2015) Spatial characteristics of an AOSLO-based micro display for in vivo retinal function testing on single photoreceptor level. *Pro Retina Meeting*, Potsdam, Germany.

Harmening WM**, Domdei N**, Tuten WS, Holz FG, Sincich LC (2014) Einzelzellpsychophysik. *Jahrestreffen des Arbeitskreises Ophthalmische Optik (AOO)*, Ilmenau, Germany.

Acknowledgements

I thank my mentor Dr. Wolf Harmening for giving me the opportunity to pursue these fascinating and challenging projects during my time as the first PhD student of the AO Vision lab. He enabled me to immerse into the field of vision science, broaden my scientific skills, and allowed me to develop and implement my own ideas. Even more, I value the well-grounded arguments and corrections from him.

I also thank Prof. Gerhard von der Emde for his willingness to be the second reviewer of my thesis and his assistance during the registration process of my doctorate. Furthermore, I thank Dr. Vera Schlüssel and Prof. Jochen Dingfelder for their willingness to serve as the third and fourth member of my doctoral committee and Prof. Frank G. Holz for the opportunity to write this thesis in his clinic.

I sincerely thank all the employees of the AO vision Lab I have meet during my time in the lab. They built an encouraging and vibrant working environment. In particular, I will always remember, Michael "Beton-Michen" Linden and my fellow doctorate student Jenny "JLo" Reiniger. You are true friends and I could always count on you when I needed technical assistance, constructive feedback or simply an eye for my studies.

My thanks go to the entire Augenkeller of the University Eye Hospital for the numerous helpful conversations during my doctorate and fun activities outside the lab. My special thanks goes to Dr. Johanna Meyer for her continuous helpful support and reviewing the very first draft of my thesis.

Thanks to Roland and Elke Schulz for proofreading my thesis.

I thank my family for their endless support, throughout my entire life. Without you I would not have been able to achieve all this.

Finally, I heartfully thank Leonie for always providing a safe haven in stormy times, for taking my mind off my work when I needed it and for encouraging me to get back on my feet. Thank you!